SILVER (AG) NANOROD ARRAY-BASED DETECTION OF OLIGONUCLEOTIDE COMPLEXES OF INFLUENZA BY SURFACE-ENHANCED RAMAN SPECTROSCOPY (SERS)

by

PIERRE NEGRI

(Under the Direction of Professor Richard A. Dluhy)

ABSTRACT

Recent progress in substrate nanofabrication has led to the development of Ag nanorod arrays as uniform, reproducible, large area SERS-active substrates with high signal enhancement. These novel nanostructures fabricated by oblique angle vapor deposition (OAD) offer a robust platform for the rapid detection of biological agents and open new perspectives for the development and integration of biomedical diagnostic for clinical and therapeutic applications. Ag nanorod arrays have been investigated as SERS-active substrates for the label-free optical detection of nucleotide complexes by monitoring the surface-enhanced Raman spectra of the oligonucleotide probe-viral target complex. The assays presented in this work consist of oligonucleotide-based arrays immobilized on the surface of a SERS-active substrate that allow binding of viral nucleoprotein constituents of the viruses contained in a commercially available split-virion inactivated influenza vaccine, as well as detection of various influenza RNA strains containing a

gene mutation coding for a viral protein associated with high virulence of influenza. Multivariate statistical methods were employed to confirm statistically significant differences between the spectra of the DNA probes and their complexes after binding to the viral targets. These results provide the first evidence for the use of oligonucleotide-modified SERS substrates as diagnostic tools for influenza virus detection in a complex biological matrix. The findings demonstrate that bio-nanotechnology combined with vibrational spectroscopy has the ability to enhance both detection and diagnosis of emerging viral infections while allowing point-of-care testing in clinical applications to rapidly determine disease risk and the appropriate course of action to reduce its spread.

INDEX WORDS: Surface-Enhanced Raman Spectroscopy, Ag Nanorod Arrays, Influenza Virus

SILVER (AG) NANOROD ARRAY-BASED DETECTION OF OLIGONUCLEOTIDE COMPLEXES OF INFLUENZA BY SURFACE-ENHANCED RAMAN SPECTROSCOPY (SERS)

by

PIERRE NEGRI

B.S., University of South Carolina Aiken, 2008

A Dissertation Submitted to the Graduate Faculty of

The University of Georgia in Partial Fulfillment

of the Requirements for the Degree

DOCTOR OF PHILOSOPHY

ATHENS, GEORGIA

2012

SILVER (AG) NANOROD ARRAY-BASED DETECTION OF OLIGONUCLEOTIDE COMPLEXES OF INFLUENZA BY SURFACE-ENHANCED RAMAN SPECTROSCOPY (SERS)

by

PIERRE NEGRI

Major Professor:	Richard A. Dluhy
Committee:	Jason Locklin Gary Douberly

Electronic Version Approved:

Maureen Grasso
Dean of the Graduate School
The University of Georgia
December 2012

ACKNOWLEDGMENTS

I would like to first and foremost thank my parents, family members, and friends for their support and encouragement throughout my graduate career. I would also like to thank my advisor, Dr. Dluhy for his supervision and guidance, as well as the members of my research committee, Dr. Locklin and Dr. Douberly for their suggestions, diligence, and constructive criticism over the past few years.

In addition to family, friends, advisor, and committee members, I would like to thank my co-workers and peers that have greatly contributed to my learning experience at the University of Georgia. More particularly, Dr. Driskell for sharing his knowledge and experience at the beginning of my research, Dr. Zhu and Dr. Hennigan for the tremendous help with chemometrics, Dr. Abell for the fruitful discussions regarding the fabrication, characterization, and functionalization of Ag nanorod substrates, as well as my current group members Sharon Martin and Omar Rivera for the help and support.

Last, I would like to graciously acknowledge the UGA Office of the Vice President for Research through a UGA Faculty of Infectious Disease Seed Grant, the U.S. Army Research Laboratory, as well as the National Institutes of Health for providing the necessary funding.

TABLE OF CONTENTS

CHAPTER 3

CHAPTER 4

CHAPTER 5

LIST OF TABLES

Page

LIST OF FIGURES

Page

LIST OF SYMBOLS AND ABBREVIATIONS

CHAPTER 1

υ_0	incoming radiation frequency
$\upsilon = 0$	ground vibrational state
$\upsilon = 1$	first vibrationally excited state
υ_v	frequency of a Raman active mode (at a specific virtual state υ)
$h\upsilon_{ex}$	energy difference between the ground state and a particular virtual state
υ_s	Stokes shift
υ_a	Anti-Stokes shift
P	dipole moment
E	external electric field
α	polarizability of a molecule
$d\alpha$	polarizability derivative
dQ	derivative of the normal coordinate of the vibration
Ar^+	argon ion
Kr^+	krypton ion
He-Ne	helium-neon
Nd: YAG	Neodynium-Doped Yttrium Aluminum Garnet ($Y_3Al_5O_{12}$)
SHG	Second Harmonic Generation
ITO	Indium Tin Oxide
CCD	Charge-Couple Device

CHAPTER 2

V	Volt
SCE	Saturated Calomel Electrode
Å	Angstrom (1.0×10^{-10} m)
SPR	Surface Plasmon Resonance
LSPR	Localized Surface Plasmon Resonance
UV	UltraViolet
IR	InfraRed
RPM	Rotation Per Minute
NIR	Near InfraRed
R6G	Rhodamine-6G
D_2O	deuterated water
S/N	Signal-to-Noise ratio

CHAPTER 3

RF	Radio Frequency
DC	Direct Current
W	Watt
QCM	Quartz Crystal Microbalance
SEM	Scanning Electron Microscopy
GLAD	GLancing Angle Deposition
SAM	Self-Assembled Monolayer

DSSC	Dye Sensitized Solar Cells
SEM	Scanning Electron Microscopy
CVD	Chemical Vapor Deposition

CHAPTER 4

Ar	Argon
Ti	Titanium
Ag	Silver

CHAPTER 5

PCA	Principal Component Analysis
HCA	Hierarchical Clustering Analysis
PLS-DA	Partial Least Squares Discriminant Analysis

CHAPTER 6

RT-PCR	Real-Time Polymerase Chain Reaction
PDMS	PolyDiMethylSiloxane
Hz	Hertz
AFM	Atomic Force Microscopy

CHAPTER 7

ELISA	Enzyme-Linked ImmunoSorbent Assay

CHAPTER 1

Introduction to Raman Spectroscopy

The purpose of this chapter is to introduce the reader to the theory and basic principles of Raman spectroscopy, the vibrational spectroscopic technique employed in this work. A retrospective of the discovery of the Raman effect is provided, as well as a brief description of the origin of the fundamental vibrations observed in Raman. Also included in this chapter are a short summary of the components making up a Raman spectrophotometer followed by an overview of the early Raman studies conducted on a variety of samples with an emphasis on biological samples.

1.1. Discovery of the Raman Effect

In 1928, Chandrasekhara Venkata Raman and Kariamanickam Srinivasa Krishnan reported the results of their studies on the scattering of light entitled "A New Type of Secondary Radiation" in the scientific journal Nature.(1) In their paper, their described a modified scattered radiation of degraded frequency resulting from irradiation of atoms or molecules by a powerful illumination source and discovered what is now referred to as the Raman effect. Raman received the Nobel Prize in Physics in 1930 for the discovery of the scattering of light and his contribution to the development of the technique. The Raman effect was designated an American Chemical Society National Historical Chemical Landmark in 1998, demonstrating the significance of the discovery.

Raman is a spectroscopic technique based on inelastic scattering of monochromatic light, usually from a laser in the visible, near infrared, or near infrared range.(2) When light is scattered from a molecule or atom, most photons are scattered with the same frequency as the incoming light source. This phenomenon is deemed an elastic or Rayleigh scattering event. However, Sir Raman and Sir Krishnan discovered that about one in a million photons is inelastically scattered at a different frequency than that of the incident photons. Upon irradiation of the sample with the light source, the frequency of the reemitted photons is shifted up or down in comparison with the original monochromatic frequency, which is called the Raman effect.

Figure 1.1 shows the energy level diagram that represents the Stokes and Anti-Stokes transitional schemes. When monochromatic laser light with a particular frequency excites atoms or molecules, it creates oscillating dipoles that emit light of three different frequencies. In the case where a photon is scattered from an atom or molecule as a result of their excitation from the ground vibrational state, $\upsilon = 0$, to a virtual state designated by j with the same frequency as the incoming frequency υ_0, the photon is said to be elastically scattered or Rayleigh scattered. However, when a photon is scattered off a molecule in a ground vibrational state, a momentary change in the energy state of the molecule corresponding to the virtual state takes place. Atoms or molecules in the ground state may absorb a photon corresponding to an energy of $h\upsilon_{ex}$ and emit a photon with a change in energy represented by $h(\upsilon_0 - \upsilon_v)$. In this case, part of the photon's energy is transferred to the Raman-active mode with frequency υ_v and the resulting frequency of scattered light is reduced to $\upsilon_0 - \upsilon_v$. This is referred to as a Stokes shift and written as v_s.

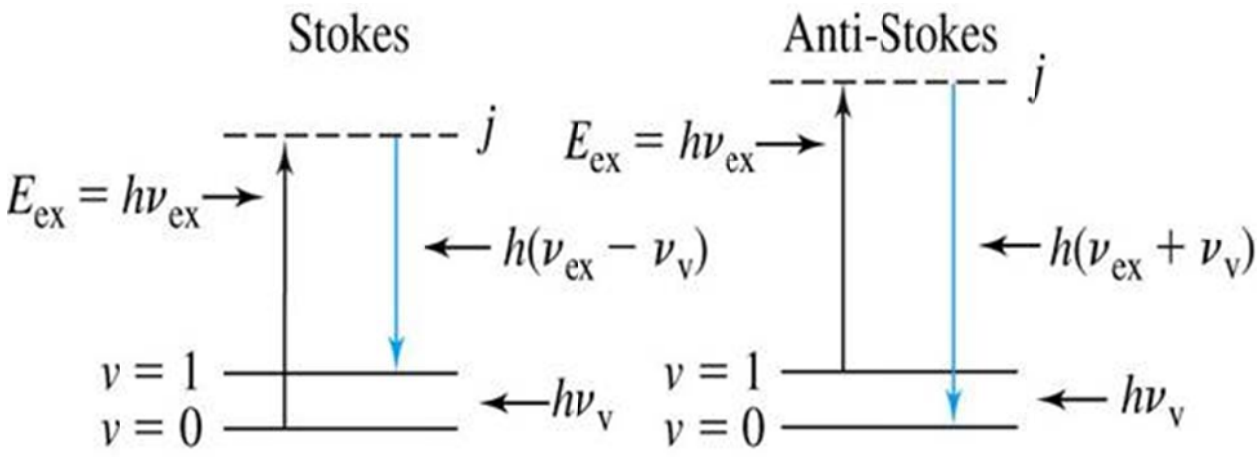

Figure 1.1. Energy level diagram for the Stokes and Anti-Stokes transitional schemes.

Conversely, atoms or molecules in an already vibrationally excited state, $\upsilon = 1$, scatter and return to their ground state by emitting a photon with energy corresponding to $h(\upsilon_0-+\upsilon_v)$. In this case, excessive energy of the excited Raman-active mode is released as the molecule returns to the basic vibrational state and the resulting frequency of scattered light goes up to $\upsilon_0+\upsilon_v$. This Raman frequency is called anti-Stokes shift and written as v_a.(3)

The absorption of energy (Stokes) results in a red shift in the Raman spectrum, whereas a loss in energy (anti-Stokes) results in a blue shift. According to the Maxwell-Boltzmann distribution law, the population of atoms or molecules at $\upsilon = 0$ is much greater than that at $\upsilon = 1$. It follows that the red shifted Stokes lines are about thirteen times greater in intensity when compared to the blue shifted anti-Stokes lines when the system is at equilibrium. The intensity of anti-Stokes shifts increases when the system is at an elevated temperature, increasing the population of vibrational excited molecules in the system.(2-4)

Raman scattering is representative of the rotational, vibrational, or pure electronic transitions of the molecules. Figure 1.2 presents the full spectrum of scattered light for carbon tetrachloride. The most intense band at wavenumber 0 corresponds to the Rayleigh scattering. The bands present at higher (Stokes) and lower (anti-Stokes) frequencies correspond to the Raman shifts for carbon tetrachloride. The Raman shift is a value associated with the bonds in the system and is expressed in cm^{-1}, referred to as wavenumbers. Raman vibrational bands are not characterized by their absolute wavenumber value, but rather, by the magnitude of their wavenumber shift from the incident excitation energy. This value is representative of variation of energy and is used to

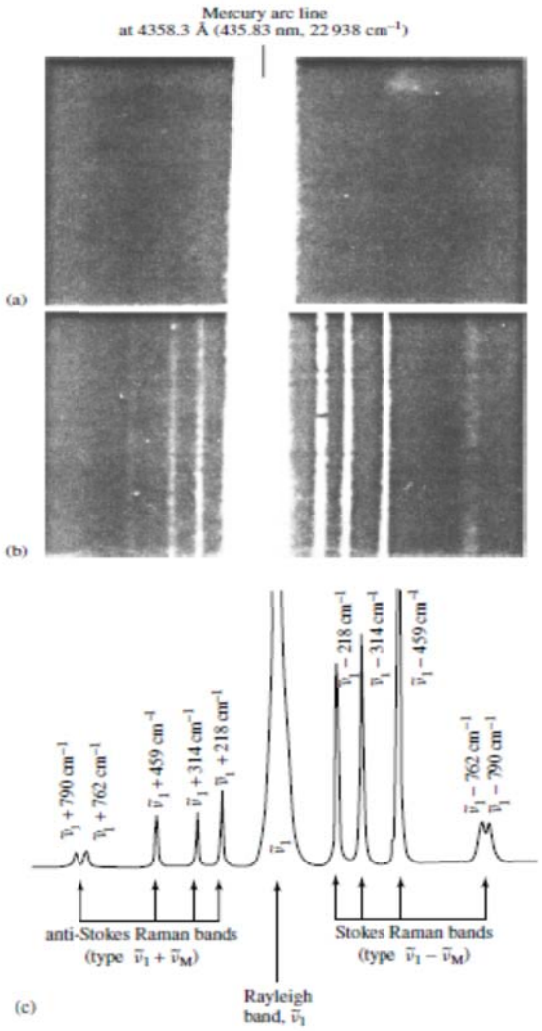

Figure 1.2. (a) Spectrum of a mercury arc in the region of 4358.3 Å (435.83 nm, υ_1 =22,938 cm^{-1}). (b) Rayleigh and Raman spectra of carbon tetrachloride (liquid) excited by mercury arc radiation, υ_1 =22,938 cm^{-1}. (c) Rayleigh and Raman spectra of carbon tetrachloride (liquid) excited by an argon ion laser, υ_1 =20,487 cm^{-1} (4 879.9 Å, 487.99 nm) and recorded directly. The spectra in (a) and (b) are facsimiles of spectra reported by Raman and Krishnan (1929) and were photographically recorded.

account for any variation in the shift with a change in excitation wavelength. In other words, using wavenumber shifts for Raman vibrations insures that these bands are always plotted the same, independent of the particular laser excitation energy used in the experiment.

1.2. Polarizability and Raman Selection Rules

A simple classical electromagnetic field description of Raman spectroscopy may be used to explain many of the dominant spectral features of Raman band intensities. The dipole moment, P, induced in a molecule by the external electric field, E, from the laser beam, is proportional to the field:

$$P = \alpha E \quad (1)$$

The proportionality constant α is the polarizability of the molecule. Polarizability is the ability of a charge distribution, such as an electron cloud of an atom or a molecule, to be distorted from its original shape by an external electric field.(5) When a molecule is placed in an electric field, it suffers distortion since the positively charged nuclei are attracted towards the negative pole, and the electrons towards the positive pole. This charge separation polarizes the molecule and produces scattering of light, which is associated with the oscillation of an electric dipole moment induced by the electric field of the laser beam. The induced dipole emits or scatters light at the optical frequency of the incident light wave. The direction of the induced dipole is depending on both the molecule and the direction of the electromagnetic wave. The fundamental selection rules established by quantum mechanics stipulate that a vibration is Raman-active when there is a net change in the polarizability of the molecule during the course of the vibration of the bonds.

Raman scattering occurs because a molecular vibration changes the polarizability of the molecule. This change is characterized by the polarizability derivative, $d\alpha/dQ$, where Q is the normal coordinate of the vibration. The selection rules for a Raman-active vibration states that there must a change in polarizability during the course of the vibration.(3-5) Mathematically, this statement may be described as follows:

$$d\alpha/dQ \neq 0 \quad (2)$$

The Raman selection rule is analogous to the more familiar selection rule for an infrared-active vibration, which states that there must be a net change in the dipole moment during the course of the vibration. From group theory, it is straightforward to show that if a molecule has a center of symmetry, vibrations that are Raman active will be silent in the infrared, and *vice versa*. Note that the scattering intensity is proportional to the square of the induced dipole moment, *i.e.*, to the square of the polarizability derivative. The degree of polarizability of a molecule also determines the vibrational Raman cross section. The cross section of a molecule is characteristic of the area available for interaction with the electric field of the incident monochromatic laser light. It follows that the larger the Raman cross section, the more likely the molecule will produce a strong Raman spectrum.

1.3. Vibrational Modes and Intensities

A molecule may absorb and emit energy by interacting with photons that may excite molecules to higher vibrational states. These vibrations are quantized and are called the normal modes of the molecule. A linear molecule with N atoms has 3N-5 normal modes, whereas a non-linear

molecule has 3N-6 normal modes. The motions that characterize each normal mode may be: (i) bending motions between three atoms connected by two bonds, (ii) stretching motions between two bonded atoms, and (iii) out-of-plane deformation modes that change an otherwise planar structure into a non-planar one. The vibrational spectrum of a molecule is composed of bands representative of some active normal vibrations characteristic of the molecule. The spectrum depends on the masses of the atoms in the molecule, the strength of their chemical bonds and their atomic arrangement.(6) In addition, Raman vibrational bands are characterized by their frequency (energy), intensity (polarizability), and band shape (environment of bonds). Since the vibrational energy levels are unique to each molecule, Raman spectra provide a "fingerprint" of a particular molecule. The frequencies associated with these molecular vibrations depend on the masses of the atoms, their geometric arrangement, and the strength of their chemical bonds. Note that the frequency of the laser is independent of the frequency of the vibration but that scattering intensity in general is dependent on the frequency of the excitation source to the fourth power.(4, 5) Additionally, Raman spectra provide information on molecular structure, dynamics, and environment of the molecule of interest.(6)

1.4. Raman Spectroscopy Instrumentation

In common with most instrumental techniques, instrumentation for Raman spectroscopy has evolved over time. Conducting Raman experiments requires a variety of elements of instrumentation that have evolved over the years with the advancement of technology. Typically, a Raman spectrometer consists of a laser source, a cell to hold the sample, a wavelength selector,

a radiation transducer and the appropriate signal processor, and a detector or read-out device. Figure 1.3 presents a schematic of these components. A detailed description of each follows.

Laser Source

The sample to be analyzed is normally illuminated with a laser beam in the ultraviolet (UV), visible (Vis) or near infrared (NIR) range. The laser source is generally a He-Ne, Ar^+, or Kr^+ laser delivering different wavelengths. He-Ne lasers emit a highly collimated beam of light at a wavelength of 632.8 nm; Ar^+ lasers emit wavelengths at 488.0 and 514.5 nm, and Kr^+ lasers emit wavelengths at 530.9 and 647.1 nm.(3) Bandpass filters or pre-monochromators are usually needed to filter out the extra (atomic) laser plasma lines for these ion lasers. Diode lasers emitting in the near-infrared region (NIR) are also commonly used for Raman spectroscopy and are typically used for biomedical applications to minimize potential problems with sample fluorescence and sample damage. The most commonly used emission wavelengths produced by diode lasers for Raman studies are 785 nm and 830 nm. The incident wavelength must be chosen carefully, as many samples undergo photodecomposition at shorter wavelength. Additionally, some samples fluoresce and others absorb the incident radiation or the Raman scattered Radiation. Ideally, the optimum wavelength for a system would result in high intensities, low photodecomposition, low fluorescence, and low absorbance.(2) Solid-state lasers such as Nd: YAG (Neodynium-doped Yttrium Aluminum Garnet) lasers may also be used to collect Raman measurements. Nd: YAG is a crystal that is used as a lasing medium for solid-state lasers. It is the neodymium ion that allows the lasing activity in the crystal and provides the emission wavelength at 1064 nm. Frequency doubling or second harmonic generation (SHG) may be achieved using a Nd: YAG laser in combination with a doubling crystal to produce a wavelength that is one-half of the fundamental wavelength of the laser (532 nm in the case of the Nd: YAG laser). Pulsed lasers have also been implemented in a variety of Raman studies to optimize

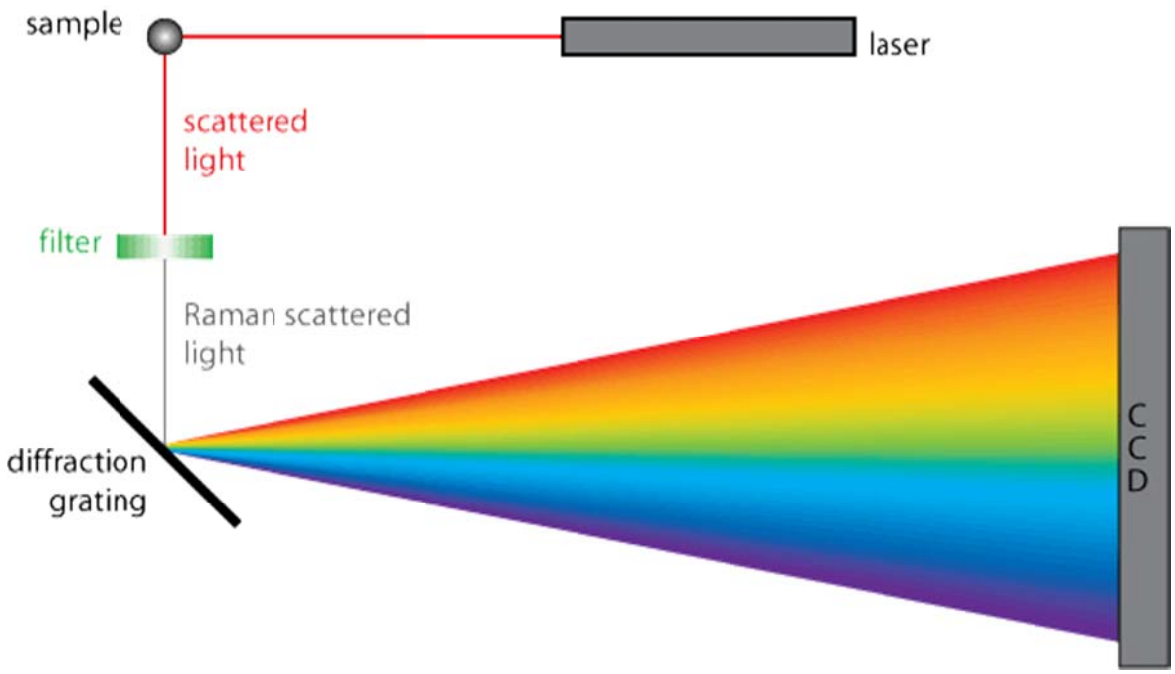

Figure 1.3. Schematic representation of the components making up a Raman spectrometer. The components include a laser source, a sample cell, a wavelength selector (filter), a radiation transducer (diffraction grating) and the appropriate detector (CCD).

the excitation wavelength. These lasers typically generate high peak power which may damage and/or induce photochemistry on the sample. However, these lasers have found usefulness in a variety of studies where short pulses allow for time-resolution techniques to reject background fluorescence.

Sample Cell

Raman measurements may be conducted on gas, liquid, and solid samples. Sample handling for Raman spectroscopic measurements is simpler than for infrared spectroscopy where glass may not be used for windows, lenses, and other optical components of the system. In Raman spectroscopy, both the exciting and scattered radiation is in the visible region, and therefore glass and quartz may be used as sample chambers. However, glass chambers may produce a high level of fluorescence background at certain excitation wavelengths and therefore indium tin oxide (ITO) glass is usually preferred. In the most recent Raman systems, the laser source is easily focused on a small sample area using a set of objectives and lenses and the scattered radiation efficiently focused on a slit. Consequently, very small samples may be investigated. For liquid analytes, an ordinary melting point capillary is typically used as a sample holder.(3) Since water is a weak Raman scatterer, the solutions may be analyzed in an aqueous environment. This advantage is particularly important for both inorganic and biological samples. Analysis of solid samples requires very little sample preparation. Raman spectra of solid samples are often acquired by filling a small cavity preferably with a fine powder of the sample. The solid may be mounted with the laser beam and not dot required to be in a special sample holder. For Raman analysis of gaseous samples, a higher powered laser is usually required and a specially designed sample cell is needed to contain the gas.

Radiation Transducer

The use of a wavelength selection device is critical to conduct Raman measurements. Since Raman scattering is intrinsically very weak, the main challenge is to collect Raman spectra with a high degree of resolution (usually less than 5 cm^{-1}) in order to separate the intense Rayleigh line from the weaker Raman lines. To obtain better resolution, a number of monochromators may be utilized. Presently, holographic diffraction gratings are the dispersive elements of choice to improve the resolution in comparison to the ruled gratings used previously.(3) A diffraction grating is an optical element with a fine periodic structure of lines used to split and diffract light into its constituent wavelengths. A holographic dispersion grating consists if equally spaced parallel grooves with characteristic groove spacing formed on a reflective coating surface. The dispersion arises from the wavefront division and interference of the incident radiation from the periodic structure of the grating. The dispersed light in then re-imaged by the spectrograph and the required wavelength range is directed to a detection system.

Detector

Historically, Raman spectrometers were equipped with photomultiplier tubes as detecting devices. Recent technological advances allowed replacement of photomultiplier tubes by photon counting systems. The inherent properties of photo counting systems offer improvement of signal to noise ratio of the weak Raman signal and its residual background. Additionally, photon counting systems are robust and provide accurate results even at high photon intensities.(3) Currently, the state of the art detectors are linear diode arrays and CCD detectors. Linear diode

arrays produce a voltage when light energy is detected. This voltage is amplified, multiplexed, and converted to a digital signal. Unlike linear diode arrays, CCD detectors are integrated circuits etched onto a silicon surface forming light sensitive elements called pixels. Initially designed as memory devices, CCD detectors are becoming the read-out devices of choice in Raman spectroscopy due to their fast readout speed, wide dynamic range and high quantum efficiency.

1.5. Applications of Raman Spectroscopy

Although the Raman effect was demonstrated in 1928, it took several years for Raman spectroscopy to become a routine analytical tool. The main reason behind this lack of utility is the inherently weak nature of the Raman scattering effect; that is, only a small fraction of light (less than one photon in a million) impinging upon a sample is scattered inelastically. Thus, intense monochromatic light is required to ensure that sufficient scattered light is produced to allow detection. As a result, development of applications of Raman spectroscopy has become feasible with significant improvement of instrumentation. Development of the laser allowed stimulation of the Raman effect as detectable levels. Later, the development of methods for microscopic sampling represented a major advance for the emergence and development of Raman spectroscopy in the biological field. The following sections highlight the initial development of Raman spectroscopy as an analytical tool and present a brief introduction of the early Raman-based studies for bioanalytical applications.

Early Development

Since the discovery of the Raman effect, Raman spectroscopy has become one the principal methods of nondestructive chemical analysis for both organic and inorganic compounds. In the years following the discovery of the effect, Raman spectra of many diatomic, linear, and symmetric top polyatomic molecules were investigated. The unique spectrum of Raman scattered light acquired for these molecules initially served as a "fingerprint" that could be used for quantitative analysis, even in a mixture of materials. These initial studies laid the ground work for the development and confirmation of the theory of the Raman effect in molecules. Initial work by Placzek and Teller aimed to elucidate the theory of the Raman effect established the rotational structure of Raman bands.(7) Following this achievement, very little further work, either experimental or theoretical, was done on this subject. In the early 1950's, developments in instrumentation such as the water-cooled mercury arc lamp and the introduction of photoelectric recording spectrometers have invigorated the field into a new spurt of activity. Shortly after, the invention of the laser in 1961, especially the argon ion laser in 1964, offered the availability of a high power, continuous-wave (CW), coherent and monochromatic light source that gave Raman spectroscopy a re-birth in terms of its applicability as an analytical technique.

Initial Raman Studies

Shortly after the early stages of experimental and theoretical development of the technique, Raman spectroscopy established itself as the analytical method of choice for the study of a variety of sample analytes. The intrinsic capabilities of Raman spectroscopy to probe structural

and electronic characteristics of molecules opened a new door for the study of molecular structure. Due to its non-invasive properties, Raman spectroscopy could be applied not only to liquids, but also to gases and solids. Unlike many other analytical methods available at the time, Raman spectroscopy was also applicable to the analysis of aqueous solutions. Gas-phase Raman spectroscopy was also extensively studied using Raman in the mid 1900's.(8-16) The recording of a Raman spectra of gases was not straightforward and limited due to experimental limitations. First, the spectra of molecules in the gas phase, predominantly due to spontaneous or incoherent scattering, were limited in terms of resolution by the width of the exciting line or, if narrow line laser sources were used, by Doppler and pressure broadening of the transition.(17) Even with the largest grating spectrographs available at the time, the best resolution attained was never better, i.e., smaller, than ca. 0.05 cm^{-1}. Second, the low number density of molecules in the gaseous or vapor state made it difficult to acquire Raman spectra due to the inherently low intensity of the scattered radiation. In spite of these shortcomings, however, a large amount of useful data was obtained using spontaneous Raman spectroscopy.

Raman spectra of a number of simple molecules in the gaseous phase have been collected. A few examples are methane,(18) inorganic halogenides,(19) oxygen,(20) carbon disulphide,(21) carbon dioxide,(22) and methylamine.(23) Raman spectra acquired in gaseous state were also compared to the spectra obtained in the liquid state. In the study of methylamine, the spectral bands acquired in both phases varied in both intensity and shift in wavelength. For example, the magnitude of the band representative of the N-H shift due to hydrogen bonding between NH_2 groups in the liquid phase did not take place to an appreciable extent at the lower pressure

conditions required in the gas phase.(23) In spontaneous (or linear) Raman spectroscopy of gases, commercial Raman spectrometers with a high resolving power may be used, but dedicated spectrometers have been constructed to achieve the required specifications.(6) The resolution is limited by the slit width of the spectrometer and the half-width of the exciting line. Typically, analysis of gaseous samples required a powerful light source and a fast spectrograph. Careful precautions must be taken in the studies of gaseous sample to eliminate stray light. Confinement of the gaseous sample is usually accomplished using a glass chamber. Columnation of the scattering beam is usually required to avoid scattering by the glass chamber holding the gas itself.

Analysis of Biological Samples

Up until the 1970's, little has been made of Raman spectroscopy for the study of biomolecular interactions in aqueous media. The applications of Raman spectroscopy for the investigation biological molecules became possible shortly after the advent of commercial photoelectric-recording instruments of high performance. Additionally, the development of the laser allowed stimulation of the Raman effect at detectable levels routinely, resulting in the first laser Raman spectrum of a protein in 1970.(24) Of particular importance is the development of near-infrared lasers, which allowed stimulation of the Raman effect with reduced or even abolished contributions from fluorescence from biological molecules. Furthermore, the development of methods for microscopic sampling was crucial to the emergence of Raman spectroscopy in the biological arena. In particular, the instrumentation designed by Delhaye and Dhamelincourt in 1975,(25) which allowed Raman microscopic imaging to be performed, represented a major

advance for the induction of Raman spectroscopy as a technique for biomedical applications. However, the application of Raman spectroscopy to study biological samples really made major strides with the integration of the charge coupled device (invented in the 1970's) into Raman imaging systems as the imaging element, allowing detection of the extremely weak Raman effect with high sensitivity.

Raman studies have been performed on a variety of biological elements. The molecular specificity of Raman spectroscopy is such that it offers a sensitive probe for many biomolecular interactions of interest, i.e., hydrogen bonding, isomeric changes, tautomeric equilibria, etc.(6) For example, receptor binding induced conformational changes have been studied using Raman spectroscopy.(26-32) One study looked into the secondary structure of the cAMP receptor protein, referred to as CRP.(27) Raman spectra of CRP in solution and CRP cAMP cocrystals were acquired and compared. More specifically, two amide regions of the spectra, Amide I 1630 - 1700 cm^{-1} and Amide III 1220 - 1300 cm^{-1}, were compared for varying concentrations of CRP in solution. In this study, the distribution of conformations appeared to be the same for all solutions despite buffer and CRP concentration. In contrast, comparison of the spectra acquired on the CRP-cAMP cocrystals to spectra of CRP alone showed spectral differences in the two amide regions, suggesting conformational changes in the secondary structure upon cAMP binding to CRP.

Oligonucleotides

Raman studies of other biological molecules such as oligonucleotides have been carried in the early 1950's. The recent progress in Raman instrumentation at the time provided the ability to study samples in solution, hydrated fibers or films, polycrystalline and crystalline states. Raman spectroscopy allowed correlations to be made between structures determined in the solid state by X-ray crystal diffraction and in solution by NMR.(33, 34) Thus the structural conclusions obtained by single-crystal studies could be extended (or otherwise) to aqueous solutions simply by comparing the corresponding Raman spectra. For example, the combination of X-ray and Raman techniques using the same DNA or RNA crystals has allowed sets of marker Raman lines to be obtained, characteristic of different geometries in solid state and further detected in amorphous (hydrated fibers and films) and solution states.(35, 36) For early Raman studies of DNA, bulk samples were required, typically in solid form or concentrated aqueous solutions. Otto and co-workers studied aqueous solutions of individual DNA bases to establish the spectral bands associated with each base.(37) In this study, the DNA bases were devoid of their phosphate backbone or sugar moiety. Other studies have emphasized on the structural changes of DNA oligonucleotides.(38-45) In these studies, the characteristics of B-type conformations of DNA were monitored based on the Raman intensities of the Raman bands. One particular study focused on eight oligonucleotide strains, four of which having varying GC content and the other four simply being periodic DNA polymers.(43) The results from this study correlated the spectral variations in the region of 800 - 850 cm^{-1} to the GC content of the DNA strains as well as the base pair sequence within those strains. Additionally, bands attributed to A-family and B-family at 809 and 835 cm^{-1}, respectively, were observed, indicating that DNA was in both

conformations in solution. These initial protein and DNA-based studies built the ground work for the structural characterization of biomolecules and their change in conformation. The development of Raman spectroscopy in the early 1960's for biological analysis has proven effective for the advancement of spectroscopy-based biomedical applications. These early investigations allowed determination of the biomolecular structure of important biological molecules by Raman spectroscopy and paved the way for future work in the field using vibrational spectroscopy.

Raman spectroscopy involves the study of the interaction of electromagnetic radiation with molecular vibrations and provides viable means to elucidate the molecular structure of a number of sample types. Raman spectroscopy is an excellent technique that has a broad range of applications and provides solutions to a host of important and challenging analytical problems. As a vibrational technique, Raman spectroscopy may be carried out from a simple identification test to an in-depth, full spectrum analysis and allows for rapid, accurate qualitative and quantification of a wide range of analytes.

CHAPTER 2

Surface-Enhanced Raman Spectroscopy (SERS)

The purpose of this chapter is to introduce the reader to surface-enhanced Raman spectroscopy, the detection technique predominantly used throughout this work. A retrospective of the discovery of surface-enhanced Raman spectroscopy is provided, as well as a thorough description of the mechanisms responsible for the observed signal enhancement. Also included in this chapter is a short review of the common fabrication methods currently in use to produce SERS-active substrates followed by a summary of the applications of SERS in bioanalytical sensing.

2.1. Discovery of Surface-Enhanced Raman Spectroscopy

Raman spectroscopy arises from the vibrational frequencies of molecules and provide a "molecular fingerprint" that is particularly valuable in chemistry.(2) However, the inherent low sensitivity of spontaneous Raman scattering makes it a very weak technique in nature and limits its applicability as an analytical technique.(3-5) Conventionally, special measures are to be taken to distinguish it from the predominant Rayleigh scattering. As previously noted, about 99.999% of all incident photons in spontaneous Raman undergo elastic Rayleigh scattering. Consequently, only about 0.001% of the incident light produces inelastic Raman signal with frequencies $\upsilon_0 \pm \upsilon_v$. This type of signal is useless for practical purposes of molecular characterization. It was not until 1974 that the first surface-enhanced Raman spectroscopy (SERS) experiment was

serendipitously performed.(46) SERS is a phenomenon in which the Raman scattering intensity from molecules adsorbed or interacting with finely divided metal surfaces, typically gold (Au) or silver (Ag).(47, 48) Sensitivity enhancement by SERS has resulted in more widespread applications, especially in surface chemistry where the environmental sensitivity of vibrational spectra reveals how molecules interact with surfaces. Under ideal conditions, the Raman scattering intensity of molecules is enhanced by a factor of about 10^6 compared to standard Raman scattering.(49) The following sections include an introduction of the first experiments leading to the discovery of surface-enhanced Raman scattering as well as the initial characterization of the phenomenon responsible for the observed enhancement.

Adsorption of Molecules on Metallic Electrode Surface

In 1974, Fleishmann and co-workers studied the absorption of molecules at metallic electrode surfaces using Raman spectroscopy.(46) In their experiment, pyridine at a silver electrode surface was investigated to study monolayer adsorption of molecules at electrode surfaces. Silver was chosen as the metal due to its electrochemical properties and pyridine due to its strong Raman scattering cross section as well as its ability to readily absorb at the solid-gas interface.(50, 51) The working electrode was subjected to cyclic linear potential sweeping in the electrochemical cell for 15 minutes at 0.5 V/sec between + 200 and -300 mV in preparation for studies. The formation and reduction of silver chloride during each cycle resulted in substantial etching of the silver interface, resulting in an increase in surface area of approximately an order of magnitude. Spectroscopically, Raman spectra acquired on pyridine adsorbed to the electrode surface differed considerably when compared to those acquired using acidic oxide surfaces as the

substrate.(50, 51) Spectra acquired at the electrode showed Raman bands at 1008, 1025, and 1036 cm^{-1} whereas those acquired in aqueous pyridine exhibited bands at 1005 and 1037 cm^{-1}, respectively. Interestingly, the band at 1025 cm^{-1} decreased with potential in the cathodic direction, indicative of pyridine coordinating to the metallic surface through the nitrogen atom. The results showed surprisingly strong and potential-dependent Raman signals from the pyridine adsorbed on the silver electrode that had been electrochemically roughened in potassium chloride aqueous electrolyte. However, the spectra of pyridine adsorbed on the roughened silver electrode were very intense. The intensity of the spectra was initially attributed to an increase in molecular packing on the surface, which (due to successive oxidation and reduction cycles) had an increased surface area. Further research showed that this increased packing density alone could not account for the intensity increase observed at the silver electrode and in 1977, two independently developed theories explaining that the increase in intensity was due to an intrinsic surface enhancement.(52, 53) The enhancements observed in these two separate studies were in the magnitude of 10^5-10^6 in comparison to bulk material, marking the birth of a new technique that is now known as surface-enhanced Raman spectroscopy (SERS).(54)

Observation of Pyridine Adsorbed on a Roughened Silver Electrode

Albrecht and Creighton first expanded on Fleishmann's studies in 1977.(52) In a similar fashion, they acquired and compared Raman spectra of pyridine adsorbed to a silver electrode before and after a single oxidation-reduction cycle. Following a single voltage sweep, the spectral bands recorded at the end of the electrochemical cycle showed a drastic increase in intensity. Specifically, the bands at 1000, 1036, 1218, and 1605 cm^{-1} were nearly five times more intense

when compared to those in the spectra acquired before the sweep. The Raman spectrum acquired for the bulk pyridine solution after removal of the electrode was devoid of the 1025 cm^{-1} band, confirming that this band was due to pyridine adsorbed at the surface of the silver electrode.(46) Calculations of the surface area due to electrochemical roughening established a 10-20% increase when compared to an electrode prior to the cycle.(55) Further estimations performed by Fleishmann showed that the increase in pyridine adsorbed at the electrode surface could not account for the observed increase in intensity.(46) Albrecht and Creighton suggested that a surface effect may account for the increased molecular Raman scattering cross sections observed in their studies.(52) Previously, a study conducted by Haarer and co-workers had suggested the existence of a broadening of the electronic energy levels for molecules in proximity to roughened metallic surfaces.(56) Based on this observation, it was proposed that an interaction between the molecules and the surface plasmons at the roughened metallic surface may be responsible for the intensity increase in the Raman spectra.(57)

Investigation of the Observed Enhanced Raman Signal

In addition to Albrecht and Creighton, Jeanmaire and Van Duyne both independently studied pyridine adsorbed on a roughened silver electrode.(53) They set out to validate and expand on previous studies that employed Raman scattering to investigate species adsorbed on electrode surfaces.(58, 59) In previous studies, the Raman intensity was dependent upon the method of preparation of the electrode.(53) When the pyridine solution was held at a potential of -0.6 V in relation to the SCE, the signal was roughly one order of magnitude higher than pyridine in solution. In their investigation, Jeanmaire and Van Duyne carried out anodization in the presence

of pyridine, the signal increased up to a factor of 50. Addition of pyridine post anodization provided similar results. In addition, spectra of adsorbed pyridine acquired at a silver electrode lead to the appearance of a new band at 3067 cm^{-1} corresponding to a C-H stretch that was obstructed in aqueous solution.(53) As expected, bands at 1008 and 1036 cm^{-1} were observed at higher intensity when compared to the spectra acquired in aqueous solution. This observed increase in Raman intensity prompted a systematic investigation to determine the factors influencing the intensity using pyridine as the probe molecule. Jeanmaire and Van Duyne attempted to draw a direct correlation between the increased intensity and the number of molecules occupying the surface of the electrode. A pyridine molecule occupies 38 $Å^2$ in a flat configuration, and 25 $Å^2$ in a standing orientation, respectively.(60) Based on these dimensions, as well as the parameters of the Raman experiment, i.e., the sampling diameter of the laser source, the number of molecules sampled on the electrode surface was approximately 3×10^{13}. The recorded standard Raman spectra of pyridine adsorbed on the electrode was 5 to 6 orders of magnitude higher than those acquired in aqueous solution, suggesting that the electrode surface was indeed acting to enhance the signal.(53)

Further studies at various excitation wavelengths showed that the response was not due to a coupling mechanism of the scattering process with an electronic transition of the adsorbed molecule. This phenomenon is typically observed with molecules such as crystal violet and methyl orange where the electronic transition of the analyte is in resonance with a specific wavelength, leading to an increased Raman signal. Through continued experimentation, Jeanmaire and Van Duyne concluded that an increase on signal only occurred when the AgCl at

the electrode surface was indeed reduced, creating a roughened or etched surface. Upon further investigation, it was demonstrated that etching the surface did not create a large enough surface area increase to give rise to the observed enhancement. Hendra and co-workers determined that electrochemical etching the surface could only increase the surface area by a factor of ten. Since the observed signal increase was 50 fold, the surface area increase could not account for the observed enhancement alone. Jeanmaire and Van Duyne suggested that the observed enhancement was originating from the formation of active sites on the surface as a possible explanation in addition to the increase in surface area. In their subsequent publication, Jeanmaire and Van Duyne clarified the degree of Raman signal enhancement in the pyridine-on-silver system and both proposed enhancement mechanisms based on electromagnetic and chemical effects, respectively.

2.2. Surface Enhancement Mechanisms

Albrecht and Creighton as well as Jeanmaire and Van Duyne hinted that the observed enhancement could not be solely attributed to the increase surface area on the silver electrode. They rather suggested the existence of a surface mechanism responsible for the observed enhancement. Albrecht and Creighton proposed the existence of a mechanism based on resonance from electronic states(52) whereas Jeanmaire and Van Duyne proposed an electric field enhancement mechanism present on the surface of the silver electrode.(53) Parts of each proposed mechanism, were in fact, correct. Over the years, the observed surface enhancement has been attributed to two different mechanisms. The details of these two proposed mechanisms of the surface enhancement remain a matter of debate.

The SERS enhancement has been amply described in the literature and is primarily thought to be the result of two distinct mechanisms: a long-range classical electromagnetic (EM) and a short-range chemical enhancement (CE).(61) It is considered that the first proposed mechanism, the "Electromagnetic Model" (EM) operates in the majority of cases, although the second proposed mechanism, the "Chemical Enhancement" (CE) or "Charge Transfer Enhancement" is also often involved. As Raman scattering is governed by the relationship $P = \alpha E$ (1),then SERS must involve an increase in either or both of the terms E (amplitude of the electric field), and α (molecular polarizability).(48) The EM theory essentially addresses the enhancement of E, and the CE model is concerned with the enhancement of α. One common feature between these two theories is that they both require surface roughness for the surface enhancement to take place. The following sections describe the contribution of each of the two proposed mechanisms and shortly address the close distance dependence required between the analyte and the metallic surface with the appropriate morphologies for the spectral enhancement to occur.

Electromagnetic Enhancement (EM)

The electromagnetic enhancement (EM) model deals with E, the electric field of light (a molecule independent factor) and stipulates that enhancement is due to the structure of the surface, and interaction of adsorbed molecules with surface plasmons.(62, 63) The overall excitation of conduction electrons i.e., electron band, within a material, such as a metal, is referred to as a plasmon; when confined to a surface, it is deemed a surface plasmon. Surface plasmons are oscillating electromagnetic fields which exist at interfaces and decay exponentially on each side of the interface.(47) Their amplitude may be resonantly enhanced by radiation of a

suitable wavelength.(48, 63) The external electric field of the radiation provides an excitation causing conduction electrons in the metallic surface (typically gold or silver) to oscillate collectively, leading to a surface plasmon resonance (SPR).(49) Figure 2.1 depicts a schematic representation of a surface plasmon confined to a spherical metal particle (represented by a blue sphere). Metals commonly employed include, but are not restricted to silver, gold, and copper due to their ability to support a surface plasmon.(64-67) The external electric field of the incident radiation (represented by the blue arrow) provides an excitation causing the conduction electrons in the metal surface to oscillate collectively, leading to a surface plasmon resonance (represented by the orange sphere). On smooth surfaces, plasmon excitation energy is lost as heat, whereas roughed surfaces allow a portion of the plasma energy to be radiated. If the scale of the surface roughness is small in comparison to the wavelength of the incident radiation (λ), then a dipolar plasmon will radiate.(48) If this radiation is resonant with the Raman and Rayleigh scatter of a molecule on the surface, then the scatter will become substantially amplified. Using the spherical particle model,(68-70) molecules located within the external electric field experience an induced electric field $E_{induced}$ corresponding to:

$$E_{induced} = [\ \varepsilon_1(\omega) - \varepsilon_2 / \varepsilon_1(\omega) + 2\ \varepsilon_2\ ]\ E_{laser} \quad (3)$$

In the above equation, $\varepsilon_1(\omega)$ is the dielectric function of the metal, ε_2 is the relative permittivity of the environment, and E_{laser} is the applied external field from the laser. From this equation, it results that excitation of the surface plasmon significantly increases the local electric field

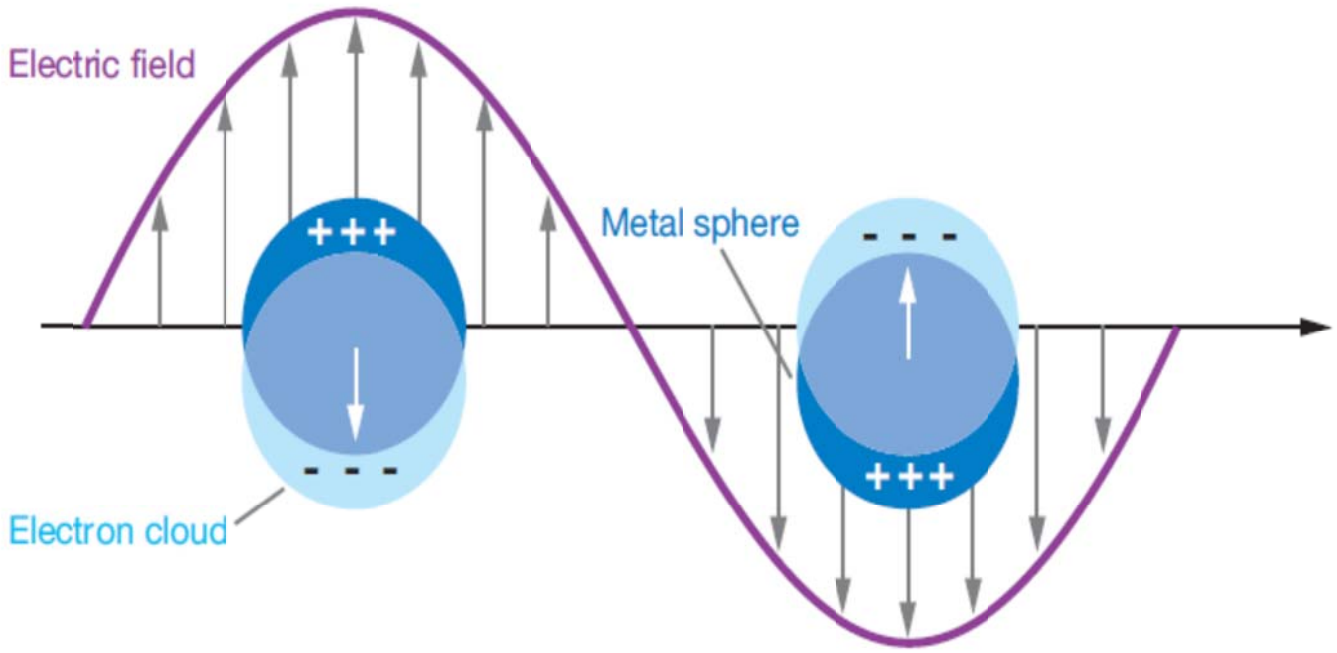

Figure 2.1. Schematic representation of surface plasmons confined to a spherical metal surface. Upon excitation from an external electric field, the conduction electrons in the metal collectively oscillate leading to a surface plasmon resonance. The interaction of the incident laser with the surface plasmon on these metal surfaces is responsible for the electromagnetic enhancement mechanism for SERS.(48, 63)

experienced by the molecule on the surface. With a small increase in the local field, the Raman scattering is greatly enhanced. Typically, the electromagnetic field due to the generation of localized surface plasmons at nanostructured metallic surfaces results in an EM enhancement on the order of E^2. An additional E^2 EM enhancement arises from the Stokes-shifted Raman scattering due to the induced dipole of the surface-adsorbed analyte molecule, thus leading to a total SERS EM field enhancement at the nanoparticle surface that scales as E^4.(71) The interaction of the incident electric field of the incident laser with the surface plasmon of metallic surfaces makes up the electromagnetic enhancement mechanism for SERS.

Chemical Enhancement (CE)

Measured enhancement factors are usually in good agreement with values calculated using the EM model, but in some cases it is apparent that the EM alone is not enough to account for the magnitude of the enhancement. For example, spectra acquired on CO and N_2 differ greatly in intensity by a factor of 200 even though the polarizabilities are comparable and the experimental conditions were held constant.(49) This observation was difficult to explain with strictly an electromagnetic enhancement and led to believe in the existence of a second mechanism contributing to the observed intensity differences. The chemical enhancement (CE) is based around the principle that an adsorbed molecule may, under specific conditions, interact with a metal surface in such a way that there is a large increase in molecular polarizability, α.(72) Specifically, the highest occupied molecular orbital (HOMO) and the lowest unoccupied molecular orbital (LUMO) of the adsorbed scatterer are symmetrically placed energically in relation to the Fermi level of the metal.(49) When this condition is met, charge transfer reactions

occur between the surface-adsorbed analyte molecule and the metal through the formation of localized adsorbate electronic resonances or metal-to-adsorbate charge-transfer complexes. These charge transfer reactions occur at half the energy of the molecular vibrations intrinsic to the adsorbate. In this scenario, the metal is irradiated by the incoming radiation source to create an electron-hole pair, hence creating a negatively charged excited molecule. The molecular geometry of this excited molecule differs greatly from that of the neutral species. This charge transfer induces a nuclear relaxation within the excited molecule which results in a transfer of energy to the analyte molecule through its bonds connecting it to the metal surface and the emission of a wavelength shifted (Raman) photon from the analyte molecule. Chemical enhancement required chemisorption of the Raman scatterer directly on the surface.(73) Evidence of this has been reported where metal-molecule stretching modes have been observed.(74) Additional evidence was demonstrated in a separate study where pyridine was adsorbed on different metals and the intensity of the Raman bands intrinsic to pyridine greatly differed in relative intensity from one metal to the other.(75) It was later determined that a change in the polarizability of the scattered due to charge-transfer of chemical bond formation between the metal surface and the molecule contributes to this mechanism. The enhancement requires that an overlap between the adsorbate and the metal substrate exist and scales at approximately E^2.(53) While the existence of the CE enhancement is itself not in doubt, the level to which it contributes to SERS signals is still a matter of debate.

In systems where both the chemical and electromagnetic enhancements come into action, the mechanisms are multiplicative.(49) Estimations regarding the overall enhancement per molecule

for the contribution of both chemical and electromagnetic enhancement mechanisms, scales on the order of $10^5 – 10^6$.(52, 53) It is commonly thought that the EM enhancement contributes the greater extent (~10^4-10^6) to the signal enhancement observed in SERS while the CE enhancement is thought to contribute to a smaller extent (~10-10^2) to the overall enhancement.(76, 77) Although calculation of the enhancement factor is both substrate and molecule dependent, a simple generic expression has been developed for any particular substrate and molecule.(78) This expression is as follows:

$$EF = (\text{SERS Intensity} / \#\text{ of molecules}) / (\text{Raman Intensity} / \#\text{ of molecules}) \quad (4)$$

Note that the integration time used in the measurements must be considered when calculating the signal intensities. Likewise, both incident surface power and beam dimensions must be taken into consideration when computing the number of molecules excited when comparing SERS and standard Raman intensities.(79) Taking these parameters into consideration, the SERS surface enhancement factor (SSEF) may be determined using the following expression:

$$SSEF = (I_{SERS}/\mu_M\mu_S A_M) / (I_{RS}/C_{RS}H_{eff}) \quad (5)$$

In the above expression, I_{SERS} and I_{RS} are the SERS and standard Raman intensities, respectively. μ_M is the surface density of the individual nanostructures, μ_s is the surface density of molecules on the substrate surface, A_M is the surface area of the metallic surface, C_{RS} is the concentration of the solution used, and H_{eff} is the effective height of the scattering volume. Using the above

expression, enhancement factors of up to 10^{14} have been reported for single molecule detection.(80, 81)

Distance Dependence

Characterization of the SERS enhancement has been amply described in the literature and is primarily thought to be the result of the two distinct aforementioned mechanisms: a long-range classical electromagnetic (EM) and a short-range chemical enhancement (CE). As previously stated, the electromagnetic enhancement (EM) is a long range effect that does not require the adsorbate to be in direct contact within but within a few nanometers of the metallic surface.(54, 73) In contrast, the chemical enhancement (CE) is short-ranged and requires the adsorbate to be chemisorbed directly to the surface. Gersten and Nitzan investigated the distance dependence of hemispheroids of varying dimensions.(82) In their study, the enhancement ratio was plotted as a function of distance from the surface for the particles and it was observed that the enhancement was greatest at the surface and fell off with increasing distance away from the particle surface. The hemispheroid shape of the particle played a role in the severity of the intensity fall off where a less eccentric particle had a more gradual fall-off of intensity with "significant" enhancement factors out to a larger distance than more eccentric spheroid particles. Essentially, a more spherical particle will have less severe distance dependence, whereas an ellipsoidal particle will have more significant distance dependence. Gersten proposed that this effect was due to the image enhancement effect previously discussed, a contributing factor to the overall electromagnetic enhancement mechanism.(82) Recently, Dieringer and co-workers studied the effect of nanoparticle distance on the overall SERS enhancement.(83) In their study, atomic layer

deposition (ALD) was sued to fabricate a spacer of a controlled distance from the roughened metal surface. ALD was used to deposit layers of aluminum oxide (Al_2O_3)(84, 85) at varying thicknesses ranging from 0.0 nm to 4.8 nm. Ag film over nanosphere (AgFON) substrates (a detailed description of these substrates is provided in section 2.3 of this chapter) were used as the base substrate for SERS studies. Studies of pyridine on AgFON with increasing Al_2O_3 showed that when the spacer distance was 2.8 nm away from the surface, the enhancement decreased by an order of magnitude. The acquired data was plotted and compared to Equation 3 and was almost a perfect fit, showing that little to no enhancement at a distance of 4.8 nm from the surface was observed. Previously, Equation 3, explained by the dipole decay law, had been used to correlate the fall-off of SERS intensity with distance from the surface for a monolayer of molecules. Other studies have also shown that the large electromagnetic field produced by the plasmons at the surface of a nanoparticle is approaching a zero value at a distance of over 10 nm away from the surface.(86)

2.3. Fabrication Methods of SERS-Active Substrates

Since the discovery of the SERS effect, a wide variety of fabrication techniques have been utilized to produce SERS-active substrates. The strongest SERS enhancements are observed with coinage metals (silver, gold, and copper) due to their ability to support a surface plasmon;(64-67) however the effect is expected for all metals with outer shells of $(n-1)d^{10}ns^1$.(48, 53, 66, 87, 88) In addition to composition, the shape of the substrate plays a crucial factor in the surface enhancement.

In recent years, advances in nanofabrication have led to the emergence of a number of novel nanostructures of various composition, morphology, size and shape that have proven to be successful SERS substrates. SERS enhancement theory stipulates that the creation of a high electromagnetic field is dependent on the metallic surface morphology.(48, 89) For example, the electromagnetic (EM) field is at maximum for regions with high curvature.(90, 91) Evidence of this has been reported by Murphy and co-workers on isolated silver and gold nanoparticles of various aspect ratios.(92) As a result, experimental conditions that affect the geometry and size of the particles must be carefully defined and controlled for generation of optimum EM enhancement. The following sections summarize the various nanofabrication techniques used to produce SERS-active substrates.

Chemical and Electrochemical Methods

Original fabrication of SERS-active substrates was based on chemical and electrochemical methods such as electrochemical oxidation-reduction cycles (ORC),(93) chemical etching,(94) and metal island films.(95) ORC is an electrochemical method in which Ag is subjected to successive oxidation-reduction cycles that create nano-roughened, SERS-active substrates. Chemical etching has also been widely used to produce roughened metallic substrates. This method consists of immersing a metallic substrate into a highly concentrated acidic solution (typically HNO_3) for a short period of time to chemically etch the metallic surface. The resulting roughened surface may then be used for SERS characterization. Metal island films are another form of specific nanostructures with high aspect ratios that have been developed as SERS substrates. They consist of vapor-deposited Ag film on a suitable surface to produce

discontinuous island-like particles that may act as SERS substrates. Although these methods allow production of large surface area substrates, they provide relatively low SERS enhancements and suffer from poor reproducibility.

Lithographic Techniques

Other nanofabrication techniques have been investigated to produce substrates for SERS applications. High aspect ratio nanostructures have been fabricated using lithographic techniques such as electron beam lithography (EBL),(96) nanosphere lithography (NSL),(97) as well as other approaches such as template(98) and hybrid methods.(99) Substrates produced by e-beam lithography are particularly beneficial for SERS because of the stringent control over the localized surface plasmon resonance (LSPR) that may be modified by varying the spacing and aspect ratios of the particles produced. EBL is a mask-less semiconductor fabrication technique that is routinely used for the growth and patterning of nanometer-scale features. Typically, SERS-active substrates produced by EBL produce an array of highly ordered structures produced by a focused beam of electrons capable of drawing patterns over the resist wafer in a serial manner with nanometer resolution.(96) Briefly, a beam of electrons focused across approximately 100 kV potential (beam current = 0.5 – 1.0 nA) is directed onto an electron resist-coated support. Regions of the resist film impacted by the focused electron beam are structurally modified to have an increased solubility in alcohol solutions (*e.g.*, methyl isobutyl ketone/isopropyl/isopropyl alcohol). Following vapor deposition with the noble metal (*i.e.*, gold or silver), the remaining metal-coated resist film is removed by a subsequent wash with N-methylpyrrolidone. This final wash typically yields an array of size-controlled, precisely placed

nanostructures constituting a spatially uniform, highly reproducible SERS-active substrate with the potential of providing large calculated SERS enhancements.

Nanosphere lithography (NL) is another lithographic technique that has shown to produce large-enhancement substrates. Particles arrays produced by NL have been experimentally demonstrated to provide enhancements up to 10^9. These substrates are created by vapor deposition of metal through a template created by the self-assembly of polystyrene nanospheres. Substrates fabricated by NSL typically consist of arrays of well-ordered nanospherical structures produced by vapor deposition of metal through a template usually consisting of a self-assembly of polystyrene nanoparticles.(100, 101) Lithographic techniques are reproducible, flexible and easily implemented to a large variety of templates and hence may produce numerous types of nano-features with different plasmonic properties; however, EBL methods suffer from high cost and the need for specialized infrastructure.

A monodispersed population of nanoparticles may be fabricated and confined to a surface using nanosphere lithography.(97, 102, 103) Specifically, a suspension of nanospheres are coated onto a base substrate and allowed to self-assemble into a hexagonally closed-packed colloidal crystal serving as a deposition mask. Once the colloidal crystal deposition mask if formed, Ag films of various thicknesses are deposited over the nanosphere mask. Van Duyne and coworkers deemed these structures film over nanosphere (FON) substrates. Specifically, they employed silver over silica nanospheres (AgFON) as the SERS-active substrate for a variety of SERS-based studies. These substrates proved to be thermally stable, SERS-active, and suitable for use in ultrahigh

vacuum (UHV) conditions.(103) AgFON have also been used to study the localized surface plasmon properties of nanostructures,(62, 71, 86) distance dependence of the SERS electromagnetic enhancement mechanism,(85) detect single molecules, and detect biomolecules.(104-109)

Template and Hybrid Methods

The lithography techniques discussed provide efficient methods of controlling the formation of specific nanostructures that are otherwise relatively expensive to produce. Another way of producing ordered structures is with template self-assembly of colloidal nanoparticles, a process pioneered by Velev and coworkers.(110, 111) Similar in structure and morphology to the substrates produced by lithographic techniques, SERS-active substrates produced by template methods consist of an array of nanostructures onto which Ag or Au is deposited via an electrochemical patterning method.(98) This procedure results in the formation of metallic nanorod arrays of high aspect ratios capable of supporting surface plasmons. These substrates show long term stability, allowing for continuous sampling experiments. They are very easily produced, inexpensive, and fabricated without any complex equipment. Likewise, the hybrid method results in the formation of a variety of nanostructures capable of producing EM hotspots. These substrates are produced by depositing metal particles onto nanoporous scaffolds such as porous silicon, nanowire arrays, and highly ordered pillars or toroids that may sustain plasmonic behavior for SERS applications.(99) These nanofabrication techniques allow stringent and rigorous control over the growth of the various nanostructures and hence have demonstrated enhancements up to 10^9. While these relatively simple methods provide inexpensive and flexible

ways of producing highly sensitive SERS-active substrates, they have not proven to be scalable to large surface areas.

Nanoshells

Metallic nanoshells typically consist of a dielectric core with a metallic shell of nanometer thickness, whose optical resonance may be optimized by varying their fabrication in a controlled manner. By tailoring the dimensions of the core and shell material in relation to one another, the optical resonance of these nanoparticles may be varied by over hundreds of nanometers in wavelength across the visible and into the infrared region of the spectrum.(112-115) Nanoshells are usually synthesized by reduction of $HAuCl_4$ by the reducing agent Na_2S in aqueous solution. Combining these two reagents results in a shift of the extinction coefficient as the nanoshells form in solution.(116) The progress of the reaction may be monitored by UV-visible spectroscopy from 400 to 1050 nm. Mercaptoproprionic acid is then added to halt this shift and stop the growth of the nanoshells when the extinction peak is centered around 1050 nm. The nanoshell solution is then brought to pH 10.5 by adding NaOH, centrifuged at 3000 RPM for 20 minutes four times, and stored at 4°C. Nanoshells exhibit long term stability and provide strong Raman enhancements. Halas and co-workers have developed these metallic nanospheres as SERS-active substrates for various biomolecular applications.(113, 114, 117, 118) Specifically, a silica core is used as a base and a gold shell is deposited around the outside of the nanoshell to serve as the SERS-active portion. Strongest Raman enhancements have been reported when enough gold is deposited on the silica cores to form a nearly complete metal shell, creating a consistent electromagnetic enhancement throughout the surface of the particle.(113)

Nanoparticles

Perhaps the most widely used method of producing ordered nanostructures for SERS is by self-assembly of colloidal nanoparticles.(119) Silver and gold nanoparticles are the most frequently used SERS substrates due to their ease of preparation, relatively low production cost, and well characterized SERS properties.(61, 89, 120-123) Metal nanoparticles are composed of suspended particles that have defined diameter size. The dispersive colloidal aggregates are readily prepared by reducing a dilute solution of metal salts. Silver nanoparticles are usually produced by reduction of a silver salt (typically silver nitrate) by reducing agents such as sodium citrate,(124) EDTA, or sodium borohydride.(125) Nanoparticles produced from citrate or EDTA reduction tend to be more stable over time and are thus the preferred reducing agents.(126) Gold nanoparticles are made in a similar fashion as silver. Typically, chloroauric acid is reduced by reducing agents such as sodium citrate,(127) tetraoctylammonium bromide (in an organic layer such as toluene),(128) or hydroquinone.(129) For the same reason as silver, the citrate reduction is usually the most common and stable method of preparation. The size of the nanoparticles may be controlled based on the amount of the metal used in comparison to the amount of reducing agent. Junctions between the nanoparticles where electromagnetic fields may overlap generate large enhancements and may even allow single molecule detection.(80, 122) These fields are generated by the localized surface plasmon resonance of the nanoparticles and may be tuned based on the size, shape, and degree of aggregation of the nanoparticles.(130) Through controlled aggregation, the “hot spots” created by the electromagnetic field overlap may be taken advantage of.(131, 132) Additionally, nanoparticles may be used in combination with other metal surfaces where both metal surfaces contribute to the SERS enhancements.(133, 134)

Despite the simplicity of nanoparticle preparation, undesired experimental effects remain as metal colloids tend to aggregate into macroscopic clusters and precipitate from solution following the addition of an adsorbate. The variation in aggregation of the particles results in discrepancy of the resulting SERS intensity.

Commercial Substrates

Commercial available Au substrates are also available for SERS sensing. Among several companies, Renishaw Diagnostics (Glasgow, UK) has commercialized the Klarite® (and more recently the Klarite Plus®) substrates designed from silicon surfaces made of regular inverse pyramidal pattern arrangements coated with Au.(135, 136) The Klarite® substrates are designed from silicon surfaces with a regular arrangement of inverse pyramid patters that have been coated with gold. The plasmonic bands generated by this substrate permit a variety of wavelengths to be used for spectroscopic interrogations. The company Real Time Analyzers produces sol-gel based SERS substrates in solution, microplate, or capillary form. These patented sol-gel SERS substrates may be applied to any type of glass or plastic surface. The ability to coat many different surfaces gives sol-gel SERS a big advantage over other techniques like colloid SERS and lithographic substrates. Figure 2.2 presents SEM and macroscopic (inset) images of six of the aforementioned substrates.

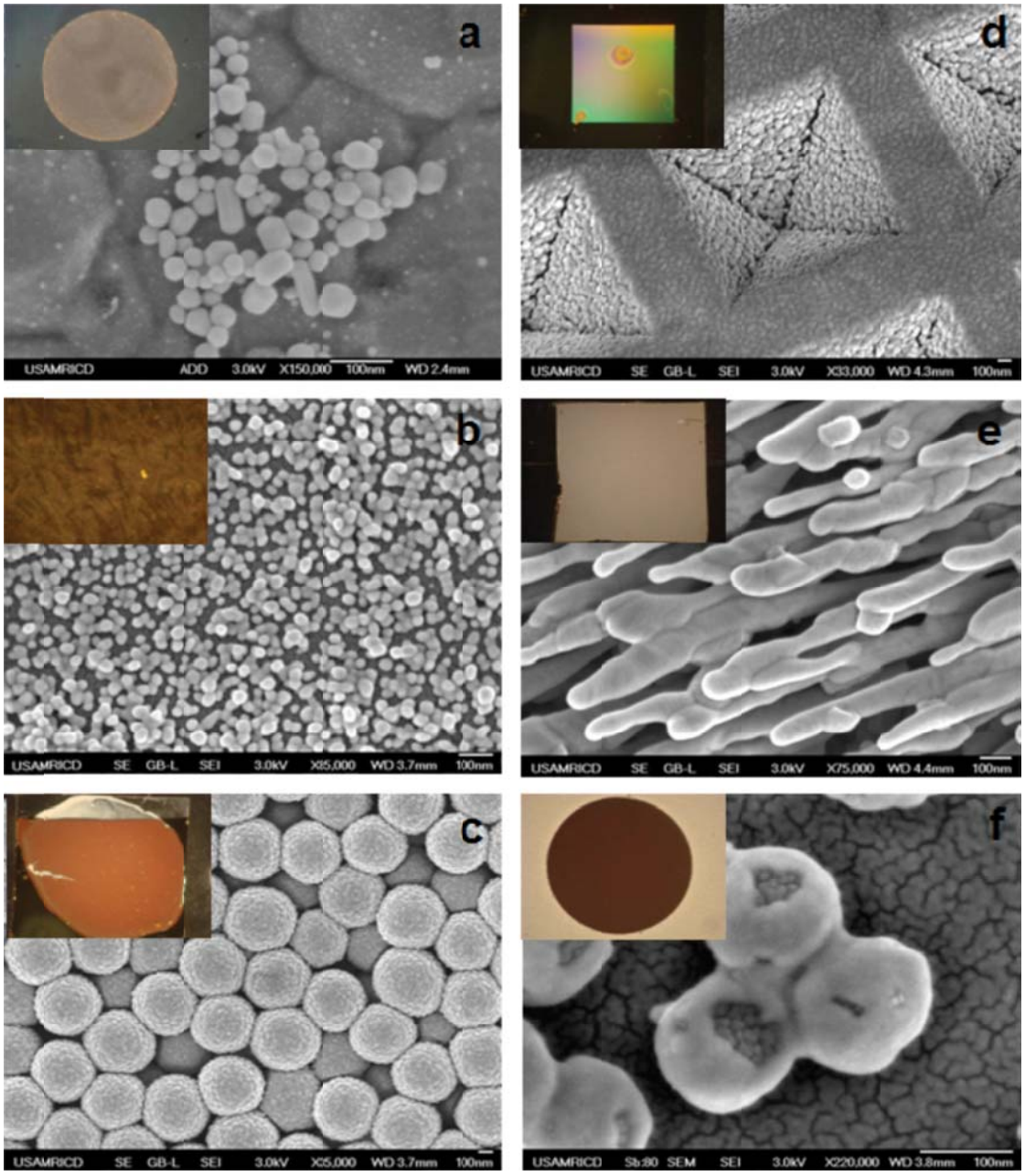

Figure 2.2. SEM and macroscopic (inset) images of six of the aforementioned substrates. (a) silver deposited colloids, (b) gold deposited colloids, (c) gold film over nanospheres (FON), (d) Klarite®, (e) silver nanorods, and (f) gold nanoshells.(137)

2.4. Applications of SERS

Since its discovery in the 1970s, surface-enhanced Raman spectroscopy (SERS) has become a powerful analytical technique that provides identification and quantitative information about a variety of molecules with a high degree of sensitivity and specificity. The inherent chemical specificity of Raman spectroscopy offers a number of attractive features for detection and identification of a wide variety of samples. Raman provides a unique, chemically specific molecular fingerprint for each analyte, which eliminates the need for indirect detection via conjugated synthetic fluorophores.(138) Raman has inherently narrow spectral lines that enable multi-component analysis without special experimental techniques or multi-fluorophore approaches. For the SERS method, in particular, the phenomenon is due to the nanoparticle physics of the substrate and not the chemistry of a fluorophore; thus, photobleaching and quenching are of minor concern. In particular, SERS distinguishes itself from other analytical techniques by its tremendous structural fingerprint capabilities with highly resolved band (0,1 nm), which is advantageous for multiplexed detection.(139) The following sections present the capabilities of SERS for single molecule detection as well as its application in bioanalytical sensing, and more specifically for SERS-based detection of bacteria, viruses, and oligonucleotides.

Single Molecule SERS (SMSERS)

Single molecule detection has been accomplished in a variety of ways using SERS. For instance, Kneipp and co-workers have reported NIR-SERS-based detection of single molecule of crystal

violet in a solution of silver colloids.(80) In their study, a water immersion lens was used to provide direct contact of the laser beam with the solution while acquiring spectra. Prior to the experiment, they pre-determined the ratio of molecules to colloid to be 0.6 in order to ensure that less than one molecule was adsorbed on a single colloid. Experimentally, spectra were acquired every second and plotted for comparison as molecules were likely to come in and out of the sampling volume of solution interrogated by the laser beam. Single molecule detection was claimed based on the fact that the majority of the spectra were void of spectral bands associated with crystal violet. However, a few spectra exhibited bands corresponding to crystal violet. Based on the experimental conditions, Kneipp and co-workers concluded that the rare appearance of the crystal violet bands was due to the detection of single molecules at the silver colloid surface.(80)

Nie and co-workers also investigated single molecule SERS around the same time as Kneipp.(81) Individual silver colloidal nanoparticles were used to enhance the spectral signature of adsorbed rhodamine-6g (R6G) molecules. Raman enhancement factors on the order of 10^{14} to 10^{15} were reported, constituting much larger enhancements when compared to the ensemble-averaged values derived from conventional measurements. The magnitude of these enhancements provided the first evidence of vibrational Raman signals being more intense and more stable than single-molecule fluorescence. Van Duyne and co-workers have also reported detection of single R6G molecules on silver nanoaggregates.(62) In this study, SERS spectra were collected from individual and ensembles of R6G molecules as a function of excitation frequency. Single molecule detection was achieved by measuring the molecular resonance of

R6G using a tunable excitation source. This study demonstrated the first surface-enhanced Raman excitation profiles (REDs) of R6G on Ag surfaces by combining both single-molecule detection of R6G and excitation across the molecular resonance of the molecule.(62)

Bioanalytical Sensing

SERS has been used as a biosensing platform to detect a variety of biomolecules. This technique is particularly valuable for studying biological samples since it has a fluorescence-quenching effect that is extremely useful when examining microorganisms, which often exhibit a high fluorescence background under excitation in the near-infrared to visible regions of the electromagnetic spectrum.(139) Moreover, since excitation is in this part of the electromagnetic spectrum, there are no drawbacks associated with photochemical degradation of the sample. For example, over the last few years, nanoparticles coupled with SERS have been applied for the detection of infectious diseases(140-143) and therapeutic drugs.(144-147) Nanoparticles coupled with SERS have been used to detect a variety of biomolecules. Specific examples include, but are not limited to proteins,(148-152) whole cells, bacteria,(153-156) and oligonucleotides.(133, 157-163) Nanoparticles aggregation has also been employed to study biomolecular interactions. A few examples include antibody-antigen,(164, 165) and streptavidin/biotin binding interactions.(166, 167) Additionally, adenosine,(168) glucose,(169) and toxic ions such as lead,(170) lithium,(78) and cadmium(170) have been studied using ligand-based aggregation of nanoparticles. Aptamers have also been exploited as biological recognition elements in the detection of a variety of biological analytes. Aptamers are single-stranded DNA or RNA oligonucleotides that are selected through an in vitro combinatorial selection process with high

affinity and specificity.(171, 172) Aptamers have been developed against a wide array of targets ranging from proteins(173) to whole cells,(174) and have been integrated in a variety of biosensors.(175, 176) They have also proven valuable in a variety of fundamental virology studies, including genome replication, gene expression, and virus entry.(175-177)

Pathogens Detection: Bacteria and Viruses

SERS has recently been shown to be a potentially powerful whole-organism fingerprinting technique and is attracting interest for the rapid identification of bacteria.(178) The unique biochemical specificity inherent to vibrational spectroscopy had led to the development of SERS-based methods for detection of bacteria and other micro-organisms. A number of studies have been performed using SERS with a variety of substrates: *in situ* silver(179-181) or gold(182) colloids, silver(183-192) or cold colloids(193) added post cell growth, silver coatings,(179) silver nanoparticles with antibodies,(194) and biofilms.(195) Zeiri and co-workers performed SERS with a sodium borohydride-reduced silver colloid at 514.5 nm excitation.(179) Perhaps surprisingly, they noted very little difference between SERS from the surface of chemically diverse Gram-positive and Gram-negative bacteria. The features on the SERS spectra acquired revealed the presence of of one molecule, flavin adenine dinucleotide. In another study, Culha and co-workers used a gold SERS-active substrate with 785 nm excitation to investigate the individual components of bacteria and concentrated their analysis on the study of the spectral features of nucleic acids, amino acids, and peptides.(193) However, they stated that SERS spectra obtained from bacteria under these conditions will take their major contribution from cell

surface biochemistry but omitted to analyze the carbohydrate components associated with the outer cell membrane present in the SERS spectra.

The main challenge associated with the detection and identification of bacteria lies in distinguishing the protein and carbohydrate components present along the outside of the bacterial cell, which is characteristic to a specific cell line and different between bacterial strains. This change in composition has been investigated by SERS in various reports. Notably Goodacre and co-workers have focused on the detection of various bacterial strains and species using silver colloids prepared by citrate reduction.(178, 185, 186) In their study, they analyzed the SERS spectra of bacteria acquired at 785 nm excitation and used multivariate statistical techniques such as discriminant function analysis (DFA) and Hierarchical Cluster Analysis (HCA) to differentiate the organisms based on their spectra fingerprints. Methods for bacteria detection have also been employed using Raman with optically trapped bacteria,(196) optically trapped bacteria coupled with confocal Raman,(197) as well as studies performed using confocal Raman alone.(183, 184, 198, 199)

Recently, there have been several reports for the use of SERS for virus detection. Direct virus spectroscopic detection has been accomplished by recording spectral signatures of an intact virus. Specifically, virus specimens have been identified using very small sample volumes and without pre-treatment of the virus.(200) A SERS-based study showed that enveloped and non-enveloped viruses could be distinguishable using intrinsic SERS spectra.(201, 202) Indirect detection of viruses was also accomplished using virus biomarkers.(203) Additionally, a

"sandwich" assembly using more than one metal surface has also been reported for the SERS-based detection of viruses.(204-206) Using the sandwich structure, Hepatitis B virus surface antigen has been detected using murine monoclonal antibodies. To improve the limit of detection of the virus surface antigen to 0.5 μg/mL, a silver staining step was incorporated into the immunoassay as well. The SERS-based detection of feline calicivirus has also been demonstrated by Porter and co-workers.(204) In this study, the measurements were carried out using a second capture antibody immobilized on a organothiol SAM-coated Au surface, a key point being that the assay is apparently enhanced by optical coupling between the metal nanoparticle and the macroscopic Au surface; making the measurement somewhat more complicated than with most SERS-based detection of labeled biomolecules. In addition, because these particles are not encapsulated, one assumes that the SERS signal generated could be influenced by variation in ambient conditions, including pH, temperature, etc.

Oligonucleotides

The very first SERS-based study focusing on detection of oligonucleotide was performed by Otto and co-workers in 1986 on a silver electrode surface.(37) In this study, SERS spectra were acquired for single nucleotide bases using both Raman and SERS and the spectral band locations were compared directly. As a comparison, the standard Raman spectra were also acquired on these oligonucleotides. Comparison of the spectra revealed a significant shift in spectral lines as well as new bands between standard Raman and SERS. Otto and co-workers concluded that the appearance of the new bands in the SERS spectra originated from the active modes resulting from the interactions between the metal substrate and the oligonucleotides adsorbed on it. The

same observations were made by Moskovits and co-workers the same year.(207) In this study, they reported the SERS spectra of nucleotide bases adsorbed on silver and acquired using a 514.5 nm excitation. Aditionally, they acquired SERS spectra of adenine, cytosol, and uracil obtained in D_2O colloid solution. Therefore, the SERS spectra acquired correspond to the N-deuterated adenine, cytosine, and uracil. As a result, they observed a red shift in the resulting SERS spectra due to the deuteration of nitrogen atoms of the ring. Overall, these studies yielded detailed information regarding the disposition and mode of bonding of oligonucleotides adsorbed on appropriate metal surfaces. In another study, Mirkin and co-workers used nucleotide induced aggregation of gold nanoparticles for detection of DNA hybridization.(161) Specifically, nanoparticles functionalized with a probe oligonucleotide were forced to aggregate upon addition of nanoparticles functionalized with the complementary DNA strand. The spectral signatures resulting from the formation of the hybrid were enhanced due to the spatial location of the oligonucleotide between two particles.(161, 165, 208) Halas and co-workers have employed gold nanoshell structures(112-115, 117, 118, 152, 157, 209-212) to detect DNA hybridization. In a similar fashion to Mirkin and co-workers, one nanoshell solution was functionalized with a probe oligonucleotide and another with the strand complementary to the probe. Hybridization of the DNA probe to the complementary oligonucleotide sequence target was monitored using SERS after combining the two nanosphere solutions. Hybridization of DNA located within the nanometer-sized gap between the two nanospheres, i.e. within the “hot spots”, was suggested as the basis for the observed enhancement of the spectral bands observed corresponding to the vibrational modes of the nucleotide bases.(157, 213)

The use of thermal cycling of the oligonucleotide was reported by Halas and co-workers prior to deposition of the DNA probes onto the gold nanoshell surface as a way to allow DNA to pack more tightly at the nanoshell surface.(213) This thermal pre-treatment was shown to lead to better signal-to-noise ratio (S/N) as well as less spectral variability from substrate to substrate. Additionally, the thermal pre-treatment was allowed more efficient hybridization of the DNA probes to the complementary oligonucleotide. It is important to note, however, that no distance dependence was observed or reported for DNA ranging from 20 to 70 bases in any of the studies. Adenine bands were visible in the spectrum regardless of concentration or distance the base was located from the surface.

Green and co-workers have developed a silver toroid SERS-active substrate for DNA detection.(159) In this study, SERS spectra were acquired on 18-mer oligonucleotide in combination and alone. The results showed that the relative intensity changed with composition and the ratio between the adenine band at 731 cm^{-1} and the cytosine band at 790 cm^{-1} was used to compare the different sequences to one another. In addition, DNA hybridization was investigated and single bade mismatches were identified with no distance dependence noted in a label-free fashion. Graham and co-workers have performed numerous studies using nanoparticle aggregations and assemblies for detection of oligonucleotides using Raman dyes for detection.(158, 214-218) Specifically, they employed nucleotides in combination with a Raman label for DNA hybridization. Since changes in nucleotide sequence are often difficult to distinguish, a Raman reporter molecule is coupled to the DNA probe to ensure that hybridization has taken place. Specifically, silver nanoparticles were functionalized with single stranded DNA,

complementary to a fluorescently tagged oligonucleotide in solution. Upon successful hybridization, the fluorescent label was enhanced by the silver surface and its spectral signature appeared in the resulting Raman spectrum.

A crucial aspect of DNA hybridization assays is the orientation of the DNA on the substrate surface. X-ray photoelectron spectroscopy (XPS) has been used to investigate the conformation of thiolated and non-thiolated DNA at gold surfaces.(219, 220) In these studies, the XPS spectra were monitored for the response associated with the nitrogen atoms in the base for both thiolated and non-thiolated oligonucleotides consisting of only thymine bases. Additionally, the formation of a complete monolayer was monitored based on the nitrogen response and correlated to the surface coverage. Results from this study suggested that thiolated DNA, when allowed to form a complete monolayer, was standing up off the surface. The contribution from the nitrogen ring of the thymine base was no longer present in the XPS spectra upon monolayer formation. In addition to XPS, electrochemical methods have been employed to investigate the conformation of DNA electrode surfaces.(221-225) One study looked into the surface density of DNA at a gold electrode surface to evaluate hybridization efficiency as a function of monolayer coverage.(223) Specifically, the number of nucleotide phosphate residues was calculated using the amount of cationic redox marker measured at the electrode surface. Based on the electrode response observed, monolayer coverage of thiolated DNA was estimated. The results of this study showed that hybridization was the most successful when a spacer was implemented in the assay to allow room for the complementary strand of DNA to bind to the probe for *in situ* studies.

SERS is a sensitive and viable means for detecting analytes at the surface of a roughened metallic surface. The coupling of both an electromagnetic and chemical enhancement mechanisms produces enhancement factors up to 10^{14} relative to standard Raman, thus allowing for single molecule detection. Additionally, SERS may be used for biomolecule detection since the resulting SERS spectrum contains spectral bands unique to the molecule being investigated, a multiplex advantage often referred to as "whole-organism fingerprinting" and more recently coined "metabolic fingerprinting".(178)

CHAPTER 3

Introduction to Oblique Angle Vapor Deposition (OAD)

The purpose of this chapter is to introduce the reader to the fabrication technique employed to produce the silver nanorod array SERS-active substrates used in this work. A broad background of the physical vapor deposition technique is provided, as well as a thorough description of the various processes leading up to the use of oblique angle vapor deposition to fabricate the silver nanorod arrays.

3.1. Physical Vapor Deposition (PVD)

Physical vapor deposition (PVD) is a process used to deposit thin films by condensation of a vaporized form of the desired metallic film sputtered at an atomic level onto a surface at nanometer to micrometer thicknesses. PVD encompasses a number of deposition methods that are used for a variety of applications in research and development as well as in industry. PVD processed are carried out under vacuum conditions in a sealer chamber and typically involve four steps: evaporation, transportation, reaction, and deposition.(226-229) Figure 3.1 depicts the PVD process schematically. During evaporation, the metal source in a crucible is bombarded with a high energy source such as an electron beam or an ion beam. This bombardment results in the dislodgment of single atoms or atom clusters from the surface of the metallic target as it is

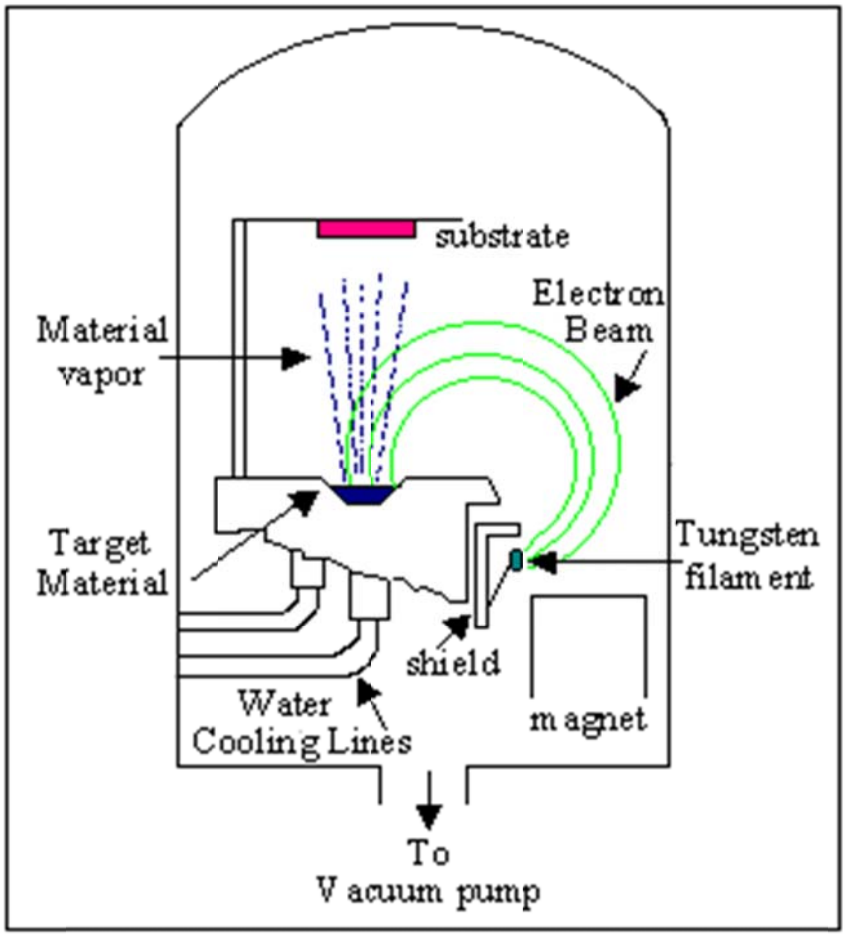

Figure 3.1. Schematic representation of the physical vapor deposition (PVD) process. A target material is bombarded with an electron beam and atoms are dislodged and transported towards the substrate surface. The material is in vapor form prior to depositing on the substrate surface.

irradiated by the beam. Some source materials required a high degree of heating, which in turns, required a lengthy cooling period upon completion of the evaporation.(228) Following evaporation, vaporized atoms move from the metallic target to the substrates held on a substrate holder located directly above the crucible. The low pressure environment inside the vacuum chamber promotes a linear path of the vaporized atoms towards the substrates. During an atom transport, reaction steps may occur depending upon the nature and partial pressure of the gas present in the chamber during the evaporation process. For examples, reactive gases such as nitrogen, methane, acetylene or oxygen may be introduced into the vacuum chamber during metal deposition to create various compound coating compositions. The atoms of the metal react with the appropriate gas during the transportation stage. Likewise, the evaporated material may undergo chemical reactions prior to the atoms depositing on the surface of the substrate. This generally occurs when depositing metal oxides, nitrides, carbides and other such materials are used as the source materials. However, chemical reactions do not take place in PVD processes where the metal source alone is the desired material.(226, 227) The final step of the deposition is the evaporation. This step results in the coating of the substrate by the vaporized metal atoms to the desired thickness. Deposition rates are typically slow to ensure even distribution of material as well as lower temperatures at the substrate surface.(226, 228)

Sputter Deposition

Sputtering is form of PVD for depositing thin films onto a substrate surface. This substrate fabrication process relies on the generation of a gaseous plasma under vacuum produced to

accelerate ions from the plasma into the metal source. Vaporization of the coating material is typically accomplished by ion bombardment of the source electrode to generate the vapor phase composed of vaporized metal atoms.(230) Figure 3.2 depicts a schematic representation of sputtering deposition. For sputtering to occur, a high energy source (RF, DC) is required to generate and sustain the gaseous plasma. The gaseous plasma is produced by introducing the gas to the electric field generated by the high energy source. The excitation of the reactive gas molecules results in a partially ionized medium that will generate the gaseous plasma. Upon collision with the metal source, material is eroded away and atoms of a neutral charge are ejected towards the substrate. This process results in continuous deposition of the source material onto the substrate surface. This energy source is kept steady in the chamber to maintain the plasma state throughout the deposition process. However, the deposition rate may be controlled by varying the applied power and the size of the source electrode. An advantage to sputtering deposition in comparison to filament evaporation is that high melting point materials are easily sputtered without the concern f system heating. Consequently, sputtering deposition is used to deposit metal oxides that required a high melting temperature to vaporize.(231)

Thermal Evaporation

Sputtering evaporations differ from resistive evaporation in that a heating element is the energy source responsible for vaporizing the material as opposed to an ion source. In sputtering systems, heat is typically produced by applying a high current through a resistive element. Small metallic pellets are usually heated within an aluminum oxide crucible where the metal vaporizes and ultimately condenses of the substrate surface.(227, 232) Low pressures in the order of 10^{-6} to 10^{-5}

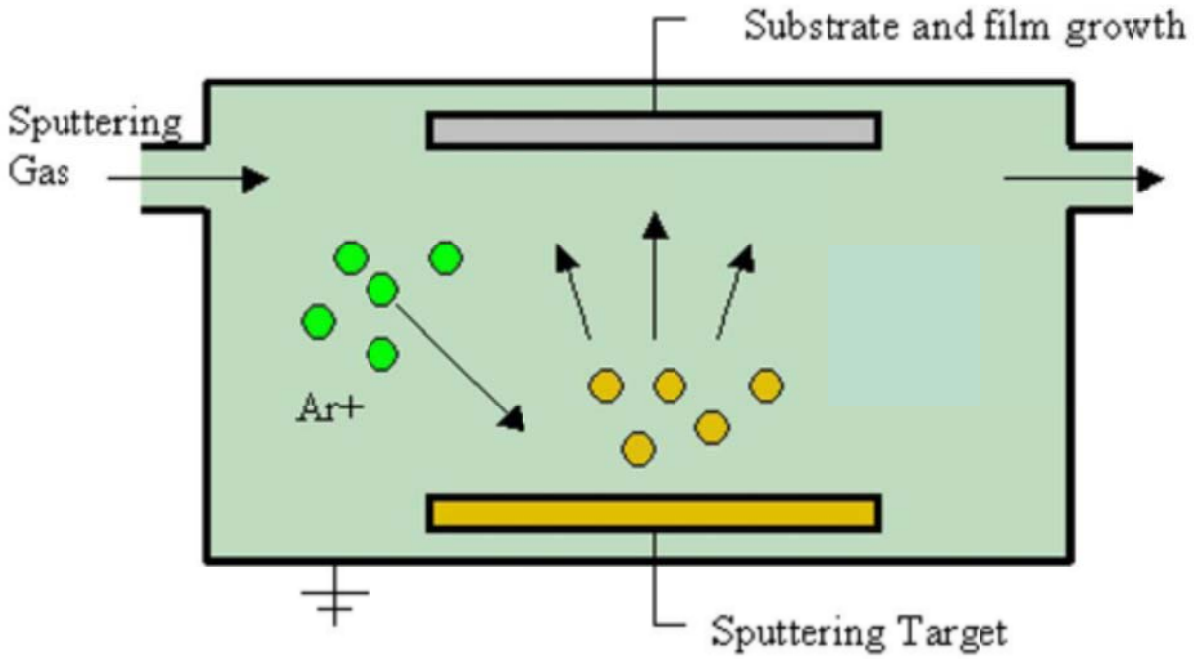

Figure 3.2. Schematic representation of the sputtering deposition process. During this process, argon gas ions Ar^+ (represented by the green circles) are causing atoms of the target material (represented by the yellow circles) to dislodge and evaporate towards the substrate surface. During sputtering deposition, a sputtering gas is flown in using the inlet and purged via the outlet to keep to keep the deposition chamber at a low pressure environment.

are used throughout the evaporation to prevent vapor atoms from colliding within the plume.(232) Liquid nitrogen may be used to maintain vacuum and cool down the chamber to reduce the water pressure of water.(232) Sputtering of the atoms results in the formation of a metallic plume that vaporizes onto the sample surface in a linear fashion to form a thin metallic film. The sample thickness is usually controlled by varying the deposition rate and the chamber pressure. Careful control of these parameters is critical in sputtering evaporation since a high degree of heat is required to melt the metallic pellets, causing the chamber to reach a high temperature. As a result, meticulous regulation of the chamber pressure and temperature results in formation of a smooth and homogeneous film on the substrate surface.

Electron Beam Evaporation

Electron beam (e-beam) evaporation is the most common PVD method used to deposit metals. This technique relies on the bombardment of a source material to heat the metal and generate a plume in a high vacuum chamber.(230) In this method, the metal source is heated using an electron beam as opposed to sputtering evaporation where direct heating is employed to vaporize the metallic sample. The quality of the deposited film is highly dependent of the vacuum inside the chamber. Ultra high vacuum is commonly used in electron beam evaporation to generate high quality films. The pressure inside the chamber is kept sufficiently low enough (10^{-6} to 10^{-9} Torr) so that the flux undergoes a nearly collisionless transport to the substrate surface.(228, 229) In such conditions, the mean free path of the vaporized atoms usually equals or exceeds the vacuum chamber dimensions so that the metallic particles travel essentially in straight lines from the evaporation source towards the substrate.(227)

An electron beam evaporator consists of a few key components. A hearth holds the metal source in crucible at the bottom of the chamber where the electron beam may be focused in a small region. Focus of the electron beam is accomplished by applying a magnetic field during the evaporation.(227) A rotating hearth with multiple pockets is commonly used to allow sequential depositions with a single pump-down.(226) This is a crucial advantage over resistive evaporation. The hearth holding the rotating crucibles is typically water cooled to reduce the amount of heat given off upon melting the ingot. A mechanical shutter is used to prevent flux from reaching the substrate surface during initial stages until the optimal temperature and pressure levels are reached within the chamber. When these conditions are reached, the shutter is opened and the flux of atoms is deposited onto the substrate surface at a constant evaporation rate. The deposition rate and thickness measurements are controlled by a quartz crystal microbalance (QCM) located inside the chamber and positioned at normal incidence to the vapor source. Generation of the electron beam usually required between 1 to 10 kW of electrical power to ensure steady vaporization of the metal atoms. During the ramping step, a higher power is used to initially melt the metal while a slightly lower power is used during the deposition process.(227)

Plume Characteristics

During evaporation, the vaporized atoms form a plume of vapor inside the evaporation, the vaporized atoms form a plume of vapor inside the evaporation chamber.(233) The distribution of particle density within the plume during the deposition is represented in a schematic diagram in Figure 3.3. The inner, dark blue regions are representative of denser atomic regions whereas the

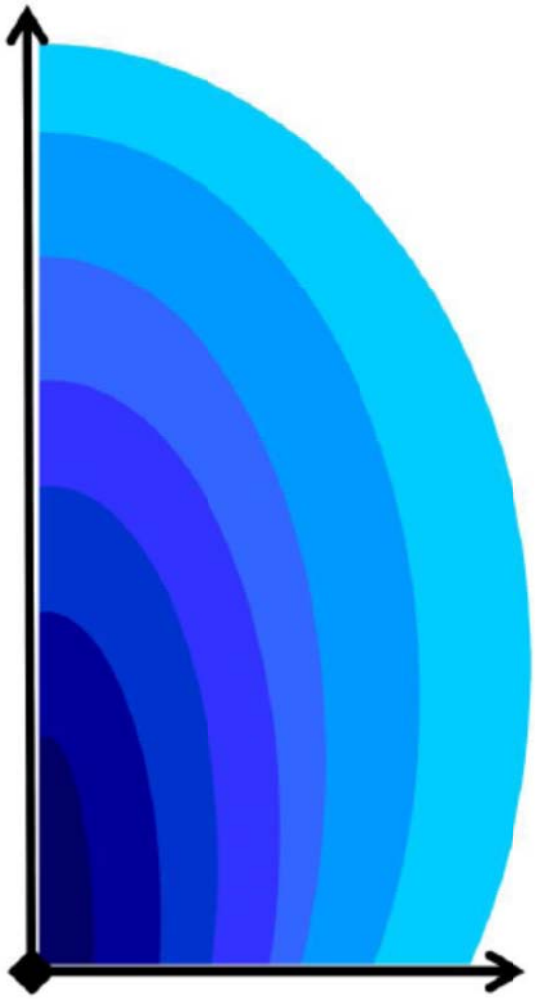

Figure 3.3. Schematic representation of the particle density within the evaporation plume during deposition. The darker blue depicts regions with higher particle density whereas the lighter blue represents regions with lower particle density. The arraows on the x and y axis indicate the increasing distance from the source material. Typical ranges for high to low particle density are in the order of 10^{14} to 10^{10} particles/cm^3.(233)

outer, light blue regions are representative of lower particle densities. As seen in Figure 3.3, there is a higher particle density directly above the source material (dark blue regions) and the particle density decreases with distance away from the source in both a horizontal and vertical direction (light blue regions). Therefore, careful control of the placement of the substrate within the chamber is critical to fabricate reproducible thin films.(233) Additionally, the angle at which particles strike the surface also changes with distance because of the dimensions and trajectory of atoms in the plume. Upon rotation of the substrate, the vaporized atoms still follow a linear path but will deposit on the substrate surface at a non-normal incidence. As a result, the features at the surface of the substrate are directly affected. Based on vapor plume characteristics, a longer throw distance is desired for some processes. Increasing the distance between the metal source and the substrate will result in a decreased particle density since the deposition rate also decreases with distance. These conditions ultimately lead to fabrication of substrates with better reproducibility and surface uniformity.

3.2. Glancing Angle Deposition (GLAD)

GLAD is a physical vapor deposition method where the deposition flux is incident onto a substrate with a large angle with respect to the surface normal. During thermal evaporation, the substrate is typically oriented in such a way that the flux material strikes the substrate surface at an angle of incidence of 0°. However, during the GLAD process, the substrate is rotated to a glancing angle at some point during the evaporation to allow growth of columnar structures through the effect of shadowing during the film growth.(234) During GLAD, the deposition rate not only has a vertical component (with respect to the substrate surface), but also a lateral

component. The lateral growth rate contributes to the shadowing effect, which gives rise to two major advantages of GLAD over other PVD methods: the self-alignment effect and the lateral sculpturing effect. These benefits allow fabrication of thin films consisting of unique structures. Since GLAD is a physical vapor deposition technique, it possesses many advantages in terms of controlling the growth of nanostructured thin films. First, GLAD allows natural formation of nano-column array. The porosity of the film may be controlled by simply changing the incident angle. GLAD also has the advantage of self-alignment due to the shadowing effect. In addition, there is virtually no restriction on materials since the growth process is a thermal evaporation. These advantages make GLAD very promising for the fabrication of nanostructures of various shapes and forms.(234)

Early investigations on the use of GLAD as the PVD technique consisted of evaporation of metal vapors onto substrates at non-normal, or oblique angles.(235-240) Analysis of the thin films produced in these early studies showed that the grains grew towards the metal source, a detail later confirmed by Nieuwenhuizen and Haanstra.(241) More specifically, Konig and Helwig observed an increase in the atomic-scale shadowing, now referred to as “self- or ballistic shadowing” during deposition of the metal vapor at these oblique angles.(242) An important feature of GLAD is that the incident flux coupled with limited atom diffusion at the substrate surface results in a film with columnar-like microstructures oriented towards the metal source.(243) Rotation of the substrate along the azimuthal axis during the evaporation process may be used to sculpt columns of various shapes. A schematic of the experimental set-up for GLAD is depicted in Figure 3.4.

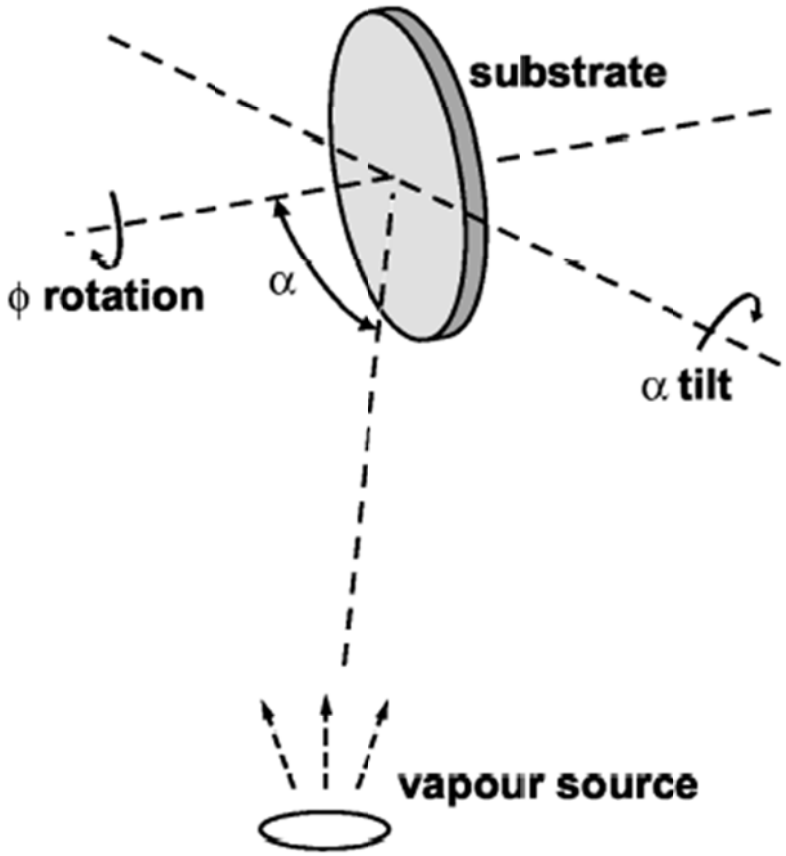

Figure 3.4. Schematic representation of the GLAD process. A motor is typically used to rotate the substrate (line labeled as ϕ, rotation angle). The tilt angle (line labeled as α, flux angle) is presented as well.

Columnar Structure Formation

Physical vapor depositions result in fabrication of thin films whose morphology may be controlled during the growth. During this process, the metal source being vaporized undergoes a phase transition from a vapor state to solid state at the substrate surface.(228) The phenomenon of nucleation initiates when growth regions begin to form upon condensation of the flux of metal atoms.(244-246) The plume of vapor provides a constant flux of metal atoms incident on the substrate that create nucleation sites once they reach the surface and diffuse. These adsorbed atoms either re-evaporate off the surface (or detach from existing nucleates) or join other atoms and form nuclei.

Nucleation

The latter phenomenon is usually favored once large nucleation sides have formed on the substrate surface.(234) Figure 3.5 shows a scanning electron micrograph (SEM) of nucleation sites that typically form at the start of the deposition. The image depicts a number of nucleates of various sizes. It should also be noted that nucleation is random and that the nucleates are polycrystalline in nature. During the nucleation process, atoms bound more strongly to the substrate surface grown in a monolayer type manner, a growth process referred to as Frank-van Merwe growth.(247, 248) In contrast, if binding of the vaporized atoms to the substrate surface is stronger between the atoms themselves, three dimensional nanostructures result, a growth process referred to as island or Volmer-Weber growth.(248) A combination of these two growth

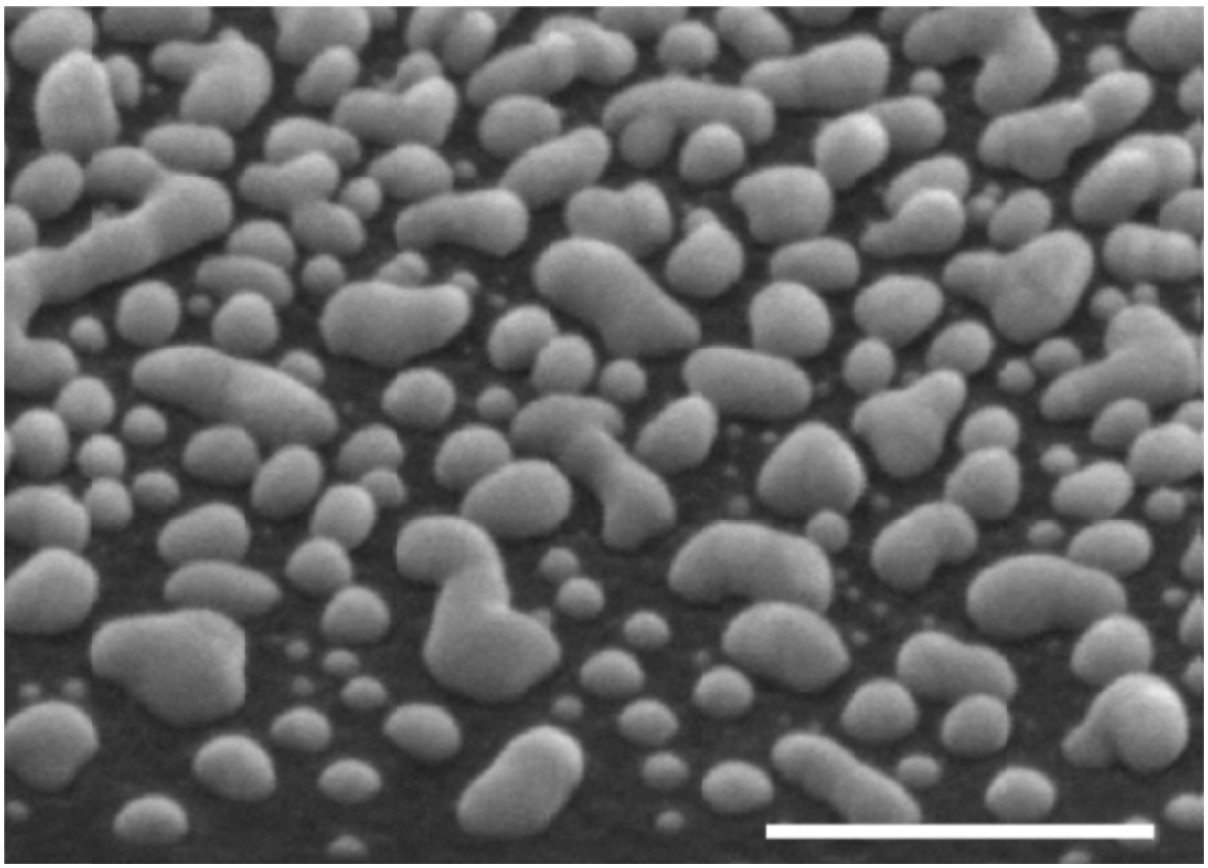

Figure 3.5. Top-view SEM micrograph (40K) showing nucleation on the substrate surface at the beginning of a silver deposition. In this particular image, the incident flux angle was 86°. The scale bar represents 200 nm.

processes may occur as well and are deemed layer plus island or Stranski-Krastanov growth.(247-250) These nucleation sites form regardless of the angle of the incident flux in most PVD methods. However, the Volmer-Weber growth mechanism is the most dominant growth process observed in GLAD.(249, 250)

Ballistic Shadowing

Ballistic shadowing refers to the process by which one particle blocking the region directly behind if from a second particle. The principle behind ballistic shadowing in GLAD relies on nucleation of the evaporated material on the substrate surface at the beginning of the deposition process (see Figure 3.5). At an early stage of the deposition, the nucleation sites present of the substrate surface are an important factor for the subsequent growth of the three-dimensional nanostructures. As the evaporation proceeds, regions directly behind these nucleation sites are blocked from the incident vapor. This phenomenon promotes deposition and accumulation of material on the nucleation sites, eventually resulting in creation of micro-column structures.(234) Additionally, since atoms favorably deposit onto these nucleation sites, columnar structures form the direction of the flux material. A few factors may affect the process of ballistic shadowing. Since this process is heavily influenced on the linear vapor trajectories of the incident flux, increasing the distance between the metal source and the substrate surface is desirable for improvement of the collimation of the vapor material. Upon collision, particles do not travel towards the substrate surface along the original path and may deposit in shadowed regions. This effectively decreases with particle columniation at the substrate surface as well as formation of columnar structures. Consequently, careful control of the chamber temperature and pressure are

essential to prevent this from happening. Likewise, a large working distance between the metal source and the substrate surface is advantageous in GLAD. Those are a few reasons why e-beams and sputterers are preferred tools for GLAD.(234) Resistive evaporators are not commonly used due to excessive heating of the system which tends to degrade the surface of the three-dimensional nanostructures.

Column Development

During the initial growth, micro-columns are symmetrical about the growth axis. As the evaporation proceeds, atoms deposit in such a way that they begin to fan out from the center, resulting in a loss of symmetry of the columnar nanostructures. As a result, continued growth is an anisotropic process where growth is parallel to the incident flux.(251) In other words, there is no restriction on the lateral growth of the structure. Consequently, columns will continue to broaden until they become wide enough to merge with neighboring structures.(239) Column growth is overall competitive process, and due to ballistic shadowing, smaller micro-columns may exist in the shadowed region behind a larger structure.(252) A turning point of the evaporation process is when the growth of these shadowed columns ceases and when the larger columns begin to dominate the thin films. As this growth goes on, the columns become larger and decrease in number. This growth process is a distinguishing factor in the GLAD process.

Structure Control: Seeding

An additional aspect of the GLAD process that may be controlled is the periodicity of the three-

dimensional nanostructures surface. The initial nucleation process is a random event that makes the grown structures aperiodic.(253, 254) The continued growth of the nucleation sites results in unordered nanostructures with inconsistent spacing. Control of the growth of these nanostructures may be accomplished in a variety of ways. For example, an additional step may be used prior to the evaporation; the substrate may be pre-patterned in order to dictate the precise location of the growth of the columns.(255) This patterning step helps in controlling the nucleation at the sample surface, and in turn the shadowing effect. As a result, nucleation at the beginning of the deposition is mimicked and the presence of the pattern on the surface promotes the growth of periodic structures consisting of single, evenly-spaced columns. Uniform and periodic columns usually result from this pre-patterning process. Another way of controlling the growth of the nanostructures consists of a post-fabrication step that etches undesired growth of the sample or to create new structures within the thin film to change the surface morphology.(256-260) This process effectively changes the height and width of the structures but will not result in a change of the spacing or location.

Structure Control: Angles and Rotations

Tait and co-workers established a relationship between the incident flux angle, α, and the columnar growth angle, β, of the nanostructures comprising he thin films. In their studies, they investigated the effect that changing α had on β.(251) Figure 3.6 shows the relationship between α and β along with the Tait equation. Based on this equation, the desired growth angle may be achieved through the deposition at the corresponding flux angle. For example, a flux angle of 0° will allow formation of a dense array of columns whereas a large, or oblique, flux angle around

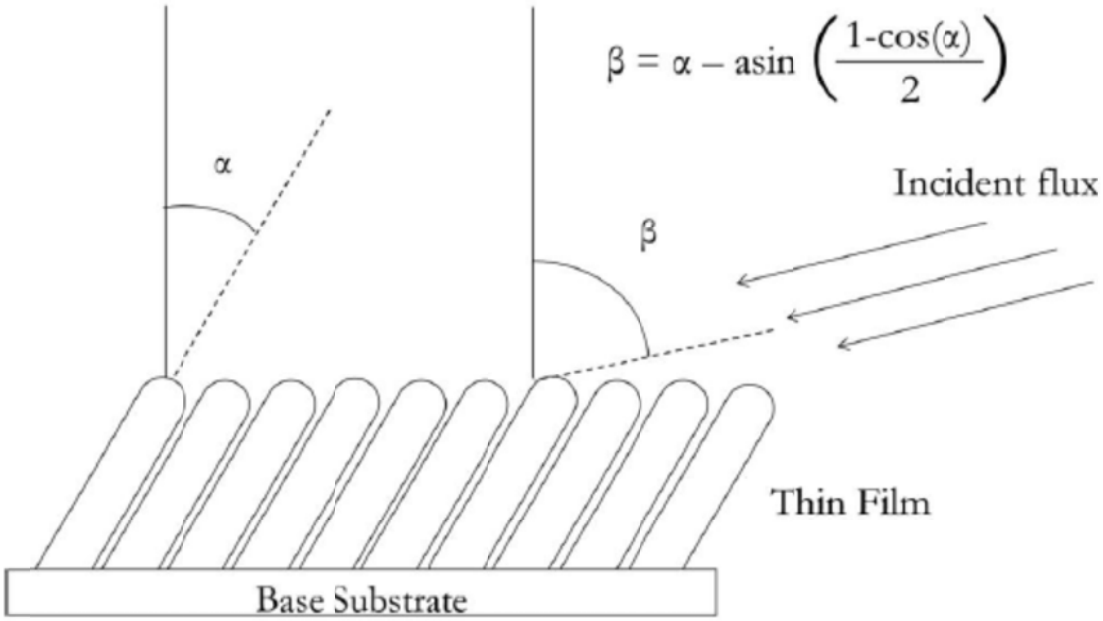

Figure 3.6. Schematic of the flux angle, α, and the growth angle, β, for GLAD. Because of self-shadowing during deposition, the flux angle determines the growth angle. Both angles are measured from the substrate normal.(261) Also included in the Tait equation showing the fixed relationship between α and β.(251)

80° will result in a more porous array of columnar nanostructures.(261) Since the array density varies with the flux angle, the range of nanostructures attainable is limited using a conventional single source deposition. The capability of the GLAD method to simultaneously implement multiple metal sources while changing the amount of flux material coming from different angles results in constant porosity while altering the growth angle. GLAD also allows variation of the location of the source material relative to the substrate. As a result, the growth angle is maintained throughout the deposition. In addition to porosity, the physical nature of the grown structures within the array may be controlled. Column broadening due to atomic shadowing was previously described in section 3.2 of this chapter. The rotation of the substrate during the deposition reduces the column broadening phenomenon. Rotation in a normal incidence relative to the substrate, ϕ rotation, allows for the flux to deposit equally from all azimuthal directions and keep α constant (refer to Figure 3.6).(243) Rotation using an angle of 0.2° may be utilized to account for slight movement of the sample holder during the deposition and hold the substrate at the same position throughout evaporation.(262) An additional technique was developed to control the growth of the structures at the surface. This technique, also known as serial bideposition, consists in depositing material at oblique angles then abruptly rotating the substrate holder by 180° every few nanometers.(263) This process typically results in a reduction of the overall anisotropy of the thin film as a result of the column broadening phenomenon and tilting mechanisms performed inside the chamber.

3.3. Applications of Substrates Fabricated Using GLAD

GLAD may be used to produce a wide variety of substrates with a high degree of anisotropy dependent upon the deposition parameters. The resulting nanostructured produced by GLAD may be used as platforms to accommodate a variety of applications. The following sections provide an overview of the practical applications of the substrates fabricated by GLAD.

Optical Components

Optical materials are specifically engineered to provide characteristic refractive indices and usually consist of coatings with specific transmission and reflection properties.(264) The refractive index of thin films fabricated by GLAD may be varied using a single source material in a controlled fashion by adjusting the vapor flux angle throughout the deposition. The refractive index may also be varied by tailoring the porosity of the thin films. Since the nanostructures are uniform in nature, light passes through the arrays in a homogeneous fashion due to the small structure sizes.(265) However, the refractive index of the thin films may be altered upon appropriate manipulation of the structural elements. As a result, careful control of the thin film growth allows fabrication of nanostructures with refractive index profiles desirable for optical elements such as interference filters, broadband anti-reflection coatings and birefringent omnidirectional reflectors.(266-271) In addition, improvement of the sensitivity to environmental changes of optical coatings may be attained by tailoring the nanostructures produced by GLAD.(272) For example, functionalization of hydrophilic GLAD-based fibers with hydrophobic self-assembled monolayers (SAMs) was shown to result in optical filters

insensitive to ambient water pressure.(273) Furthermore, thin films fabricated by GLAD may be purposely created with defects to allow narrow bandpasses whose spectral location may be easily tracked as a function of humidity and therefore used as humidity sensors. For example, the peak resulting from the increase in humidity shifts to longer wavelengths within the stop band.(265, 272)

Optical Sensors

The formation of columnar nanostructures during GLAD results in a drastic increase of the surface area of the produced thin films. This increase, however, depends heavily on the material and deposition conditions. It has been reported that the maximum surface enhancement in relation to a flat surface is achieved with a flux angle of 70°.(274) The results of this study showed that the increase in surface area was the bi-product of an increase in column size coupled with a decreased in the number of columns resulting from an increased spacing between adjacent columns. Consequently, the resulting surface area increase may accommodate a larger number of analytes to adsorb onto the surface. This is particularly advantageous in sensing applications where the limit of detection of chemicals adsorbed on the surface may be drastically improved. An example of this is with titanium dioxide (TiO_2), commonly used for dye sensitized solar cells (DSSCs).(275) Essentially, the greater number of dye molecule bound directly to the metal electrode increases the efficiency of this sensor. This method has been used by Kiema and co-workers specifically using GLAD to fabricate the TiO_2 structures.(246) Solid oxide fuel cells have also been constructed using GLAD.(276) Yttria-stabilized zirconium columns were back-

filled with cerium oxide (CeO_2) using a sol-gel, making a high interface density electrode structure. This technique has been shown to enhance the efficiency of the reaction.

Gas Sensors

Substrates fabricated by GLAD have also been used as gas sensors. Since the nanostructures grown are porous in nature, gaseous analytes may be introduced easily. Diffusion of the gases through the column structures typically results in a change of the dielectric constant. For example, thin films of oxides, specifically silicon monoxide (SiO), TiO_2, and aluminum oxide (Al_2O) may be utilized as gas sensors. Their hydrophilic nature causes capillary condensation of water vapor within the array.(257) Because of the free flowing nature of gases, molecules are able to adsorb and desorb rapidly. The response time achieved for the detection of the various gas analytes studied was an improvement when compared to other techniques. Currently, a response time of 42 ms has been reported.(277) In this study, thin films consisting of less porous arrays resulted in a lower sensitivity to humidity changes when compared to those with a denser array because of the decreased pore size. With this knowledge, the porosity and morphology of these sensors may be tailored for a specific process.

Chemical Reactions

Additionally, GLAD substrates have been employed to monitor chemical reactions at the surface of the nanostructures. Specifically, platinum helical columns have been used to detect the catalysis of oxidation for automobile exhaust species such as CO, C_3H_6, and C_3H_8.(259) The

results of this study showed that the conversion was not as efficient as other methods. However, the broad applicability of this sensor system may be advantageous for future applications. Another use of TiO_2 thin films has been shown in monitoring the photo catalysis of the degradation of organic compounds bound to the surface. The GLAD nanostructures were analyzed by changing the flux angle and monitoring photobleaching of the methylene blue dye.(278) The results showed that the sensor response was optimal at a flux angle of 75°, close to angle at which the surface area is the greatest. Functionalization of metal oxide GLAD thin films has also been studied.(279, 280) In these studies, the column structures became targets for siloxane-based chemical reactions following hydroxyl functionalization of the sensor surface. Based on the treatment method, vapor or solution based, it was shown that the wettability of the surface may be controlled. Based on this pre-functionalization method (vapor or solution-based), the results showed that pre-treatment of the columns may be a promising approach for chemically tuning a surface.(234)

Multifunctional Patchy Particles

Pawar and Kretzshmar used GLAD to fabricate multifunctional patchy particles consisting of nanostructures of various dimensions.(281, 282) They coined the structural characteristics of these particles with various morphologies of “patchiness”, “branching”, and “chemical ordering”. The substrates in this study were fabricated using a “bottom up” approach by combining GLAD with a stamping technique used to isolate particles that allowed access of the entire particle surface during the deposition. The size of the patch on each particle was carefully controlled by changing the glancing angle throughout the deposition. In this study, the thin film

was deposited in close-packed colloidal monolayers on pre-cleaned glass slides using a convective assembly method. The microspheres were coated with 5 nm of titanium followed by 20 nm of gold inside the evaporator maintained at a pressure of 10^{-6} mbar. Particles with patches of sizes ~25% and ~11% of the total particle surface area were fabricated at an angle of metal deposition (adjusted by tilting the sample inside the evaporator) of 30° and 10°, respectively. This process was performed so that the nanoparticles facing the incident flux to achieve varying degrees of anisotropy on the same particle, producing "patches". Although the particles have varying patch geometries (originating from different monolayer domain orientations), the total patch size on each particle is identical for a fixed angle of metal deposition. This technique allows for the production of particles with varying anisotropic dimensions. These particles have found applications in electrical connectivity applications where they are used as colloidal motors due to the electrical contacts resulting from metal overlap on the particle surface.(283)

Silver Nanorod Arrays

Recently, a nanofabrication technique called oblique angle deposition (OAD), a slight variation of GLAD, has been developed that allows the growth of aligned silver nanorod arrays for high sensitivity SERS application. OAD, a slight variation of GLAD, is a physical vapor deposition technique in which the substrate is rotated to a specific angle such that the vapor from the metal source is incident on the substrate close to the grazing angle. The two phenomena controlling the growth of the silver nanorod arrays during OAD are the shadowing effect and surface diffusion. These conditions result in preferential growth of cylindrical, irregularly shaped rods that are randomly, yet uniformly, distributed on the surface. The growth of the nanorods arises from

initial metal nucleation sites in the direction of vapor deposition. The nanorods produced by OAD are cylindrical in shape but encompass a variety of random protrusions and irregularities. Figure 3.7 displays a scanning electron micrograph (SEM) of a silver nanorod array.

3.4. Silver Nanorod Arrays as SERS-Active Substrates

Recently, silver nanorod arrays have proven to be excellent substrates for use in surface enhanced Raman scattering (SERS) experiments.(284-303) These SERS-active substrates have been shown to be highly uniform in structure, easy to fabricate, reproducibly made, and provide strong, highly reproducible, SERS signal enhancements. This high SERS signal enhancement observed with silver nanorod arrays results from the chemical and/or chemical electromagnetic enhancement mechanisms previously discussed in Chapter 2.(52, 53) Enhancements associated with high curvature regions have been deemed the "lightning rod effect" and contribute to the high enhancement factor observed for molecules at the tips of the nanorods or in pores.(304-306) It has been determined that oscillations of the localized surface plasmon take place along the width (transverse plasmon band) and the length (longitudinal plasmon band) of the nanorods.(307) The overlap of both the longitudinal and lateral plasmon bands is primarily responsible for the strong electromagnetic (EM) enhancement at the tips of the nanorods. As a result, the maximum SERS intensity observed for these Ag nanorod arrays is in the polarization direction perpendicular to the long axis of the nanorods.(308) The high aspect ratio of the Ag nanorods results in a blue shift to below 400 nm of the transverse mode (TM) of the plasmon resonance in the nanorods and a red shift to above 1000 nm of the longitudinal mode of the resonant wavelength. However, the two waves may be tuned accordingly based on the aspect

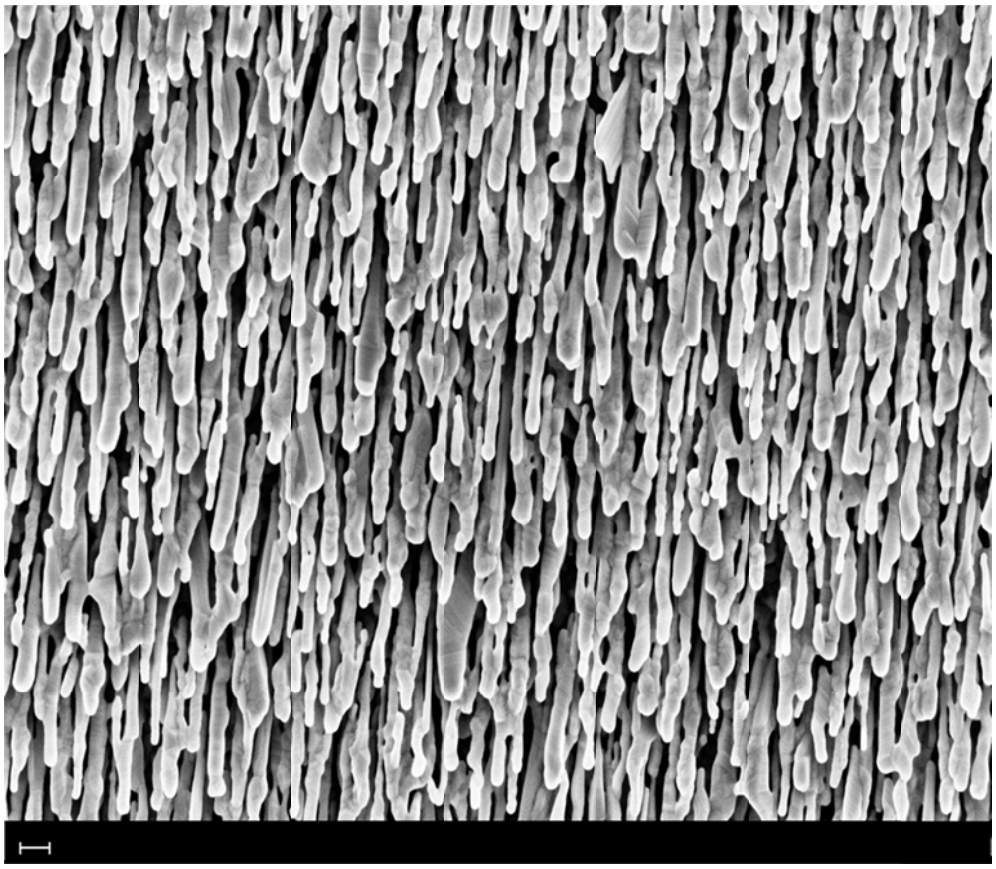

Figure 3.7. Top-view SEM micrograph (40K) of a silver nanorod array substrate fabricated using oblique angle vapor deposition (OAD). The scale bar represents 200 nm.

ratio of the nanorods to produce the enhanced signal observed in SERS. Based on these effects, the large SERS enhancement observed on Ag nanorod substrates may be attributed to either a plasmon mode in the gap between two adjacent nanorods or a multimode plasmon resonance. Theoretical calculations on these localized plasmon modes and previous experiments are in agreement with these observations.(131) Overall, the electromagnetic field contributing to the electromagnetic enhancement is theorized to be at a maximum for points with high curvature, further supporting the use of nanorod arrays fabricated by OAD as SERS-active substrates. Figure 3.8 shows the electric field distribution of a Ag nanorod array calculated by Finite-Difference Time-Domain (FDTD) at 785 nm. In Figure 3.8.a and 3.8.b, the E-field distribution in the xz and yz plane was calculated under p-polarization incidence, whereas in Figure 3.8.c and 3.8.d, the E-field distribution in the yz and xz plane was calculated under s-polarization incidence. Further details on silver nanorod fabrication, characterization, and cleaning will be provided in Chapter 4.

GLAD is a physical vapor deposition technique that offers a number of advantages for fabricating nanostructures. Using this technique, vertically aligned nanorods may be formed naturally by simply varying the incident angle of the substrate relative to the metal source. As a result, GLAD is superior to most of the conventional chemical vapor deposition (CVD) or vapor-solid-liquid (VLS) techniques where a great deal of effort has been made to fabricate aligned nanowires. Unlike any other nanostructure fabrication methods, provides the ability to control the size and density of the nanorods by adjusting the vapor incident angle. Additionally, there is virtually no materials limit, i.e., as long as the material may be evaporated, it may form vertically

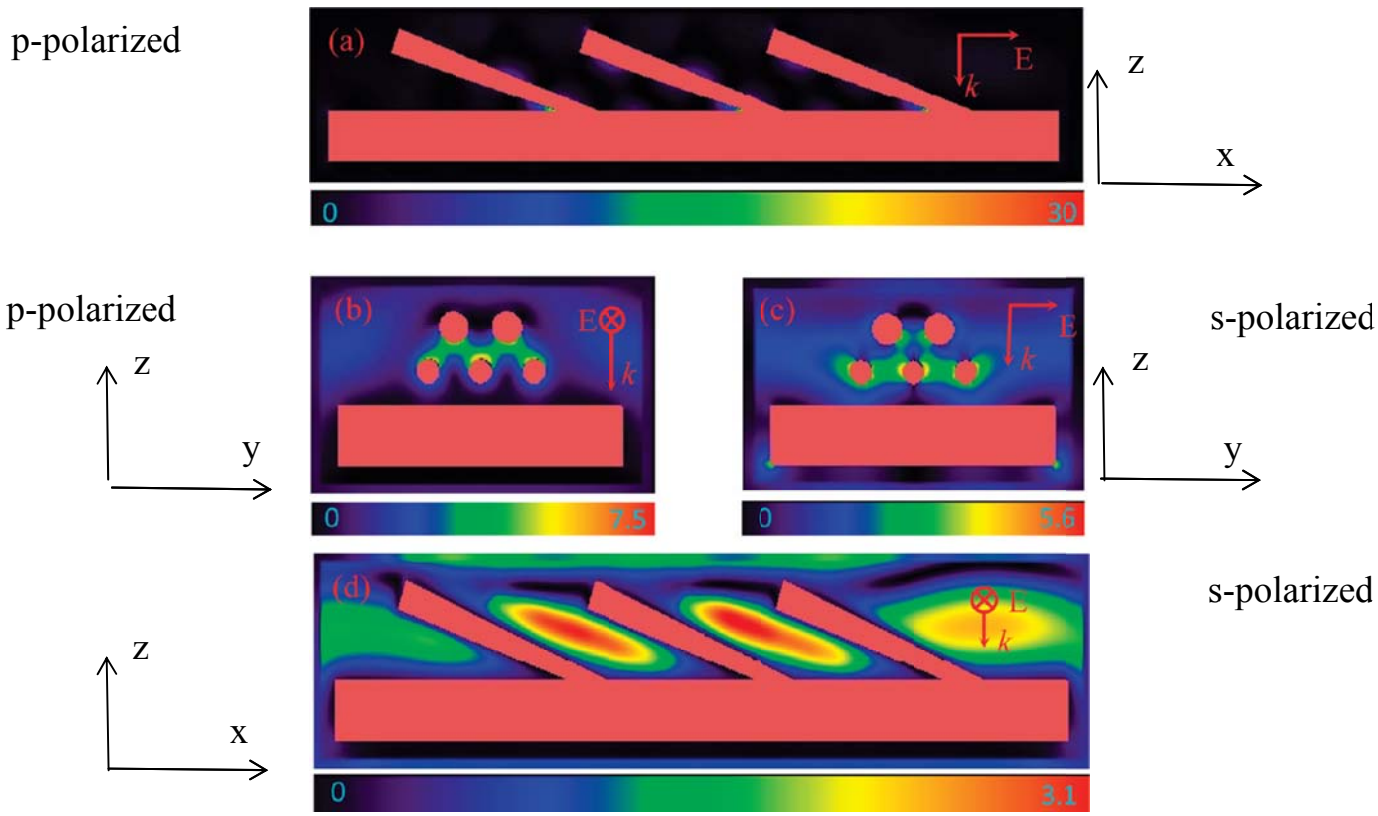

Figure 3.8. The E-field distribution of a Ag nanorod array calculated by FDTD under λ = 785 nm: (a, b) the E-field distribution in the xz and yz plane under p-polarization incidence and (c, d) the E-field distribution in the yz and xz plane under p-polarization incidence.

aligned nanorod structures. The shape, alignment, porosity, and orientation of the nanorods may be easily tailored by changing the deposition and rotation procedures. These nanostructures have been extensively used for a variety of sensing applications. Specifically, silver nanorod arrays fabricated by OAD have been used as SERS-active substrates for detection of a variety of analytes. The focus of the work presented in this dissertation is based on the use of these silver nanorod arrays as SERS-active substrate. The following chapters will introduce the reader to the use of these silver nanorods for a variety of sensing and bioanalytical applications.

CHAPTER 4

Removal of Surface Contamination and Self-Assembled Monolayers (SAMs) from Silver (Ag) Nanorod Substrates by Plasma Cleaning with Argon

The purpose of this chapter is to introduce the reader to a simple and versatile cleaning procedure developed to eliminate surface contamination present on the surface of the Ag nanorod arrays. This mild physical-chemical method consists of short exposure of the OAD fabricated SERS substrate to ionized Ar gas plasma under low pressure conditions and is aimed to remove detectable background contamination such as carbonaceous contamination and small organic molecules as well as thiolate SAMs from Ag nanorod. The results of this investigation are presented in this chapter and include: (i) a thorough investigation on the Raman band intensities, (ii) a description of the nanorod morphology following the cleaning procedure, as well as (iii) a study of the surface hydrophobicity as a function of exposure time of the Ag nanorod arrays to the Ar^+ plasma.

4.1. Introduction

The fabrication of uniform, reproducible nanoparticles with high surface enhancements is the key feature for the use of SERS as a practical analytical technique. To date, many nanofabrication techniques have been developed to produce SERS-active substrates for various applications. Such techniques include, but are not limited to, roughened electrodes by oxidation-reduction cycles (ORC), Ag film electrodes via electrocrystallization, Ag island films, Au or Ag

nanorod arrays, Au or Ag colloids and nanoshells, and nanoparticle lithography.(97, 101, 309-313) A thorough description of these various nanofabrication techniques was previously presented in section 2.3 of Chapter 2. Recently, our laboratories demonstrated that oblique angle vapor deposition (OAD) is an easily-implemented, reproducible SERS nanofabrication method, and showed that the Ag nanorod arrays that result from this fabrication technique exhibit uniformly high SERS enhancements over large substrate areas.(287, 288, 291)

Irrespective of the nature of the fabrication method, the presence of carbonaceous contamination on SERS-active substrates affects the reproducibility of measurements and is a limitation to the analytical utility of SERS. While there have been numerous attempts to remove organic contamination from SERS-active metallic surfaces under ambient conditions, none have been uniformly successful at eliminating background contamination on SERS substrates.(314-317) For example, electrochemical cleaning of graphitic carbon contamination on Ag surfaces has been one method employed as a surface cleaning protocol.(317) Other published electrochemical cleaning protocols have demonstrated removal of surface-confined carbon contamination on mechanically polished Ag surfaces but were ineffective at completely removing monomolecular layers.(318) Unfortunately, a side result of some electrochemical desorption techniques may be the introduction of surface defects where the carbon contamination was present or highly oxidized surfaces due to the high chemical reactivity of Ag.(319, 320)

A number of methods have been developed to chemically remove adsorbed self-assembled monolayers (SAMs) from the underlying substrates as an economical way of re-using substrates.

Examples include immersing SAMs in 0.5 M NaBH4 solution, application of suitable surface potentials to induce desorption, and photooxidation, in which thiolate SAMs undergo oxidation upon exposure to ultraviolet (UV) radiation in air and ion bombardment.(321-325) Another chemical cleaning procedure for removing SAMs from SERS-active surfaces consists of submerging the substrate in chemical oxidants such as concentrated acids.(326) These methods appear to be effective for cleaning substrates but have the disadvantage of causing oxidation, with increased probability of substrate corrosion. Alternative methods such as ozone cleaning or plasma cleaning with air result in a high degree of oxidation of the Ag surface and hence yield poor SERS-active substrates.(327)

In addition to physical/chemical methods of cleaning SERS substrates, several authors have reported on the use of self-assembled monolayers (SAMs) adsorbed onto SERS substrates as a way of displacing "adventious material" from the metal.[320,332,333] SAMs have been widely used in the areas of interfacial phenomena, biological processes, electrochemistry, photoelectrochemistry, photoactivity and molecular interaction.(315, 327, 328) Many of the long-chain alkyl disulfides and thiols have been shown to form SAMs at noble metal surfaces.(329, 330) These complex coatings are strongly anchored to the surface and only desorb under strongly acidic or basic conditions.(331) Unfortunately, the results of the investigations into the use of SAMs for displacing surface contamination suggested that adsorbed alkanethiols do not completely displace contaminants. Impurities were still observed despite multiple efforts at alkanethiol adsorption. It is likely that the original carbonaceous surface

species remained sequestered within the SAM film and affected structural order, orientation, and packing of the alkanethiol.(316)

In this study, a milder physical-chemical method for removing surface contamination from Ag substrates is introduced. The cleaning procedure consists of exposing the Ag nanorod array substrate to ionized Ar gas plasma for 4 min under low-pressure conditions. The efficiency of Ar^+ plasma cleaning on Ag nanorod substrates was observed by monitoring the SERS intensity of a conventional SERS-active reporter molecule, 1,2-bis(4-pyridyl)ethylene (BPE) before and after exposure. We also investigated the broader applicability of this plasma cleaning technique as an effective method for removing SAMs from SERS-active Ag substrates, using 1-propanethiol as the model SAM presented here, but also longer chain thiols such as 1-hexanethiol, C_6SH, and 1-dodecanethiol, $C_{12}SH$ (data not shown). SERS, scanning-electron microscopy (SEM) and contact angle measurements were used to characterize the cleanliness and morphology of the Ag substrates.

The results of this study show that for short time periods (<4 min), Ar^+ plasma cleaning essentially eliminated any detectable organic contamination from Ag nanorod substrates and did not substantially change their morphology. After this short Ar^+ plasma exposure, SERS intensities for re-adsorbed molecules decreased, but to acceptable levels for spectroscopic purposes. However, a large decrease in SERS intensity was observed upon longer time exposure (>10 min) to the Ar^+ plasma. This decrease in intensity was associated with distinct morphological changes observed on the SEM images of the aligned Ag nanorod arrays as well as

a decrease in their hydrophobicity as measured by static contact angle. The results presented here suggest that Ar^+ plasma cleaning is an efficient process for removing carbonaceous and organic contamination as well as SAMs from SERS-active Ag surfaces, as long as the cleaning conditions and exposure times are carefully controlled.

4.2. Methods and Materials

Materials and Reagents

1-propanethiol (C_3SH, ≥99%), 1,2-bis(4-pyridyl)ethylene (BPE) (99.9+%), and EtOH (100%) were purchased from Aldrich. All other chemicals were of analytical grade and used without any further purification.

Preparation of Ag Nanorod SERS Substrates

SERS-active Ag nanorod array substrates were prepared from 1 × 1 cm glass substrates using an oblique angle vapor deposition (OAD). Prior to deposition, the glass substrates (Gold Seal Cat. 3010) were cleaned using Piranha solution (4:1 mixture of conc. H_2SO_4: 30% H_2O_2) for 15 minutes, rinsed with copious amounts of deionized water and dried under a gentle stream of nitrogen gas. SERS-active Ag nanorod substrates were fabricated by OAD using an electron-beam/sputtering evaporation system. First, a 20 nm layer of Ti (99.99%, Kurt J. Lesker Company, Clairton, PA) was deposited onto the cleaned glass substrates at a rate no greater than 1.0 Å/s for adhesion and stability purposes for the subsequent Ag layer. Next, a 500 nm layer of Ag (99.99%, Kurt J. Lesker Company) was deposited on the substrates at a rate of 3.0-4.0 Å/s.

Previous studies have demonstrated that the addition to the Ag layer prior to the growth of the Ag nanorods enhances the SERS signal compared to growing the nanorods directly to the underlying Ti layer.(291, 332) After deposition of the Ti:Ag underlayer, the substrate was rotated to 86° relative to the incident vapor. Ag nanorods were then deposited at a constant rate of 2.5-3.0 Å/s to a final nominal thickness of 2000 nm, as monitored by a quartz crystal microbalance (QCM) placed inside the deposition chamber and positioned at normal incidence to the vapor source. The growth of the metallic layers was performed in a background deposition pressure maintained at less than 5 x 10^{-6} Torr. After deposition, the substrates were allowed to cool down to room temperature in vacuum before they were removed from the chamber. The SERS-active substrates were stored in a nitrogen purge type glove box to avoid any surface contamination or deterioration of the surface condition due to temperature or atmospheric humidity.

Solution Preparation

10 mL of a 10^{-3} M solution of C_3SH was prepared by mixing 0.9 μL of 1-propanethiol in 10 mL of EtOH. 10 mL of a 1 M solution of BPE was prepared by dissolving 1.8223 g of BPE in EtOH. Serial dilutions were made to obtain a 10^{-5} M BPE solution.

Monolayer Preparation

The procedure for preparation of BPE-covered or C_3SH-covered substrates consisted of soaking the 1 × 1 cm Ag nanorod substrates in the relevant solution. The concentration of the C_3SH solution was 1×10^{-3} M in EtOH; the concentration of the BPE solution was 1×10^{-5} M in EtOH.

In both cases the nanorod substrates were immersed for 12 hours. The substrates were then removed from the solution, rinsed carefully with copious amounts of 100% EtOH, and allowed to completely dry prior to analysis.

Raman Spectroscopy

Measurements were performed using a confocal Raman microscope (InVia, Renishaw, Inc., Gloucestershire, United Kingdom). Laser excitation was provided by a 785 nm near-IR diode laser. The incident laser beam was delivered to the sample by epi-illumination through a 20× (N.A. = 0.40) objective onto an automated sample stage. The laser illumination spot produced by this system through this objective has a rectangle pattern that is approximately 4.8 × 27.8 μm. The laser power used was 0.1% (~0.72 mW) for C_3SH, and 0.0001% (~5.5 μW) for BPE, respectively, as measured at the sample. SERS spectra were collected from five different spots on a given substrate using a 30 second acquisition time with one accumulation. Spectra were collected between 2000 and 500 cm^{-1}. For SERS mapping measurements, each of the 1 × 1 cm aligned Ag nanorod array substrates was scanned over a 45,000 μm^2 area (300 × 150 μm). Spectral maps were recorded every 5 μm from the previous laser spot horizontally across every 5 μm vertical lines for a total of 1,891 collected data sets on each substrate. The spectral range collected at each spot was from 2000 to 500 cm^{-1}. The laser power was 5% and one accumulation was used to collect the SERS spectra using a 1 second acquisition time. The 1604 cm^{-1} BPE peak intensity was used to quantify the SERS response for each Ag nanorod array substrate. Off-line spectral manipulation and analysis, *i.e.*, baseline correction, band

height/band area and peak frequency determination, was performed using GRAMS 32/AI Version 6.0 (Galactic Industries Corporation, Nashua, NH).

Scanning Electron Microscopy

Scanning electron micrographs were obtained using a Zeiss SEM Ultra60 scanning electron microscope (Carl Zeiss SMT Inc., Peabody, MA). Images were acquired with an accelerating voltage of 5 eV and at an incident angle of 0° relative to the surface normal. Images were acquired at a magnification of 40K and 100K for comparison purposes. To minimize charging artifacts, slides were attached to the holder using double-sided copper tape. Analysis of image features was performed using Smart Tiff™, a software tool made available by Zeiss.

Contact Angle Measurements

The wetting properties of the Ag nanorod array substrates were measured using a Krüss GmbH (Hamburg, Germany) DSA 100 Drop Shape Analyzer. 2 μL of molecular grade water was dispensed by the needle tip of the direct dosing system using software control DS3210 on the aligned Ag nanorod arrays surface mounted on the sample stage of the instrument. Calculations of the static contact angles were performed using DSA3, an instrument software tool provided by Krüss, and the pictures were taken using illumination from a standard Krüss camera mounted on the instrument and protected against external influences in a housing unit inside the apparatus.

Plasma Cleaning

The Ag nanorod array substrates were cleaned using plasma cleaner model PDC-32G (115V) manufactured by Harrick Plasma (Ithaca, NY). The substrates were cleaned using the high RF setting with a constant flow of Argon coming from an ultra-pure Argon tank (American Welding and Tank). The high RF setting consists of 100 W input power, which corresponds to a DC voltage of 720 V and a DC intensity of 25 mA (18 W) at the RF coil. The pressure gauge was kept at 0.8 mBar during the course of the cleaning procedure. Exposure times were varied depending on the experiment. The cleaning procedure consisted of placing the sample in the reaction chamber evacuated using an oil free dry scroll pumping system with a minimum pumping speed of 1.4 m^3h^{-1} (0.83 ft^3 min^{-1}) and an ultimate total pressure of 200 mTorr (0.27 mBar) or less. Ultra-pure Ar gas was flowed into the chamber at flow rates typically between 1-2 SCFH and at low-to-medium pressure (typically between 0.5 mBar and 1.0 mBar). Within the chamber, the process gas was subjected to MHz-range RF electromagnetic radiation, accelerating the ions in the gas and ionizing them to form an Ar^+ plasma at near ambient temperature. The Ar^+ plasma removes surface adsorbed molecules by mild ablation of the surface. The molecules desorbed from the surface are then pumped away using a vacuum pump (Edwards, Model XDS-5).

4.3. Results and Discussion

Removal of Carbonaceous and Organic Contamination from Ag Nanorod Substrates by Plasma Cleaning with Argon

Our previous studies have shown that OAD is a versatile and reproducible method of preparing high sensitivity SERS-active substrates.(287, 288, 291, 332, 333) These previous studies have also reported that impurities are common on these SERS-active substrates due to the highly reactive nature of the Ag surface.(291) The surface contamination present on OAD-prepared Ag nanorod arrays is mostly due to the presence of carbon, graphite, and hydrocarbons.(291, 315, 327) Figure 4.1.A shows the background SERS spectrum of the bare Ag nanorod substrate after the fabrication process and before any analytes were deposited on the surface. The spectral features present on the background SERS spectrum shown in Figure 4.1.A are in agreement with the observation reported by Driskell and co-workers which attributed the bands to carbonaceous material and organic contaminants adsorbed on the Ag nanorods.(291) The dominant features on the SERS background spectrum in Figure 4.1.A are the three broad bands near 1133, 1340 and 1580 cm^{-1}. The 1340 cm^{-1} band (D band) has been attributed to disorder in the graphite chains while the 1580 cm^{-1} band (G band) has been attributed to the in-plane stretching mode. In addition, the absence of bands in the v(C-H) region is also a clear evidence of the presence of graphitic carbon contamination on the SERS-active Ag substrate.(334) The other bands in the spectrum are attributed to organic impurities originating from the out-gassing of the OAD deposition chamber. Similar contamination peaks were observed from other spots on the same

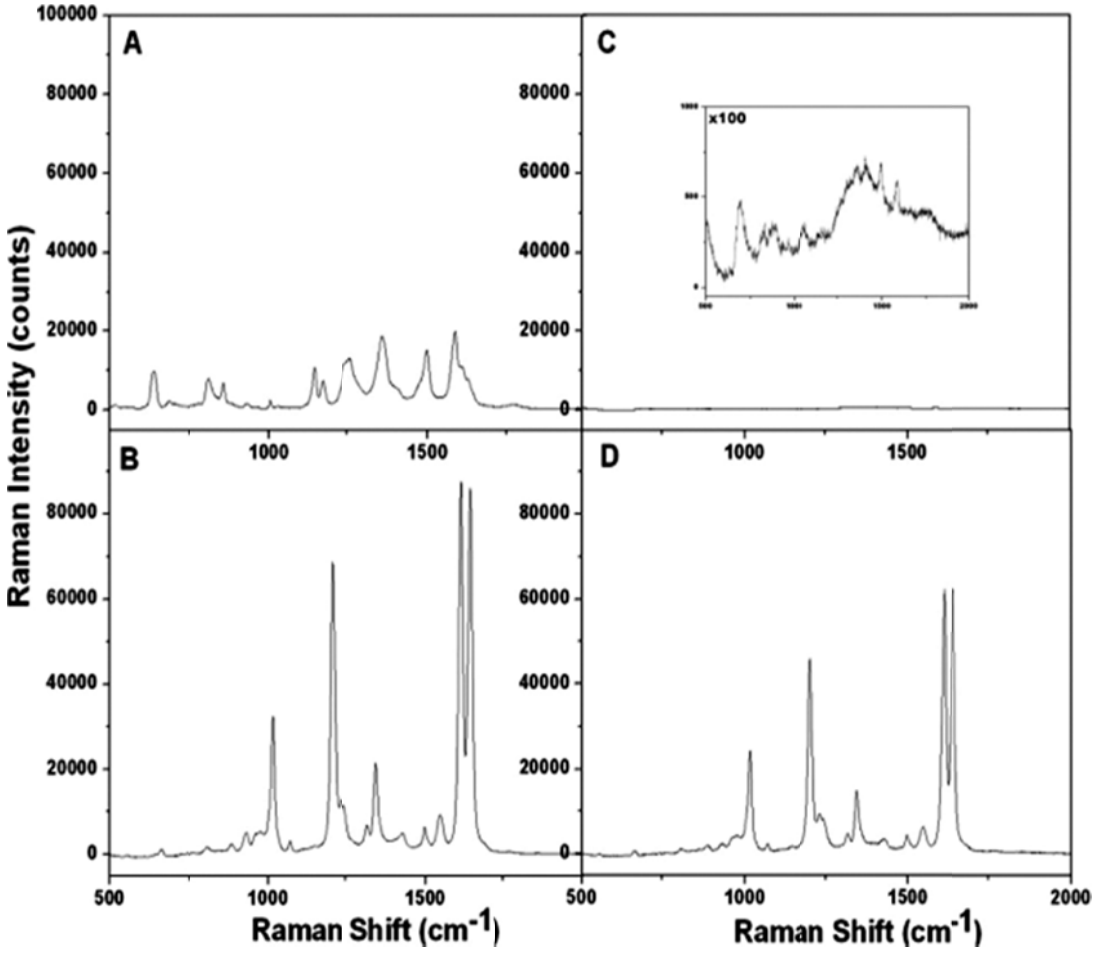

Figure 4.1. (A) Background SERS spectrum of uncleaned Ag nanorod substrate. (B) SERS spectrum of 10^{-5} M BPE deposited on an uncleaned Ag nanorod substrate. (C) SERS spectrum of Ag nanorod substrate with BPE from panel (B) after 4 min exposure to Ar^{+} plasma. (D) SERS spectrum of 10^{-5} M BPE deposited on Ag nanorod substrate from panel (C).

substrate and from other substrates with minor changes in peak intensities but no differences in band positions.

Figure 4.1.B shows the spectrum of a 10^{-5} M solution of BPE deposited on a plasma-cleaned nanorod substrate. The Raman modes of BPE seen in this spectrum are identical to previously observed SERS spectra on Ag nanorod arrays.(288, 291) The assignments of these vibrational modes have been previously reported in the literature.(335) Figure 4.1.C shows the SERS spectrum of the BPE-coated substrate seen in Figure 4.1.B after a 4 min exposure to an Ar^+ plasma. The spectrum is characterized by a noticeably flat baseline, indicating the absence not only of the adsorbed BPE, but also of any original organic contaminant on the Ag nanorod substrate. The insert (x100) shows the relatively low noise level on the spectrum after the cleaning procedure. The SERS spectrum in Figure 4.1.C provides clear evidence that the Ar^+ plasma has removed any adsorbate.

To characterize the SERS response of a plasma-cleaned substrate, a 10^{-5} M solution of BPE in EtOH was spotted on the same Ag nanorod substrate. The SERS spectrum BPE re-adsorbed onto the cleaned Ag nanorod substrate is shown in Figure 4.1.D. A comparison of Figure 4.1.B and 4.1.D shows that the plasma-clean Ag nanorod substrate (Figure 4.1.D) retained about 60% of the BPE intensity when compared to the SERS spectrum of BPE measured on a fresh, non-cleaned substrate (Figure 4.1.B). While a 4 min exposure in Ar^+ plasma cleaning has reduced the observed SERS intensity of the Ag nanorod array, the cleaning procedure did not alter bandwidths, frequencies or relative intensities in the SERS spectrum of the re-applied BPE.

Effect of Plasma Cleaning on Self-Assembled Monolayers (SAMs) Adsorbed on Ag Nanorod Substrates

We investigated the effect of Ar^+ plasma cleaning on the removal of SAMs of alkanethiols adsorbed onto Ag nanorod substrates. Figure 4.2.A shows the SERS spectrum of a SAM of 10^{-3} M C_3SH adsorbed onto the Ag nanorod substrate. The spectral features observed in Figure 4.2.A were found to be in agreement with the literature band assignments of C_3SH.(336)

SAMs of alkanethiols have been shown to strongly adhere to Au and Ag surfaces. Attempts to desorb SAMs from these surfaces have been shown to deteriorate the substrates when subjected to harsh treatments. Alternative methods to remove SAMs from these surfaces have resulted in oxidized (RSO_x) sulfur species that either do not desorb completely from the SERS-active surface or induce strong corrosion of substrates. In other cases, the SERS-active surface itself is oxidized and the SERS enhancement is altered or inhibited by the presence of oxygen at the surface of the substrate.(337) As a result, the local electromagnetic field enhancement produced by both the excitation of the surface plasmon and the chemical adsorption of the analyte on substrate's surface is hindered by the presence of oxygen on the surface. Consequently, poor SERS enhancement is observed when the Ag making up the nanorod array is oxidized by the presence of oxygen.

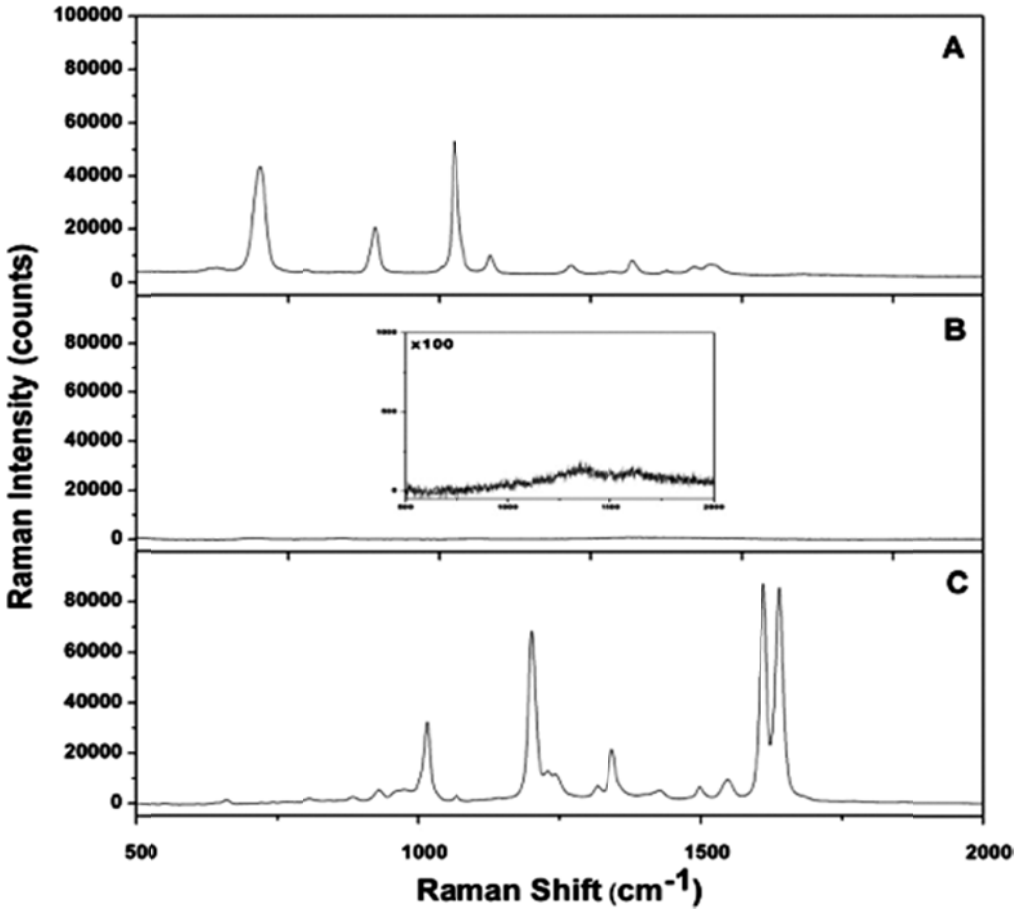

Figure 4.2. Spectral and structural parameters for Ag nanorod array substrates after Ar^+ plasma cleaning. Intensity counts obtained from the 1064 cm^{-1} band in the SERS spectrum of BPE. Nanorod dimensions obtained from SEM images.

We investigated whether Ar^+ plasma cleaning is applicable for removal of thiolate monolayers from Ag nanorods. In these experiments, the C_3SH-covered Ag nanorod array was exposed for 4 min in an Ar^+ plasma in the same manner as described above for BPE-covered substrates. Figure 2B shows the SERS spectrum of the cleaned Ag nanorod substrate recorded immediately after Ar^+ plasma cleaning. The absence of any features in Figure 4.2.B illustrates that a 4 min exposure to the Ar^+ plasma was sufficient to completely remove the C_3SH monolayer from the Ag nanorod surface. The insert (x100) shows that the noise level is extremely low on the spectrum, suggesting that the cleaning procedure is more efficient when alkanethiol chains are adsorbed on the Ag nanorod surface. This plasma cleaning technique showed the same cleaning effectiveness for longer alkanethiol chains such as 1-hexanethiol, C_6SH, and 1-dodecanethiol, $C_{12}SH$ (data not shown). These results support the applicability of Ar^+ plasma cleaning for desorption of thiolate SAMs from Ag nanorod substrates.

To investigate whether the SERS response of the Ag nanorod substrate could be recovered after the removal of the alkanethiol from the Ag nanorod surface by the plasma cleaning procedure, a 10^{-5} M solution of the molecular probe BPE in EtOH was deposited onto the plasma-cleaned Ag nanorod substrate. Figure 4.2.C shows the SERS spectrum of BPE deposited, after Ar^+ plasma cleaning, onto the substrate on which the SAM C_3SH was originally formed. Similar to the spectrum of BPE applied to a plasma-cleaned substrate in Figure 1D, the spectrum of BPE after plasma cleaning of a C_3SH-covered substrate (Figure 4.2.C) shows a comparable SERS intensity to that of BPE measured on an unprocessed Ag nanorod substrate (Figure 4.1.B). The higher intensity on the spectrum of BPE shown in Figure 2C also suggests that the Ar^+ plasma cleaning

procedure is more effective in retaining the substrate enhancement when alkanethiol chains are adsorbed on the Ag nanorod surface, which is in agreement with the low noise level present on the spectrum shown in Figure 4.2.B. Spectral features such as bandwiths, relative intensities and S/N were unaltered between the two spectra, acquired under the same conditions.

Morphology and Structural Characterization of the Ag Nanorod Array SERS Substrates upon Exposure to Ionized Argon Gas Plasma

The morphology of the Ag nanorods was investigated to determine what changes, if any, occurred to the SERS-active substrates upon exposure to Ar^+ plasma. The effect of exposing Ag nanorods to Ar^+ plasma was evaluated using SEM images and contact angle measurements. These measurements were correlated with the SERS response of the substrates.

Figure 4.3.A depicts a schematic side-view of the Ag nanorod arrays and includes the approximate dimensions of the tilted parallel nanorods resulting from the shadowing effect during the OAD deposition procedure. The tilted parallel alignment seen in Figure 4.3.A is due to the shadowing effect encountered during the OAD deposition procedure when the substrate is rotated to 86° with respect to the vapor incident direction.

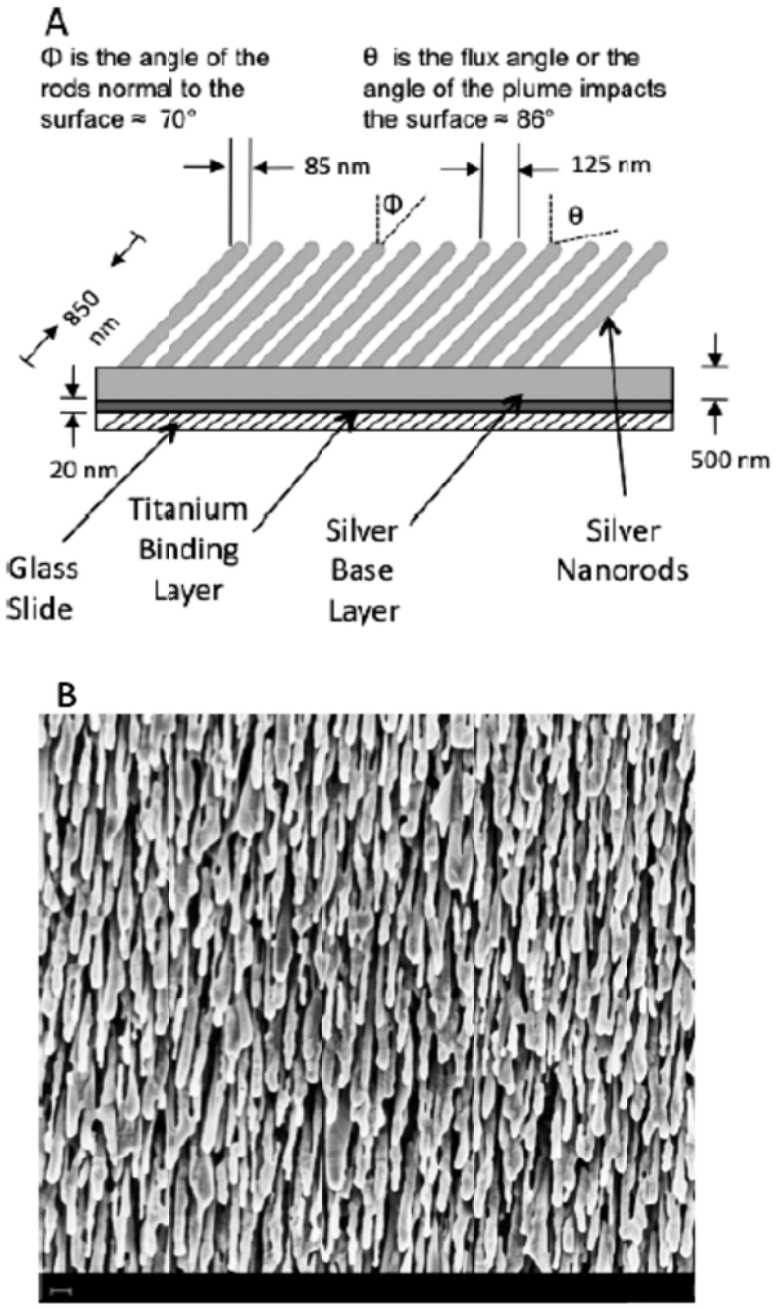

Figure 4.3. (A) Schematic of the Ag nanorod array with approximate dimensions. (B) Top-view micrograph (40K) of a Ag nanorod array deposited onto a glass slide, using methods described in the Methods and Materials section. The scale bar represents 200 nm.

SEM images of Ag nanorod arrays were acquired as a function of Ar^+ plasma exposure time ranging from a control of 0 min to a maximum of 14 min in 2 min intervals. Scanning electron microscopy (SEM) has been used to characterize Ag nanorod arrays. Figure 4.3.B displays the top view SEM image of a Ag nanorod control substrate. The micrograph (40K) shows that the Ag nanorods are randomly, yet uniformly, distributed on the substrate and preferentially aligned along the vapor deposition direction. Ag nanorods produced by OAD are generally characterized by protrusions, corrugations and bifurcations along the cylinder surface. These SERS-active substrates consist of aligned Ag nanorod arrays with: i) nanorod lengths of ~800-900 nm, ii) diameters ~80-90 nm, iii) tilt angles of ~71° with respect to the surface normal, iv) nanorod densities of 15-25 per μm^2, and v) average spacing between two adjacent rods of approximately 150 nm. Minor variations in nanorod morphology, including length, diameter, and shape are caused by the polycrystalline nature of the Ag nanorods. The preferential growth of the Ag nanorods results in uniform, homogeneous and reproducible substrates. These attributes make OAD-fabricated Ag nanorod arrays excellent sources of SERS substrates. The structures shown in Figure 4.3.B are consistent with previously published results on OAD Ag nanorods.(285, 287, 291, 333)

The polycrystalline nature of the Ag nanorods introduces some variation in their morphology, including length, diameter, and shape. SEM images provided a qualitative assessment of nanorod shape and quantitative measurement of nanorod length and density. Data obtained from the SEM image of the Ag nanorods shown in Figure 4.3.B showed that the nanorods were aligned parallel to each other at an angle of 70.8±3° with respect to the surface normal. The average spacing

between two adjacent rods was approximately 169±15 nm with an average nanorod length of 875±103 nm and an average diameter of 104±23 nm. Additionally, the nanorod density was determined to be 12.6±0.7 rods/μm^2. These values are collected in Table 4.1 and are consistent with the aforementioned dimensions reported from previously published results.(287, 291)

Figures 4.4.A, 4.4.B and 4.4.C are representative SEM images of the Ag nanorod substrates after 0, 4 and 14 min exposure to the Ar^+ plasma, respectively. The morphology and heterogeneity of the nanorods seen in Figures 4.4.A and 4.4.B is consistent with previously published SEM images of the Ag nanorods prepared by OAD.(287, 291) Based solely on the shape and morphology seen in the SEM micrographs in Figures 4.4.A (0 min exposure) and 4.4.B (4 min exposure), it is difficult to discern any morphological or size changes of the Ag nanorods after a 4 min exposure to the Ar^+ plasma. Although very slight variations in nanorod shape and protrusion (i.e. welding of adjacent nanorods) are noticeable when comparing Figure 4.4.A and Figure 4.4.B, these phenomena did not seem to be discernable qualitatively over the whole substrate area imaged when comparing three SEM images acquired on the same substrate subjected to a 4 minute exposure to the argon ion plasma. However, when comparing the SEM micrographs in Figure 4.4.A (0 min exposure) and 4.4.C (14 min exposure), it is evident that the nanorod array does change after 14 min exposure to the Ar^+ plasma. Figure 4.4.C clearly shows that the original nanorod shape and structure have altered. A comparison of Figure 4.4.A and 4.4.C indicates that long (14 min) exposure to the Ar^+ plasma changes the shape, length and density of the Ag nanorods.

Table 4.1. Spectral and structural parameters for Ag nanorod array substrates after Ar^+ plasma cleaning. Intensity counts obtained from the 1064 cm^{-1} band in the SERS spectrum of BPE. Nanorod dimensions obtained from SEM images.

Exposure Time (min)	BPE Intensity (counts)	Nanorod Length (nm)	Nanorod Diameter (nm)	Nanorod Density (rods/μm^2)	Spacing Between Adjacent Nanorods (nm)
0	90,600 ±16,800	875±103	104±23	12.6±0.7	169±15
4	46,800 ±2,800	868±96	113±31	11.4±0.6	182±11
14	4,300 ±500	642±168	159±56	6.8±0.3	319±42

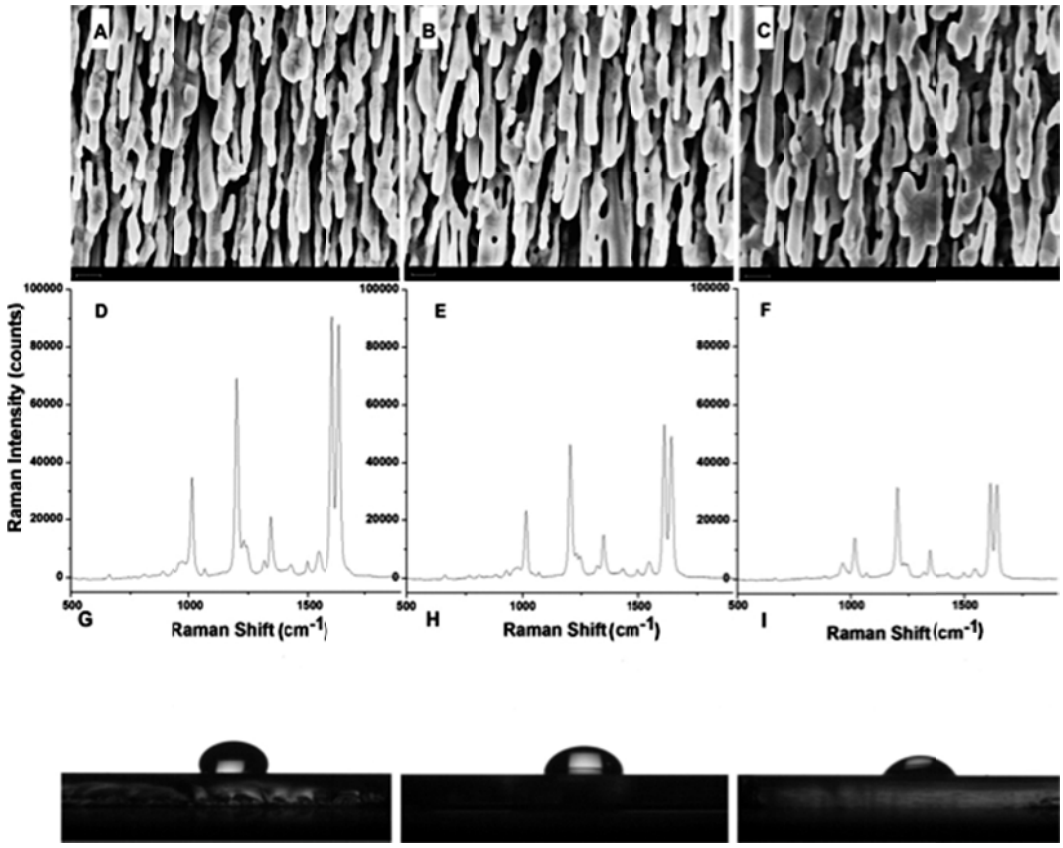

Figure 4.4. Top row: Top-view SEM micrographs (100K) of a Ag nanorod substrate: (A) after 0 min exposure, (B) after 4 min exposure, and (C) after 14 min exposure, to Ar^+ plasma. Scale bars in the images denote 200 nm. Middle row: SERS spectrum of BPE deposited on a fresh Ag nanorod substrate. (D) after 0 min exposure, (E) 4 min exposure, and (F) after 14 min exposure, toAr^+ plasma. (Bottom row) Contact angle picture of 2μL molecular grade water deposited on a Ag nanorod substrate: (G) after 0 min exposure, (H) after 4 min exposure, and (I) after 14 min exposure to Ar^+ plasma.

Quantitative measurements of Ag nanorod morphology upon Ar^+ plasma exposure were obtained directly from the SEM images in Figures 4.4.A – 4.4.C. The average length of the Ag nanorods decreased from 875±103 nm (0 min exposure, Figure 4.4.A) to 642±168 nm (14 min exposure, Figure 4.4.C). The nanorod average diameter increased from 104±23 nm (Figure 4.4.A) to 159.4±56 nm (Figure 4.4.C). The average decrease in length and increase in diameter led to a decrease in the density of the Ag nanorods on the surface, from 12.6±0.7 rods/μm^2 (Figure 4.4.A) to 6.8±0.3 rods/μm^2 (Figure 4.4.C). The decrease in nanorod density is also reflected in the fact that the average gap between the rods was found to increase from 169±15 nm to 319±42 nm. These findings show that exposure of the Ag nanorod substrates to an Ar^+ plasma for >10 min significantly changes the morphology of the Ag nanorods. Table 4.1 provides a listing of the nanorod dimensions obtained for the substrates as a function of Ar^+ plasma exposure.

The large changes in nanorod structure observed with increasing exposure to the Ar^+ plasma should significantly impact the observed SERS response. Nanoscale irregularities on SERS-active Ag nanoparticles are directly related to the generation of the electric field responsible for the SERS-enhancement.(76, 130, 338, 339) Previous studies from our laboratory have demonstrated a marked dependence of the SERS enhancement with the length of the OAD-prepared aligned Ag nanorod substrates.(298, 307, 340) In addition to nanorod length, the unique SERS enhancement properties of these Ag nanorod arrays are postulated to be caused by highly localized plasmon modes created by strong electromagnetic coupling between adjacent metallic nanorods. Therefore, changes in inter-rod dimensions should affect the observed SERS spectra.

As expected, the change in nanorod structure upon long exposure times to the Ar^+ plasma had a direct effect on the resulting SERS intensity. This is easily seen when the spectrum of BPE is compared to the SEM image of the nanorod array acquired after the same exposure time. Figures 4.4.D, 4.4.E, and 4.4.F are the SERS spectra of BPE acquired after 0, 4 and 14 min exposure to Ar^+ plasma. These spectra were acquired using the substrates shown in Figures 4.4.A, 4.4.B and 4.4.C, respectively. After 4 min Ar^+ plasma exposure, the intensity of the BPE bands decreased by approximately a factor of 2 (55%, Figure 4.4.E *vs.* Figure 4.4.D). However, after a 14 min Ar^+ plasma exposure, the BPE SERS intensity decreased by approximately a factor of 10 (95%, Figure 4.4.F *vs*. Figure 4.4.D). Table 4.1 provides a list of the average intensity of the 1064 cm^{-1} BPE band as a function of Ar^+ plasma exposure time.

Figure 4.5 further illustrates the evolution of the BPE SERS intensity as a function of Ar^+ plasma exposure time. While there was no difference in the relative band intensities, bandwidths or positions of the major BPE bands, there is clear evidence from Figure 5 that the morphological changes in the Ag nanorods due to prolonged Ar^+ plasma exposure results in a decreased SERS efficiency as the exposure time is increased.

To determine the evolution of the SERS response, the peak intensity (as measured from the CCD detector counts) of the 1604 cm^{-1} BPE band was plotted as a function of Ar^+ plasma exposure time. The resulting plot is shown in Figure 4.6. The average integrated intensity of the 1604 cm^{-1} BPE band are useful to quantify the decreased SERS response since this band is insensitive to orientation on the surface.(327, 335) Figure 4.6 shows that any exposure to Ar^+ plasma will

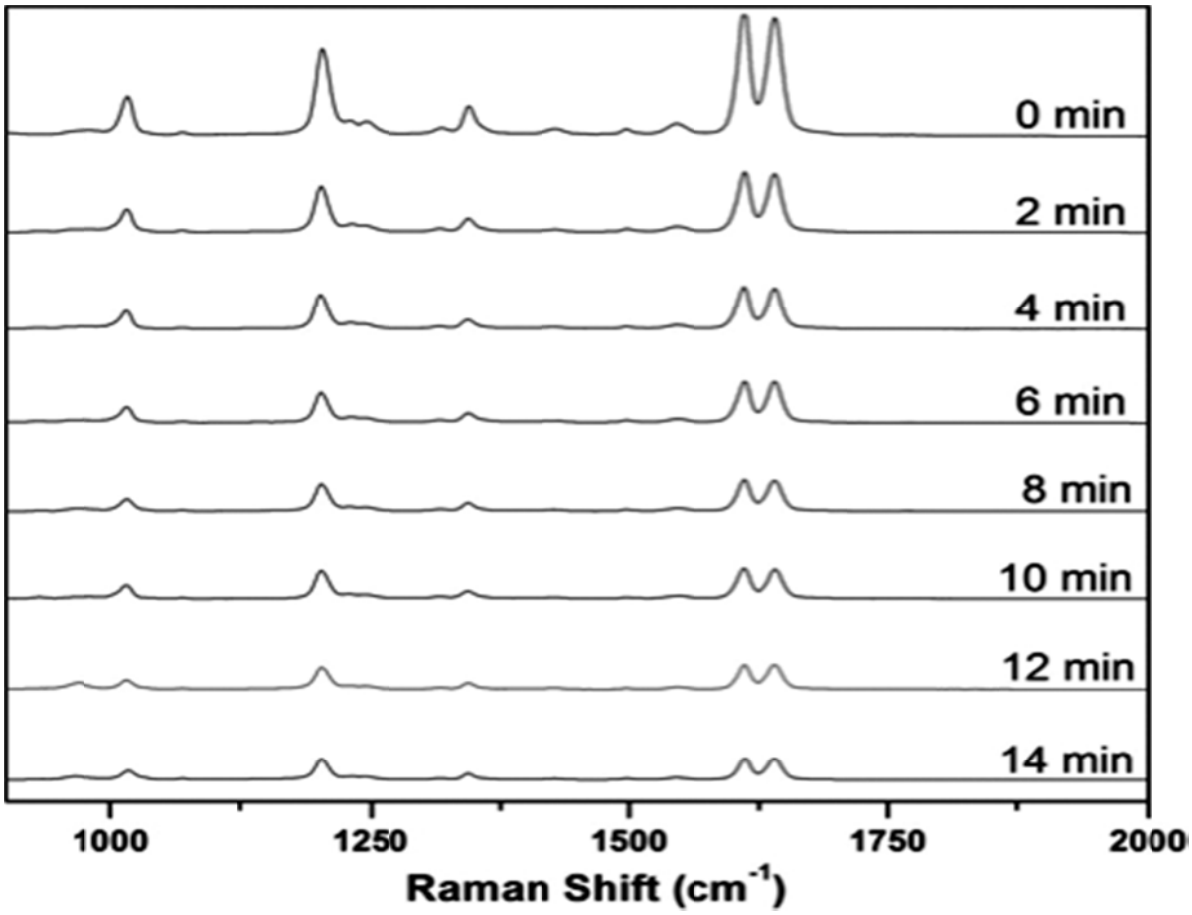

Figure 4.5. Spectra of 10^{-5} M BPE deposited on Ag nanorod substrates after various exposure times. The spectra have been baseline corrected, plotted on the same scale, and offset for visualization.

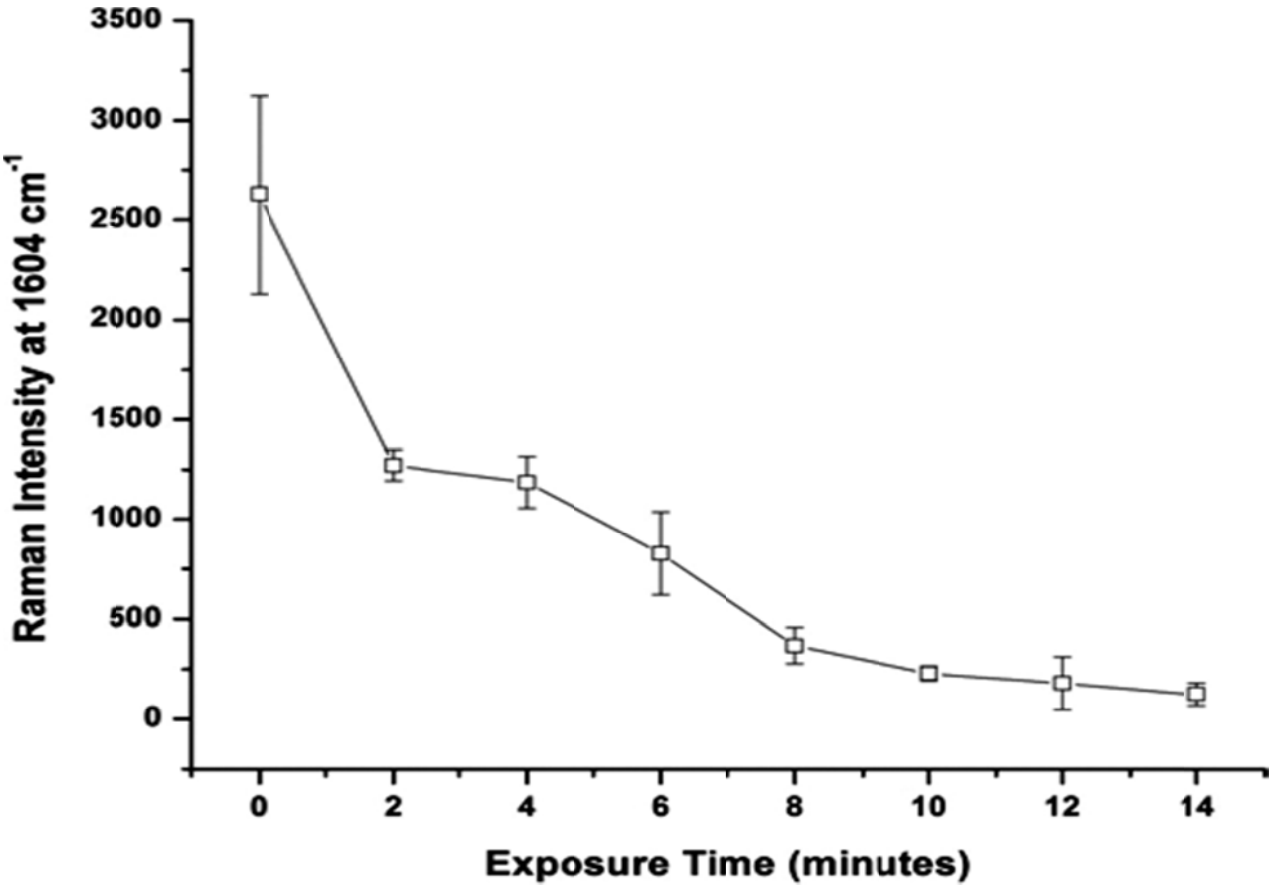

Figure 4.6. Plot of Raman intensity at 1604 cm^{-1} as a function of exposure time to the plasma cleaner. Each data point represents the average intensity of the spectral map data at 1604 cm^{-1} taken from 1,891 collected data sets on each substrate. The error bars represent the standard deviation.

decrease the observed BPE signal, however a 2 – 4 min exposure only decreases the observed SERS intensity by approximately 55%. When exposure time is increased to over 10 min, however, there is approximately an order of magnitude decrease in measured SERS intensity. These results for longer time periods (approximately a 10× decrease) are consistent with those intensity changes previously reported for thermally-annealed Ag nanorod arrays.(285)

We have also measured the static contact angle of the Ag nanorod substrates as a function of exposure to an Ar^+ plasma. The contact angle of a drop on a flat homogeneous solid is given by the classical Young's equation as follows:

$$\gamma_{LV}\cos\theta = \gamma_{SV} - \gamma_{SL} \quad (6)$$

where γ_{LV} , γ_{SV} γ_{SV} γ_{SV} , and γ_{SL} are the different surface tensions (liquid/vapor, solid/vapor, and solid/liquid) involved in the system. By definition, the contact angle is highest when the surface is hydrophobic and is reduced as the surface becomes more hydrophilic.(341) The main parameter that determines the contact angle of a drop on freshly evaporated metallic films is the nanoscopic surface morphology of the substrate onto which the liquid is dispensed.(328) In general, the wetting behaviors observed on such nanostructured surfaces is highly depend on the aspect ratio of the nano-array present on the surface.(342, 343)

Figures 4.4.G – 4.4.I present static contact angle images obtained for water droplets on Ag nanorod arrays as a function of Ar^+ plasma exposure. These images qualitatively support the

conclusion that the control substrate is the most hydrophobic of the three substrates, with the hydrophobicity of the substrate decreasing as the exposure time increased. This finding was consistent with the interpretation that the presence of organic and carbonaceous contamination leads to a hydrophobic surface, and that removal of this contamination results in an increase in hydrophilicity.

The response of the static contact angle to Ar^+ plasma exposure time is shown in Figure 4.7. The form of the decrease in the contact angle with exposure time is similar to that of the Raman intensity shown in Figure 4.6, that is, a sharp decrease (of contact angle or Raman intensity) after initial plasma exposure, followed by a slower decrease with increasing plasma cleaning. Although the most likely explanation for the decrease in contact angle is the increasing hydrophilicity of the Ag surface after cleaning, additional mechanisms may also contribute. The change in the nanomorphology of the Ag nanorod substrates shown in the SEM micrographs in Figure 4.4.A – 4.4.C may be contributing to the hydrophobicity change as well. A recent paper on the Lotus effect suggests that high contact angle droplets form on hydrophilic nanostructures when the droplet size is comparable to the nanoscale roughness, however, the contact angle decreases upon change in surface roughness.(344) This conclusion agrees with our observation that the static contact angle decreases with the change in surface roughness and morphology of the Ag nanorods.

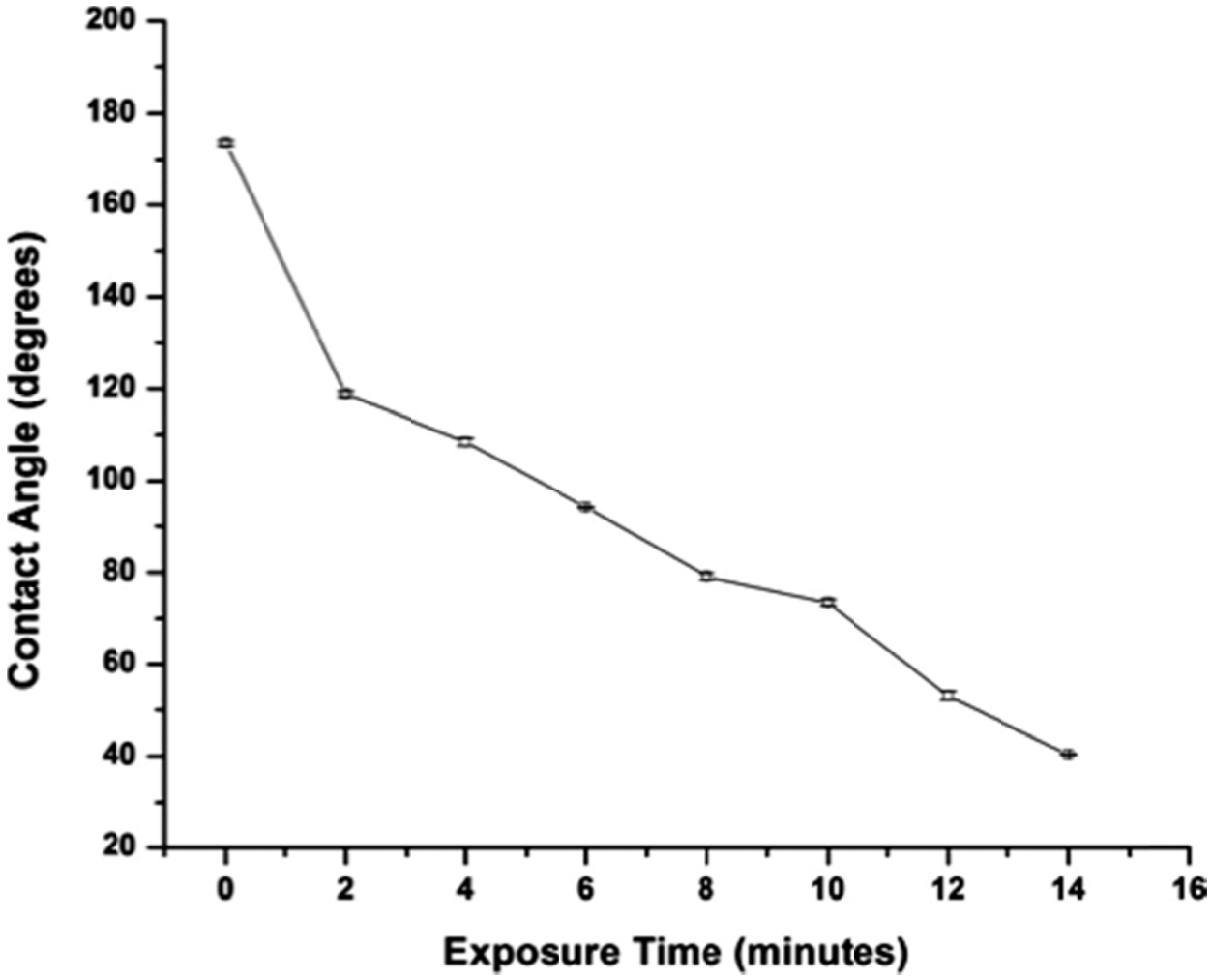

Figure 4.7. Static contact angles plotted as a function of exposure time to the plasma cleaner. Each data point represents the average static contact angle taken from 10 different measurements and the error bars represent the standard deviation.

4.4. Conclusions

Significant progress has been made in the past few years in the development of reproducible nanofabrication techniques for the preparation of highly sensitive SERS substrates. However, one of the major drawbacks limiting the reproducibility and sensitivity of this measurement is the presence of contamination on the SERS-active substrates. To overcome this issue, we have developed a rapid procedure for cleaning SERS-active Ag nanorod substrates that utilizes a short (4 min) exposure to Ar^+ plasma, which is successful in removing essentially all carbonaceous and organic contamination present on the surface, see *e.g*. Figures 1 and 2. The use of Ar^+ plasma to clean the Ag nanorod substrates does reduce the observed SERS response, as seen in Figure 6. However, the decrease in intensity noted within the first 2-4 min of plasma cleaning, approximately 2×, is an acceptable trade-off for a clean substrate, especially when compared to the high SERS enhancements originally produced by the Ag nanorod substrates (~10^8).

The principles behind cleaning via plasma generation rely on the ionization of an inert gas that interacts with the material present on the substrate surface. Ar is used for its high ablation efficiency and chemical inertness. Typically, the energy of the plasma electrons and ions is sufficient to mechanically remove surface contaminants by both energetic electron and ion bombardment. Increasing the pressure in the chamber results in reduced dissipation energy of the Ar^+ plasma. The type of interaction between the plasma and the surface depends on parameters such as the intensity and frequency of the RF power used to excite the plasma, the type of gas that is ionized, the pressure and flow rate of the gas, the type of sample and the amount of time

the surface is exposed to the plasma. Excess energy is usually dissipated throughout the substrate through chemical and physical processes to attain a desirable surface modification without changing the bulk materials properties of the substrate.

The findings presented here demonstrate that Ar^+ plasma cleaning works well even for analytes having strong adsorption tendencies towards Au and Ag surfaces such as small organic analytes and thiolate SAMs. Our findings show that, given short (2 – 4 min) Ar^+ plasma exposure, contaminant materials and alkanethiols may be efficiently removed from the surface of Ag nanorods without apparent deterioration of the substrate morphology and only a moderate decline in their SERS response. However, our results also show that the optimum conditions for plasma cleaning are very time-dependent. Longer (>10 min) exposure of the Ag nanorod substrates to Ar^+ plasma results in significant changes to nanorod shape, length and density. These large changes in nanorod morphology have a dramatic deleterious effect on the SERS response. Thus, carefully controlling the plasma conditions and exposure time is critical for successful cleaning of Ag SERS substrates.

CHAPTER 5

Ag Nanorod Based SERS Applied to Bioanalytical Sensing

The purpose of this chapter is to introduce the reader to the applications of Ag nanorod arrays fabricated by OAD as a sensitive SERS-active substrate for the rapid detection of biological agents as well as a robust biomedical diagnostic platform for both clinical and therapeutic applications. Presented in this chapter is a thorough review of the use of Ag nanorod substrates for the SERS-based detection and identification of pathogens, including bacteria and viruses, as well their chemical modification with oligonucleotides for quantitative detection of micro RNA (miRNA) and sequence profiling.

5.1. Introduction

Since its discovery in the 1970s, surface-enhanced Raman spectroscopy (SERS) has become a powerful analytical technique that provides identification and quantitative information about a variety of biomolecules with a high degree of sensitivity and specificity.(138) SERS is a nano-optical technique that has been applied to a wide array of bioanalytical problems, e.g. genetics and proteomics,(345) medical diagnostics,(346, 347) biochemistry,(348) and the life sciences,(349) and is emerging as a very powerful biochemical detection method.

SERS originates from molecules located in close proximity to a metallic (typically Au or Ag) nanostructured surface that is capable of generating a localized surface plasmon (LSP).(47-49)

The LSP results from surface electrons that oscillate in resonance with the frequency of the incident radiation. For SERS, the optimum excitation frequency is provided by a visible/near-IR laser whose wavelength is in close proximity to the maximum in the extinction profile of the localized surface plasmon.(62) The SERS enhancement has been amply described in the literature and is primarily thought to be the result of two distinct mechanisms: a long-range classical electromagnetic (EM) and a short-range chemical enhancement (CE).(61) An EM enhancement on the order of E^2 results from an increase in the electromagnetic field due to the generation of LSPs at nanostructured metallic surfaces. An additional E^2 EM enhancement arises from the Stokes-shifted Raman scattering due to the induced dipole of the surface-adsorbed analyte molecule, thus leading to a total SERS EM field enhancement at the nanoparticle surface that scales as E^4.(71) The CE mechanism originates from the analyte-specific interactions between the surface-adsorbed analyte molecule and the metal through the formation of localized adsorbate electronic resonances or metal-to-adsorbate charge-transfer complexes.(350) In this scenario, the metal is irradiated by the incoming radiation source to create an electron-hole pair that results in a transfer of energy to the analyte molecule through its bonds connecting it to the metal surface. The subsequent energy is transferred back into the metal, resulting in the emission of the scattered light from the analyte molecule.(77) It is commonly thought that the EM enhancement contributes the greater extent ($\sim 10^4$-10^7) to the signal enhancement observed in SERS while the CE enhancement is thought to contribute to a smaller extent (~ 10-10^2) to the overall enhancement.(76)

The inherent biochemical specificity of Raman spectroscopy offers a number of attractive features for detection and identification of biological samples. Raman provides a unique, chemically specific molecular fingerprint for each analyte, which eliminates the need for indirect detection via conjugated synthetic fluorophores. Raman has inherently narrow spectral lines that enable multi-component analysis without special experimental techniques or multi-fluorophore approaches.(139) For the SERS method, in particular, the phenomenon is due to the nanoparticle physics of the substrate and not the chemistry of a fluorophore; thus, photobleaching and quenching are of minor concern.

SERS has proven itself to be highly adaptable as a bioassay platform for biomedical sensing.(351) Routine sensitivity of SERS-based analytical methods rivals that of fluorescence, with pico/femto/attomolar detection limits, and the ability to detect single molecules or binding events.(80, 81) The SERS approach also has advantages over other label-free biosensing methods such as surface plasmon resonance (SPR), in that SERS is molecule-specific, unlike SPR, which relies only on a general signal response for any captured analyte. In addition, detection, identification, classification and quantification of individual analytes are possible using well-validated multivariate statistical methods.(352)

The unique analytical assets of SERS have enabled the development of a variety of diagnostic applications requiring low detection levels and a high degree of specificity. However, despite the remarkable advances in recent years, the overall sensitivity and reproducibility of SERS has been constrained by non-optimized nanofabrication methods that result in variability in substrate

nano-morphology. Since the LSP is dependent on nanoparticle morphology, stringent control of feature size and inter-particle distance is vital to ensure high and reproducible enhancements.(89) The successful transition of SERS to a practical biosensing methodology requires the development of SERS substrates that may not only provide strong enhancement factors, but that may also be fabricated easily, reproducibly, inexpensively, and with potential for long-term storage.

Recently, a nanofabrication technique based on an oblique angle vapor deposition (OAD) has been developed that offers a versatile, simple and inexpensive way of producing Ag nanorod arrays for high sensitivity SERS applications.(287) OAD is a physical vapor deposition technique that offers a reliable means of fabricating uniform, reproducible, large area SERS-active substrates with high signal enhancement. Details regarding the fabrication and cleaning of the Ag nanorod arrays are provided in Chapter 3 and 4, respectively. These Ag nanorod arrays fabricated by OAD have been investigated as SERS-active substrates for the detection of pathogens including viruses and bacteria, as well as to assess the potential of nucleotide-modified Ag nanorod arrays for a variety of bio-recognition and biosensing applications. This chapter provides a summary of the most recent uses of these substrates as applied to bioanalytical sensing.

5.2. Advantages of SERS-Based Bioanalytical Sensing

Rapid and sensitive detection of pathogens is an essential tool in disease outbreak intervention strategies. Current diagnostic methods available for the detection of pathogens rely on

immunofluorescence tests and antigen-capture immunoassays such as enzyme-linked immunosorbent assay (ELISA),(353-355) hemi-nested multiplex RT-PCR,(356-358) or hemadsorption.(359, 360) Many of these assay techniques suffer from lack of sensitivity and reproducibility or require the use of synthetic labels, species-specific reagents (genotyping primers), or amplification of nucleic acid coupled with polymerase chain reaction (PCR). In addition, most of the currently used biochemical assays are limited by the time required to grow cell or bacterial cultures. Consequently, new diagnostic approaches for rapid and sensitive means of detecting pathogens both in the laboratory and in the field are urgently needed to successfully curb potential disease outbreaks.

The unique ability of SERS to provide an analyte-specific response has allowed the development of this method for rapid bio-medical diagnosis of infectious diseases.(182, 203, 361) The ultrasensitive, rapid, and label-free attributes of SERS seem to satisfy all criteria needed for routine analysis of different species and strains of pathogens. As a label-free, molecularly specific detection method, SERS allows detection of pathogens with a high degree of sensitivity and specificity. In contrast with the other diagnostic methods previously noted, SERS offers several advantages, including the ability to provide molecular vibrational information for both *in-vivo* and *in-vitro* applications, hence allowing discrimination of subtle structural differences and classification of pathogen types and species.(185, 186, 352, 362, 363) Another advantage of SERS over fluorescent-based assays includes the multiplexed detection capabilities due to the narrower SERS bands relative to broad fluorescent bands. In addition, the intrinsic detection

mode of SERS eliminates the need for synthetic labels and enables the direct detection of the spectral fingerprint of the whole organism.(178)

Over the last several years, Ag nanorod arrays have been evaluated as SERS-active substrates for a variety of biosensing applications. The unique signal enhancement offered by Ag nanorod substrates allows nondestructive detection and discrimination of pathogens at the strain level with minimal sample or culture preparation. Ag nanorod arrays have been employed for the SERS-based detection of a variety of bacterial and viral species to allow classification of bacterial and viral types as well as discrimination between pathogen strains and pathogens having single gene mutations. In addition, oligonucleotide-modified Ag nanorod arrays have been used to directly probe sequence information and detect binding of complementary targets. The following sections summarize recent applications of the use of these SERS substrates for pathogen detection and provide an outlook on the future of Ag nanorod arrays for bioanalytical and diagnostic applications.

5.3. Ag Nanorod SERS Substrates For Bioanalytical Sensing

Detection of Bacteria

Bacteria are single-celled prokaryote microorganisms that contain neither a nucleus nor other membrane-enclosed organelles like mitochondria and chloroplasts.(364) Rapid means of detecting and identifying pathogenic bacteria play a pivotal role in medical diagnostics, food safety, water quality, pharmaceutical production and biological warfare. Conventional detection methods of bacteria range from immunological approaches(365) to nucleic acid-based

assays.(366) These techniques may be cumbersome, time-consuming, and suffer from other shortcomings such as lack of specific chemical information, and a high false positive rate. There is an urgent need for rapid, sensitive and specific detection of pathogenic bacteria. As a vibrational spectroscopic method, SERS provides specific chemical information about the bioanalyte and presents real-time diagnostic capabilities for rapid species identification.

SERS substrates fabricated by OAD have been assessed as a potential analytical sensor for rapid pathogenic bacteria detection. The first report on the bio-detection and identification of bacteria by SERS reported the use of Ag nanorod arrays to detect and identify foodborne pathogenic bacteria.(289) Principal Component Analysis (PCA) was used to analyze and identify the SERS spectra of generic *Escherichia coli* (*E. coli*), *E. coli* O157:H7, *Staphylococcus aureus*, *Staphylococcus epidermidis*, *Salmonella typhimurium* 1925-1 poultry isolate, *E. coli* DH 5α and bacteria mixtures. A detailed description of PCA as a multivariate statistical technique is provided in Chapter 6. This multivariate statistical method demonstrated the ability to distinguish different bacterial species and allowed differentiation between viable and nonviable cells. The results of this study also highlighted the potential of this technique to classify different bacterial strains as well as the ability to differentiate pure cell samples from mixed cell samples of high spectral similarity.

A separate study compared the SERS spectra of several bacterial species with commonly used bacterial growth media.(300) The findings demonstrated that Raman spectra of various bacterial growth media shared similarities with those of the bacteria themselves, suggesting that

previously published reports on Raman detection of bacteria may have misattributed the spectral features of the organisms with their background matrix. The findings of this study called for a re-investigation of the current protocols used for SERS-based detection and identification of bacteria and suggested development of new protocols for acquisition of SERS spectra on bacterial samples so that the spectral bands specific to the bacteria's structure and biomolecular composition may be identified and differentiated from those of the growth medium.

Mycoplasma is a genus of small bacteria lacking a cell wall, which are unaffected by many common antibiotics, and are a major cause of respiratory disease with an increasing threat to human and animal health.(367) Detection of mycoplasma is typically achieved using serologic tests including serum plate agglutination, hemagglutination inhibition, and enzyme-linked immunosorbent assay (ELISA).(368) These assays are usually time-consuming, cumbersome, expensive, lack sensitivity, and often yield false positives. Therefore, there is a critical need for a new diagnostic platform to detect mycoplasmas with high sensitivity, specificity, and expediency.

Ag nanorod arrays have been evaluated as a diagnostic platform for the SERS-based detection and identification of different species of mycoplasmas. One of the first studies on the bio-detection of Mycoplasma focused on the detection and differentiation of different strains of *Mycoplasma pneumoniae* in culture and in both spiked and true clinical throat swab samples by SERS.(295) Figure 5.1 shows (A) three sets of baseline corrected and offset raw SERS spectra of *M. pneumoniae* strain FH collected from five random locations on three different Ag nanorod

substrates as well as (B) three sets of first derivative spectra for strain FH from Figure 5.1.A. Figure 5.1 illustrates the high degree of reproducibility of the data. Principal Components Analysis (PCA), Hierarchical Cluster Analysis (HCA), and Partial Least Squares Discriminant Analysis (PLS-DA) were used to analyze and identify SERS spectra of three *M. pneumonia* strains (FH, II-3, and M129). A detailed description of PCA, HCA, and PLS-DA as multivariate statistical methods is provided in Chapter 6. These multivariate statistical techniques allowed robust differentiation of all three mycoplasma strains. In particular, the PLS-DA model generated from 90 spectra (30 of each strain) classified FH, II-3, and M129 with 93-100% sensitivity and specificity. The limit of detection of *M. pneumoniae* was also assessed using spectra from the serial 10-fold dilution of strain II-3, starting as a concentration of 1.8×10^9 CFU/mL. PLS regression analysis revealed a lower limit of detection of 0.02 CFU/sample, a concentration exceeding the sensitivity of standard PCR.

Simulated and true clinical throat samples were also evaluated using PLS-DA to assess the performance of the assay in a biologically complex background. Spectra from individual and pooled throat swab samples were spiked with *M. pneumonia* and analyzed against control throat swab samples. A PLS-DA model was built with all dilutions and classification as positive or negative for *M. pneumoniae* indicated >90% accuracy in cross-validated analysis, showing the ability of Ag nanorod array SERS substrates to detect mycoplasma in a biologically complex, clinically relevant background with 98.1% specificity and 95.2% sensitivity.

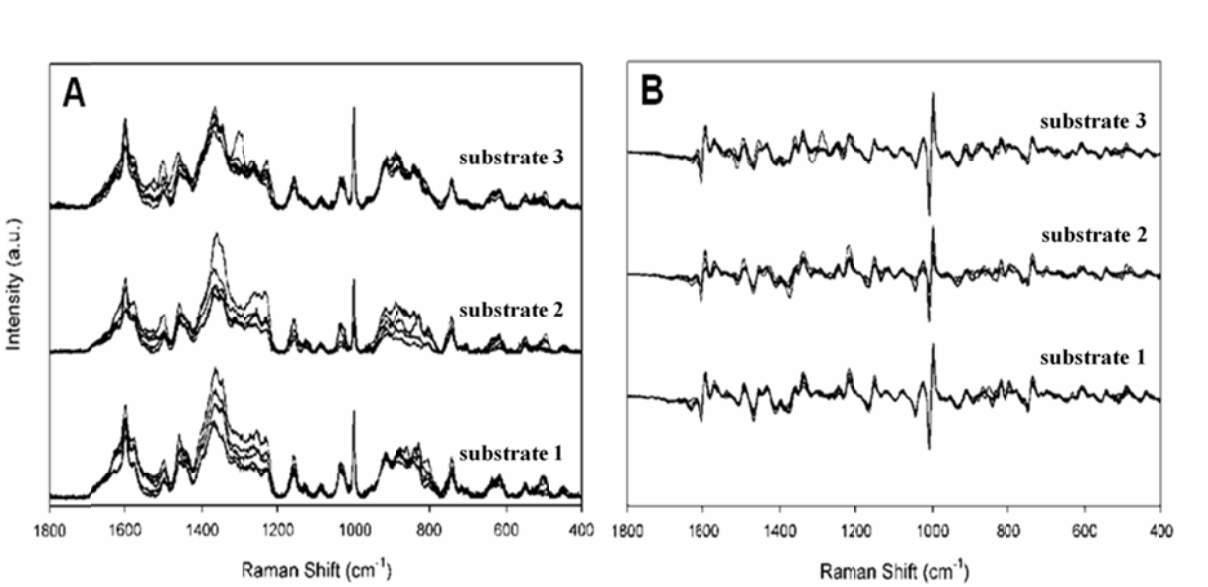

Figure 5.1. Reproducibility of spectra. Raw spectra (A) of *M. pneumoniae* strain FH collected from five random spots from three separate NA substrate wells, baseline corrected and offset. (B) First derivative spectra for strain FH from Figure 5.1.A.

In a more recent study, Raman spectral signatures of multiple strains of avian mycoplasma species including *Acholeplasma laidlawii*, *Mycoplasma gallinarum*, *Mycoplasma gallinaceum*, *Mycoplasma synoviae*, and *M. gallisepticum,* and vaccine strains 6/85, F, and ts-11 were collected and processed by multivariate analysis to differentiate laboratory cultures of mycoplasma species.(296) A PLS-DA model classified the spectra for all species with 93 to 100% sensitivity and with similar specificity for all species except *Mycoplasma synoviae*, which was distinguishable with only 80% specificity. Table 5.1 summarizes the results from the PLS-DA model for the discrimination of the avian mycoplasma species. The *M. gallisepticum* strains Rlow, S6, and A5969 were examined under the same conditions and were able to be correctly classified with 69 to 100% sensitivity and specificity using PLS-DA. The findings of this study also revealed that when the vaccine strains 6/85, F, and ts-11 were included in the model, PLS-DA was unable to correctly distinguish the strains with statistical significance. When the same data set was examined according to virulence, differentiation of all members of each class occurred with >96% accuracy.

M. gallisepticum samples were also analyzed based on their virulence in a biochemically complex clinical background as part of a vaccine challenge study involving ts-11. Samples were classified as positive or negative for *M. gallisepticum* based on serologic testing. PLS-DA showed that samples from the positive field isolate and negative background/vaccine strain classes could be accurately distinguished with 88% cross-validated sensitivity and 85% cross-validated sensitivity. Moreover, the ts-11 vaccine strain and the ts-11-like field isolate K6216D were discriminated with 90% sensitivity and 82% specificity with a 14% error rate using the

Table 5.1. Specificity and sensitivity of NA-SERS discrimination of avian mycoplasma species by PLS-DA.

Modeled class[a]	Sensitivity (CV[b])	Specificity (CV)	Class error (CV)	RMSECV[c]
M. gallisepticum	0.944	0.951	0.053	0.246
M. gallinaceum	0.933	0.992	0.038	0.201
M. laidlawii	0.933	0.950	0.058	0.236
M. synoviae	0.933	0.800	0.133	0.287
M. gallinarum	1.000	1.000	0	0.033
Methanol	1.000	0.930	0.035	0.238

[a] *Six latent variables (n = 135), accounting for 77% of the captured x variance, were used to generate the model.*
[b] *CV, cross validation by Venetian Blinds with 10% of the data.*
[c] *RMSECV, root mean squared error in cross validation.*

same multivariate statistical technique. Using the Ag nanorod arrays as the diagnostic platform, the limit of detection for *M. pneumonia* was assessed on 10 serial 10-fold dilutions with a starting concentration of 4.67×10^5 CFU/μL and was able to be detected down to 1 CFU.

The results suggest that Ag nanorod arrays for SERS-based detection constitute a promising biosensing platform for rapid and sensitive detection of mycoplasma in various complex, biological backgrounds with excellent sensitivity and specificity, and show similar, if not improved, limits of detection when compared to standard molecular strategies. The results demonstrate the potential of this technology for practical diagnosis of pathogens for clinical and point-of-care applications.

Detection of Viruses

Viruses are microscopic infectious agents that may infect the cells of a wide variety of organisms.(369) The current state-of-the-art viral diagnosis methods rely on antibody-based methods such as immunofluorescent testing of isolated viral preparations,(370) enzyme-linked immunosorbent (ELISA)(353), or PCR,(357) a method that amplifies genetic material fragments for detection. Methods relying on antigen detection and serology are unable to discriminate between virus species or strains of the same virus. Therefore, development of novel strategies to overcome limitations of current viral detection methods is in the forefront of infectious disease detection strategies.

Ag nanorod arrays produced by OAD provide a flexible and sensitive method for SERS-based detection of viruses. An early study demonstrated that SERS using Ag nanorod arrays could detect and differentiate the molecular fingerprints of several important human pathogenic viruses.(292) The spectral variations observed result from the differences in molecular composition of the genomes and proteins of these pathogens as well as adsorption of these components to the Ag surface. PCA and HCA were used to classify the four sample types successfully based solely on their intrinsic spectra. These initial results demonstrated that SERS could be used in combination with multivariate statistical methods for rapid identification and classification of various infectious agents.

Ag nanorod arrays were also used to establish molecular fingerprints of several human viruses.(201) SERS spectra of adenovirus, rhinovirus, and HIV virus were collected; the Raman bands of the viral nucleic acid bases and protein amino acids were identified. The biological media did not confound the viral spectra or prevent band assignments. The results demonstrate that Ag nanorod arrays may readily detect viruses in a variety of biological media.

In a follow up to that study, PCA and HCA were used to classify four different strains of respiratory syncytial virus (RSV).(202) The Raman spectra of RSV strains A/Long, B1, A2, and ΔG were acquired. SERS spectra of different virus strains of influenza and RSV were collected to determine if Ag nanorod arrays provide enough sensitivity to distinguish different strains from a single pathogen. Analysis of the SERS spectra collected on the three strains of influenza A (A/HKx31, A/WSN33, and A/PR/8/34) and the four strains of RSV (A/Long, B1, A2, and A2

with gene deletion (ΔG)) suggests that although the spectra of each strain from a single pathogen are very similar, distinct spectral differences between the spectra of the strains of each of the two virus species exist and may be detected via SERS. Figure 5.2 shows the SERS spectra of the four RSV strains examined in this study. The results suggested that SERS offers a high level of sensitivity for the detection of viruses at extremely low concentrations and permits their rapid and accurate identification, including differentiation of a single pathogen at the strain level.

The reproducibility of measurements in this study allowed distinction of the SERS spectra based on the slight nucleic acid and protein composition differences between the four strains. PCA clustered the three main virus strains (A/Long, A2, and B1) together into individual groups. RSV strains A2 and ΔG clustered together due to their extreme similarity in biochemical composition. HCA allowed classification of the RSV strains into their respective classes. SERS spectra of RSV strains A/Long and B1 were identified with 100% accuracy, whereas 88% of the ΔG spectra and 63% of the A2 were identified correctly using HCA. The mismatches accounting for these percentages are due to their close molecular similarity resulting from G gene deletion differences. Table 5.2 shows the results of the RSV virus strains classification based on HCA.

A SERS-based detection scheme has been developed to qualitatively identify eight rotavirus strains and classify them according to genotype.(294) SERS spectra of each of the eight rotavirus strains were collected on three different OAD-fabricated substrates to assess the reproducibility of measurements and the variation in terms of substrate and sampling homogeneity. SERS

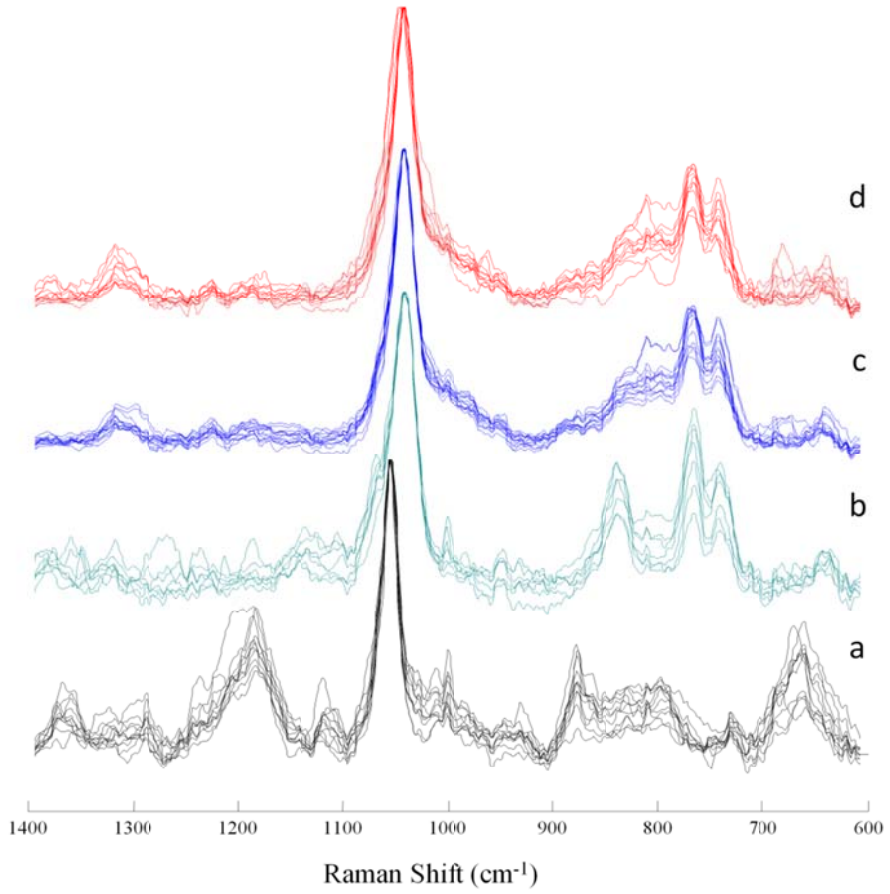

Figure 5.2. SERS spectra of the RSV strains (a) strain A/Long (A/Long), (b) strain B1 (B1), (c) strain A2 with a G gene deletion (ΔG), and (d) strain A2 (A2), collected from several spots on multiple substrates and normalized to the peak intensity of the most intense band (1045 cm^{-1}) and overlaid to illustrate the reproducibility on the Ag nanorod substrate.

Table 5.2. Virus strain classification based on Hierarchical Cluster Analysis (HCA).

Viral Strain	Correctly classified	Falsely classified	Also classified as	Sensitivity[a]	Specificity[b]
RSV A/Long	17	0	–	1.0	1.0
RSV B1	17	0	–	1.0	0.92
RSV ΔG	15	2	A2(2)	0.88	0.94
RSV A2	12	7	ΔG(3), B1(4)	0.63	0.96

[a]Probability of correctly classifying a SERS virus spectrum as belonging to the virus strain class (i.e., true positive)
[b]Probability of correctly classifying a SERS virus spectrum as not belonging to the virus strain class (i.e., true negative)

spectra of rotavirus strains F45, RV3, RV4, RV5, S2, ST-3, Wa, and YO corresponding to either G or P genotypes were analyzed in cell lysate, applied directly to the Ag nanorod array substrates and allowed to dry at room temperature prior to SERS measurements. Figure 5.3 shows the SERS spectra of the eight strains of rotavirus and the negative control MA104 cell lysate (left panel), as well as the difference SERS spectra of the eight strains after subtraction of MA104 spectrum (right panel). The spectra collected showed a high degree of similarity among each strain. Subtle structural differences inherent to antigenic variations between the virus strains permitted discrimination of the strains, and differentiation of rotavirus positive and negative samples was accomplishedusing PLS-DA with 100% accuracy. Overall, the model resulted in >98% sensitivity and 100% specificity for G and P genotypes, as seen in Table 5.3. Partial Least Squares (PLS) regression analysis was also used to quantitatively assess the detection limits of these rotavirus strains. The PLS regression model predicted concentration based on intrinsic SERS spectra to be accurate for concentrations $\geq 10^4$ pfu/mL.

Ag nanorod arrays have also been used for rapid genotyping of four separate measles virus (MeV) genotypes (Mev A, D4, D9, and H1).(297) Analysis of the genetic sequences of the MeV genotypes examined in this study determined that the four MeV genotypes exhibited >96% genetic similarity. PCA analysis based on the SERS spectra of each genotype showed close similarity between the genotypes, but effective identification of MeV genotypes and differentiation of MeV from controls was possible. The dendrogram generated by HCA correctly distinguished the spectra of the four MeV samples, the media controls, and the solvent background, but neither PCA nor HCA could differentiate the SERS spectra of the closely

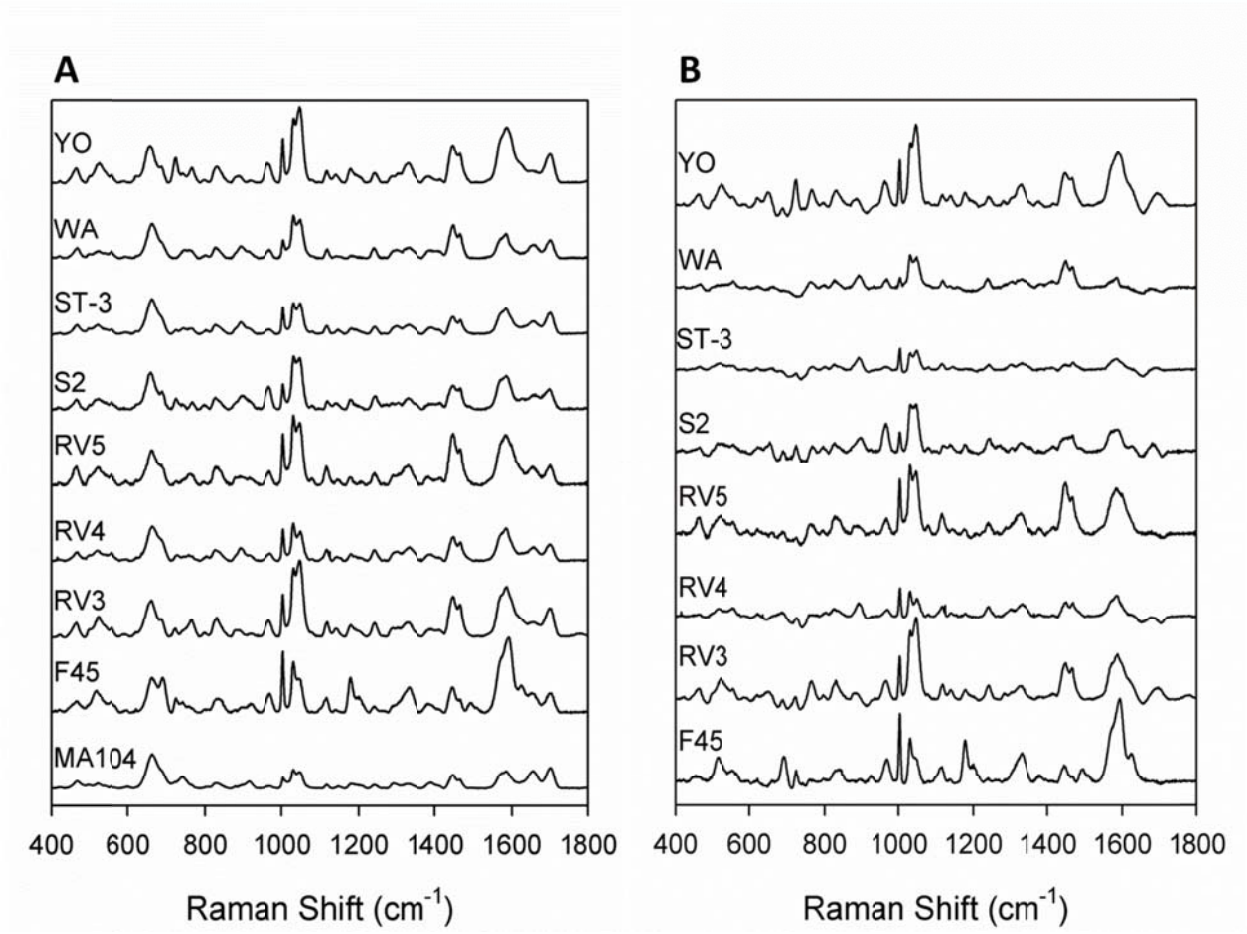

Figure 5.3. Rotavirus SERS spectra. (A) Average SERS spectra for eight strains of rotavirus and the negative control (MA104 cell lysate). Spectra were baseline corrected, normalized to the band at 633cm^{-1}, and offset for visualization. (B) Difference SERS spectra for eight strains after subtraction of MA104 spectrum.

Table 5.3. Summary of the PLS-DA cross-validation results for classification according to three different models based on the strain, G genotype and P genotype.

P genotype Classification									
	P8	**P4**	**P6**	**neg ctrl**					
sensitivity	0.983	1.000	1.000	1.000					
specificity	1.000	1.000	1.000	1.000					
G genotype Classification									
	G9	**G3**	**G1**	**G2**	**G4**	**neg ctrl**			
sensitivity	1.000	1.000	0.967	1.000	1.000	1.000			
specificity	0.992	1.000	0.990	1.000	1.000	1.000			
Strain Classification									
	F45	**RV3**	**RV4**	**RV5**	**S2**	**ST-3**	**Wa**	**YO**	**neg ctrl**
sensitivity	1.000	1.000	1.000	1.000	1.000	1.000	1.000	1.000	1.000
specificity	0.992	1.000	1.000	1.000	1.000	0.992	1.000	1.000	1.000

related MeV-D4 and Mev-D9 genotypes. However, PLS-DA was able to correctly differentiate between each of the four MeV genotypes and the negative controls with high accuracy. The PLS-DA model demonstrated cross-validated sensitivities of >90% and specificities of >96% for each MeV genotype. The results of this study demonstrated the accuracy these multivariate statistical methods to effectively differentiate between four MeV genotypes, two media controls, and a background with high sensitivity and specificity.

The results of these studies highlight the potential of Ag nanorod arrays for SERS-based detection of important pathogenic viruses. This platform allows rapid and accurate identification and classification of viruses at the species, strain, and genotype levels. SERS-based virus detection appears to be a highly promising alternative to current diagnostic assays and has the potential to be broadly applicable to a variety of viral targets.

Oligonucleotide-Modified Ag Nanorod Substrates for miRNA Detection and Sequence profiling

The studies on SERS-based detection of bacteria and viruses established the proof of principle that Ag nanorod SERS has the ability to directly probe biochemical information in a label-free fashion. In addition to direct detection of whole organisms, chemical modification of Ag nanorod substrates with oligonucleotides allows for specific detection of miRNAs.

MicroRNAs (miRNAs) have been studied using Ag nanorod substrates. miRNAs are non-coding RNAs that play a key role in the regulation of gene expression and have been extensively

studied as candidates for diagnostic and/or prognostic biomarkers.(371, 372) However, miRNA detection involves a number of analytical challenges. First, miRNA are small (19-25 nucleotides), which makes it difficult for traditional DNA-based methods to sensitively detect these sequences with any reliability. Second, current technologies for detection and profiling miRNA expression may have limited specificity when closely related miRNA family members exhibiting single base-pair polymorphism are analyzed. These drawbacks emphasize the need for novel methods with high specificity that may discriminate between single nucleotide mismatches.

miRNA profiling has been demonstrated using Ag nanorod of SERS-based array substrates.(373) Five unrelated miRNAs having dissimilar sequences were examined, as well as eight members of the hsa-let-7 family containing similar miRNA sequences, including sequences differing by a single base mismatch. Analysis of the SERS spectra of let-7a reveals reproducible spectral features that may be attributed to nucleic acid vibrations, with similar band position and shape and with only slight variations in relative intensities. Figure 5.4 shows the average SERS spectra of five unrelated miRNA sequences. PLS-DA classified the five unrelated miRNAs based on unique SERS molecular signatures and correctly assigned each let-7a sequence in its correct class, with 100% sensitivity and specificity. Figure 5.5 shows the PLS-DA Y predicted plots for the 5 miRNA classes. The SERS spectra of the seven has-let-7a family members (having 71-95% sequence homology) were classified with 100% sensitivity and 99-100% specificity, proving that SERS may be used as a rapid, specific and sensitive miRNA detection technology without target amplification.

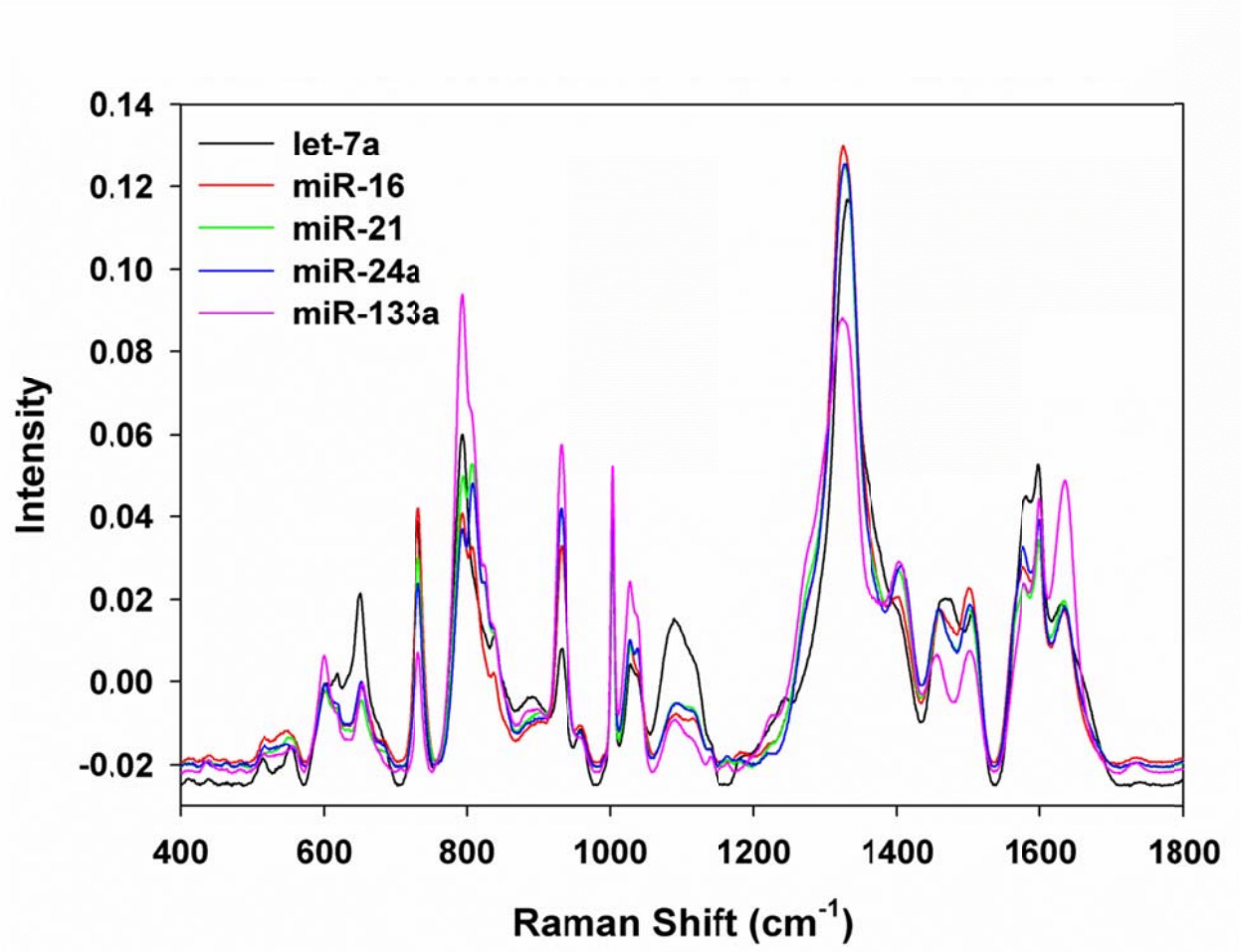

Figure 5.4. Overlaid average SERS spectra (n=18) for each unrelated miRNA. The spectra have been baseline corrected and unit-vector normalized for visualization of spectral differences.

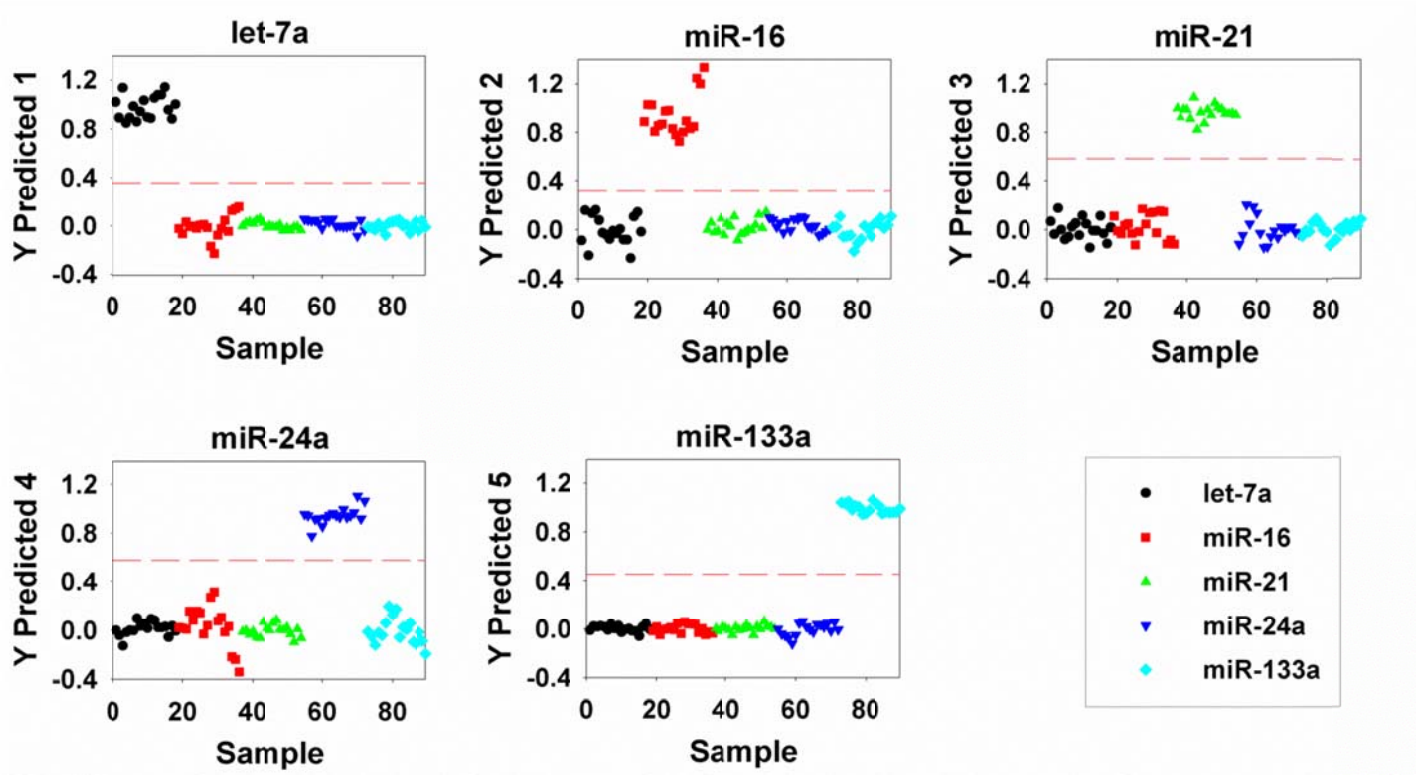

Figure 5.5. PLS-DA Y predicted plots. Each plot predicts a sample as belonging to or not belonging to the specified miRNA class. Let-7a (●), miR-16(■), miR-21 (▲), miR-24a (▼), and miR-133a (◇).

Quantitative detection of miRNA sequences in multicomponent mixtures has also been accomplished.(290) In this study, two-, three-, and five-component mixtures of miRNA were prepared with the total miRNA concentration in the component mixtures held constant at 1.00 μg/mL while the relative ratios of each component varied from 6 to 150 μM. Plots of PLS cross-validated predictions for each of the miRNA sequences in the mixtures for the calibration model were generated for all three sample mixtures. The results indicated that the PLS regression model was able to accurately detect and quantify individual miRNA sequences in multicomponent mixtures in a label-free fashion.

The binding affinities of miRNAs in ssRNA and dsRNA:DNA duplexes have been evaluated, both with and without thiol modification.(293) The findings from this study showed that thiolated probes adsorb better than non-thiolated probes on the surface of Ag nanorod arrays. Additionally, it was shown that a thiolated RNA:DNA solution complex does not bind to the Ag nanorod substrate due to the rigid structure of the duplex. Following these observations, an assay was designed for miRNA detection in which a constant concentration (500 nM) of let-7f probe was mixed with various concentrations of let-7f and allowed to hybridize prior to incubation of the mixture on the Ag nanorod substrate. As expected, the SERS intensity linearly decreased as the concentration of the let-7f increased from 125 to 500 nM. Incubation of the let-7a probe with a mismatched miRNA indicated no detectable hybridization. These results show that miRNA sequences may be detected and quantified based on affinity of the probe to its complementary target. Intrinsic SERS detection allowed detection of target miRNA by providing a molecularly specific signal, thus offering the double advantage of multiplexed label-free detection.

5.4. Conclusions

The ability of SERS to provide a unique, chemically specific molecular fingerprint with high sensitivity and specificity offers a powerful diagnostic platform that is well-suited for a variety of bioanalytical problems. Aligned Ag nanorod arrays fabricated by OAD have been investigated as potential SERS-active substrates for the detection of a variety of pathogens and oligonucleotide-based bio-recognition and biosensing applications. This novel biosensing platform has the advantage to rapidly, accurately, and cost-effectively detect extremely low levels of virus and bacteria, thus fulfilling a critical need for sensitive and reliable means of pathogens detection not currently existing. The level of spectral reproducibility offered by the Ag nanorod arrays allows acquisition of molecular fingerprints of pathogens and permits differentiation between microorganisms or viral pathogens based on their inherent structural and biochemical differences.

Of the current nano-based bioanalytical methods under investigation, SERS shows potential for multiplexed detection and identification of the biochemical components of pathogenic microorganisms with minimum sample preparation. The inherent attributes of SERS overcome many of the limitations of current immunologic- or PCR-based diagnostic tests for pathogenic microorganisms, most notably, the elimination of amplification and labeling steps. The results of investigations conducted using Ag nanorod arrays as SERS-active substrates demonstrate the use of spectral fingerprinting in biomedical vibrational spectroscopy may potentially: i) provide a unique spectral signature specific for a pathogen of interest, ii) facilitate identification through

comparison with spectral libraries, iii) eliminate the use of species-specific monoclonal antibodies, and iv) minimize false positives common to indirect methods.

Additionally, the high sensitivity of the SERS data coupled with the statistical method of data opens new perspectives for the development and integration of ultrasensitive detection of biorecognition events for early clinical diagnostic and biomedical applications. Ag nanorod arrays also have the potential to be integrated into biomedical diagnostic platforms accommodating a wide variety of biospecific recognition events in a label-free fashion. Overall, the advantages of this biosensing platform open new perspectives for the development and integration of ultrasensitive detection of pathogens for early clinical diagnostic and biomedical applications central to human health. The attributes of Ag nanorod arrays as SERS-active substrates open the door to various sensor applications and demonstrate the applicability of this biosensing platform to a wide range of infectious agents for rapid medical diagnostics of infectious diseases.

CHAPTER 6

Direct Optical Detection of Viral Nucleoprotein Binding to an Anti-Influenza Aptamer

The purpose of this chapter is to introduce the reader to the use of Ag nanorod arrays for the SERS-based, label-free optical detection of viral nucleoprotein binding to a polyvalent anti-influenza aptamer. The assay consists of aptamer-modified Ag nanorod substrates that serve as a biosensing platform for the detection of the nucleoprotein constituents of three virus strains contained in a commercially available vaccine. The results of this investigation are presented in this chapter and include: (i) SERS spectra demonstrating selective binding of the aptamer-nucleoprotein complex and controls, (ii) detailed multivariate statistical analysis of the SERS spectra, as well as (iii) AFM images confirming morphological changes consistent with formation of the influenza aptamer-nucleoprotein complex.

6.1. Introduction

Influenza is a severe respiratory disease that induces epidemics of illnesses ranging from symptomless infections through various respiratory syndromes, to acute primary viral and secondary bacterial pneumonia.(374) This potentially fatal respiratory infection is the result of several influenza viruses highly effective in human infection due to the ability of the surface glycoproteins to mutate overtime, leading to epidemics and pandemics of diseases caused by re-assortment between human and avian viruses.(375) Influenza remains a major source of morbidity and mortality worldwide.(374) Severe outbreaks, such as the 1918 and 1957 flu

pandemics caused by the highly pathogenic avian influenza viruses, resulted in a ~60% mortality rate. More recently, the 2009 influenza A (H1N1) outbreak reached a high pandemic alert level.(376) The infectious nature of the virus poses a significant threat on healthcare due to its continuous evolution and zoonotic potential. Current means of prevention are not entirely satisfactory, as the vaccines do not offer complete efficacy and the anti-viral drugs are only marginally effective.(377) As a result, surveillance methods are being implemented to track outbreaks of current and emerging strains, as well as aid in the development of vaccine and disease intervention strategies.

Current diagnostic tools available for routine laboratory diagnosis of influenza rely on the detection of viral particles or typing of the viral genome.(360, 378, 379) These assays include enzyme-linked immunosorbent assay (ELISA),(380, 381) hemadsorption,(360) and hemi-nested multiplex RT-PCR.(378) However, these assays suffer from a lack of sensitivity and reproducibility, or often require synthetic labeling or species-specific reagents. Additionally, these methods require expensive equipment and appropriate laboratory facilities. As a result, new approaches for rapid, reliable, and sensitive means of detecting influenza virus in clinical diagnostics are urgently needed.

Aptamers are single-stranded DNA or RNA oligonucleotides generated through an *in vitro* combinatorial selection process called Systematic Evolution of Ligands by Exponential Enrichment (SELEX).(382) First reported in 1990, this method allows selection of aptamers

specific for the molecules present on the targeted cell from very large populations of random sequence oligomers (DNA or RNA libraries).(383) The high affinity and specificity of aptamers for their molecular targets is given by their ability to undergo a conformational change upon binding.(384) As a result, aptamers may incorporate small molecules into their nucleic acid structure or integrate into the structure of larger molecules such as proteins. In comparison with their equivalents of antibodies, aptamers possess several advantages that make them very promising in therapeutic and diagnostic assays.(385, 386) First, they prevail over antibodies in analytical applications due to their stability, robustness and in vitro preparation method which prevent the need to infect host systems.(387) To that extent, the animal-free production of aptamers allows receptors toward analytes that are toxic or nonimmunogenic to organisms, prevents batch variation exhibited by polyclonal antibodies and enhances the purity of the overall production.(388) Furthermore, the small size of aptamers and their ruggedness provide a critical edge over antibodies; that is, a greater surface coverage of the receptor may be attained, and hence multiple binding sites may occur.(382) Last, aptamer-based assays may be regenerated more easily than antibody-based assays owing to their simple structure, their lack of immunogenicity and stability against biodegradation and denaturation.

Aptamer have been developed against a wide variety of targets ranging from protein(173) to whole cells(174) and bacteria,(389) and have been integrated in a variety of biosensors.(175, 176) The use of aptamers as biological recognition elements has also been largely exploited in the detection of biological threat agents,(390) cancer biomarkers,(391) foodborn pathogens,(392) as well as other important biological molecules such as cytokines, amino acids and

peptides.(393) Aptamers have also been raised against a broad range of proteins such as thrombin,(394) vasopressin,(395) immunoglobulin E,(396) HIV-1 Rev protein(397) and influenza virus hemmagglutinin,(398, 399) as well as several other viral proteins.(400) They have also proven valuable in a variety of fundamental virology studies, including genome replication, gene expression, and virus entry and consequently have found a niche in applied research areas such as gene therapy, antiviral drugs, biomolecule purification, and biosensors.(175-177) These inherent characteristics of aptamers make them extremely attractive for investigations such as diagnostic applications, diagnostic tools, and new drugs development.

The development of affinity biosensors for specific recognition and low-level detection of analytes has been a major challenge for the advancement of bioanalytical science and accurate understanding of specific biomolecular interactions.(401) Coincidently, the area of aptamer-based molecular recognition assays has been a rapidly emerging field that is commonly associated with other competitive applications such as biosensors, immunoassays, and other analytical formats in use.(402) The integration of aptamers in biosensing assays has generated a new breed of detection platforms exploiting various strategies to probe the binding affinities of biomolecular interactions.(403) Often called “aptasensors”, these new sensing devices constitute an unmatchable level of diversity and offer remarkable convenience in the design and the modification of their structure, which has recently lead to the emergence of their use in diagnostic and clinical settings.(404) To that extent, the design of novel affinity biosensors for specific recognition and low-level detection of analytes constitutes a major challenge for the advancement of bioanalytical science. As a result, aptamers have been integrated to a wide

variety of platforms to probe their binding affinity to their specific targets. The conformational change of aptamers upon binding of their molecular targets may be exploited to monitor a molecular recognition event by coupling the aptamers to an appropriate sensing platform. Using this strategy as a proof of principle, aptamers may be incorporated to new sensing platforms to probe their binding affinity and to further capitalize on their change in conformation.

Raman and SERS have previously been used to directly probe sequence information in DNA/RNA complexes.(159, 207, 405, 406) Recent reports demonstrated direct detection of DNA/RNA sequences using SERS,(157, 159, 213, 407-410) including hybridization of target sequences to oligo-modified substrates,(159, 213, 407) with detection of single nucleotide polymorphisms possible.(159, 409) SERS spectra were reported sensitive to conformational changes, molecular orientation and packing density in ssDNA and dsDNA oligomers upon ligand binding.(157, 213)

Most of the Raman aptamer studies published to date have used surface-enhanced resonance Raman (SERRS), a method that employs Raman-active synthetic labels. Using this principle, aptamer-based detection of adenosine was reported by Chen and co-workers. In this study, they used a dsDNA composed of both an adenosine aptamer strand and a partially complementary short DNA strand with Raman reporter (TMR-labeled 12-mer complimentary DNA) to demonstrate structure switching upon introduction of adenosine to the aptamer.(411) They showed that the dsDNA probe adopted a stable adenosine-aptamer complex in the presence of adenosine and that hybridization of the aptamer to the target allowed TMR to approach the active

substrate, hence yielding a detectable signal for adenosine. Likewise, detection of cocaine was also achieved by Chen and co-workers who reported the first cocaine-based aptasensor by demonstrating that the addition of 1μM of cocaine caused the aptamer to fold into a rigid three-way junction, resulting in close proximity of the Raman label (tetramthylrhodamine, TMR) to Ag colloid film and enhancement of Raman scattering.(412) Detection of the protein thrombin was achieved by Wang and co-workers using a SERS-based aptasensor.(413) In this study, an aptamer-modified, Rhodamine 6G (R6G)-adsorbed AuNPs was used on a SERRS-active substrate to capture targets. After depositing AgNPs on the AuNPs, the Raman scattereing of R6G was enhanced for thrombin detection. Although sensitive and selective to their complementary targets, these SERS-based aptasensors rely on the use of a Raman label which often introduces complexity to the experiment and usually results in a reduced selectivity or sensitivity.

To date, relatively few reports have appeared that focus on non-resonant SERS detection of aptamer-target binding in a direct, label-free fashion. Such assays capitalize on the intrinsic detection of aptamer-target binding affinity using the advantages of SERS in a direct, label-free fashion. Recent work from Pagba and co-workers demonstrated the formation of a quadruplex structure of a 15-mer DNA thrombin-binding aptamer using both Raman and SERS by monitoring the characteristic bands associated with such structure.(414, 415) In another study by Ochsenkühn and co-workers, the ability to detect the binding between an aptamer and unlabelled proteins was achieved by measuring the changes in the SERS signal of the aptamer caused by the conformational changes which arises from the formation of the aptamer-protein complex.(416)

These latter studies have established the proof of principle that aptamer-target binding may be detected from the intrinsic SERS spectra of the complex.

The current study expands on these previous model studies and presents results showing that intrinsic SERS spectra may detect the binding of a real diagnostic aptamer to its influenza target in a complex biological matrix. The work presented here focuses on a commercial polyvalent anti-influenza aptamer that was developed against the nucleoprotein constituents of the viruses contained in a commercially available split-virion inactivated influenza vaccine. The intrinsic SERS spectra provide direct spectral signatures for the aptamer-nucleoprotein complexes. This chapter presents the results of this study and describes i) two separate negative controls, ii) detailed chemometric spectral analysis, and iii) AFM imaging of the binding events, to demonstrate the specificity of binding for the viral nucleoproteins to the influenza aptamer. These results provide the first detailed evidence for the use of aptamer-modified SERS substrates as diagnostic tools for influenza virus detection in a real, complex biological system.

6.2. Methods and Materials

Materials and Reagents

1-Mercaptoundec-11-y)tetra(ethyleneglycol) (95%) and [Arg^8] -Vasopressin (>95%) were purchased from Sigma-Aldrich (St. Louis, MO). All other chemicals were of analytical grade and used without any further purification.

Preparation of Ag Nanorods and Microwell Array Fabrication

Aligned Ag nanorods used as SERS-active substrates were prepared by an oblique-angle vapor deposition (OAD) technique using a custom-designed electron-beam/sputtering evaporation system according to the procedures described in Chapter 3. Prior to their use, the SERS-active Ag nanorods were cleaned for 4 minutes in an Ar^+ plasma using a plasma cleaner to remove any surface contamination according to procedures described in Chapter 4. Following nanofabrication and cleaning of the Ag nanorod substrates, a multi-well array was constructed using a polymer molding process in which liquid polydimethylsiloxane (PDMS, Sylgard® 184 Silicone Elastomer Kit, Dow Corning, Midland, MI) is added to a mold and cured by low temperature heating. The patterned substrate was produced according to previously published procedures with slight modifications as follows.(332) A stainless-steel mold/substrate assembly was pre-heated in a bench top oven (Fisher Scientific) at 55°C for 10 minutes prior to the addition of a mixture of PDMS base, curing agent, and accelerator (20:2:1, w/w) through the opening of the substrate/mold assembly. The mixture was allowed to cure on the SERS-active substrate at 55°C for approximately 45 minutes, and cool down to room temperature for about 10 minutes. Finally, the well patterning plate was de-attached gently from the patterned substrate, creating a uniform, 4 × 10 well PDMS-pattern SERS-active microwell array substrate. Figure 6.1 shows a picture of the well-patterning plate assembly as well as a photograph of the 4× 10 well PDMS-pattern SERS-active microwell array substrate after removing from mold assembly.

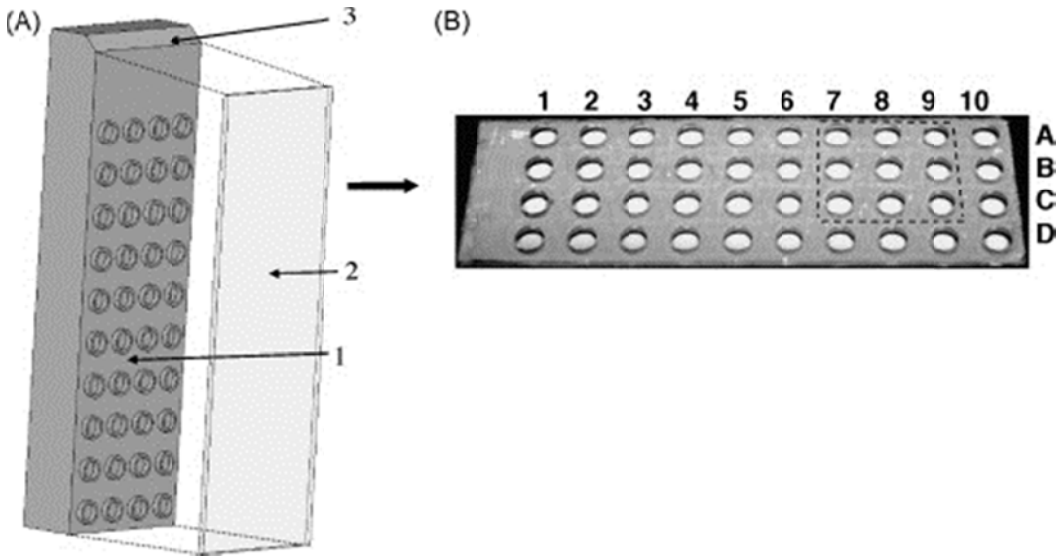

Figure 6.1. (A) Assembly of the well-patterning plate (1) mold with the SERS substrate (2) with the SERS active surface of the substrate facing the well-patterning plate. The PDMS is poured into the opening (3) between the substrate and well-patterning plate. The base and top plates of the mold assembly have been left out for clarity. (B) A photo of a patterned substrate after removing from mold assembly with well labeling scheme.

Polyvalent Anti-Influenza Aptamer

The polyvalent 5'-C6-disulfide anti-influenza aptamer was provided by AptaRes AG, Mittenwalde, Germany. The AptaRes polyvalent anti-influenza aptamer used in this study was isolated against the nucleoprotein constituents of a commercially available inactivated influenza vaccine using a cell-free, MonoLex™ combinatorial process.(417) The single-stranded DNA aptamer consisted of 63 base pairs with a molecular weight of 25,987 Daltons. The as-received lyophilized aptamer was dissolved in molecular biology grade water to a final concentration of 100 μM.

Influenza and RSV Virus Samples

The AptaRes polyvalent influenza aptamer used in this study was isolated against the nucleoprotein constituents of the viruses contained in the commercially available Fluarix™ Influsplit SSW® 2009/2010 split-virion inactivated influenza vaccine (GlaxoSmithKline, GmbH & Co., KG, Munich, Germany). The AptaRes polyvalent influenza aptamer used in this study was isolated against the nucleoprotein constituents of the viruses contained in the commercially available Fluarix™ Influsplit SSW® 2009/2010 split-virion inactivated influenza vaccine (GlaxoSmithKline, GmbH & Co., KG, Munich, Germany). The three monovalent split viruses used in this vaccine are the i) A/Uruguay/716/2007 NYMC X-175C, ii) B/Brisbane/60/2008, and iii) A/Brisbane/59/2007 IVR-148, influenza strains. The Robert Koch Institut (Berlin, Germany) supplied the influenza nucleoproteins from these viruses in the form of purified, whole virus cell

lysates. These samples consisted of cell lysates from the three isolated monovalent influenza virus strains contained in the Influsplit SSW® vaccine, and characterized as to their hemagglutinin (HA) content. The sample provided were i) 100 µl of A/Uruguay/716/2007 NYMC X-175C, HA concentration of 172 µg/ml, ii) 100 µl of B/Brisbane/60/2008, HA concentration of 207 µg/ml, and iii) 100 µl of A/Brisbane/59/2007 IVR-148, HA concentration of 144 µg/ml.

Respiratory Syncytial Virus (RSV) was used as a negative viral control. RSV strain A2 was propagated using Vero cells maintained in Dulbecco's Modified Eagles Medium (DMEM; GIBCO BRL Laboratories, Grand Island, NY) supplemented with 2% heat-inactivated (56°C) FBS (Hyclone Laboratories, Salt Lake City, UT). Upon detectable cytopathic effect (three days post-infection), RSV/A2 was harvested in serum-free DMEM followed by freeze-thaw cycles (-70°C/4°C), after which the contents were collected and centrifuged at 4,000 × g for 15 minutes at 4°C. The virus titer was approximately 10^7 PFU/mL as determined by immunostaining plaque assay as previously described.(418) Lysis of RSV/A2 was performed by mixing 35 µL of the virus sample with 140 µL AVL chaotropic lysis buffer (Qiagen, Valencia, CA). The lysate was then subjected to buffer exchange on a zebra spin desalting column (Thermo Scientific, Rockford, IL). Buffer exchange was accomplished by loading the column bed gel with 50 µL aliquots of the binding buffer and centrifuging at 1,000 × g for one minute at room temperature to pass the binding buffer through the column resin bed. The procedure was repeated four times to ensure complete pre-equilibration of the resin bed with the binding buffer. To complete the

buffer exchange procedure, 140 μL of the RSV lysate was applied to the pre-equilibrated resin bed and the column was centrifuged at 1,000 × g for two minutes at room temperature to collect the sample. The sample was then diluted to a concentration of about 10^5 PFU/mL in the binding buffer for the SERS experiment.

Use of 22-mer ss-DNA Sequence and Anti-Vasopressin Aptamer as Negative Controls

A random 22-mer DNA sequence HS-C6H12-5'ACT CCA TCA TCT AAC ATA TCA A3' and an anti-vasopressin aptamer HS-C_6H_{12}-$^{5'}$TCA CGT GCA TGA TAG ACG GCG AAG CCG TCG AGT TGC TGT GTG CCG ATG CAC GTA$^{3'}$ were purchased from Integrated DNA Technologies (IDT, Coralville, IA) and used without further purification. These DNA probes were used as negative controls in the influenza binding experiments. The immobilization of the 22-mer DNA control sequence and the anti-vasopressin aptamer was accomplished using the same experimental protocols that were employed for the immobilization of the aptamer, as described above. Also, experiments to assess the binding of the influenza nucleoproteins on these self-assembled, DNA functionalized surfaces used the same experimental protocols that were employed for the capture and binding of the influenza nucleoproteins on the aptamer-coated substrate, as described above.

Binding Buffer

The buffer used in the binding experiments was prepared by dissolving 20 mM Tris HCl, 15 mM NaCl, 4 mM KCl, 1 mM $MgCl_2$ and 1 mM $CaCl_2$ in molecular biology grade water at pH 7.3 and stored at 4°C. The buffer and working tools were DNase free.

Aptamer Immobilization and Binding of Influenza Viral Nucleoproteins

The 5' C6 disulfide anti-influenza ss-DNA aptamer was immobilized onto the Ag nanorod substrate by addition of 20 µL of 1000 nM of the oligonucleotide solution to a patterned microwell overnight at room temperature to yield a self-assembled monolayer (SAM). After 12 hours, the aptamer solution was removed from the substrate surface and the microwell was rinsed three times with 20 µL aliquots of molecular biology grade water to remove any unbound material. To promote the correct oligonucleotide conformation and minimize non-specific binding of DNA or proteins to the Ag surface, 20 µL of 100 nM of the spacer molecule (1-mercaptoundec-11-y)tetra(ethyleneglycol), $HS(CH_2)_{11}(OCH_2CH_2)_4OH$, was added to the microwell at room temperature. After a 6 hour incubation, the solution of the spacer molecule was removed from the substrate and the microwell was rinsed three times with 20 µL aliquots of molecular biology grade water to remove any unbound spacer molecules. Following formation of the aptamer-spacer complex, binding of the nucleoproteins of the virus samples to the aptamer-functionalized Ag nanorod surface was accomplished by adding 20 µL of the individual virus lysate diluted in the binding buffer to the aptamer-modified, Ag nanorod microwell. Each virus sample was adjusted to a consistent concentration of 1 µg/mL HA content. The substrate was

then incubated at 37°C for 8 hours in a humid environment to prevent dehydration of the samples on the substrate surface. This was achieved by depositing small droplets (20 μL) of molecular grade water around the SERS-active substrate in the Petri dish. The humidity was maintained by covering the Petri dish with a Parafilm® sheet and sealing it with the cover of the dish.
After incubation, the virus solution was removed from the substrate, and any non-specifically adsorbed virus components were removed by two washes with 20 μL aliquots of warm binding buffer followed by one final rinsing step with 20 μL aliquot of molecular biology grade water to remove the salts and chaotropic agents present in the buffer and virus samples. The substrate was then allowed to dry for one hour in a clean and dry environment prior to analysis. Incubation of the RSV control sample with both the aptamer-functionalized SERS-sensing surface and the 22-mer ss-DNA probe was accomplished by adding 20 μL of the RSV virus solution in binding buffer to the aptamer-modified, Ag nanorod microwell. The other binding conditions were kept identical to those of the influenza nucleoprotein samples, as described above.

The immobilization of the 22-mer ss-DNA oligonucleotide probe and the anti-vasopressin aptamer as well as the experiments to assess the binding affinity of the 22-mer ss-DNA probe to the influenza nucleoproteins and the the influenza nucleoproteins and the [Arg^8]-Vasopressin on the anti-vasopressin aptamer-functionalized SERS substrate used the same experimental protocols that were employed for the capture and binding of the influenza nucleoproteins on the influenza aptamer-coated substrate, as described above.

Raman Spectroscopy

Raman measurements were performed using a confocal Raman microscope (InVia, Renishaw, Inc., Gloucestershire, United Kingdom). A 785 nm near-IR diode laser provided laser excitation. The sample was illuminated through a 20× (N.A. = 0.40) objective resulting in a spot size of approximately 4.8 × 27.8 μm. The laser power used was ~0.36 mW, as measured at the sample. SERS spectra were collected from ten different spots within a given microwell using a 30 second acquisition time with one accumulation. Spectra were collected between 2000 and 500 cm^{-1}.

Experimental Design and Reproducibility

In order to ensure reproducibility of results, the following experimental design was used. Twenty (20) individual Ag nanorod substrates were used in this study. Each substrate was patterned in a 40-well format, as previously described;(332) at least 25-30 of those wells were used during the course of each experiment. The anti-influenza aptamer was applied to the wells at concentrations of between 1-1000 nM; each concentration of aptamer was added to a minimum of two wells.

In addition to a series of aptamer concentrations, we also studied a series of influenza samples with HA concentrations ranging from 0.1 μg/ml to 10.0 μg/ml. Each combination of aptamer and influenza sample, as well as the blanks and controls, was studied on each patterned substrate, resulting in at least 40 replicates for each combination of concentrations. A minimum of 10 SERS spectra were acquired in each well. Therefore, we acquired a minimum of 400 SERS

spectra for each specific combination of aptamer concentration with influenza nucleoprotein sample, including blanks and controls. The spectra presented in Figures 6.2, 6.7, and 6.9 are an average of 10 individual spectra for each particular type of sample.

Assay Sensitivity

The sensitivity of this SERS-based influenza assay was assessed against the standard ELISA method of viral nucleoprotein detection using the anti-influenza aptamer as outlined in the manufacturer's literature supplied with the aptamer (www.aptares.net). The standard ELISA method for detection of the influenza viral nucleoproteins is specified for a concentration range of 6.0 – 0.06 μg/ml with respect to influenza HA. All the spectra shown in the manuscript were acquired using influenza nucleoprotein samples adjusted to a concentration of 1.0 μg/ml, relative to influenza HA. We also have obtained SERS spectra at 0.1 μg/ml HA concentration with equivalent results. Therefore, the SERS-based influenza assay described here is at least as sensitive as the standard ELISA assay used for aptamer-based detection of influenza.

Data Analysis

Off-line spectral manipulation and analysis were performed using GRAMS 32/AI Version 6.0 (Galactic Industries Corporation, Nashua, NH). Multivariate statistical analysis of the samples, including Principal Components Analysis, Hierarchical Cluster Analysis, and Partial Least Squares Discriminant Analysis,(419-421) was performed with PLS Toolbox version 6.2

(Eigenvector Research Inc., Wenatchee, WA), operating in a MATLAB environment (R2011a, The Mathworks Inc., Natick, MA).

AFM Measurements

Template stripped Ag nanofilms were used as AFM substrates and prepared according to previously published procedures. AFM measurements were performed using an Agilent 5500 AFM system equipped with an inverted light microscope (ILM) system (Agilent, Chandler, AZ) combined with an Agilent multi-purpose AFM scanner with a scanning area of 10 μm^2.
Ag nanofilms substrates were prepared by vapor deposition using a custom-designed electron-beam/sputtering evaporation system. A 300 nm Ag (99.99%, Kurt J. Lesker Company) layer was deposited onto 2 cm × 3 cm mica sheets (Ted Pella, 25 mm × 75mm Highest Grade V1 Mica, Cat. # 56) taped to the substrate holder at a rate of 3.0-4.0 Å/s. 2 cm × 3 cm glass slides were cut from standard 2.54 cm × 7.62 cm glass microscope slides (Gold Seal®, Becton Dickinson Company, Franklin Lakes, NJ) and cleaned using Piranha solution (4:1 mixture of conc. H_2SO_4: 30% H_2O_2) for 15 minutes, rinsed several times with copious amounts of deionized water and dried under a gentle stream of nitrogen gas. A small drop of two-part epoxy glue was mixed and spotted on the clean 2 cm × 3 cm glass slide. Individual 2 cm × 3 cm Ag coated mica sheets were gently pressed against the glass slide using a clean pair of tweezers to remove the air bubbles between the mica sheet and the glass slide. The complex was allowed to dry for 10 minutes and then stripped apart using a clean razor blade, leaving the Ag film glued to the glass slide with the atomic roughness of mica to produce the bare template stripped Ag substrates used for AFM imaging.

The immobilization process and the binding affinity on the Ag surface were imaged in aqueous solution using the following procedures. Silicon cantilever tips with a nominal spring constant of about 0.1 N/m were used throughout the experiments. The detailed parameters for the image are as follows: drive is approximately 46%, resonance gain is 2, resonance frequency is 12.95 KHz, resonance amplitude is 1.68 V, and scan rate is 2.0 line/s. A custom-made flow-cell was used to observe the real-time variation of surface topography *in-situ*. Briefly, the new medium or solution was injected into the liquid cell by syringe passing while the imaging system monitored the changes in surface morphology on the same surface area (500 nm × 500 nm) throughout the whole imaging process, while the other syringe was in charge of drawing out the original medium inside the liquid cell in order to prevent the overflow. The bare template stripped Ag substrate was first imaged in molecular grade water, followed by the injection of the disulfide anti-influenza aptamer at a concentration of 100 pM for a duration of 3 hours. Three flushings of the flow cell with molecular grade water allowed removal of the non-adsorbed aptamer molecules from the Ag surface. The same surface area was imaged again following the rinsing steps. (1-Mercaptoundec-11-y) tetra (ethyleneglycol) was then injected into the flow cell at a concentration of 10 pM for 3 hours. After the three flushing steps, the area was imaged again followed by the injection of A/Uruguay diluted in the binding buffer to a concentration of 1 pg/mL (HA) content into the flow cell maintained at 37°C. After 3 hours, the solution was flushed out and the surface inside the flow cell was rinsed three times with the warm binding buffer to allow a final characterization of the surface morphology after binding.

6.3. Results and Discussion

Experimental Design

The disulfide-derivatized anti-influenza ss-DNA aptamer was immobilized onto the individual Ag nanorod microwells, resulting in the formation of self-assembled monolayers of DNA oligonucleotides.(422) A second immobilization step added the spacer molecule (1-mercaptoundec-11-y)tetra(ethyleneglycol), $HS(CH_2)_{11}(OCH_2CH_2)_4OH$. The functionalized microwells of the Ag nanorod substrate were then incubated with each of the three influenza virus strains or controls. A schematic diagram of the overall procedure for aptamer immobilization onto the Ag nanorod array, nucleoprotein binding, and detection strategy is presented in Figure 6.2. The full experimental details related to the diagram are described in section 6.2 of this Chapter.

SERS Spectra of the Aptamer Complex

Figure 6.3.a (top left) shows the SERS spectrum of the anti-influenza-spacer complex used in this study, while Figure 6.3.b (middle left) is the spectrum of the blank control, *i.e*. the aptamer complex incubated only with the binding buffer. Figure 6.3.b shows that no detectable spectral changes are observed when the aptamer complex is treated with a blank control. The number and position of the bands in Figure 6.3.a and 6.3.b are in agreement with those reported from SERS studies of DNA bound to Ag and Au nanoparticles.(207, 423) The dominant features present in Figure 6.3.a and 6.3.b are bands that are attributed to the motions of the oligonucleotide base pairs (phosphate backbone motion, deoxyribose conformation, and ring stretching vibration).

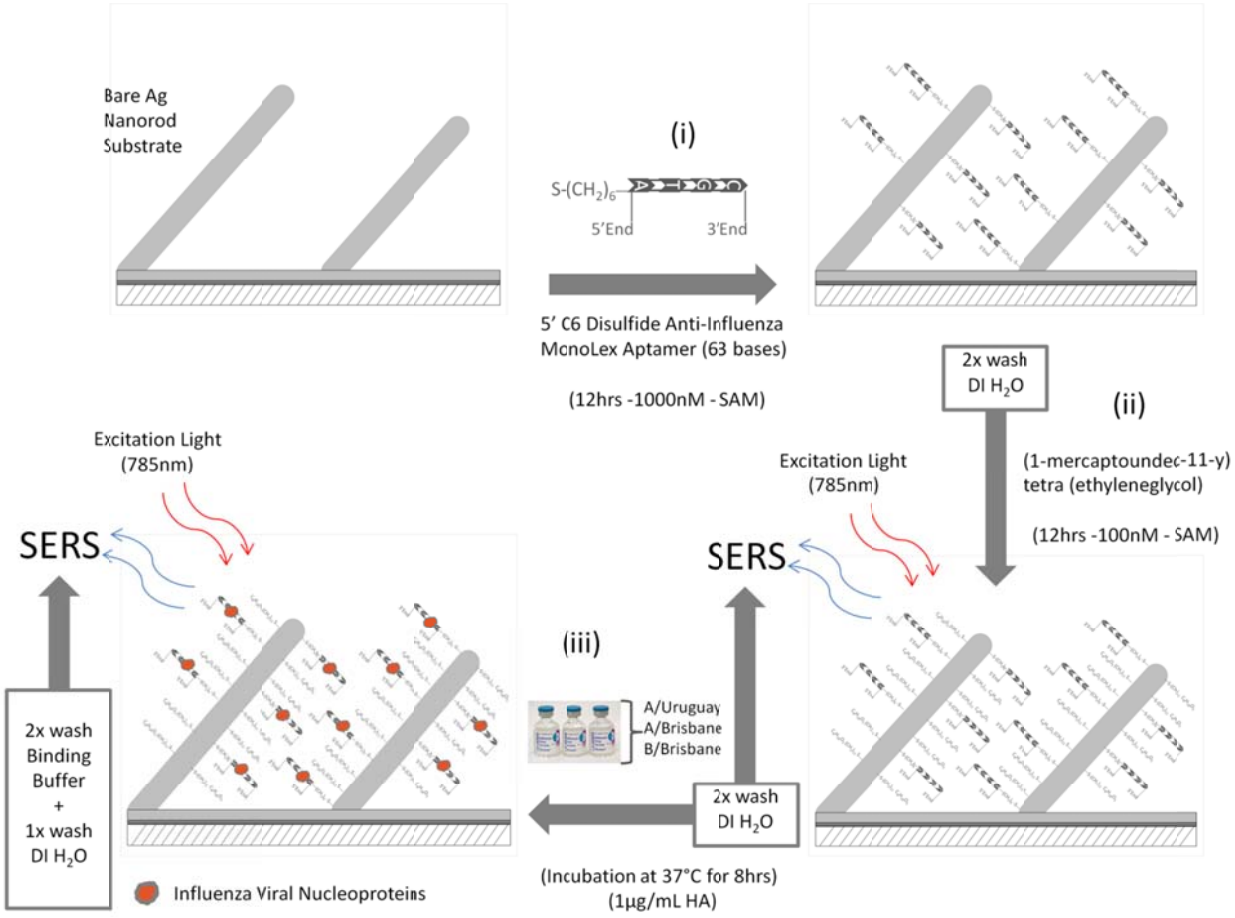

Figure 6.2. Schematic diagram of the overall strategy for aptamer immobilization onto the Ag nanorod array, virus binding, and detection strategy. Immobilization of the disulfide anti-influenza aptamer onto the surface of the Ag nanorod array (i), addition of (1-mercaptoundec-11-y) tetra (ethyleneglycol) as the spacer molecule (ii), and incubation with the three influenza virus samples (iii).

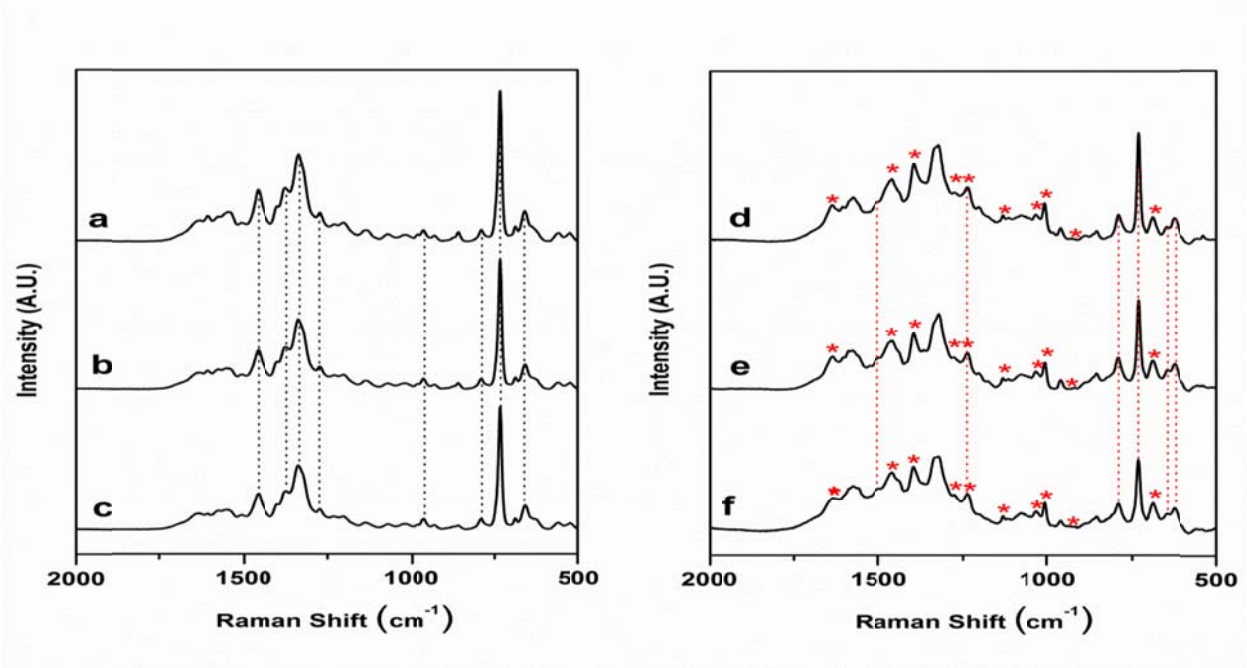

Figure 6.3. (a) SERS spectrum of the anti-influenza aptamer (1000 nM) - PEG spacer (100 nM) complex on a Ag nanorod substrate, (b) anti-influenza aptamer complex and binding buffer blank control, (c) anti-influenza aptamer complex and RSV (10^5 PFU/mL) negative control, (d) anti-influenza aptamer complex and nucleoproteins from A/Uruguay, (e) anti-influenza aptamer complex and nucleoproteins from A/Brisbane, and (f) anti-influenza aptamer complex and nucleoproteins from B/Brisbane. Virus concentrations in (d) – (f) were adjusted to 1µg/mL (relative to HA content). Each spectrum shown is an average of 10 individual spectra for each particular sample. The dashed vertical lines in (a), (b), and (c) indicate the characteristic oligonucleotide bands for the influenza aptamer and its controls. The dashed vertical lines in (d), (e), and (f) indicate the oligonucleotide bands that changed after binding of the nucleoproteins. Asterisks indicate the presence of new bands in the aptamer complex corresponding to binding of the protein target.

The spectral features present in Figure 6.3.a and 6.3.b are bands primarily attributed to the motions of the oligonucleotide base pairs (phosphate backbone, deoxyribose conformation, ring stretching and side chain vibrations). The dominant features present of the spectra shown in Figure 6.3 are the peaks at 731, 1265, 1332 and 1454cm^{-1}. The bands at 731, 1265, and 1332 cm^{-1} are assigned to the ring stretching modes of adenine and the asymmetric out-of-plane deformation of NH_2 in adenine, respectively.(37, 207, 332, 415, 424) These bands are in agreement with the observation previously reported by Suh and co-workers, which attributed bands to several vibrational modes of adenine adsorbed on silver colloid particles.(207)

Other prominent nucleic acid vibrations include the bands at 656 cm^{-1} (G), and 793 cm^{-1} (C, T), while the band at 1045 cm^{-1} is attributed to the asymmetric out-of-plane deformation of NH_2 in cytosine. We assign the band at 656 cm^{-1} to the ring breathing mode of Guanine as reported by Barhoumi and co-workers.(157, 213) This mode also shows a strong SERS signature present at 1454 cm^{-1}, as predicted by Suh and co-workers.(207) Stokes modes from ring vibrations of other base pairs are also dominant features in the SERS spectrum of the aptamer shown in Figure 6.3.a. At 1558 cm^{-1}, another band is characteristic of a ring stretch of both adenine and guanine.(416) In addition, a band at 687 cm^{-1} is indicative of the C-S stretching vibration of the thiol group, and confirms cleavage of the disulfide bond after adsorption and immobilization of the aptamer to the Ag nanorod array.(425) A complete table of the observed SERS bands in the spectrum of the anti-influenza aptamer, along with their assignments based on literature precedent, is provided in Table 6.1.

Table 6.1. Observed SERS vibrational bands with assignments in the spectrum of the anti-influenza aptamer.

Wavenumber, cm^{-1}	Assignment
623	C-C-C ring in-plane bending of A
652	Ring breathing mode of G(426)
731	Ring breathing mode of A
736 & 1337	Skeletal vibrations of the A ring
742	C-H out-of-plane bending of A
793	Ring breathing mode of both C and T
956	C-C stretching vibration of the nucleic acids
1023	Amino group vibration of C
1045	Asymmetric out-of-plane deformation of NH_2 in C
1132	C-N and C-C stretching
1265	Asymmetric out-of-plane deformation of NH_2 in A
1275	Ring stretching and C-H bending of T
1299	Breathing mode vibration of C (skeleton vibration)
1307 & 1317	V_{C-NH2} vibration of A
1320	Mixed in-plane stretching motions of the 6-membered ring
1332	Ring stretching mode of A
1360	Breathing mode vibration of T (skeleton vibration)
1391	CH_2 deformation
1454	Ring breathing vibration of A
1496	C8=N7 vibration of the G ring
1506	External phenyl ring stretching of A
1558	Ring stretching mode of G and A
1631	External phenyl ring stretching of C
1640	Carbonyl stretching mode

Surface Coverage and Reproducibility

The surface coverage of the disulfide aptamer on the Ag nanorod array was investigated by varying the concentration of the aptamer and monitoring the A ring-breathing mode at 731 cm^{-1}. This band is well-suited for characterizing the surface coverage of the aptamer since it is the most intense band in the spectrum and has been shown to be concentration dependent. Figure 6.4.A shows a plot of the normalized SERS intensity of the 731 cm^{-1} peak as a function of the aptamer concentration in the range from 0.1 to 5000 nM. The plot in Figure 6.4.A displays a sharp increase in SERS intensity in the concentration range 0.1 - 500 nM, followed by an intensity plateau. Figure 6.4.B shows the same data plotted as a log-log plot of the absolute SERS intensity of the 731 cm^{-1} band as a function of the aptamer concentration. Figure 6.4.B displays a sigmoidal increase over three orders of magnitude (10^{-1} to 10^{2} mol) in the concentration range 0.1 – 500 nM, followed by an intensity plateau. The error bars in Figure 6.4.A and 6.4.B indicate a high degree of reproducibility from spot-to-spot within a substrate as well as between the substrates used in these experiments.

The band intensity plateau effect seen in both Figure 6.4.A and 6.4.B has been previously observed in Ag nanorod SERS studies and is related to the saturation of the SERS signal with increasing surface coverage. The surface density of the aptamer on the surface of the Ag nanorod substrate was calculated by estimating the number of DNA molecules contained in the 20 μL of a 1000 nM DNA solution deposited on the surface of a microwell. The surface density was found to be ~3.7 x 10^{5} molecules/μm^{2}. This estimate is comparable (within a factor of ten) with previous s studies of the surface density of DNA SAMs on smooth Au films.

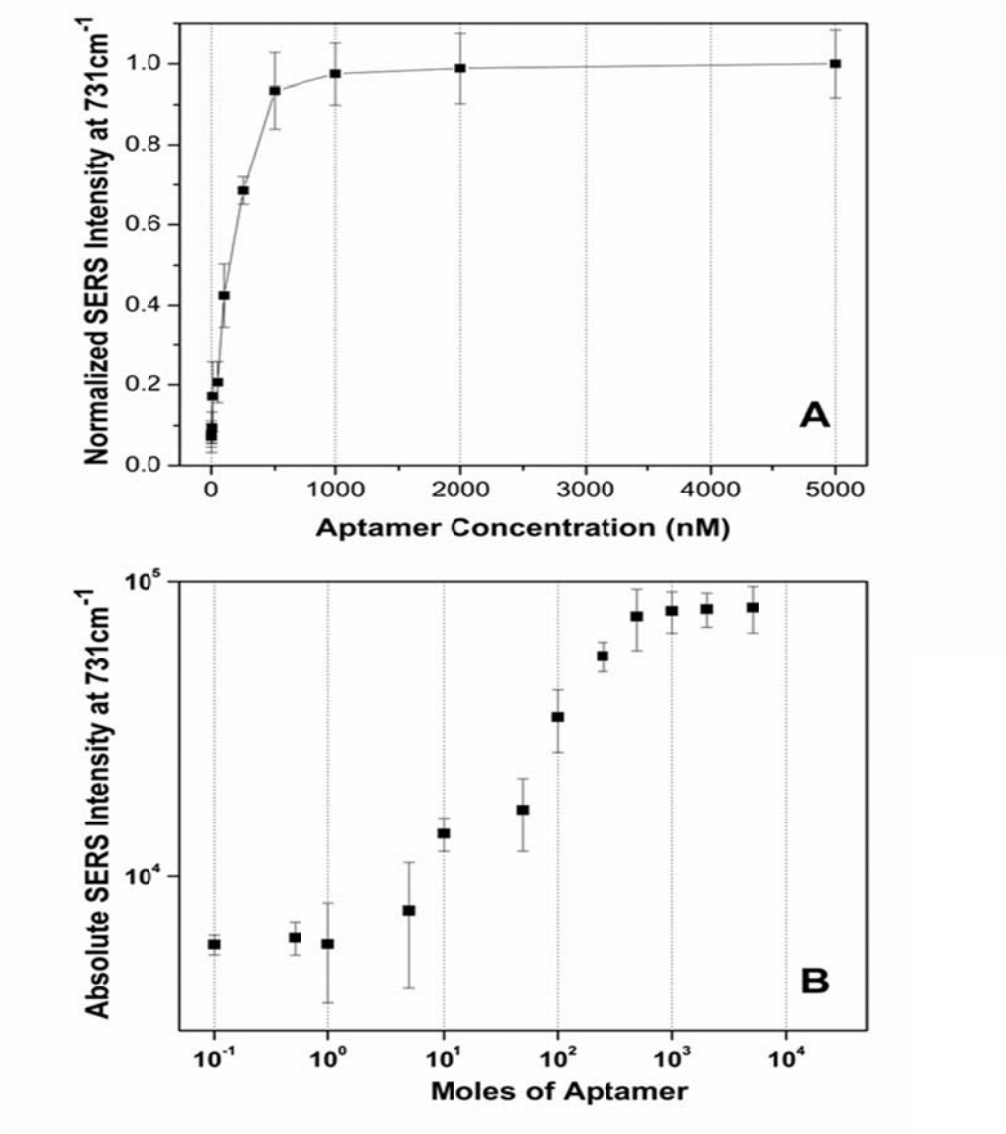

Figure 6.4. (A) Normalized band intensity of the 731 cm^{-1} peak in the SERS spectra of the anti-influenza aptamer immobilized on a Ag nanorod substrate as a function of concentratioin the range from 0.1 to 5000 nM. (B) Log-log plot of the absolute SERS intensity of the 731 cm^{-1} band of the anti-influenza aptamer as a function of concentration in the range from 0.1 to 5000 nM.

These results are also in agreement with previous surface density estimates of thiolated DNA on metal films. Some variation in surface density should be expected in the present case due to the differences in substrate composition (Au vs. Ag) and morphology (nanorods vs. smooth); however, our results agree well with previously published reports on DNA packing density.

Nucleoprotein Binding to the Polyvalent Anti-Influenza Aptamer

Aptamer-target binding leads to addition of proteins to the aptamer-modified surface, as well as changes in oligonucleotide secondary structure, both of which may be sensed via SERS. Since Raman spectra are sensitive to both DNA secondary structure and the presence of surface-bound proteins, we hypothesize that binding of the influenza nucleoproteins to the surface-bound aptamer may be sensed via analysis of the SERS spectra of the aptamer-nucleoprotein complex in comparison to that of the unbound aptamer.

Consistent with this hypothesis, distinct changes are seen in the spectra of the anti-influenza aptamer after incubation with the cell lysates from the three monovalent influenza virus strains. Figure 6.3.d shows the SERS spectrum of the aptamer and spacer on the Ag nanorod array incubated for 8 hours at 37°C with 1 μg/mL (HA) content of the influenza virus strain A/Uruguay. Major changes in bands attributed to the DNA aptamer are noticed upon nucleoprotein binding. For example, bands attributed to the bands of the nucleic acid bases at 731 cm^{-1} (A) and 652 cm^{-1} (G) decreased in intensity whereas the band at 793 cm^{-1} (C and T)

increased in intensity. The shoulder at 623 cm^{-1} in Figure 6.3.a became a sharp band in the spectrum in Figure 6.3.d. Additional spectral changes include the decrease in the band intensities at 1265 cm^{-1} (asymmetric out-of-plane deformation of NH_2 in A) and 1496 cm^{-1} (C8=N7 G ring vibration).

In addition to nucleic acid spectral features, bands present in the SERS spectra of the aptamer-nucleoprotein complex are attributed to the nucleoproteins themselves. Prominent bands indicative of protein binding in Figure 6.3.d are seen in the sharp band at 1004 cm^{-1} due to aromatic ring vibrations, as well as the band at 1034 cm^{-1} assigned to the in-plane ring CH deformation, both characteristic of Phe.(427-431) Binding of protein to the aptamer leads to the appearance of the band resulting from the C-O-C protein stretching motion at 1132 cm^{-1},(431) the band at 1238 cm^{-1} attributed to the amide III vibration,(35, 432) as well as the protein CH_2 bending mode at 1440-1460 cm^{-1}.(35, 416, 432) Amino acid side chain vibrations appear in the spectrum of the aptamer-nucleoprotein complex at 720, 960, and 1294 cm^{-1}.(427-431) Further evidence of protein binding is shown in the appearance of two other bands at 1391 and 1602 cm^{-1},(427-431) assigned to the symmetric and anti-symmetric CO_2^- stretching from protein side chains. A complete table of the observed SERS bands in the influenza nucleoprotein-aptamer complex along with their literature-based assignments is provided in Table 6.2.

To test the polyvalent nature of the aptamer, the nucleoproteins from the influenza strains A/Brisbane and B/Brisbane that are also contained in the split-virion influenza vaccine were

Table 6.2. Observed SERS vibrational bands with assignments in the spectrum of the anti-influenza aptamer-nucleoprotein complex.

Wavenumber, cm^{-1}	**Oligonucleotide Assignments (change from aptamer alone)**
623	C-C-C ring in-plane bending of A (increased in intensity)
652	Ring breathing mode of G (decreased in intensity)
731	Ring breathing mode of A (decreased in intensity)
793	Ring breathing mode of both C and T A (increased in intensity)
1265	Asymmetric out-of-plane deformation of NH_2 in A (decreased in intensity)
1319	Ring stretching mode of A (shifted from 1332 cm^{-1})
1496	C8=N7 vibration of the G ring (present as a small shoulder)

Wavenumber, cm^{-1}	**Protein Assignments**
620	Combined COO^- wagging motion, ring C-C twist in amino acids, and skeletal mode of Phe
720	COO^- deformation of amino acid side chain
860 & 1610	Symmetric ring vibration of Tyr
960	C-C stretch of amino acid side chain
1004	Aromatic ring vibration of Phe and Tyr (small contribution)
1034	In-plane ring CH deformation of Phe and C-N stretch of Gly
1132	C-N and C-C stretch of amino acids
1238	Amide III vibration
1294	CH_2 wagging motion of amino acid side chain
1391	Symmetric COO^- stretching of amino acid side chain
1440-1460	CH_2 bending mode
1602	Anti-symmetric COO^- stretching of amino acid side chain
1612	Combined amide vibration in amino acids (Tyr and Phe)

incubated with the aptamer-spacer complex in the same manner as the A/Uruguay strain. These spectra are shown in Figure 6.3.e (A/Brisbane, middle right) and Figure 6.3.f (B/Brisbane, bottom right). The identical spectral changes that are seen in the A/Uruguay complex (Figure 6.3.d) also occur in the complexes for the A/Brisbane and B/Brisbane strains, indicating a high degree of reproducibility in the nucleoprotein binding of the split virion strains to the polyvalent aptamer.

1st Negative Control: RSV Virus Incubated with Anti-Influenza Aptamer

A negative control virus was incorporated in this study to determine the specificity of binding of the influenza nucleoproteins to the anti-influenza aptamer. Respiratory syncytial virus (RSV) was used as the negative control virus. RSV is a single-stranded, negative-sense RNA virus that, worldwide, is the single most important cause of acute lower respiratory tract illness.(433) RSV is an important and ubiquitous respiratory pathogen, and as such is a good candidate to act as a control virus for influenza. Incubation of the RSV control sample was accomplished by adding 20 μL of the lysed RSV virus solution to an aptamer-coated Ag nanorod microwell. The virus sample was adjusted to a concentration of ~10^5 PFU/mL in the binding buffer, and the binding conditions were kept identical to those used for the incubation of the influenza nucleoprotein samples. Figure 6.3.c shows the spectrum of the RSV virus applied to the aptamer-modified substrate. Only minor spectral intensity changes were observed in Figure 6.3.c after incubation of the RSV virus sample, indicating no apparent binding of the RSV lysate to the anti-influenza aptamer.

This is readily apparent when comparing Figure 6.3.c to the aptamer spectrum in Figure 6.3.a and the blank spectrum in Figure 6.3.b. The lack of binding of the RSV to the anti-influenza aptamer is also apparent from comparing spectra on the left panel of the aptamer (Figure 6.3.a), the blank (Figure 6.3.b), and the negative control virus (Figure 6.3.c) with the nucleoprotein - aptamer complex spectra on the right panel (Figure 6.3.d, 6.3.e and 6.3.f). The SERS spectra in Figure 6.3 show a high degree of specificity for the binding of only influenza viral nucleoproteins to the polyvalent anti-influenza aptamer.

Chemometric Analysis of Influenza Aptamer-Nucleoprotein Spectra

Multivariate statistical analysis, including Principal Components Analysis, Hierarchical Cluster Analysis, and Partial Least Squares Discriminant Analysis, was performed to establish statistically significant differences between the SERS spectra of the samples and controls in Figure 6.3 and was used to confirm the binding specificity of the aptamer to its viral nucleoprotein targets. Multivariate statistical methods have previously been used to analyze SERS spectra of pathogens for spectral identification and classification.(294-297) Two hundred forty spectra, corresponding to 40 spectra in each sample category, were used to generate the statistical models for both the positive and negative controls. Therefore, the data analysis was performed on a total of 480 spectra. SERS spectra were first processed by taking the first derivative of each spectrum (1^{st} derivative, 2^{nd}-order polynomial, 15-point Savitzky-Golay) and then normalized to unit vector length. The normalized first derivative spectra were mean-centered and auto-scaled prior to analysis.

Figure 6.5 illustrates the Hierarchical Cluster Analysis (HCA) of the spectra of the aptamer, controls, plus influenza nucleoprotein samples. HCA is an unsupervised classification method that calculates the inter-spectrum distance in Principal Component-space and forms clusters of spectra based on their relative similarity, resulting in a two-dimensional dendrogram. The aptamer spectra were clustered based on Ward´s linkage method for minimizing variance. The vertical bars in the dendrogram specify which samples and classes are linked, while the horizontal bars represent the distance between the linked classes.

Figure 6.5 was generated from the first Principal Component of the spectral data set, which accounted for 92.19% of all the variability in the data. Figure 6.5 reveals two distinct clusters. The first red cluster contains samples A, B and C, which include the spectra of the aptamer complex (A), the blank control aptamer complex incubated only with the binding buffer (B), and the aptamer complex after incubation with the negative control RSV virus (C). The second green cluster encompasses samples D, E, and F, which refer to the spectra of the aptamer incubated with all three influenza virus strains, A/Uruguay (D), A/Brisbane (E) and B/Brisbane (F). This classification by HCA provides obvious separation between the SERS spectra of the unbound aptamers and its controls with the aptamer-nucleoprotein complexes, and demonstrated that the spectra of the influenza aptamer-nucleoprotein complexes could be differentiated from that of the unbound aptamer control spectra with 100% accuracy.

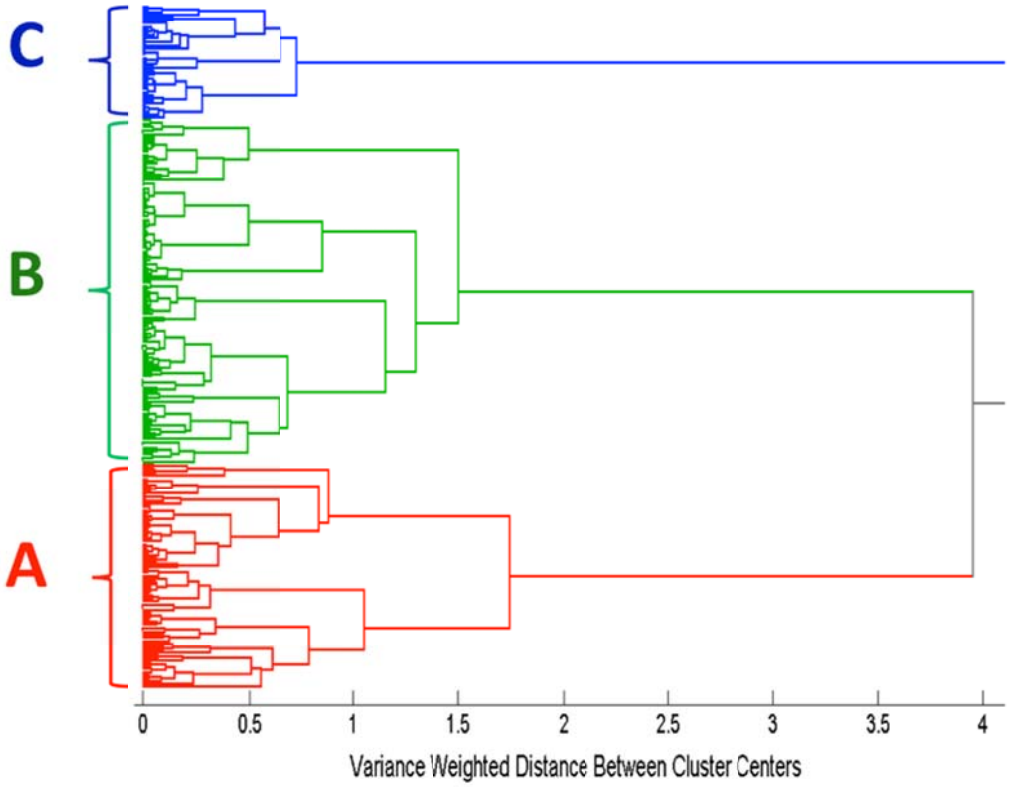

Figure 6.5. Dendrogram produced by Hierarchical Cluster Analysis (HCA) of the SERS spectra shown in Figure 6.3 using Ward´s method and label-coded as follows: (A) anti-influenza aptamer, blank buffer, and RSV negative control, (B) anti-influenza aptamer incubated with influenza nucleoproteins from A/Uruguay, A/Brisbane, and B/Brisbane. A total of 240 spectra were used to generate this dendrogram, corresponding to 40 spectra in each of the 6 sample categories.

In addition to the Hierarchical Cluster Analysis method, other multivariate statistical tests were used to analyze the spectra of the influenza nucleoprotein complexes. Both Principal Component Analysis (PCA) and Partial Least Squares Discriminant analysis (PLS-DA) were employed to confirm that the SERS spectra of the aptamer-target complexes may be differentiated from those of the blanks and negative controls. Both PCA and PLS-DA confirm the findings of the cluster analysis shown in Figure 6.5, i.e. that the SERS spectra of the influenza nucleoprotein complexes may be completely distinguished from those of the blanks and negative control.

Principal Component Analysis (PCA) was first used to analyze spectra of the aptamer-target complexes. PCA is a commonly used unsupervised multivariate statistical method that builds linear models of complex data sets using orthogonal basis vectors called Principal Components (PCs). This method reduces the dimensionality of the sample data matrix prior to displaying the data in a PC scores plot. The primary use of PCA in spectroscopy is to reduce the large number of data points (1500 data points collected at 1 cm^{-1} increments between 500 and 2000 cm^{-1}) to a smaller number of PC's that depict the most statistically significant spectral variations within the spectra, and that may be correlated to physical or chemical changes among the samples.(420) Figure 6.6 shows the PCA scores plot of the second versus first Principal Components (PC 2 versus PC1) for the spectral data of influenza aptamer shown in Figure 6.3. Each data point in Figure 6.6 is representative of a single SERS spectrum and each colored figure corresponds to a group of spectrum according to the color code. A total of 240 spectra are represented in Figure 6.6, corresponding to 40 spectra for each sample category. As seen on the scores plot in Figure

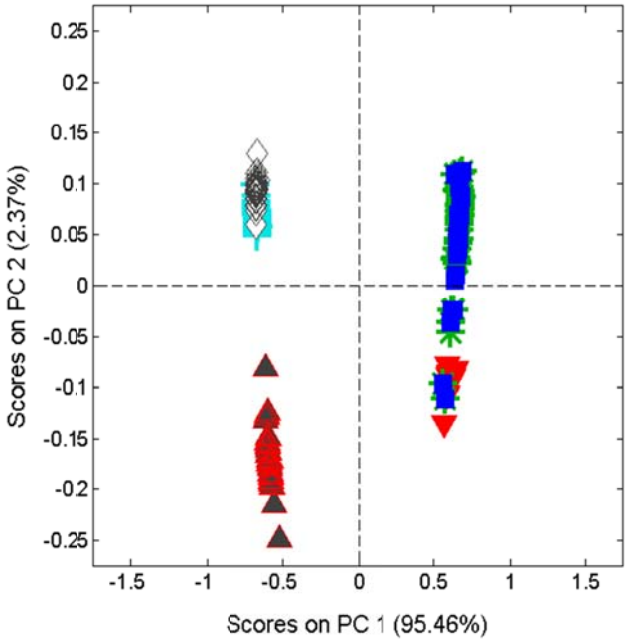

Figure 6.6. PCA scores plot of PC2 vs. PC1 computed for the SERS spectra of the influenza aptamer-spacer complex (▼) incubated at 37°C for 8 hours with the binding buffer (★), RSV (■), A/Uruguay (+), A/Brisbane (◇), and B/Brisbane (▲). Two hundred forty spectra, corresponding to 40 spectra in each sample category, are represented in this plot.

6.6, the data set clustered into two easily separable classes: (i) the unbound influenza aptamer samples (aptamer, blank and RSV control) lie on the right, positive half of the PC1 axis, and (ii) the bound aptamer-nucleoprotein complexes lie on the left, negative half of the PC1 scores axis. Figure 6.6 illustrates that PCA may accurately separate SERS spectra according to spectral features that may be correlated to a change in physical state of the aptamer as a result of binding to the nucleoproteins.

PLS-DA was also used as an alternative chemometric method to determine statistically significant spectral differences among the SERS spectra in a supervised fashion. Unlike PCA, PLS-DA is a supervised method in which latent variables (LVs) are computed to maximize the variance among different classes while minimizing the variance within each given class. This method employs LVs in combination with *a priori* knowledge of the sample classes to build a classification model and to establish class predictions based on that model for the SERS spectra in the data set. PSL-DA has been widely used in spectroscopy and has proven to be a robust statistical technique for identification, discrimination, and classification.

Figure 6.7 presents the result of PLS-DA analysis on the spectral data set containing the six groups of spectra shown in Figure 6.3. The plot shown in Figure 6.7 illustrates the results of the PLS-DA analysis, which results in calculated prediction values for each spectrum. A total of 240 spectra are represented in Figure 6.7, corresponding to 40 spectra for each sample category. The PLS-DA model calculates a threshold value of prediction; spectra with predicted values above the threshold level are determined to belong to a particular class, while spectra with predicted

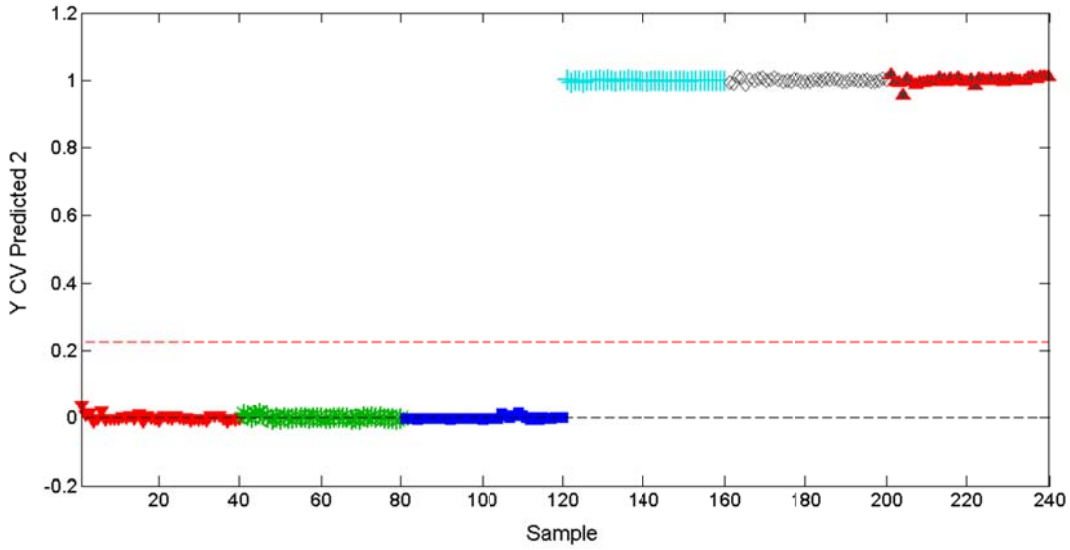

Figure 6.7. PLS-DA cross-validated prediction plot of the spectra of the influenza aptamer-spacer complex (▼) incubated at 37°C for 8 hours with the binding buffer (★),RSV (■), A/Uruguay (+), A/Brisbane (◇), and B/Brisbane (▲). Two hundred forty spectra, corresponding to 40 spectra in each sample category, are represented in this plot.

values below the threshold level are excluded from that class; the threshold value calculated for the classification model in Figure 6.7 is 0.23. Figure 6.7 shows that the spectra of the anti-influenza influenza aptamer-nucleoprotein complexes all classified together, i.e. they all belong to the class of samples that are bound to the anti-influenza aptamer. In contrast, the control samples, i.e., the spectra of the aptamer, blank, and RSV control, all have predicted values that are excluded from this class of samples. The main conclusion from Figure 6.7 is that PLS-DA may statistically identify and classify the spectra of the influenza aptamer-nucleoprotein complexes from the spectra of the unbound aptamer and controls. The results indicate the PLS-DA model was able to correctly classify each spectrum in its class with 100% accuracy.

Both PCA and PLS-DA confirm the findings of the cluster analysis shown in Figure 6.5, i.e. that the SERS spectra of the influenza nucleoprotein complexes may be completely distinguished from those of the blanks and negative control.

2nd Negative Control: Nucleoproteins Incubated with 22-mer ss-DNA Probe

A second negative control negative control experiment was performed to investigate the binding specificity of the influenza viral nucleoproteins. A 22-mer ss-DNA sequence was immobilized to the Ag nanorod arrays, followed by addition of the spacer molecule and subsequent incubation with the binding buffer and the cell lysates from the three monovalent influenza virus strains, using the procedures described in section 6.2 of this Chapter. Figure 6.8 shows the representative SERS spectra of the resulting complexes.

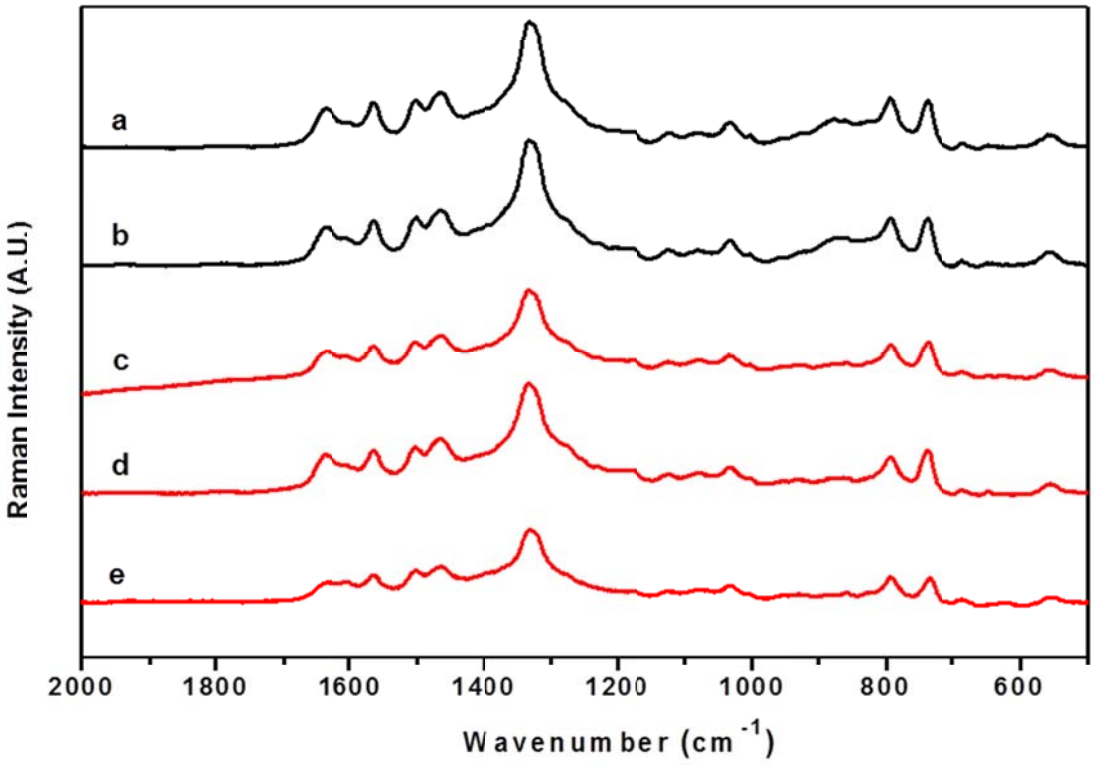

Figure 6.8. SERS spectra of: (a) 22-mer DNA probe, (b) – (e): spectra of 22-mer DNA after incubation with: (b) binding buffer, (c) A/Uruguay virus, (d) A/Brisbane virus, and (e) B/Brisbane virus.

The interpretation of the spectrum of the random DNA probe-spacer complex in Figure 6.8.a follows directly from the discussion of the anti-influenza aptamer in Figure 6.3.a. The bands present in the spectrum of the random DNA probe-spacer complex shown in Figure 6.8.a are characteristic of DNA bound to metallic surfaces. Figure 6.8.a shows no detectable changes in the spectrum of the immobilized DNA probe after incubation with either the binding buffer (Figure 6.8.b) or with any of the three influenza virus samples (Figure 6.8.c-6.8.e), indicating no viral protein binding to the random DNA probe. The lack of binding of the three influenza virus samples to the random DNA probe reinforces the high degree of specificity of the influenza viral nucleoproteins to the polyvalent anti-influenza aptamer.

Chemometric Analysis of the 22-mer ss-DNA probe-Nucleoprotein Spectra

In addition to direct spectral analysis, an objective statistical approach was used to illustrate the lack of differences between the SERS spectra of the random DNA control and those of the control probe incubated with the three influenza samples. Figure 6.9 shows the PCA score plots for the spectral dataset of the random DNA probe used as the negative control for binding of the viral nucleoproteins. The absence of defined clusters in Figure 6.9 is related to the absence of spectral differences when the random DNA probe is incubated with the three influenza virus samples. This observation is in agreement with the spectra shown in Figure 6.8. The lack of clustering in the PC scores plot of Figure 6.9 is statistical evidence for the absence of binding between the random DNA negative control probe and the influenza nucleoproteins from the virus samples. The main conclusion of Figure 6.9 is that the incubation of the viral nucleoproteins to the 22-mer ss-DNA control probes results in no statistically significant changes.

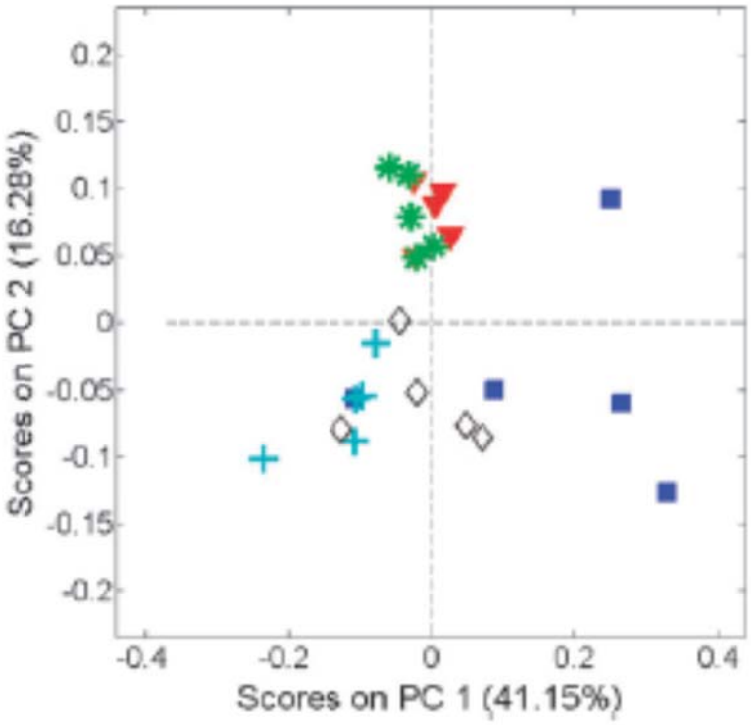

Figure 6.9. PCA scores plot of PC2 vs. PC1 computed from the SERS spectra of the random 22-mer DNA complexes shown in Figure 6.8: (▼) random 22-mer DNA probe alone, (★), random 22-mer DNA probe incubated with the binding buffer (■),random 22-mer DNA probe incubated with A/Uruguay, (+),random 22-mer DNA probe incubated with A/Brisbane (◇), and random 22-mer DNA probe incubated with B/Brisbane (▲).

3rd Negative Control: Nucleoproteins Incubated with Anti-Vasopressin Aptamer

The binding specificity of the influenza viral nucleoproteins to the anti-influenza aptamer was further investigated using a separate DNA oligonucleotide as a negative control. A 5'-C6-thiolated anti-vasopressin aptamer was used for this purpose. This aptamer was developed to bind and inhibit the neuropeptide vasopressin, a peptide hormone regulating the extracellular fluid volume in the body secreted by the posterior lobe of the pituary gland.(395)

Incubation of the influenza nucleoproteins with the immobilized anti-vasopressin aptamer was used to determine whether the binding of the nucleoproteins seen in Figure 6.3 is specific to the anti-influenza aptamer. The 5'-C6-thiolated anti-vasopressin aptamer was immobilized onto the Ag nanorod array substrate *via* the thiol group, and incubated with i) binding buffer, ii) vasopressin and iii) all three influenza virus nucleoproteins, using the procedures described in Supporting Information. Figure 6.10 shows representative SERS spectra of the SAM of the immobilized anti-vasopressin aptamer. The interpretation of the anti-vasopressin aptamer spectrum in Figure 6.10.a follows directly from the discussion of the anti-influenza aptamer in Figure 6.3.a. The main features in the spectrum in Figure 6.10.a are the bands at 731, 793, 1454, 1506, and 1558 cm^{-1}. These bands are attributed to the ring vibrations of the nucleic acids A (731, 1506, and 1454 cm^{-1}), T and C (793 cm^{-1}), as well as G and A (1558 cm^{-1}). Other dominant bands attributed to nucleic acid vibrations in the spectrum shown in Figure 6.10.a include the amino group vibration in C (1023 cm^{-1}), as well as the mixed in-plane ring skeleton stretching vibration (1332 cm^{-1}).

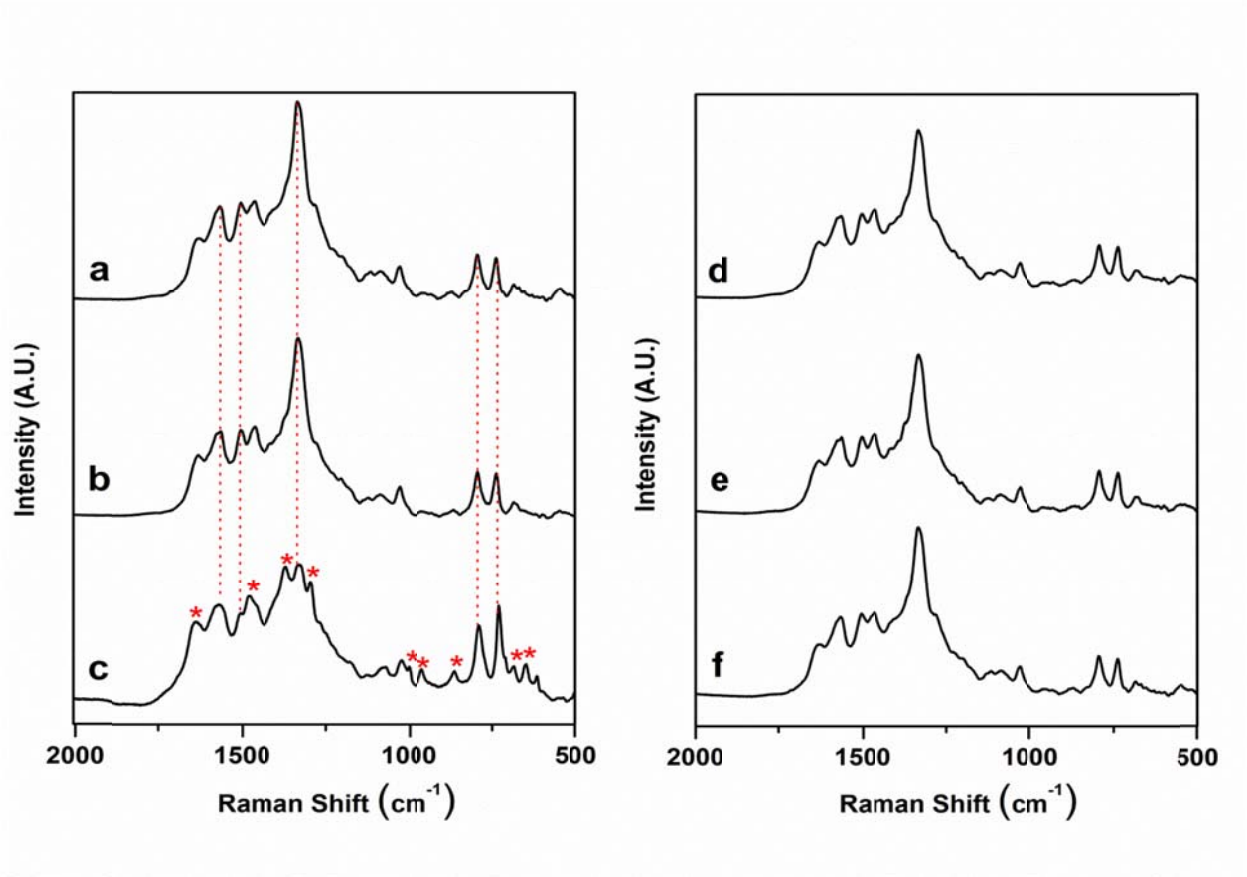

Figure 6.10. SERS spectra of the anti-vasopressin aptamer, controls, vasopressin, and influenza nucleoproteins on a Ag nanorod substrate after incubation at 37 °C for 8 hours. (a) anti-vasopressin aptamer (1000 nM) - spacer (100 nM), (b) vasopressin aptamer with blank binding buffer control, (c) vasopressin aptamer with vasopressin (1µg/mL), (d) vasopressin aptamer with nucleoproteins from A/Uruguay, (e) vasopressin aptamer with nucleoproteins from A/Brisbane, and (f) vasopressin aptamer with nucleoproteins from B/Brisbane. Virus concentrations in (d) – (f) are 1µg/mL (relative to HA content). Each spectrum shown is an average of 10 individual spectra for each particular sample. The dashed vertical lines in (a), (b), and (c) indicate the characteristic oligonucleotide bands for the anti-vasporessin aptamer. Asterisks indicate the presence of new bands in the aptamer complex corresponding to binding of the protein target.

Figure 6.10.b shows the SERS spectrum of the anti-vasopressin aptamer incubated with binding buffer as a blank control. The binding times and conditions were kept the same as those of the anti-influenza binding studies, as described above. Figure 6.10.b shows that no detectable changes are apparent in the spectra of the anti-vasopressin aptamer incubated with the binding buffer when compared to the aptamer alone, similar to that observed with of the buffer blank with the anti-influenza aptamer in Figure. 6.10.a and 6.10.b.

The anti-vasopressin aptamer was treated with the nucleoproteins isolated from the three monovalent influenza virus strains. Figure 6.10.d shows the SERS spectrum of the anti-vasopressin aptamer on the Ag nanorod array incubated with the nucleoproteins isolated from the influenza virus strain A/Uruguay. A comparison of the spectrum in Figure 6.10.d (top right) with the spectra of the anti-vasopressin aptamer and blank (Figure 6.10.a and 6.10.b) shows that no spectral differences are apparent, indicating a lack of influenza nucleoprotein binding to the anti-vasopressin aptamer. This effect also occurs in the spectra that result from the addition of the nucleoproteins from the influenza strains A/Brisbane (Figure 6.10.e, middle right) and B/Brisbane (Figure 6.10.f, bottom right). Relative to the aptamer and blank spectra, no discernable spectral changes are observed when any of the three types of influenza nucleoproteins are incubated with the anti-vasopressin aptamer.

These conclusions are confirmed when the anti-vasopressin aptamer is incubated with 1 μg/mL vasopressin. The spectrum of the vasopressin – aptamer complex is shown in Figure 6.10.c.

This spectrum illustrates that the formation of a vasopressin-anti-vasopressin aptamer complex resulted in characteristic protein and nucleic acid bands. Prominent characteristic features attributable to protein binding to the aptamer are the sharp bands at 860 and 1004 cm^{-1} assigned to the aromatic ring vibration of Tyr and Phe, respectively. Further evidence for protein binding is seen by the sharp band at 960 cm^{-1} attributed to the C-C stretch of the amino acid side chains, as well as the presence of two of the CH_2 motions of the amino acid side chain in the prominent peak at 1294 cm^{-1} (wagging) and the wide band at 1440-1460 cm^{-1}(stretching). Another feature characteristic of protein-aptamer binding is the small band at 1612 cm^{-1} attributed to the amide vibration and/or the aromatic ring vibration of Tyr at 1610 cm^{-1}.

The formation of the aptamer-vasopressin complex also leads to changes in nucleic acid vibrations. For example, band assigned to ring stretching modes of A originally observed at 731 cm^{-1} in Figure 6.10.a shifted to 728 cm^{-1} and increased in intensity by a factor of two in the spectra of the vasopressin-aptamer complex in Figure 6.10.c. Table 6.3 shows a list of the SERS bands in the vasopressin aptamer-vasopressin complex with their tentative band.

The presence of significant spectral changes upon the formation of a vasopressin – anti-vasopressin aptamer complex, combined with the absence of any spectral changes upon incubation of the three influenza virus nucleoproteins with the anti-vasopressin aptamer, strongly suggests that selective binding of the influenza viral nucleoproteins occurs only with the anti-influenza aptamer.

Table 6.3. Observed SERS vibrational bands with assignments in the spectrum of the vasopressin aptamer-vasopressin complex.

Wavenumber, cm^{-1}	**Oligonucleotide Assignment (change from aptamer alone)**
728	Ring breathing mode of A (shifted from 731cm^{-1})
Wavenumber, cm^{-1}	**Protein Assignments**
620	Combined COO^- wagging motion and ring C-C twist in amino acids
720	COO^- deformation of amino acid side chain
860 & 1610	Symmetric ring vibration of Tyr
960	C-C stretch of amino acid side chain
1004	Aromatic ring vibration of Phe and Tyr (small contribution)
1294	CH_2 wagging motion of amino acid side chain
1440-1460	CH_2 bending mode
1612	Combined amide vibration in amino acids (Tyr and Phe)

Chemometric Analysis of Negative Control Anti-Vasopressin Aptamer-Nucleoprotein Spectra

Figure 6.11 shows the HCA dendogram calculated from the anti-vasopressin spectra described above. The cluster analysis was calculated using Ward's linkage algorithm. The first Principal Component was used in these calculations, accounting for 93.27% of all the variability in the data. As seen in Figure 6.11, the anti-vasopressin control spectra separated into three distinct clusters. The bottom red cluster resulted from the spectra of the anti-vasopressin aptamer alone (A) along with the spectra of the unbound aptamer treated with only binding buffer (B). The middle green cluster (C, D and E) represents the spectra of the anti-vasopressin aptamer incubated with the three influenza viral nucleoprotein samples (A/Uruguay, A/Brisbane, and B/Brisbane, respectively). Finally, the top blue cluster (F) represents the spectra of the anti-vasopressin aptamer incubated with vasopressin. The results indicate that cluster analysis provides excellent (100%) statistical differentiation of the aptamer controls from the vasopressin target. In particular, the spectra of the influenza nucleoproteins are completely distinguished from that of the vasopressin complex and its controls, confirming the selectivity of binding of the influenza nucleoproteins only to the anti-influenza aptamer.

Additional multivariate statistical tests were used to analyze the spectra of the vasopressin negative controls. These include Principal Components Analysis (PCA) and Partial Least Squares Discriminant Analysis (PLS-DA). Figure 6.12 shows the PCA scores plot of the first versus second Principal Components (PC 1 versus PC2) for the spectral data of the

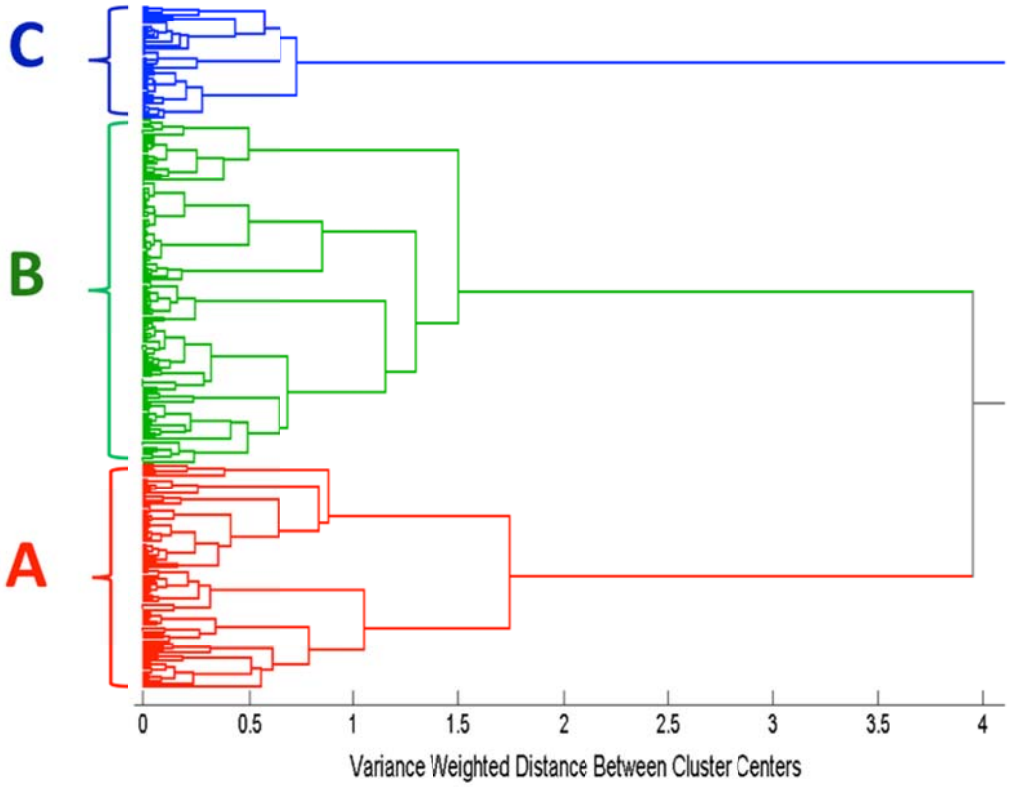

Figure 6.11. Dendrogram produced by Hierarchical Cluster Analysis (HCA) of the SERS spectra shown in Figure 6.10 calculated using Ward´s method and label-coded as follows: (A) anti-vasopressin aptamer (1000 nM) - spacer (100 nM) complex, along with blank buffer control, (B) anti-vasopressin aptamer complex and influenza nucleoproteins from A/Uruguay, A/Brisbane, B/Brisbane, and (C) anti-vasopressin aptamer complex and vasopressin (1µg/mL). A total of 240 spectra were used to generate this dendrogram, corresponding to 40 spectra in each of the 6 sample categories.

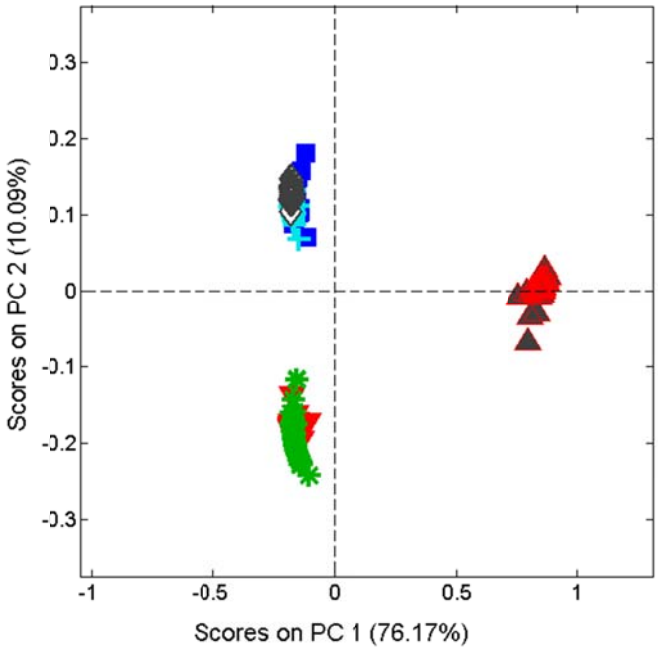

Figure 6.12. PCA scores plot of PC2 vs. PC1 computed for the SERS spectra of the vasopressin aptamer-spacer complex (▼) incubated at 37°C for 8 hours with the binding buffer (★), vasopressin (▲), A/Uruguay (■), A/Brisbane (+), and B/Brisbane (◇). Two hundred forty spectra, corresponding to 40 spectra in each sample category, are represented in this plot.

vasopressin aptamer shown in Figure 6.10. A total of 240 spectra are represented in Figure 6.12, corresponding to 40 spectra for each sample category. As seen on Figure 6.12, the PC scores plot displays three separate clusters: (i) the unbound vasopressin aptamer samples (aptamer and blank) lie in the bottom left, negative, quadrant on the PC1 axis, (ii) the vasopressin aptamer samples incubated with the three influenza strains lie in the top left, negative quadrant on the PC1 axis, and (iii) the bound aptamer-vasopressin complex samples lie centered along the PC2 zero axis in the right, positive half of the PC1 axis. The findings from Figure 6.12 demonstrate that PCA may separate spectra into three distinct clusters and classify the spectra of the aptamer-vasopressin complex apart from the others.

Further analysis of the vasopressin aptamer spectral data using PLS-DA is shown in Figure 6.13. A total of 240 spectra are represented in Figure 6.13, corresponding to 40 spectra for each sample category. The cross-validated PLS-DA prediction plot present in Figure 6.13 shows the prediction made for the vasopressin data set from Figure 6.10. The model calculated a threshold value of 0.17 and projected the spectra of the aptamer-vasopressin complexes to belong to bound aptamer samples (samples above the threshold line), while spectra of the aptamer, blank, and influenza controls did not belong to this class of samples. The findings shown in Figure 6.13 confirm that the spectra of the vasopressin aptamer bound to its target may be differentiated from the spectra of the vasopressin aptamer incubated with the binding buffer (blank), controls, and the influenza virus samples.

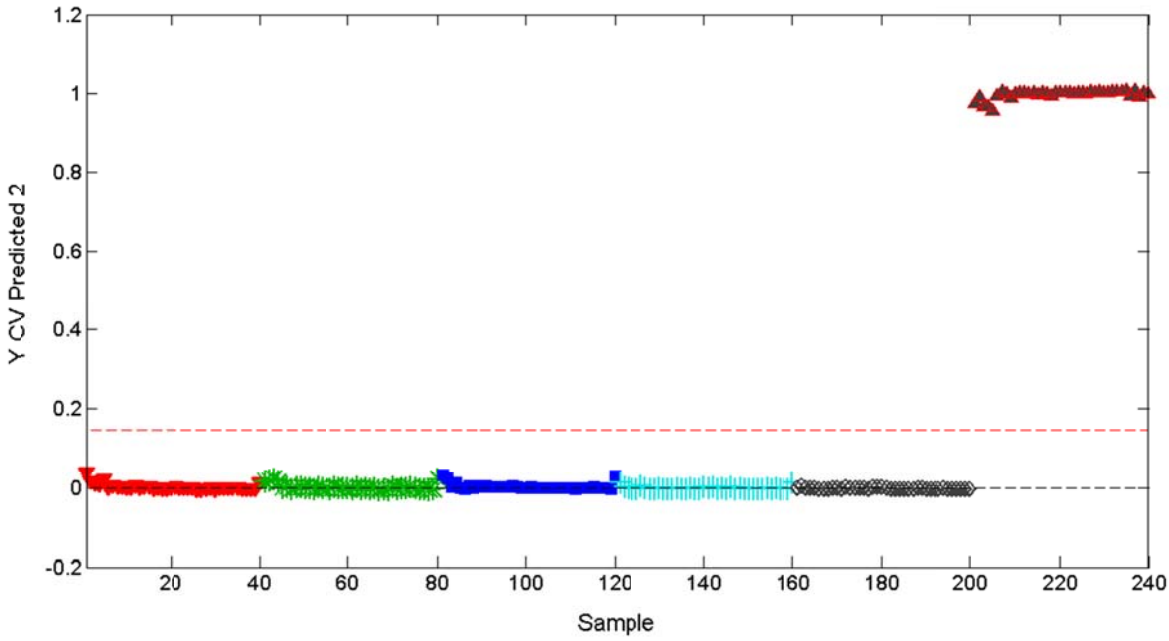

Figure 6.13. PLS-DA cross-validated prediction plot of the spectra of the vasopressin aptamer-spacer complex (▼) incubated at 37°C for 8 hours with the binding buffer (★),vasopressin (▲), A/Uruguay (■), A/Brisbane (+), and B/Brisbane (◇). Two hundred forty spectra, corresponding to 40 spectra in each sample category, are represented in this plot.

The full chemometric analysis of the SERS data sets supports the interpretation of the spectral differences described in the main article. Each of the multivariate chemometric methods of spectral analysis used in this study, *i.e.* HCA, PCA, and PLS-DA, resulted in the same conclusion; that is, the spectra of the aptamer bound to its target may be differentiated from the spectra of the aptamer in its unbound state, as well as the appropriate controls.

Characterization of the Influenza Aptamer-Nucleoprotein Complex by AFM

Atomic force microscopy was used to follow the *in-situ* evolution of viral nucleoprotein binding to the anti-influenza aptamer. A specially designed flow cell was used to image the immobilization steps as the aptamer, spacer, and nucleoproteins were introduced to the cell. This technique allowed imaging of the same surface area throughout the immobilization process between the aptamer probe and the binding to its nucleoprotein target.

Figure 6.14 shows i) two-dimensional AFM images, ii) surface roughness line scans, and iii) three-dimensional AFM images, of the four steps in the surface immobilization of the influenza nucleoproteins. The first column of Figure 6.14 (images 6.14.a and 6.14.e) illustrates the bare Ag substrate prepared by template stripping. The Ag substrate has a homogeneously flat surface with an average height of 1 nm and mean roughness of 0.5 nm. The second column of Figure 6.14 (images 6.14.b and 6.14.f) represents the same Ag surface after injection of the disulfide anti-influenza aptamer at a concentration of 100 pM. These images were acquired after the

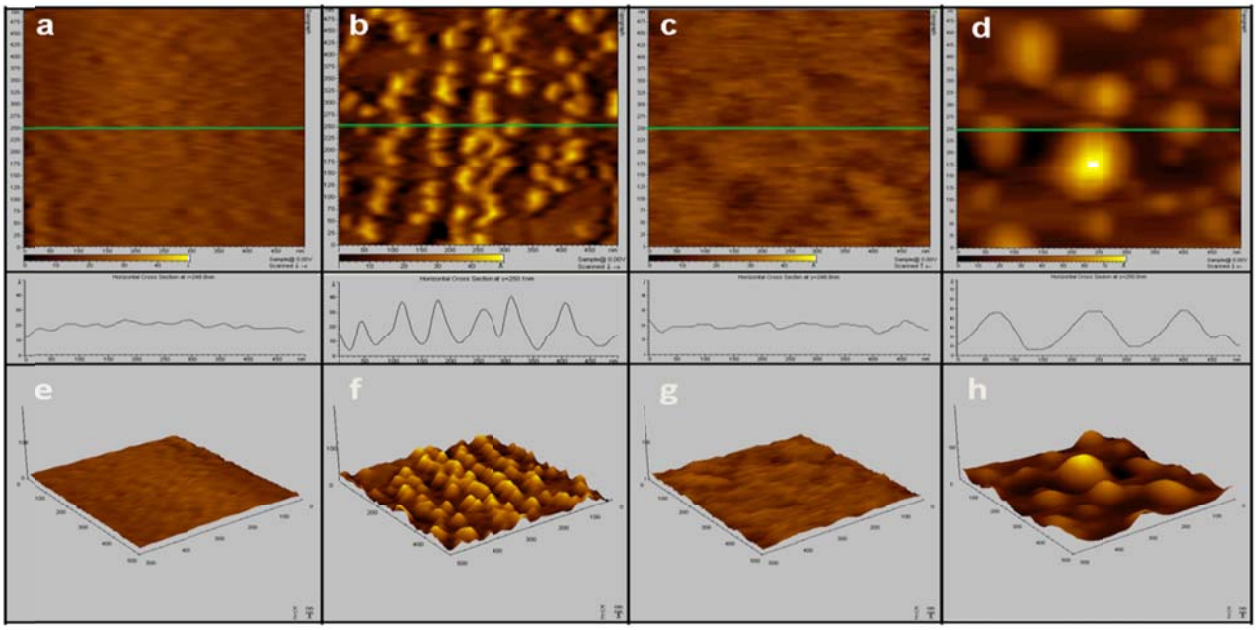

Figure 6.14. (Top) 500 nm × 500 nm 2-D AFM images of (a) bare Ag nanofilm substrate, (b) Ag substrate after injection of the disulfide anti-influenza aptamer at a concentration of 100 pM for 3 hours, (c) Ag substrate after injection of (1-Mercaptoundec-11-y)tetra(ethyleneglycol) at a concentration of 10 pM for 3 hours, (d) Ag substrate after injection of A/Uruguay diluted in the binding buffer to a concentration of 1 pg/mL (HA) content at 37°C for 3 hours.
(Middle) The plots show the surface roughness line scans corresponding to the green line on each of the 2-D AFM images immediately above it in Panels (a), (b), (c) and (d).
(Bottom) Panels (e), (f), (g), and (h) are the representative 3-D AFM images of the 2-D images in (a), (b), (c) and (d), respectively.

aptamer was allowed to interact with the Ag surface for 3 hours followed by flushing the cell with molecular biology grade water. The resulting images show a distribution of aggregates with an approximate average height of 6 nm, a mean roughness of 2.7 nm, and an average diameter of 50 nm, consistent with the changes expected upon formation of the self- assembly of flexible thiolated aptamers.(434)

The third column in Figure 6.14 (images 6.14.c. and 6.14.g) are the images obtained of the aptamer-modified surface following treatment with (1-mercaptoundec-11-y)tetra(ethyleneglycol) at a concentration of 10 pM for 3 hours, followed by rinsing of the surface. The aggregate features present in the images in Figure 6.14.b and 6.14.f are no longer apparent in panels 6.14.c and 6.14.g. The addition of the PEG-like spacer molecule induced rearrangement of the aptamers and produced a uniform distribution of the SAMs adsorbed on the Ag surface. As a result, the average height and mean roughness of the imaged surface decreased to 0.8 nm and 0.3 nm, respectively.

The last column in Figure 6.14 (images 6.14.d and 6.14.h) illustrate the aptamer-functionalized surface after incubation with the influenza nucleoprotein A/Uruguay at a concentration of 1 pg/mL (HA) content for 3 hours. Incubation of the aptamer-modified surface with the influenza virus sample resulted in surface topography changes and the appearance of bright spots on the AFM images shown in Figure 6.14.d and Figure 6.14.h. Binding of the aptamer to the

nucleoproteins is characterized by the formation of large features on the AFM images and with an average diameter of about 150 nm.

These AFM images do not depict single binding events between the aptamer and the influenza nucleoprotein targets on a molecular level, they do support the interpretation that the features in Figure 6.14.d and Figure 6.14.h are due to the aptamer binding with its target. The variations in average height (increase to 2.6 nm) and mean roughness (increase to 1.3 nm) is consistent with the formation of an aptamer-nucleoprotein complex upon incubation with influenza virus lysate. The dimensions of these features are smaller than expected for an intact influenza nucleoprotein complex,(435) which exists in a polymerase complex (ribonucleoprotein) composed of multiple (usually 10 or 12) monomeric nucleoproteins.(30, 436) However, it is likely that the experimental conditions used here resulted in the dissociation of the polymerase nucleoprotein complex, resulting in the attachment of monomeric nucleoproteins to the surface. This hypothesis is supported by the fact that each individual aggregate shown in Figure 6.14.d and Figure 6.14.h has similar dimensions, consistent with monomeric nucleoprotein binding to the aptamer.

As a control experiment, another binding experiment was repeated by incubating the aptamer-spacer complex with the binding buffer solution (data not shown). After extensive washing, no change in the images of the aptamer-modified surface (Figure 6.14.c and Figure 6.14.g) could be seen. This negative blank experiment further supports the interpretation that the images seen in

Figure 6.14.d and Figure 6.14.h result from the binding of the influenza viral nucleoprotein to the aptamer-covered surface.

The images in Figure 6.14 show that aptamer binding to nucleoprotein targets may be characterized using AFM. The AFM images support the observations obtained from the SERS-based studies that nucleoprotein binding may be sensed via direct, label-free spectroscopic detection.

6.4. Conclusions

The first evidence of use of aptamer-modified SERS substrates as diagnostic tools for influenza virus detection in a complex biological matrix was reported. In these studies, a commercially prepared aptamer isolated against a commercial influenza vaccine was used. The results showed that SERS provides a label-free optical method to detect the specific binding of the nucleoprotein target to the anti-influenza aptamer. It was further demonstrated that selective binding of the aptamer-nucleoprotein complex could be differentiated from that of the aptamer alone based solely on the direct spectral signature for the aptamer-nucleoprotein complex. Multivariate statistical methods, including Principal Components Analysis, Hierarchical Clustering, and Partial Least Squares, were used to confirm statistically significant differences between the spectra of the aptamer-nucleoprotein complex and the spectra of the unbound aptamer. Three separate negative controls were used to evaluate the specificity of binding of the viral nucleoproteins to this aptamer. In all cases, no spectral changes were observed that showed

protein binding to the control surfaces, indicating a high degree of specificity for the binding of influenza viral nucleoproteins only to the influenza-specific aptamer. Statistical analysis of the spectra supports this interpretation. AFM images demonstrate morphological changes consistent with formation of the influenza aptamer-nucleoprotein complex. These results provide the first evidence for the use of aptamer-modified SERS substrates as diagnostic tools for influenza virus detection in a complex biological matrix.

CHAPTER 7

Rapid Detection and Identification of the Genetic Markers of Highly Pathogentic Influenza A Viruses by SERS

The purpose of this chapter is to introduce the reader to the use of Ag nanorod arrays for rapid, sensitive, and specific multiplexed SERS-based detection, identification and assessment of virulence factors associated with pathogenesis in influenza A virus. The assay consists of oligonucleotide arrays immobilized on the surface of a SERS-active substrate that allow detection of various influenza RNA strains containing a gene mutation coding for the PB1-F2 protein associated with high virulence. The results of this investigation are presented in this chapter and include: (i) SERS spectra and HCA of the high and low virulence DNA probes-spacer complexes, (ii) SERS spectra and HCA of the DNA probes-spacer complex hybridized with complementary and non-complementary synthetic RNA sequences, and (iii) SERS spectra and PLS-DA of the DNA probes hybridized to complementary and non-complementary viral RNA strains extracted from five H5N1 influenza viruses.

7.1. Introduction

Influenza A is a segmented, negative-strand RNA virus that circulates worldwide and infects a wide range of species including poultry, swines, horses, seals, and humans.(437) Globally, annual epidemics of seasonal influenza A virus cause between 3-5 million severe illness and 250,000 to 500,000 deaths worldwide, with approximately 35,000 of which take place in the

United States alone.(438, 439) In particular, flu pandemics caused by influenza viruses were responsible for 50 million deaths in 1918-1919 and 1 million deaths in 1956-1957, respectively.(440) More recently, human infection with a H5N1highly pathogenic avian influenza (HPAIV) virus was reported in Hong Kong and resulted in eighteen human infections and six fatalities.(441, 442) HPAIV strains pose a significant burden on human health due to their continuous evolution and zoonotic potential.(377) Current work on these viruses is aimed to identify the virulence factors responsible for pathogenicity of influenza virus infection that lead to the severe illness and sometimes death in human beings.(443-448)

The discovery of potential precursors contributing to an increase in influenza A pathogenicity is of great concern due to the risk of future influenza pandemics and their burden on human health and economy. Recent studies suggest that specific mutated proteins conserved among these H5N1 HPAIV strains may offer a plausible mechanism of increased virulence contributing to pandemics and as such, are considered as potential precursors for future influenza pandemics.(449-451) To date, a number of mutations in influenza genes, specifically point mutations, sequence additions, and deletions in the PB1, NA, and HA genes, have been linked to virulence and pathology associated with infection.(452, 453) In particular, the proapoptotic PB1-F2 protein has been shown to contribute to increase virulence in influenza A viruses. PB1-F2 is an 87-amino acid mitochondrial protein that has previously been correlated with increased pathogenicity in vivo by delaying the host defense mechanisms.(454) Initial studies revealed that PB1-F2 induces alteration of mitochondrial membrane potential, promotes apoptosis by specifically targeting macrophages, and reduces clearance of the virus from the host immune

system.(451) The resulting delayed and debilitated acquired immune response generates more infectious virions that increase transmission rates, hence down-regulating the host immune response to infection. A subsequent study revealed a single amino acid mutation at position 66 in the PB1-F2 sequence consistent among HPAIV, *i.e.*, H5N1 (HK/97) and the 1918 influenza A virus, that is likely contributing to increased virulence.(449) The increased pathogenicity resulting from the amino acid mutation at position 66 was associated with higher levels of virus and cytokines in the lungs, hence confirming that PB1-F2 contributes to pathogenicity in the mouse model.

Current diagnostic tools for routine laboratory diagnosis of influenza virulence factors relies entirely on sequencing and alignment of the PB1, NA, and HA genes. Nucleic acid-based assays such as PCR have been developed to sequence isolates and identify virulent strains.(455, 456) However, this technique is time consuming, suffers from high cost, low throughput, and is limited by the number of isolates studied. Other common immunological approaches such as the conventional microarray techniques have not been developed yet for analysis of HPAIV virulence factors. As a result, there is a critical need for rapid, cost-effective, and multiplexed new approaches for the detection of virulence factors in influenza A.

Recently, novel bioanalytical methods that leverage nanotechnology for direct, rapid, and sensitive detection of biomolecules have shown great promises as a new generation of diagnostic platforms. Of the nano-based bioanalytical techniques currently under exploration, surface-enhanced Raman scattering (SERS) presents particular potential for the detection of virulence

factors. SERS is a signal amplification technique based on electromagnetic enhancement resulting from plasmon resonance excitation and enhancement in polarizability due to chemical effects such as charge-transfer excited states.(47, 48) Enhancement of the scattered intensity by a factor of 10^6 is routine, with 10^{11} or higher enhancement possible under well-defined conditions.(73, 89) The advantage of SERS-based sensing is that Raman spectra provide a unique chemically-specific molecular fingerprint, unlike other label-free methods, which rely on a general signal response for the captured analyte. Based on these attributes, SERS has the potential to overcome many of the limitations of current immunologic- or PCR-based diagnostic techniques for pathogenic microorganisms, most notably, the elimination of amplification and labeling steps.

Early literature on direct SERS observation of DNA/RNA complexes showed that each nucleic base yields a unique spectral signature and that SERS has the ability to probe sequence information.(207, 406, 457) More recent studies have shown that SERS possesses the following attributes for detection of oligonucleotide sequences: 1) high sensitivity (<pM); 2) high specificity; 3) good reproducibility; 4) reliable quantification; and 5) high throughput multiplexing.(144, 162, 458-463) A number of recent reports have demonstrated direct detection of DNA/RNA sequences using SERS.(157, 159, 213, 407-409, 464) For example, hybridization of target sequences to oligo-modified SERS substrates was directly measured via SERS.(159, 213, 407) In these studies, intrinsic SERS spectra were demonstrated to be statistically unique and sensitive to the hybridization of matched and mismatched target sequences, including single nucleotide polymorphisms. Other reports demonstrated spectral features changes upon

hybridization of the oligonucleotide probes to complementary targets where quantification of the relative peak intensities due to A and C was achieved by comparing spectra of hybridized and non-hybridized oligonucleotides for thiolated single stranded DNA (ssDNA) probes.(159, 465) In addition, intrinsic SERS spectra were able to study molecular orientation and packing density and to further monitor conformational changes in ssDNA and dsDNA oligomers upon ligand binding.(213, 407)

Our research laboratories have previously demonstrated the use of Ag nanorod arrays to rapidly, sensitively, and quantitatively detect gene sequences using SERS as the read-out method.(284, 290, 373, 466) The current work expands on these previous studies and presents results showing that oligonucleotide-modified Ag nanorod arrays may be used for SERS-based multiplexed profiling of RNA expression to identify the genetic mutations in the PB1-F2 protein related to influenza virulence and pandemic potential without amplification or labeling. The gene-capture assay consists of synthetic DNA oligonucleotide probes immobilized on the surface of the Ag nanorod arrays. These 5'-thiol-modified ssDNA sequences are employed as probes to capture the RNA target gene sequences corresponding to the PB1-F2 gene coding for the N66S mutation that has been shown to cause increased virulence.(449)

In this study, hybridization of the DNA probes to their complementary RNA sequences was probed using surface-enhanced Raman spectroscopy (SERS) and accomplished without amplification or labeling. The results show that the spectral signature of complementary DNA probe-RNA target hybrid resulting from their highly selective interaction may be differentiated

from that of the immobilized DNA probes alone or the DNA probes incubated with RNA with a single base pair mismatch based solely on their intrinsic SERS spectra. First, this study demonstrates the proof of principle that DNA probes may be hybridized using a synthetic version of the complementary RNA target gene sequence. The feasibility of this strategy is extended as it is demonstrated that DNA probes may be hybridized using full, purified viral RNA samples extracted from laboratory stocks of recombinant H5N1 influenza strains with and without the PB1-F2 gene mutation. The validity of the SERS-based multiplexed assay is tested using five influenza H5N1 viral RNA strains (three containing the N66S mutation and two without the mutation) as well as a control influenza H5N1 viral RNA strain not containing the PB1-F2 gene coding for the mitochondrial protein. Hierarchical Cluster Analysis (HCA) and Partial Least Squares Discriminant Analysis (PLS-DA) were used as multivariate statistical tests to differentiate the spectra of the complementary DNA probe-RNA target hybrid from those of non-complementary sequences. The affinity of binding between the DNA probes to their complementary RNA sequences was confirmed using enzyme-linked immunosorbent assay (*ELISA)*. These results provide the first evidence of the use of oligonucleotide-modified SERS substrates as a diagnostic platform for the detection of influenza virulence factors and demonstrate that bio-nanotechnology combined with vibrational spectroscopy has the ability to enhance both detection and diagnosis of emerging viral infections.

7.2. Methods and Materials

Materials and Reagents

6-mercapto-1-hexanol (MCH) was purchased from Sigma-Aldrich (St. Louis, MO). All other chemicals were of analytical grade and used without any further purification.

Preparation of Ag Nanorods and Microwell Array Fabrication

Ag nanorod SERS-active substrates were fabricated using a custom-designed electron-beam/sputtering evaporation system by an oblique-angle vapor deposition (OAD) technique according to the procedures described in Chapter 3. Prior to their use, the SERS-active Ag nanorods were cleaned for 4 minutes in an Ar^+ plasma using a plasma cleaner to remove any surface contamination and patterned with PDMS according to procedures described in Chapter 4 and Chapter 6, respectively.

DNA probes and Synthetic RNA Targets

The DNA probes and the synthetic RNA target sequences were purchased from Integrated DNA Technologies (IDT, Coralville, IA). From the analysis of the PB1-F2 protein sequence, we designed DNA probes corresponding to the minimal mitochondrial targeting sequence for both the high and the low virulence strains.(449) The gene sequence targeted is comprised of 11 amino acids in the position 60 to 70 of the PB1-F2 protein sequence. Table 7.1 presents the amino acid, RNA codon, complementary DNA and reverse DNA probe sequences for both the high and low virulence genes. Note that five thymine (T) bases were added at the beginning of

Table 7.1. Amino acid, RNA codon, complementary DNA and reverse DNA probe sequences for both the high and low virulence genes.

High Virulence	**PB1-F2 Sequence (Position 60-70)**
Amino Acid	Q W L S L K S P T Q D
RNA Codon	$_{5'}$-CAA UGG CUU UCC UUG AAG AGU CCC ACC CAG GAC-$_{3'}$
Complementary DNA	$_{3'}$-GTT ACC GAA AGG AAC TTC TCA GGG TGG GTC CTG-$_{5'}$
Reverse DNA Probe	$_{5'}$-GTC CTG GGT GGG ACT CTT CAA GAA AAG CCA TTG-$_{3'}$
Thiolated DNA Probe	$_{5'}$-/5ThioMC6-D/TTTTT GTC CTG GGT GGG ACT CTT CAA GAA AAG CCA TTG-$_{3'}$
Complementary RNA Target	$_{3'}$-CAG GAC CCA CCC UGA GAA GUU CCU UUC GGU AAC-$_{5'}$

Low Virulence	**PB1-F2 Sequence (Position 60-70)**
Amino Acid	Q W L S L K N P T Q D
RNA Codon	$_{5'}$-CAA UGG CUU UCC UUG AAG AAU CCC ACC CAG GAC-$_{3'}$
Complementary DNA	$_{3'}$-GTT ACC GAA AGG AAC TTC TTA GGG TGG GTC CTG-$_{5'}$
Reverse DNA Probe	$_{5'}$-GTC CTG GGT GGG ATT CTT CAA GAA AAG CCA TTG-$_{3'}$
Thiolated DNA Probe	$_{5'}$-/5ThioMC6-D/TTTTT GTC CTG GGT GGG ATT CTT CAA GAA AAG CCA TTG-$_{3'}$
Complementary RNA Target	$_{3'}$-CAG GAC CCA CCC UAA GAA GUU CCU UUC GGU AAC-$_{5'}$

each DNA probe sequence to provide more flexibility to the probe and promote hybridization of the complementary RNA target sequences away from the surface of the Ag nanorods. Thymine was chosen since it has the lowest Raman cross section of all bases.

The complementary RNA targets used for the ELISA experiments were purchased modified with the fluorescent label TAMRA™ (Azide) at the 5' end of the RNA sequence. TAMRA™ has an excitation wavelength of 546 nm and an emission wavelength of 579 nm.

Preparation of Synthetic DNA and RNA Samples

The 5' C6 thiolated ss-DNA probes were received lyophilized and dissolved in molecular biology grade water down to a concentration of 1000 nM for the SERS experiments, and 10 μg/ mL (~1000 nM) for the ELISA experiments, respectively. The synthetic RNA target sequences were received lyophilized and prepared in the binding buffer spanning the concentration range of 10^{3}-10^{-4} nM at 1:10 increments for the SERS experiment. The TAMRA labeled RNA target sequences were dissolved in the binding buffer for the ELISA experiment at varying concentration (1000 nM to 0.1 nM).

Viral RNA Samples Preparation

HPAIV H5N1 virus strains WH, WH N66S, WH Δ PB1-F2, A/Mute Swan/MS451072/06, A/CK/PA/13609/93, and A/CK/TX/167280-04/02 were propagated using Vero cells maintained in Dulbecco's Modified Eagles Medium (DMEM; GIBCO BRL Laboratories, Grand Island, NY)

supplemented with 2% heat-inactivated (56°C) FBS (Hyclone Laboratories, Salt Lake City, UT). Upon detectable cytopathic effect (three days post-infection), the influenza virus strains were harvested in serum-free DMEM followed by freeze-thaw cycles (-70°C/4°C), after which the contents were collected and centrifuged at 4,000 × g for 15 minutes at 4°C. The virus titers were approximately 10^7 PFU/mL as determined by immunostaining plaque assay as previously described.(418).

Lysis of the influenza virus strains was accomplished using the PureLink Viral RNA/DNA mini Kit from Invitrogen (Carlsbad, California). Viral RNA extraction was performed by mixing 200 µL of each virus sample with 25 µL of Proteinase K in 1.5 mL a microcentrifuge tube. 200 µL of 1X PBS/0.5% BSA was added to each sample. The resulting solution was vortexed for 15 seconds. The lysate was then incubated at 56°C for 15 minutes. Each microcentrifuge tube was briefly centrifuged to remove any droplets inside the lid. 250 µL of 96-100% ethanol was added to lysate the viruses. The lysate was then vortexed for 15 seconds and allowed to incubate for 5 minutes at room temperature. The lysate was transferred onto the Viral Spin Column® and centrifuged at 5,000 rpm for 1 minute. The flow-through was discarded and the spin column was placed in a new collection tube. The washing step was repeated one more time with 500 µL of the wash buffer. The collection tube was discarded and the spin column was transferred into a new collection tube and spun at 13,000 rpm for 1 minute to dry the column. The column was placed into a new recovery tube and 50 µL of sterile, RNase-free water was added to top the column. The resulting solution was incubated for one minute at room temperature. The column was then centrifuged at 13,000 rpm for 1 minute to elute the viral nucleic acids.

Viral RNA samples were quantified by UV absorption using a Thermo Fisher NanoDrop 1000 UV-Vis Spectrophotometer. Table 7.2 summarizes the concentration of the six virus strains from the UV absorption measurements, the value of their A260/A280 ratios, as well as the amino acid sequence at position 66 from sequence analysis. Each RNA sample was then diluted to a concentration of about 10 ng/μL in the binding buffer for the SERS experiments.

Binding Buffer

The binding buffer used in the hybridization experiments was prepared by dissolving 20 mM Tris HCl, 15 mM NaCl, 4 mM KCl, I mM $MgCl_2$ and 1 mM $CaCl_2$ in molecular biology grade water at pH 7.3 and stored at 4 °C. The buffer and working tools were DNase free.

Raman Spectroscopy

Raman measurements were performed using a confocal Raman microscope (InVia, Renishaw, Inc., Gloucestershire, United Kingdom). Laser excitation was provided by a 785 nm near-infrared diode laser. The incident laser beam was delivered to the sample by epi-illumination through a 20X (NA = 0.40) objective onto an automated sample stage. The laser illumination spot produced by this system through this objective creates a rectangular pattern of dimensions

Table 7.2. Strain names, concentrations, A260/280 ratios and amino acid sequences at position 66 from sequence analysis of the six HPAIV H5N1 virus strains used in this study.

Virus Strain (H5N1)	Concentration (ng/µL)	Ratio A260/280	Amino Acid Sequence at Position 66
WH	13.9	2.14	S66N
WH N66S	12.4	1.88	N66S
WH Δ PB1-F2	19.8	2.01	N/A
A/Mute Swan/MS451072/06	16.4	1.23	N66S
A/CK/PA/13609/93	13.9	1.82	S66N
A/CK/TX/167280-04/02	12.2	1.80	N66S

4.8 X 27.8 μm. The laser power used was 0.1% (~0.42 mW), as measured at the sample. SERS spectra were collected from five different spots within a given microwell using a 30 s acquisition time with one accumulation. Spectra were collected between 2000 and 500 cm^{-1}.

Data Analysis

Off-line spectral manipulation and analysis, i.e., baseline correction, band height, and peak frequency determination were performed using GRAMS 32/AI Version 6.0 (Galactic Industries Corporation, Nashua, NH). Multivariate statistical analysis of the samples, including Hierarchical Cluster Analysis and Partial Least Squares Discriminant Analysis, was performed with PLS Toolbox version 6.2 (Eigenvector Research Inc., Wenatchee, WA), operating in a MATLAB environment (R2012a, The Mathworks Inc., Natick, MA). Prior to PLS-DA, the raw SERS spectra were derivatized (first-order derivative; 9-point, second-order polynomial Savitzky-Golay algorithm), normalized to unit vector length, and mean-centered.(420, 421, 467) These preprocessing steps eliminate spectral artifacts and other confounding contributions from variations in the baseline or other heterogeneities in the substrate enhancement factors. All pre-treatment steps of the data and the PLS analysis were performed using the aforementioned software.

ELISA 96-Well Plate Functionalization and Measurements

Maleimide activates black 96-well plates were purchased from Thermo Scientific (Waltham,

MA). Prior to use, the plate wells were washed three times with the binding buffer. 100 µL of thiolated DNA probes were then added to each well at a concentration of 10 µg/mL (~1000 nM) in the binding buffer (pH 7.3) and incubated overnight at 4° C. The next day, the DNA solution was removed and the wells were rinsed three times with the binding buffer. 100 µL of cysteine solution was added to each well at a concentration of 10 µg/mL in the binding buffer and incubated for one hour at room temperature to inactivate excess maleimide groups, as suggested by the vendor. After one hour, the cysteine solution was removed and the wells were rinsed three times with the binding buffer. The fluorescent RNA target sequences were then added to each well at varying concentrations (1000, 800, 600, 400, 200, 100, 50, 10, 1, and 0.1 nM) in the binding buffer at 37°C for 2 hours. The RNA solution was removed and each well was rinsed three times with the binding buffer prior to measurements.

Fluorescent measurements were performed using a POLARstar OPTIMA multidetection microplate reader (BMG Labtech, Ortenberg, Germany). Excitation was accomplished at 544 nm and detection of the emitted fluorescent signal was recorded at 590 nm. The instrument gain was set to 95% for the wells containing the highest concentration of complementary RNA (1000 nM) and 5% for the blank wells (DNA probes incubated with the binding buffer only). Each plate was read twice by the instrument, and the results presented in this report are averages of 4 plates for a total of 8 measurements.

7.3. Results and Discussion

Experimental Design

The 5' C6 thiolated ss-DNA probes were immobilized onto the Ag nanorod substrates by addition of 20 μL of 1000 nM of the oligonucleotide solution to a patterned microwell overnight at room temperature to yield a self-assembled monolayer (SAM). After incubation, the DNA solution was removed from the substrate surface and the microwell was rinsed three times with molecular biology grade water to remove any unbound material. The surface was then blow dried with N_2 before addition of the spacer molecule. 20 μL of a 100 nM solution the spacer molecule 6-mercapto-1-hexanol (MCH) was then added to the microwell to i) prevent the nitrogenous nucleic acid bases from interacting with the Ag surface, ii) promote the vertical configuration of the oligonucleotide probes, and iii) to minimize non-specific binding of DNA/RNA molecules on the Ag surface.(220) The spacer molecule was incubated for 6 hours at room temperature before rinsing with molecular biology grade water and blow drying with N_2. Following formation of the ss-DNA-spacer complex, hybridization of the RNA samples to the oligonucleotide-functionalized Ag nanorod surface was accomplished by adding 20 μL of a 1 nM synthetic RNA solution diluted in the binding buffer. The substrate was then incubated at 37°C for 2 hours in a humid environment to prevent dehydration of the samples on the substrate surface. Following incubation, the RNA solution was removed from the substrate, and any non-specifically adsorbed RNA molecules were removed by thoroughly rinsing the microwell twice with the binding buffer followed by a final wash with molecular biology grade water to remove

the salts present in the buffer. The substrate was then dried under a gentle stream of N_2 prior to analysis. Incubation of the viral RNA samples to the oligonucleotide-functionalized Ag nanorod surface was accomplished by adding 20 μL of a 20ng/μL (~5 nM) RNA solution diluted in the binding buffer. The binding conditions were kept identical to those of the synthetic RNA samples, as described above. Figure 7.1 shows a schematic diagram that outlines the various steps of the experimental design.

SERS Spectra of the DNA Probes

Figure 7.2A (top left) and 1B (top right) show raw, unprocessed SERS spectra of the high and low virulence DNA probe-spacer complexes, respectively. In order to ensure reproducibility of results, 10 spectra were collected in two different wells (5 spectra in each well) and on two different Ag nanorod substrates for a total of 20 spectra for each DNA sequence. Figure 7.2A and 7.2.B show a high degree of spectral reproducibility and present extremely similar spectral features. The number and position of the bands in Figure 7.2.A and 7.2.B are in agreement with those of thiolated DNA bound to Au nanoshell surfaces.(207, 423) The dominant features present in the spectra shown in Figure 7.2.A and 7.2.B are the peaks at 1089 and 1332 cm^{-1}.(157, 423) These bands are assigned to the backbone phosphate stretching mode of nucleic acids (1089 cm^{-1}) and the mixed in-plane ring skeleton stretching vibration (1332 cm^{-1}), respectively. Other prominent nucleic acid vibrations include the bands at 731 and 1454 cm^{-1} (ring stretching modes of A),(207, 424) 1275 cm^{-1} (ring stretching and C-H bending of T),(37) 1496 cm^{-1} (C8=N7 vibration of the G ring),(415) 1023 cm^{-1} (the amino group vibration of C),(424) and 1045 cm^{-1} (asymmetric out-of-plane deformation of NH_2 in C).(207) Other ring vibrations of other nucleic

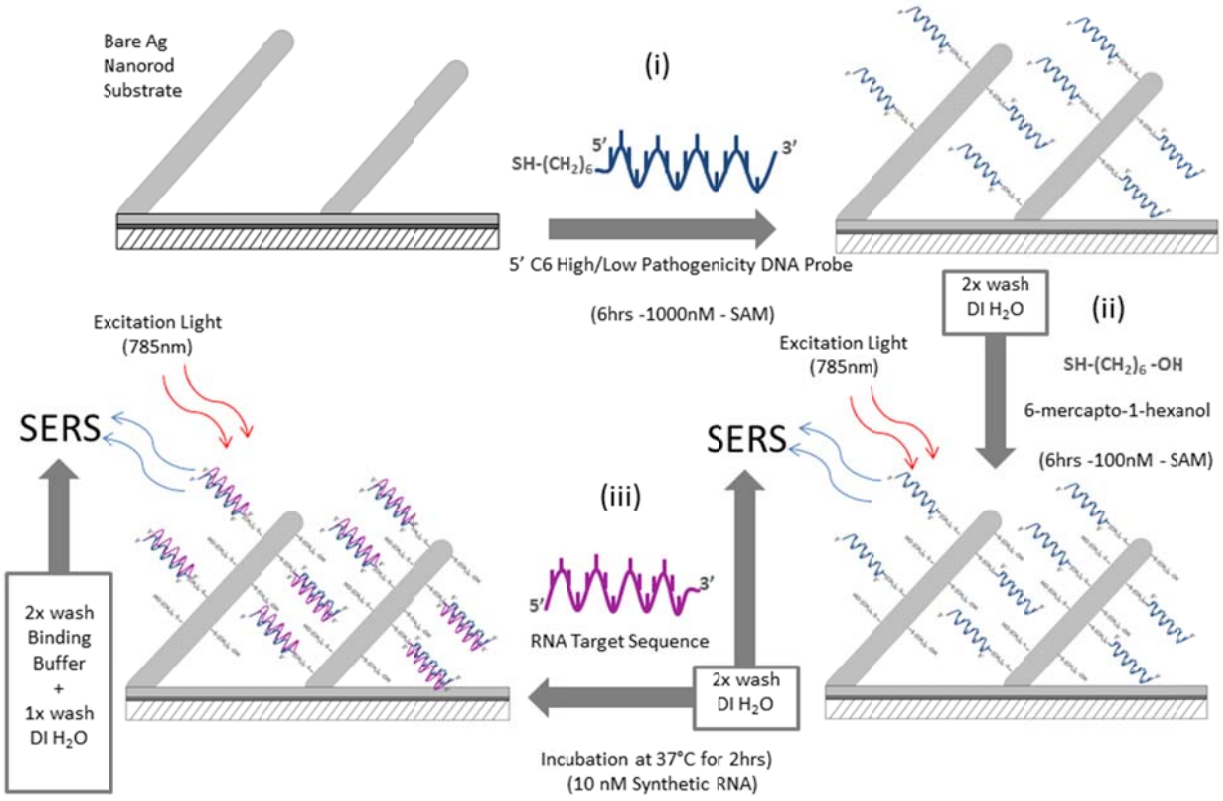

Figure 7.1. Schematic diagram of the overall strategy for DNA probe immobilization onto the Ag nanorod array, addition of the spacer molecule -mercapto-1-hexanol, and detection strategy. Immobilization of the thiolated DNA probe onto the surface of the Ag nanorod array (i), addition of -mercapto-1-hexanol as the spacer molecule (ii), and incubation with the RNA samples (iii).

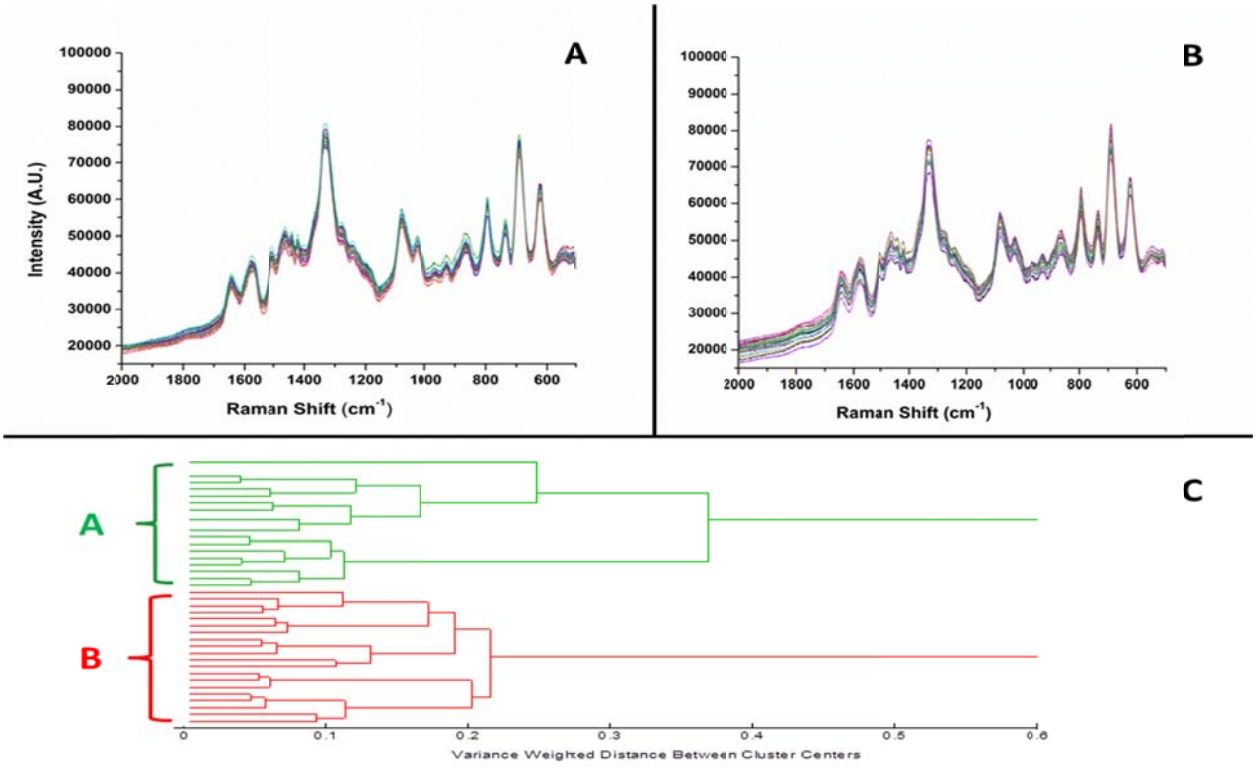

Figure 7.2. (A) Unprocessed SERS spectra of the high virulence DNA probe (1000 nM) – 6-mercapto-1-hexanol spacer (100 nM) complex on a Ag nanorod substrate, (B) low virulence DNA probe-spacer complex. Twenty individual spectra are overlaid in Figures 7.2.A and 7.2.B. Plots A and B show 20 individual SERS spectra collected on different wells on a substrate and on different substrates and demonstrate the degree of reproducibility of spectral data collection on the Ag nanorod substrates. (C) Dendrogram produced by hierarchical cluster analysis (HCA) of the SERS spectra shown in Figure 7.2.A and 7.2.B and label-coded as follows: (A) high virulence DNA probe-spacer complex shown in Figure 7.2A, (B) low virulence DNA probe-spacer complex shown in Figure 7.2.B, respectively.

acid bases appear as dominant features in the SERS spectrum of the DNA-spacer complexes shown in Figure 7.2.A and 7.2.B, for example, the 793 cm^{-1} combined ring breathing mode of C and T(423), whereas the band at 623 cm^{-1} is attributed to the ring bending mode of A and the ring breathing mode of G.(37) Another band at 1558 cm^{-1} is characteristic of a ring stretch of both A and G.(425) The bands at 1506 and 1631 cm^{-1} are assigned to the external phenyl ring stretching modes of A and G, respectively.(422) Finally, the band at 687 cm^{-1} is indicative of the C-S stretching vibration of the thiol group due to the adsorption and immobilization of the DNA probe to the Ag nanorod array.(425) The observed SERS bands in the spectra of the high and low virulence DNA probes-spacer complexes shown in Figure 7.2A and 7.2.B, with their assignments based on literature precedent, is provided in Table 7.3.

Chemometric Analysis of the DNA Probe Spectra

Multivariate statistical analysis was used to establish statistically significant differences between the SERS spectra shown in Figure 7.2.A and 7.2.B. Figure 7.2.C (bottom) illustrates the hierarchical cluster analysis (HCA) dendrogram based on the 40 SERS spectra shown in Figure 7.2A and 7.2.B. The oligonucleotide spectra were clustered based on Ward's linkage method for minimizing variance. The vertical bars in the dendrogram specify which samples and classes are linked, while the horizontal bars represent the distance between the linked classes. The dendrogram shown in Figure 7.2.C reveals two distinct clusters. The first red cluster (B) corresponds to the 20 SERS spectra of the low virulence DNA probe-spacer complex shown in Figure 7.2.B and the second cluster (A) corresponds to the 20 SERS spectra of the high virulence

Table 7.3. Observed SERS vibrational bands with assignments in the spectrum of the anti-influenza aptamer.

Wavenumber, cm^{-1}	Assignment
623	C-C-C ring in-plane bending of A
687	C-S stretching vibration of the thiolated aptamer
731	Ring breathing mode of A
793	Ring breathing mode of both C and T
1023	Amino group vibration of C
1045	Asymmetric out-of-plane deformation of NH_2 in C
1089	Backbone phosphate stretching mode of nucleic acids
1275	Ring stretching and C-H bending of T
1332	Ring stretching mode of A
1454	Ring breathing vibration of A
1496	C8=N7 vibration of the G ring
1506	External phenyl ring stretching of A
1558	Ring stretching mode of G and A
1631	External phenyl ring stretching of C

probe-spacer complex shown in Figure 7.2.A, respectively. The results provide evidence that HCA may differentiate the subtle spectral differences in the SERS spectra of two DNA probes that differ only by a single base pair polymorphism with 100% accuracy.

SERS Spectra of the DNA Probes-Synthetic RNA target Hybrids

Figure 7.3.A shows SERS spectra of the high virulence DNA probe-spacer complex alone (Figure 7.3.A (i)) incubated with the complementary high virulence synthetic RNA target sequence (Figure 7.3.A (ii)) and the non-complementary low virulence synthetic RNA sequence (Figure 7.3.A (iii)) at 37°C for 2 hours. The spectra in Figure 7.3.A show a high degree of similarity. This spectral resemblance is expected upon hybridization of the DNA probe to its complementary RNA target sequence since the target-probe hybrid is composed of the same four nucleotide components as the probe sequence. Therefore, the SERS spectra of the DNA probes before hybridization resemble those of the DNA probe-RNA target complexes after hybridization. However, subtle spectral changes are expected upon full hybridization of the DNA probe sequences complementary to the synthetic RNA target sequence due to their matching sequence. Likewise, incubation of the DNA probes with the non-complementary RNA sequence may result in minor spectral changes due to mismatched hybridization but overall, we expect to observe a distinct SERS signature for complementary DNA probe-RNA target hybrids when compared to the DNA probes alone or mismatched hybridization of the DNA probes with the non-complementary RNA sequence.

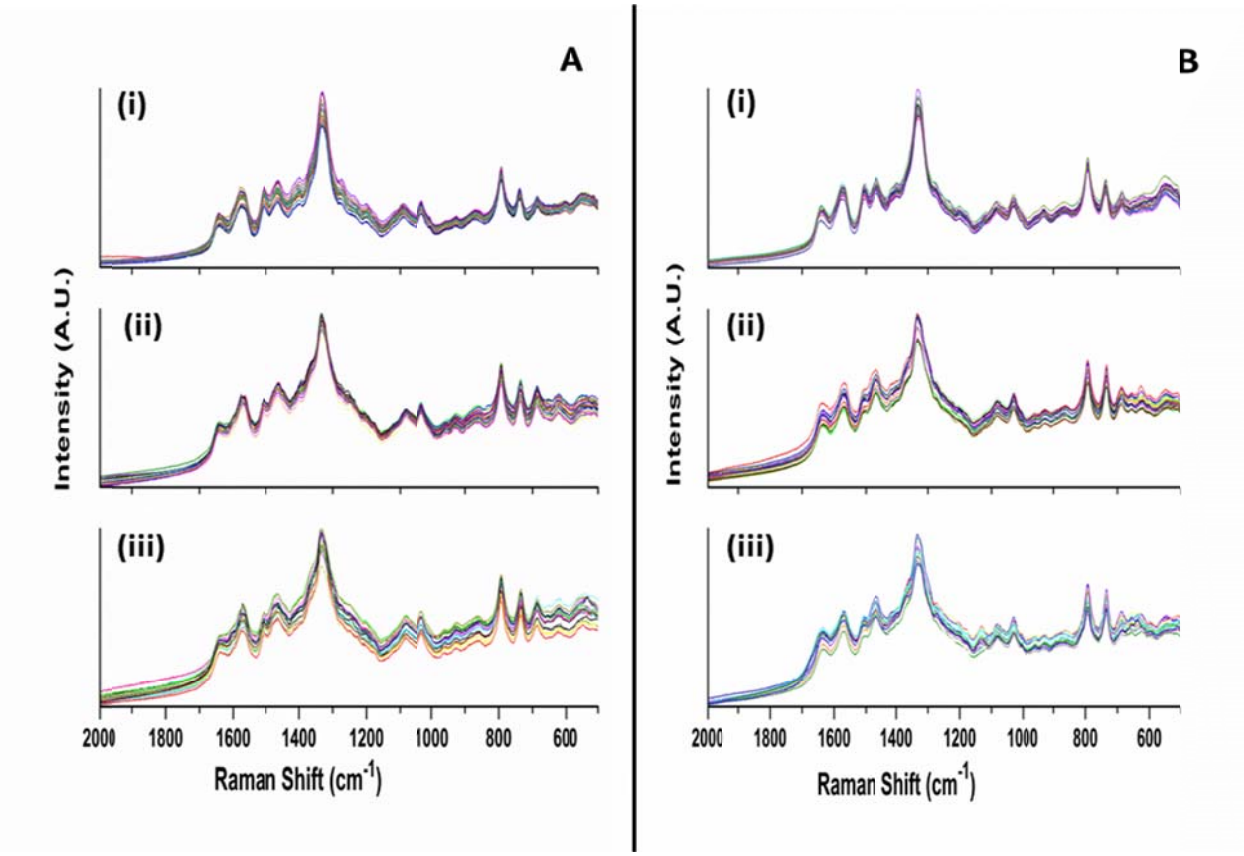

Figure 7.3. (A) Unprocessed SERS spectra of the high virulence DNA probe-spacer complex alone (i) incubated with the complementary high virulence synthetic RNA target sequence (ii) and the non-complementary low virulence synthetic RNA sequence (iii) at 37°C for 2 hours. (B) Unprocessed SERS spectra of the low virulence DNA probe-spacer complex alone (i) incubated with the complementary low virulence synthetic RNA target sequence (ii) and the non-complementary high virulence synthetic RNA sequence (iii) at 37°C for 2 hours. Each plot shows 20 individual SERS spectra collected on different wells on a substrate and on different substrates and demonstrate the degree of spectral similarity of the various classes of DNA probes-RNA samples.

Figure 7.3.B presents SERS spectra of the low virulence DNA probe-spacer complex alone (Figure 7.3.B (i)) incubated with the complementary low virulence synthetic RNA target sequence (Figure 7.3.B (ii)) and the non-complementary high virulence synthetic RNA sequence (Figure 7.3.B (iii)) at 37°C for 2 hours. The interpretation of the SERS spectra shown in Figure 7.3.B follows directly from the discussion of the spectra presented in Figure 7.3.A. The spectra are highly similar and present no apparent spectral differences visible to the eye. The high spectral similarity observed among the spectra shown in Figure 7.3 calls for the use of multivariate statistical methods to detect minor spectral differences among the SERS spectra and allow their differentiation based on intrinsic SERS signatures.

Chemometric Analysis of the DNA Probe-Synthetic RNA Target Complex Spectra

Figure 7.4 shows the HCA dendrogram generated using Ward's algorithm and computed from the SERS spectra of the DNA probe-synthetic RNA target complexes shown in Figure 7.3. One hundred and twenty spectra, corresponding to 20 spectra for each of the six sample categories pictured in Figure 7.3, were used to generate this dendrogram. As seen in Figure 7.4, the SERS spectra separated into two distinct clusters. The bottom cluster resulted from the spectra of the high (Figure 7.3.A (i)) and low virulence (Figure 7.3.A (i)) DNA probe-spacer complexes alone. HCA further successfully differentiated the spectra of the high virulence DNA probe-spacer complex (A) from the spectra of the low virulence DNA probe-spacer complex (B). The top cluster represents the spectra of the two DNA probes incubated with both the high (Figure 7.3.A (ii) and 7.3.B (iii)) and the low virulence (Figure 7.3.A (iii) and 7.3.B (ii)) RNA targets. As seen in the top cluster of the dendrogram, HCA was able to differentiate each of the four classes of

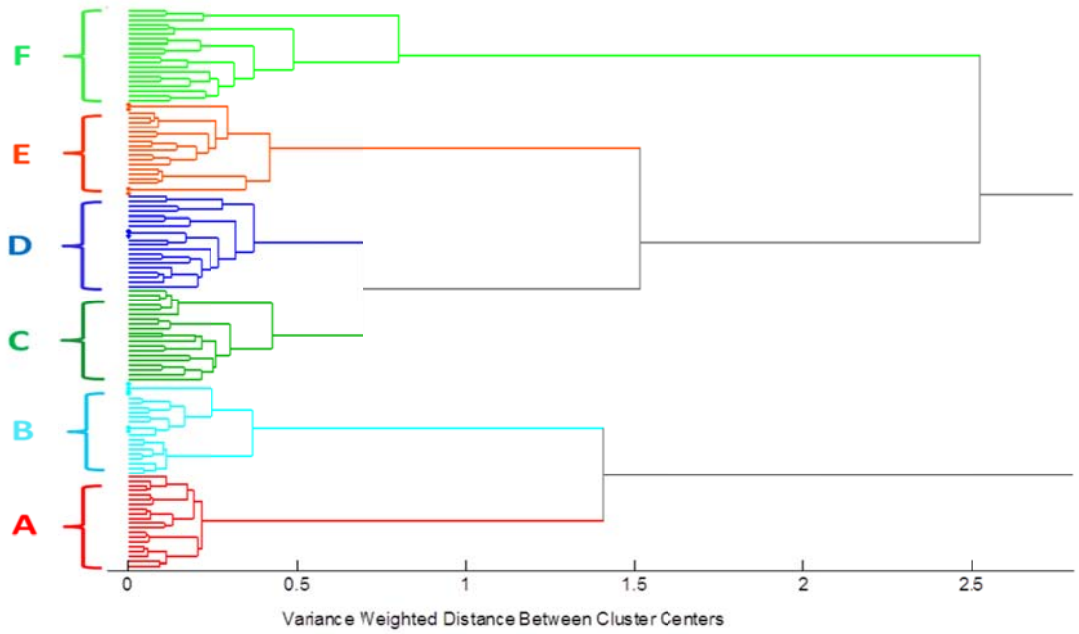

Figure 7.4. Dendrogram produced by hierarchical cluster analysis (HCA) of the SERS spectra shown in Figure 2 A (i), (ii), and (iii) and Figure 2 B (i), (ii), and (iii) and label-coded as follows: (A) SERS spectra of the high virulence DNA probe-spacer complex alone, (B) SERS spectra of the low virulence DNA probe-spacer complex alone, (C) SERS spectra of the high virulence DNA probe-spacer complex incubated with the complementary high virulence synthetic RNA target sequence, (D) SERS spectra of the low virulence DNA probe-spacer complex incubated with the complementary low virulence synthetic RNA target sequence, (E) SERS spectra of the high virulence DNA probe-spacer complex incubated with the non-complementary low virulence synthetic RNA target sequence, and (F) SERS spectra of the low virulence DNA probe-spacer complex incubated with the non-complementary high virulence synthetic RNA target sequence. A total of 120 spectra were used to generate this dendrogram, corresponding to 20 spectra in each of the 6 DNA probes-RNA samples categories.

complexes. The SERS spectra of the high virulence DNA probe incubated with its complementary RNA target (D) and non-complementary RNA (E), as well as the low virulence DNA probe incubated with its complementary RNA target (D) and non-complementary RNA (F) were respectively differentiated from the other classes and separated in their own sub-cluster. These results demonstrate that cluster analysis allows statistical differentiation of the two DNA probe-spacer complexes only in one cluster and the two DNA probes incubated with their complementary and non-complementary RNA targets in a separate cluster. In particular, each of the six classes was classified in its own sub-cluster, showing the accuracy and robustness of the HCA classification model for differentiation of highly similar SERS spectra of DNA probes and hybridized probe-target complexes.

Sensitivity and Limit of Detection of Synthetic RNA Target Sequences Binding to Complementary DNA Probes

The binding sensitivity of the assay was further investigated by incubating the oligonucleotide-modified SERS substrates with varying concentrations of the complementary RNA target sequences. Following immobilization of the DNA probe-spacer complex on the surface of the Ag nanorods, incubation of the complementary RNA target sequences was accomplished using the aforementioned procedures. Ten SERS spectra from eight serial ten-fold dilutions (1000 nM to 1 pM) of complementary RNAwere acquired for each concentration and loaded into a PLS regression model to assess the sensitivity of the SERS-based hybridization assay. PLS regression is a recent technique that generalizes and combines features from Principal Components Analysis and multiple regression.(421) This technique has been widely used to predict a set of dependent

variables from a large set of independent variables. Figure 7.5 shows the PLS regression curve for both the high virulence (Figure 7.5.A) and the low virulence (Figure 7.5.B) assays, respectively. Each plot was generated using a total of 80 spectra (10 for each the 8 complementary RNA concentrations) and 4 latent variables. The PLS regression plots reveal a correlation between the predicted complimentary RNA concentration for cross-validated samples versus the true measured complimentary RNA concentration based on intrinsic SERS spectra. As is evident, the PLS predicted model for the binding of synthetic RNA target sequences to immobilized complementary DNA probes is accurate for concentration ≥10 nM of complementary RNA for both assays. The plots positively deviate from the green predicted line at concentrations lower than 10 nM, meaning that the PLS regression model may no longer quantify hybridization of the DNA probes for concentrations of complementary RNA target sequences lower than this value. As a result, the SERS spectra represented by the data points on the PLS plots are falling off the green RNA predicted concentration line and merging along the red line representing the true measured RNA concentration resulting from each concentration of the serial dilution assay for concentrations lower than 10 nM. This observation is consistent for both the high virulence (Figure 7.5.A) and the low virulent (Figure 7.5.B) assays.

Detection of Fluorescently Tagged RNA Target Sequences Binding to DNA Probes by ELISA

Enzyme-linked immunosorbent assay (ELISA) was used to detect the binding affinity of immobilized DNA probes to fluorescently labeled RNA target sequences. ELISA is one of the most widely used diagnostic tools for serological detection and is commonly employed to

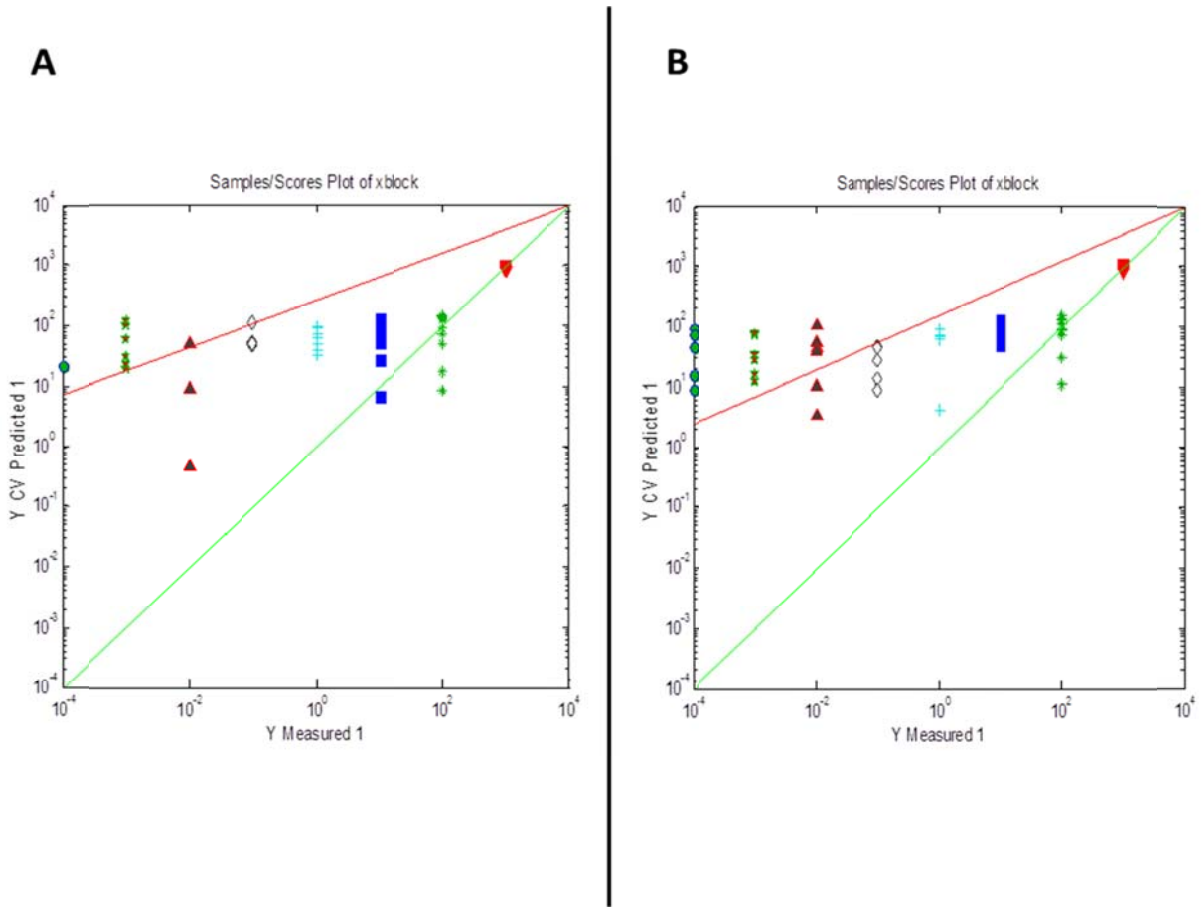

Figure 7.5. PLS regression analysis of serial dilutions of complementary RNA target sequence for (A) high and (B) low virulence assays, respectively. Serial 10-fold dilutions of complementary RNA target sequences (1000 nM to 1 pM) incubated with the DNA probe-spacer complex at 37°C for 2 hours were assessed by PLS regression for degree linearity in actual intensity of the measured spectra plotted against the predicted intensity. In both plots, the green line represents the RNA predicted concentration and the red line represents the true measured RNA concentration.

provide qualitative and quantitative information on the binding affinity and specificity of an analyte to its specific target. ELISA has previously been used to detect antibody against avian influenza viruses.(381) The high and low virulence thiolated DNA probes were immobilized on the surface of the maleimide activated black 96-well plates via formation of stable thioether bonds. Following functionalization of the plate wells, the fluorescently labeled synthetic RNA target sequences corresponding to minimal mitochondrial targeting sequence of the PB1-F2 protein with and without the mutation at position 66 were added to the oligonucleotide-modified wells at 37°C for 2 hours at various concentrations. The plate wells were then rinsed with copious amount of the binding buffer and read on a microplate reader. Full details on the DNA probes immobilization, RNA target sequences incubation, and fluorescent measurements are provided in section 7.2 of this Chapter. Figure 7.6 shows the plots of the fluorescent intensity for the high (Figure 7.6.A) and low (Figure 7.6.B) virulence assays recorded on the 96-well plates as a function of RNA concentration. As expected, the fluorescent intensity increases with increasing concentration of complementary RNA with the same order of magnitude for both the high and low virulence assays. Both plots display a steady, quasi-linear increase in fluorescent intensity over a concentration range of 10-1000 nM of complementary RNA target sequences (black plots). Conversely, the fluorescent intensity is constant when the oligonucleotide-modified wells are incubated with non-complementary RNA sequences that differ only by a single base pair polymorphism (red plots). The fluorescent intensity for non-complementary RNA sequences remains at a baseline level even for high concentration of non-complementary RNA, suggesting that binding of DNA probes to RNA sequences only occurs for complementary sequences. From this observation, the limit of detection of the ELISA assay was determined by subtracting the

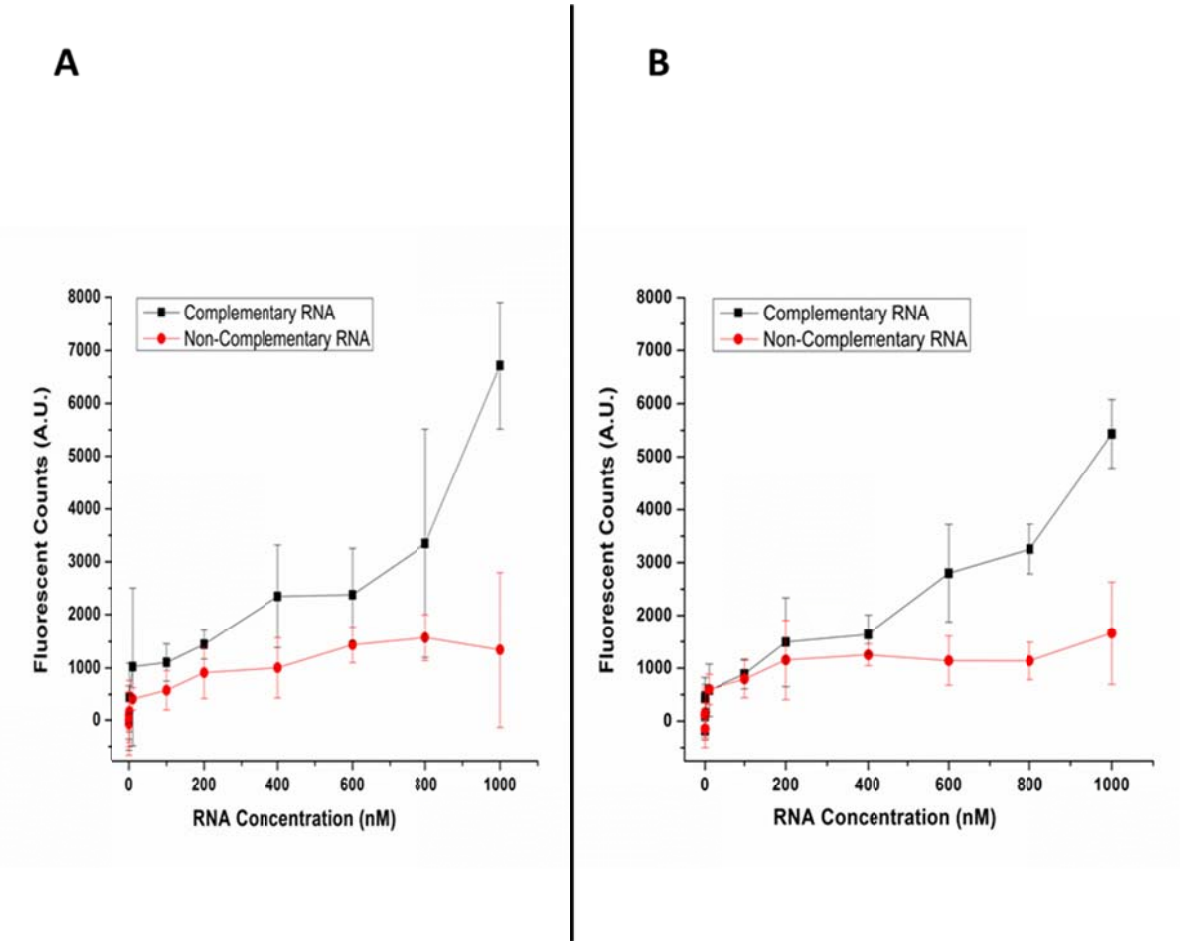

Figure 7.6. Fluorescent intensity recorded from oligonucleotide-modified 96-well plates incubated with the complementary and non-complementary fluorescent RNA target sequences at 37°C for 2 hours for the high (A) and low (B) virulence assays. Each data point is an average of 8 measurements recorded on four different plates. Error bars represent the standard deviation of measurements.

baseline level recorded from the non-complementary RNA signal to the fluorescent intensities generated by each of the complementary RNA concentration. The lowest complementary RNA concentration for which the intensity value is positive after subtraction is 100 nM, meaning that concentrations of complementary RNA lower than this value may not be detected by ELISA. The plots shown in Figure 7.6 support this statement for both the high and low virulence assays.

Hybridization of Viral RNA Samples to Complementary DNA Probes

The previous sections have established the proof of principle that oligonucleotide-modified Ag nanorod arrays may serve as a detection platform for artificial RNA sequences in a label free fashion. We further investigated the robustness of this biosensing platform by detecting the binding affinity of the DNA-functionalized SERS substrates to full viral RNA samples extracted and purified from whole H5N1 influenza virus strains with and without the PB1-F2 gene mutation as described in section 7.2 of this Chapter.

Incubation of the full viral RNA samples to the oligonucleotide-modified Ag nanorod arrays was accomplished in the same manner as the synthetic RNA target sequences. In this experiment, the high and low virulence DNA probes were immobilized onto the Ag nanorod array substrates via the thiolate group, followed by addition of the spacer molecule, and incubated with (i) the binding buffer, (ii) the high synthetic RNA target sequence, and (iii) the low virulence synthetic RNA target sequence, (iv) three high virulence viral RNA strains (WH N66S, A/Mute Swan/MS451072/06, and A/CK/TX/167280-04/02), two low virulence viral RNA strains (WH and A/CK/PA/13609/93), and (v) a negative control viral RNA sample from an influenza strain

not containing the gene coding for the PB1-F2 protein (WH Δ PB1-F2). Twenty spectra were acquired for each combination of DNA probe-viral RNA samples and used for analysis (data not shown). The interpretation of the SERS spectra of the DNA probe-viral RNA hybrids follows directly from the discussion of the DNA probe-synthetic RNA target complexes in Figure 7.3. The SERS spectra of the DNA probes incubated with complementary viral RNA samples share a high degree of similarity with the SERS spectra of the DNA probes incubated with non-complementary viral RNA samples. However, upon hybridization of the DNA probes with the 33 complementary base pairs in the sequence of the full viral RNA, we expect subtle spectral changes similar to those observed for the binding of DNA probes to complementary synthetic RNA target sequences. These observations suggest the use of a supervised, multivariate classification method to identify the spectral contributions of the SERS signature of complementary DNA probe-viral RNA hybrids from those of the DNA probes incubated with non-complementary viral RNA samples.

Chemometric Analysis of the DNA Probe-Viral RNA Target Complex SERS Spectra

Partial Least Squares Discriminant Analysis (PLS-DA) was used to establish statistically significant differences between the SERS spectra of complementary DNA-probe-viral RNA hybrids and the spectra of the DNA probes incubated with non-complementary viral RNA samples with a sequence mismatch of a single base pair. PLS-DA is a multivariate, full-spectrum calibration technique that establishes the best fundamental relations between a descriptor matrix, i.e., SERS spectra, and a class matrix, i.e., sample identities.(419) As a supervised classification

method, PLS-DA employs latent variables (LVs) in combination with *a priori* knowledge of the sample classes to build a classification model and to establish class predictions for the SERS spectra in the dataset.(467) LV's are generated by the model to maximize the variance of spectral features among different classes while minimizing the variance of spectral features within each given class.(468) In PLS-DA, the response vector Y is qualitative and is recorded as a dummy block matrix where each of the response categories is coded via an indicator factor (either 0 or 1). This method provides a categorical response variable that is used to classify and discriminate sample classes based on intrinsic SERS spectra.

Twenty SERS spectra were collected from two substrates for each combination of DNA probe-RNA target sequence for both the high and the low virulence DNA probes as described above. The spectra were pre-processed as described in section 7.2 of this Chapter. For analysis, each dataset was further split into a training (calibration) and a prediction (validation) dataset to build a classification model and determine whether the SERS spectra of complementary DNA probe-viral RNA hybrids could be differentiate from those of the DNA probes incubated with non-complementary viral RNA samples. The training (calibration) datasets consisted of the SERS spectra of (i) DNA probe-spacer complex alone, DNA probe-spacer complex incubated with (ii) the binding buffer, (iii) the high virulence synthetic RNA sequence, and (iv) the low virulence synthetic RNA sequence. The prediction (validation) datasets consisted of the SERS spectra of DNA-probe-spacer complex incubated with full viral RNA strains (v) WH N66S, (vi) A/CK/TX/167280-04/02, (vii) A/Mute Swan/MS451072/06, (viii) WH, (ix) A/CK/PA/13609/93, and (x) WH Δ PB1-F2. Each spectrum in the training dataset was assigned a class rank (1 to 4)

according to sample identity while all the spectra in the prediction dataset were assigned a class rank of 0 for the purpose of being tested as unknown samples by the PLS-DA classification model. The sample classes corresponding to the SERS spectra of complementary DNA probe-RNA hybrids were assigned a value of 1 in the response vector Y while the remaining sample classes were assigned a value of 0. In the current case, sample classes assigned a value of 1 correspond to samples that are expected to fully hybridize (DNA probes incubated with complementary RNA target sequences) whereas other sample classes assigned a value of 0 correspond to samples that are expected to either not fully hybridize (DNA probes incubated with non-complementary RNA samples) or not hybridize at all (DNA only or DNA incubated with blank buffer). This binary numerical discrimination is used in PLS-DA to effectively build the classification model using the spectra of the training dataset having a non-zero class rank as reference spectra and test the remaining spectra making up the validation dataset with a class rank value of 0 as unknown spectra to assess their classification accuracy. The PLS-DA model was built using cross-validation (Leave One Out, 10 splits) which allows the SERS spectra making up the validation test to be tested iteratively, for a total of 10 iterations, until each sample is withheld from the model and tested as an unknown.

Figure 7.7 shows the cross-validated predictions plots for each of the collected spectrum for both the high virulence (Figure 7.7.A) and the low virulence (Figure 7.7.B) assays, respectively. In Figure 7.7, each data point is representative of a single SERS spectrum. The first 80 colored data points in each plot are representative of the training dataset and correspond to the SERS spectra of: (i) represented by the red triangles, (ii) represented by the green stars, (iii) represented by the

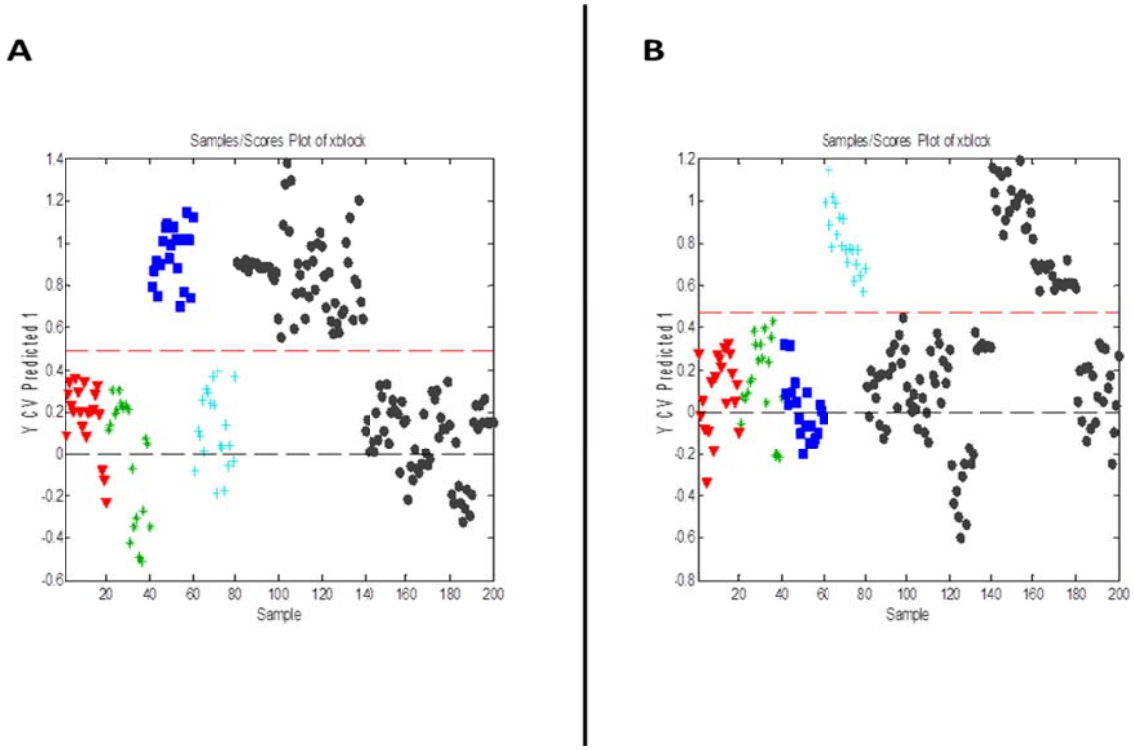

Figure 7.7. PLS-DA cross-validated prediction plots for (A) high and (B) low virulence assays, respectively. Each data point is representative of a single SERS spectrum. The colored signs are representative of the SERS spectra of the DNA probe-spacer complex (▼) incubated at 37°C for 2 hours with the binding buffer (★), the complementary synthetic RNA target sequence (■), the non-complementary synthetic RNA sample (+). The solid black dots are representative of the SERS spectra of the DNA probe-spacer complex incubated at 37°C for 2 hours with full viral RNA strains WH N66S (samples 80-100), A/CK/TX/167280-04/02 (samples 100-120), A/Mute Swan/MS451072/06 (samples 120-140), WH (samples 140-160), A/CK/PA/13609/93 (samples 160-180), and WH Δ PB1-F2 (samples 180-200). Two hundred spectra, corresponding to 20 spectra in each sample category, are represented in each plot.

blue squares, and (iv) represented by the turquoise crosses. The solid black dots are representative of the validation dataset and correspond to the SERS spectra of DNA-probe-spacer complex incubated with full viral RNA strains (v), (vi), (vii), (viii), (iv), and (x) as listed in order above. The PLS-DA model generated an optimum threshold value of prediction for sample classification that is represented in Figure 7.7.A and 7.7.B by the red dashed line. SERS spectra with predicted Y values greater than the threshold value are classified as fully hybridized complexes while those with Y predicted values lower than the threshold value are classified as not fully hybridized complexes or not hybridized at all. Five latent variables were used in both Figure7.7.A and 7.7.B to minimize classification error of the cross-validated samples. The threshold values calculated for the high and low virulence classification models are 0.49 in Figure 7.7.A and 0.47 in Figure 7.7.B, respectively.

As seen in Figure 7.7.A, the spectra of the high virulence DNA probe-spacer complex incubated with the high virulence synthetic RNA target sequence represented by the blue squares classified above the threshold line along with the spectra of the high virulence DNA probe-spacer complex incubated with the three full viral RNA samples containing the N66S mutation associated with high virulence (WH N66S, A/CK/TX/167280-04/02, and A/Mute Swan/MS451072/06). All the data points that classified above the threshold line by the PLS-DA model in Figure 7.7.A represent SERS spectra of high virulence complementary DNA- RNA hybrids that fully hybridized.

Likewise, the plot in Figure 7.7.B shows that the spectra of the low virulence DNA probe-spacer complex incubated with the low virulence synthetic RNA target sequence represented by the turquoise crosses classified above the threshold line along with the spectra of the low virulence DNA probe-spacer complex incubated with the two full viral RNA samples not containing the N66S mutation and considered as low virulence strains (A/Mute Swan/MS451072/06 and WH, (ix) A/CK/PA/13609/93). In both cases, the PLS-DA model correctly identified all the solid black dots as SERS spectra of high (Figure 7.7.A) and low (Figure 7.7.B) virulence DNA that fully hybridized to complementary viral RNA target sequences as a result of the 33 base pairs match. In contrast, the solid black dots that classified below the threshold line in Figure 7.7.A all have predicted values that are excluded from this class of sample and represent SERS spectra of high virulence DNA probes incubated with non-complementary viral RNA samples that did not hybridize. In the same manner, the solid black dots below the threshold line in Figure 7.7.B represent SERS spectra of low virulence DNA probes that did not hybridize to non-complementary viral RNA samples. It is worth noticing that in both Figure 7.7.A and 7.7.B, the SERs spectra of DNA probes incubated with the negative control viral RNA strain not containing the gene coding for the PB1-F2 protein (WH Δ PB1-F2) classified as non-hybridized samples in both assays, confirming the robustness of the PLS-DA model in classification accuracy. The main conclusion from Figure 7.7.A and 7.7.B is that PLS-DA may correctly identify and classify spectra of complementary DNA-viral RNA hybrids from spectra of non-complementary DNA-viral RNA samples. The results indicate that the PLS-DA model was able to correctly classify each spectrum in its class with 100% accuracy for both the high and low virulence assays.

7.4. Conclusions

A rapid, label-free, SERS-based assay consisting of an array of oligonucleotides immobilized on the surface of a Ag nanorod substrate was used to allow detection of various influenza RNA strains containing a gene mutation coding for the PB1-F2 protein associated with high virulence. In these studies, we demonstrate that SERS provides a label-free optical method to detect the hybridization of the surface immobilized DNA probes to their complementary RNA sequence targets without amplification. Statistical analysis of the data confirmed that the intrinsic SERS spectra were able to differentiate DNA probe-RNA target hybrids from DNA probes incubated with non-complementary RNA sequences. This was demonstrated using synthetic RNA sequences as well as five full viral RNA samples extracted and purified from whole H5N1 influenza virus strains with and without the PB1-F2 gene mutation. In both cases, PLS-DA confirmed statistically significant differences between the spectra of the DNA probes hybridized with the complementary viral RNA sequence targets containing the point mutation from those of the same DNA probes incubated with viral RNA sequences not containing the point mutation. ELISA supported these results and reinforced evidence that DNA probes only hybridize to complementary RNA target sequences. The results of these studies show that recent advances in SERS-based diagnostic provide a new clinical tool to accurately define virulence potential for early detection of the genetic markers in influenza A viruses associated with pathogenicity. The development of this rapid and sensitive method for screening highly pathogenic influenza virulence factors would significantly improve the ability to identify emerging strains with a risk of high mortality, and allow public health professionals to effectively respond to prevent widespread infection and/or death.

CHAPTER 8

Conclusions

The goals of this work involved the fabrication of Ag nanorod arrays as SERS-active substrates for use in detection of oligonucleotide complexes of influenza. Fabrication of Ag nanorod array SERS substrates was accomplished by oblique angle vapor deposition (OAD) using a custom-built electron-beam/sputtering evaporation system. Meticulous control of the evaporation settings resulted in fabrication of SERS-active substrates with nominal variability in morphology and SERS performance from substrate to substrate and batch to batch. Post fabrication, cleaning of substrate was accomplished by exposing the Ag nanorod arrays to an ionized argon plasma for 4 minutes to remove the presence of carbonaceous and organic contamination. Patterning of the substrates using a PDMS mold provided an increase in the number of assays performed from a single batch of substrates. Using this method, the variability in SERS response was reduced to 6% across a single substrate, 25% down a substrate, 15% from substrate to substrate and 8% from batch to batch.

Ag nanorod arrays were used for the label-free detection of viral nucleoprotein binding to a polyvalent anti-influenza aptamer by monitoring the SERS spectra of the aptamer-nucleoprotein complex. The SERS spectra demonstrated that selective binding of the aptamer-nucleoprotein complex could be differentiated from that of the aptamer alone based solely on the direct spectral signature for the aptamer-nucleoprotein complex. Multivariate statistical methods, including

Principal Components analysis, hierarchical clustering, and partial least squares, were used to confirm statistically significant differences between the spectra of the aptamer-nucleoprotein complex and the spectra of the unbound aptamer. Two separate negative controls were used to evaluate the specificity of binding of the viral nucleoproteins to this aptamer. In both cases, no spectral changes were observed that showed protein binding to the control surfaces, indicating a high degree of specificity for the binding of influenza viral nucleoproteins only to the influenza-specific aptamer. Statistical analysis of the spectra supported this interpretation. AFM images demonstrated morphological changes consistent with formation of the influenza aptamer-nucleoprotein complex. These results provide the first evidence for the use of aptamer-modified SERS substrates as diagnostic tools for influenza virus detection in a complex biological matrix.

Further studies related to this work include the development of a rapid, sensitive, and specific multiplexed SERS-based assay allowing detection, identification, and assessment of virulence factors associated with pathogenesis in influenza A virus. The assay consists of an oligonucleotide-based array immobilized on the surface of a SERS-active substrate that allows detection of various influenza RNA strains containing a gene mutation coding for the PB1-F2 protein associated with high virulence. Hybridization of the DNA probes to their complementary RNA sequences was probed using surface-enhanced Raman spectroscopy (SERS) and accomplished without amplification or labeling. The spectral signature due to their highly selective interaction was differentiated from that of the immobilized DNA probes alone or the DNA probes incubated with non-complementary RNA sequences based on their intrinsic SERS spectra. Multivariate statistical methods were employed to differentiate the spectra of the

complementary DNA probe-RNA target hybrid from those of the DNA probes incubated with non-complementary sequences. This approach has the potential to provide scientific foundation for the development of new screening methods critically needed for risk assessment in human influenza infections. The results demonstrate that bio-nanotechnology combined with vibrational spectroscopy has the ability to enhance both detection and diagnosis of emerging viral infections while allowing point-of-care testing in clinical applications to rapidly determine disease risk and the appropriate course of action to reduce its spread.

These studies suggested that oligonucleotide-modified Ag nanorod arrays may be used as a SERS diagnostic platform for the rapid identification of diagnostic indicators of disease severity and facilitate rapid implementation of disease intervention strategies. This approach has the potential to provide scientific foundation for the development of new screening methods critically needed for risk assessment in human influenza infections. These findings demonstrate that bio-nanotechnology combined with vibrational spectroscopy has the ability to enhance both detection and diagnosis of emerging viral infections while allowing point-of-care testing in clinical applications to rapidly determine disease risk and the appropriate course of action to reduce its spread.

REFERENCES:

1. Raman CV, Krishnan KS. A New Type of Secondary Radiation. Nature. 1928;121(3048):501-2.
2. Chalmers JM, Griffiths PR. Handbook of Vibrational Spectroscopy. Griffiths JMCaPR, editor: Wiley & Sons; 2002. 71-87 p.
3. Ingle JD, Crouch SR. Spectrochemical Analysis. New Jersey: Prentice Hall: Englewood Cliffs; 1988.
4. Lewis IR, Edwards HGM. Handbook of Raman Spectroscopy: From the Research Laboratory to the Process Line. Ann Arbor, Michigan: H. G. M. Edwards; 2001.
5. McCreery RL. Raman Spectroscopy for Chemical Analysis. New York: Wiley and Sons; 2000.
6. Herzberg G. Molecular Spectra and Molecular Structure: Van Nostrand Reinhold Company; 1945.
7. G. P, E. T. Die Rotationsstruktur der Ramanbanden mehratomiger Molekule. Z Phys. 1933;81:209-58.
8. Brodersen S, Richardson EH. The Raman Spectrum of Gaseous Allene. J Mol Spectrosc. 1960;4(5):439-45. doi: Doi 10.1016/0022-2852(60)90105-3. PubMed PMID: WOS:A1960XD22700007.
9. Claassen HH. Raman Spectra of Chlorofluoromethanes in the Gaseous State. J Chem Phys. 1954;22(1):50-2. PubMed PMID: WOS:A1954UC15500011.
10. Gullikson CW, Nielsen JR. Raman Spectrum of Gaseous Trifluoroacetonitrile. J Mol Spectrosc. 1957;1(2):155-7. doi: Doi 10.1016/0022-2852(57)90019-X. PubMed PMID: WOS:A1957XD20800008.
11. Gullikson CW, Nielsen JR, Stair AT. Raman Spectrum of Sulfur Hexafluoride in the Gaseous and Solid States. J Mol Spectrosc. 1957;1(2):151-4. doi: Doi 10.1016/0022-2852(57)90018-8. PubMed PMID: WOS:A1957XD20800007.
12. Matterson AHS, Woodward LA. Relative Intensities of Totally Symmetrical Vibrations in the Raman Spectrum of Gaseous Neopentane. Proc R Soc Lon Ser-A. 1955;231(1187):514-21. doi: DOI 10.1098/rspa.1955.0192. PubMed PMID: WOS:A1955WU25400008.
13. Nakagawa I, Mizushima SI. The Assignments of the Raman and Infrared Frequencies of 1,2-Dichloroethane Observed in the Gaseous, Liquid, and Solid States. J Chem Phys. 1953;21(12):2195-8. doi: Doi 10.1063/1.1698809. PubMed PMID: WOS:A1953UC11800017.
14. Nielsen JR, Albright JC. Raman Spectrum of Gaseous 1-Fluoro-1-Chloroethylene. J Chem Phys. 1957;26(6):1566-7. doi: Doi 10.1063/1.1743582. PubMed PMID: WOS:A1957WA16900037.
15. Richards CM, Nielsen JR. Raman Spectra of Cis-2 and Trans-2-Butene and 1,3-Butadiene in the Gaseous and Liquid States. J Opt Soc Am. 1950;40(4):255-. PubMed PMID: WOS:A1950UG39800021.
16. Taylor RC, Vidale GL. Raman Spectrum and Vibrational Assignments of Gaseous Dimethyl Ether. J Chem Phys. 1957;26(1):122-3. doi: Doi 10.1063/1.1743235. PubMed PMID: WOS:A1957WA16400019.

17. Coates J. Vibrational spectroscopy: Instrumentation for infrared and Raman spectroscopy (Reprinted from Analytical Instrumentation Handbook, 1997). Appl Spectrosc Rev. 1998;33(4):267-425. doi: Doi 10.1080/05704929808002060. PubMed PMID: WOS:000077608800001.
18. Biswas SC. Raman Spectra of Liquid and Gaseous CH4. Philosophical Magazine. 1932;13((84)):455-8.
19. Braune H, Engelbrecht. On the Raman-Effect of Some Ionorganic Halogenides in the Liquid and Gaseous State. Zeitschrift Fur Physikalische Chemie-Abteilung B-Chemie Der Elementarprozesse Aufbau Der Materie. 1932;19((5)):303-13.
20. Weber A, Mcginnis EA. The Raman Spectrum of Gaseous Oxygen. J Mol Spectrosc. 1960;4(3):195-200. doi: Doi 10.1016/0022-2852(60)90081-3. PubMed PMID: WOS:A1960XD22500001.
21. Imanishi S. Raman Spectrum of Gaseous Carbon Dioxide. Nat Med. 1935;135:396-.
22. Adel A. The Raman Spectrum of Gaseous Carbon Dioxide. Physical Review. 1933;44((8)):0691-.
23. Smith JSK, Bonner LG. The Raman Spectra of Gaseous Substrates: I Apparatus and the Spectrum of Methylamine. J Chem Phys. 1939;7((10)):880-3.
24. Lord RC, Yu NT. Laser-Excited Raman Spectroscopy of Biomolecules .1. Native Lysozyme and Its Constituent Amino Acids. J Mol Biol. 1970;50(2):509-&. doi: Doi 10.1016/0022-2836(70)90208-1. PubMed PMID: WOS:A1970G577300023.
25. Delhaye M, Dhamelincourt P. Raman Microprobe and Microscope with Laser Excitation. J Raman Spectrosc. 1975;3(1):33-43. doi: DOI 10.1002/jrs.1250030105. PubMed PMID: WOS:A1975AA63800004.
26. Degrazia H, Brown D, Cheung S, Wartell RM. Solution Conformations of Dnas Containing Binding-Sites of the Catabolite Gene Activator Protein and Lac Repressor Protein - Characterization by Raman-Spectroscopy. Biochemistry-Us. 1988;27(17):6359-65. doi: Doi 10.1021/Bi00417a025. PubMed PMID: WOS:A1988P882100025.
27. Degrazia H, Harman J, Wartell RM. Investigation of Camp Receptor Protein Secondary Structure by Raman-Spectroscopy. Biophysical Journal. 1990;57(2):A67-A. PubMed PMID: WOS:A1990CN42800225.
28. Goodwin DC, Brahms J. Form of DNA and Nature of Interactions with Proteins in Chromatin. Nucleic Acids Res. 1978;5(3):835-50. doi: Doi 10.1093/Nar/5.3.835. PubMed PMID: WOS:A1978ER60500016.
29. Mansy S, Engstrom SK, Peticolas WL. Laser Raman Identification of an Interaction Site on DNA for Arginine Containing Histones in Chromatin. Biochem Bioph Res Co. 1976;68(4):1242-7. doi: Doi 10.1016/0006-291x(76)90330-2. PubMed PMID: WOS:A1976BL28900031.
30. Martin JC, Wartell RM, Oshea DC. Conformational Features of Distamycin-DNA and Netropsin-DNA Complexes by Raman-Spectroscopy. P Natl Acad Sci USA. 1978;75(11):5483-7. doi: DOI 10.1073/pnas.75.11.5483. PubMed PMID: WOS:A1978FY61700053.
31. Tan GS, Kelly P, Kim J, Wartell RM. Comparison of Camp Receptor Protein (Crp) and a Camp-Independent Form of Crp by Raman-Spectroscopy and DNA-Binding. Biochemistry-Us.

1991;30(20):5076-80. doi: Doi 10.1021/Bi00234a034. PubMed PMID: WOS:A1991FM71200034.
32. Zuo ET, Tanious FA, Wilson WD, Zon G, Tan GS, Wartell RM. Effect of Base-Pair Sequence on the Conformations and Thermally Induced Transitions in Oligodeoxyribonucleotides Containing Only at Base-Pairs. Biochemistry-Us. 1990;29(18):4446-56. doi: Doi 10.1021/Bi00470a027. PubMed PMID: WOS:A1990DC56900027.
33. Wang AHJ, Quigley GJ, Kolpak FJ, Crawford JL, Vanboom JH, Vandermarel G, et al. Molecular-Structure of a Left-Handed Double Helical DNA Fragment at Atomic Resolution. Nature. 1979;282(5740):680-6. doi: Doi 10.1038/282680a0. PubMed PMID: WOS:A1979HX29200025.
34. Wing R, Drew H, Takano T, Broka C, Tanaka S, Itakura K, et al. Crystal-Structure Analysis of a Complete Turn of B-DNA. Nature. 1980;287(5784):755-8. doi: Doi 10.1038/287755a0. PubMed PMID: WOS:A1980KM41100049.
35. Benevides JM, Wang AHJ, Rich A, Kyogoku Y, Vandermarel GA, Vanboom JH, et al. Raman Spectral Studies of Nucleic-Acids .30. Raman-Spectra of Single-Crystals of R(Gcg)D(Cgc) and D(Ccccgggg) as Models for a-DNA, Their Structure Transitions in Aqueous-Solution, and Comparison with Double-Helical Poly(Dg).Poly(Dc). Biochemistry-Us. 1986;25(1):41-50. doi: Doi 10.1021/Bi00349a007. PubMed PMID: WOS:A1986AYU2800007.
36. Erfurth SC, Kiser EJ, Peticolas WL. Determination of the backbone structure of nucleic acids and nucleic acid oligomers by laser Raman scattering. Proc Natl Acad Sci U S A. 1972;69(4):938-41. PubMed PMID: 4502943; PubMed Central PMCID: PMC426599.
37. Otto C, Vandentweel TJJ, Demul FFM, Greve J. Surface-Enhanced Raman-Spectroscopy of DNA Bases. J Raman Spectrosc. 1986;17(3):289-98. PubMed PMID: ISI:A1986C822400010.
38. Biscar JP, Burczyk RF, Kollias N. Emer-Raman Analysis of DNA Base Conformation. B Am Phys Soc. 1974;19(3):264-. PubMed PMID: WOS:A1974S164700449.
39. Brown DM, Wartell RM. Raman-Spectroscopic Studies of Ribonuclease a Bound to D(Pa)4 in Solution. Biophysical Journal. 1986;49(2):A525-A. PubMed PMID: WOS:A1986A176801484.
40. Lu KC, Prohofsky EW, Vanzandt LL. Vibrational Modes of a-DNA, B-DNA, and a-Rna Backbones - Application of a Green-Function Refinement Procedure. Biopolymers. 1977;16(11):2491-506. doi: DOI 10.1002/bip.1977.360161112. PubMed PMID: WOS:A1977EC62800011.
41. Small EW, Peticola.Wl. Conformational Dependence of Raman Scattering Intensities from Polynucleotides. Biopolymers. 1971;10(1):69-&. doi: DOI 10.1002/bip.360100107. PubMed PMID: WOS:A1971I551700006.
42. Thomas GA, Peticolas WL. Fluctuations in Nucleic-Acid Conformations .2. Raman-Spectroscopic Evidence of Varying Ring Pucker in a-T Polynucleotides. J Am Chem Soc. 1983;105(4):993-6. doi: Doi 10.1021/Ja00342a058. PubMed PMID: WOS:A1983QD13400058.
43. Wartell RM, Harrell JT. Characteristics and Variations of B-Type DNA Conformations in Solution - a Quantitative-Analysis of Raman Band Intensities of 8 Dnas. Biochemistry-Us. 1986;25(9):2664-71. doi: Doi 10.1021/Bi00357a056. PubMed PMID: WOS:A1986C353900056.

44. Wartell RM, Harrell JT. Characteristics of B-Type DNA Conformations in Solution - Analysis of Raman Band Intensities of 8-Dnas. Biophysical Journal. 1986;49(2):A129-A. PubMed PMID: WOS:A1986A176800364.
45. Wartell RM, Harrell JT, Zacharias W, Wells RD. Raman-Spectroscopy Study of the B-Z Transition in (Dg-Dc)N.(Dg-Dc)N and a DNA Restriction Fragment. J Biomol Struct Dyn. 1983;1(1):83-96. PubMed PMID: WOS:A1983SC35600004.
46. Fleischmann M, Hendra PJ, Mcquillan AJ. Raman-Spectra of Pyridine Adsorbed at a Silver Electrode. Chem Phys Lett. 1974;26(2):163-6. doi: Doi 10.1016/0009-2614(74)85388-1. PubMed PMID: WOS:A1974T347700004.
47. Kneipp K, Kneipp H, Kneipp J. Surface-enhanced Raman scattering in local optical fields of silver and gold nanoaggregatess - From single-molecule Raman spectroscopy to ultrasensitive probing in live cells. Acc Chem Res. 2006;39(7):443-50. doi: Doi 10.1021/Ar050107x. PubMed PMID: ISI:000239086100003.
48. Moskovits M. Surface-Enhanced Spectroscopy. Rev Mod Phys. 1985;57(3):783-826. PubMed PMID: ISI:A1985APC5700006.
49. Campion A, Kambhampati P. Surface-enhanced Raman scattering. Chem Soc Rev. 1998;27(4):241-50. PubMed PMID: ISI:000075103200002.
50. Hendra PJ, Horder JR, Loader EJ. Laser-Raman Spectrum of Pyridine Adsorbed on Oxide Surfaces. J Chem Soc A. 1971(11):1766-&. doi: Doi 10.1039/J19710001766. PubMed PMID: WOS:A1971J586500026.
51. Hendra PJ, Turner IDM, Loader EJ, Stacey M. Laser Raman-Spectra of Species Adsorbed on Oxide Surfaces .2. J Phys Chem-Us. 1974;78(3):300-4. doi: Doi 10.1021/J100596a023. PubMed PMID: WOS:A1974R994400023.
52. Albrecht MG, Creighton JA. Anomalously Intense Raman-Spectra of Pyridine at a Silver Electrode. J Am Chem Soc. 1977;99(15):5215-7. doi: Doi 10.1021/Ja00457a071. PubMed PMID: WOS:A1977DN51700071.
53. Jeanmaire DL, Vanduyne RP. Surface Raman Spectroelectrochemistry .1. Heterocyclic, Aromatic, and Aliphatic-Amines Adsorbed on Anodized Silver Electrode. J Electroanal Chem. 1977;84(1):1-20. doi: Doi 10.1016/S0022-0728(77)80224-6. PubMed PMID: WOS:A1977DZ86400001.
54. Schatz GC. Theoretical-Studies of Surface Enhanced Raman-Scattering. Accounts Chem Res. 1984;17(10):370-6. doi: Doi 10.1021/Ar00106a005. PubMed PMID: WOS:A1984TT29300007.
55. Katan T, Szpak S, Bennion DN. Silver-Silver Chloride Electrodes - Surface Morphology on Charging and Discharging. J Electrochem Soc. 1974;121(6):757-64. doi: Doi 10.1149/1.2401904. PubMed PMID: WOS:A1974T114700006.
56. Haarer D, Philpott MR, Morawitz H. Field-Induced Charge-Transfer Exciton-Transitions. J Chem Phys. 1975;63(12):5238-45. doi: Doi 10.1063/1.431310. PubMed PMID: WOS:A1975BA16200027.
57. Fleischmann M, Hendra PJ, Mcquillan AJ, Paul RL, Reid ES. Raman-Spectroscopy at Electrode-Electrolyte Interfaces. J Raman Spectrosc. 1976;4(3):269-74. doi: DOI 10.1002/jrs.1250040308. PubMed PMID: WOS:A1976BM67100006.

58. Mcquillan AJ, Hendra PJ, Fleischmann M. Raman Spectroscopic Investigation of Silver Electrodes. J Electroanal Chem. 1975;65(2):933-44. doi: Doi 10.1016/0368-1874(75)85167-7. PubMed PMID: WOS:A1975AY45900030.
59. Paul RL, Mcquillan AJ, Hendra PJ, Fleischmann M. Laser Raman-Spectroscopy at Surface of a Copper Electrode. J Electroanal Chem. 1975;66(3):248-9. doi: Doi 10.1016/S0022-0728(75)80007-6. PubMed PMID: WOS:A1975BB08600007.
60. Barradas RG, Hamilton PG. Chemical Structure and Adsorption of Organic Molecules at Polarized Mercury-Electrolyte Interface. Can J Chemistry. 1965;43(9):2468-&. doi: Doi 10.1139/V65-340. PubMed PMID: WOS:A19656806100004.
61. Kneipp K, Kneipp H, I I, Dasari RR, Feld MS. Ultrasensitive chemical analysis by Raman spectroscopy. Chem Rev. 1999;99(10):2957-+. PubMed PMID: ISI:000083158200005.
62. Dieringer JA, Wustholz KL, Masiello DJ, Camden JP, Kleinman SL, Schatz GC, et al. Surface-Enhanced Raman Excitation Spectroscopy of a Single Rhodamine 6G Molecule. J Am Chem Soc. 2009;131(2):849-54. doi: Doi 10.1021/Ja8080154. PubMed PMID: WOS:000262521800079.
63. Dieringer JA, McFarland AD, Shah NC, Stuart DA, Whitney AV, Yonzon CR, et al. Surface enhanced Raman spectroscopy: new materials, concepts, characterization tools, and applications. Faraday Discuss. 2006;132:9-26. doi: Doi 10.1039/B513431p. PubMed PMID: ISI:000236772600001.
64. Chang RK, Furtak TE. Surface Enhanced Raman Scattering. Chang RK, Furtak TE, editors. New York: Plenum Press; 1980.
65. Furtak TE, Reyes J. A Critical Analysis of Theoretical-Models for the Giant Raman Effect from Adsorbed Molecules. Surf Sci. 1980;93(2-3):351-82. doi: Doi 10.1016/0039-6028(80)90270-8. PubMed PMID: WOS:A1980JP34100010.
66. Otto A, Mrozek I, Grabhorn H, Akemann W. Surface-Enhanced Raman-Scattering. J Phys-Condens Mat. 1992;4(5):1143-212. PubMed PMID: ISI:A1992HC71000001.
67. Van Duyne RP. Chemical and Biochemcail Aplications of Lasers. Moore CB, editor. New York: Academic Press; 1979.
68. Ford GW, Weber WH. Electromagnetic Effects on a Molecule at a Metal-Surface .1. Effects of Nonlocality and Finite Molecular-Size. Surf Sci. 1981;109(2):451-81. doi: Doi 10.1016/0039-6028(81)90500-8. PubMed PMID: WOS:A1981ME74000019.
69. Ford GW, Weber WH. Electromagnetic Effects in the Surface Enhanced Raman-Scattering from a Molecule at a Liquid Hg Surface. Surf Sci. 1981;110(1):L587-L92. doi: Doi 10.1016/0039-6028(81)90577-X. PubMed PMID: WOS:A1981MJ49100004.
70. Weber WH, Ford GW. Enhanced Raman-Scattering by Adsorbates Including the Nonlocal Response of the Metal and the Excitation of Nonradiative Modes. Phys Rev Lett. 1980;44(26):1774-7. doi: DOI 10.1103/PhysRevLett.44.1774. PubMed PMID: WOS:A1980JX11300017.
71. Willets KA, Van Duyne RP. Localized surface plasmon resonance spectroscopy and sensing. Annu Rev Phys Chem. 2007;58:267-97. doi: DOI 10.1146/annurev.physchem.58.032806.104607. PubMed PMID: ISI:000246652300011.

72. Campion A, Ivanecky JE, Child CM, Foster M. On the Mechanism of Chemical Enhancement in Surface-Enhanced Raman-Scattering. J Am Chem Soc. 1995;117(47):11807-8. PubMed PMID: ISI:A1995TG89900024.
73. Aroca RF. Surface Enhanced Vibrational Spectroscopy. Chichester: J. Wiley and Sons; 2006. 260 p.
74. Wetzel H, Gerischer H, Pettinger B. Surface-Enhanced Raman-Scattering from Silver-Cyanide and Silver-Thiocyanate Vibrations and the Importance of Adatoms. Chem Phys Lett. 1981;80(1):159-62. doi: Doi 10.1016/0009-2614(81)80080-2. PubMed PMID: WOS:A1981LS53300037.
75. Allen CS, Schatz GC, Vanduyne RP. Tunable Laser Excitation Profile of Surface Enhanced Raman-Scattering from Pyridine Adsorbed on a Copper Electrode Surface. Chem Phys Lett. 1980;75(2):201-5. doi: Doi 10.1016/0009-2614(80)80496-9. PubMed PMID: WOS:A1980KP67400001.
76. Stiles PL, Dieringer JA, Shah NC, Van Duyne RR. Surface-Enhanced Raman Spectroscopy. Annu Rev Anal Chem. 2008;1:601-26. doi: DOI 10.1146/annurev.anchem.1.031207.112814. PubMed PMID: ISI:000262525200020.
77. Zhang YX, Aslan K, Previte MJR, Geddes CD. Metal-enhanced fluorescence from copper substrates. Appl Phys Lett. 2007;90(17). doi: Artn 173116 Doi 10.1063/1.2732185. PubMed PMID: ISI:000246568600107.
78. Murphy CJ, Gole AM, Hunyadi SE, Stone JW, Sisco PN, Alkilany A, et al. Chemical sensing and imaging with metallic nanorods. Chem Commun. 2008(5):544-57. doi: Doi 10.1039/B711069c. PubMed PMID: WOS:000252553300002.
79. Le Ru EC, Blackie E, Etchegoin PG. Surface Enhanced Raman Scattering Enhancement Factors: A Comprehensive Stury. J Phys Chem C. 2007;111:13794-803.
80. Kneipp K, Wang Y, Kneipp H, Perelman LT, Itzkan I, Dasari R, et al. Single molecule detection using surface-enhanced Raman scattering (SERS). Phys Rev Lett. 1997;78(9):1667-70. PubMed PMID: ISI:A1997WL50600016.
81. Nie SM, Emery SR. Probing single molecules and single nanoparticles by surface-enhanced Raman scattering. Science. 1997;275(5303):1102-6. PubMed PMID: ISI:A1997WJ50300037.
82. Gersten J, Nitzan A. Electromagnetic Theory of Enhanced Raman-Scattering by Molecules Adsorbed on Rough Surfaces. J Chem Phys. 1980;73(7):3023-37. doi: Doi 10.1063/1.440560. PubMed PMID: WOS:A1980KJ69300001.
83. Dieringer JA, McFarland AD, Shah NC, Stuart DA, Whitney AV, Yonzon CR, et al. Surface enhanced Raman spectroscopy: new materials, concepts, characterization tools, and applications. Faraday Discuss. 2006;132:9-26. PubMed PMID: 16833104.
84. Elam JW, Groner MD, George SM. Viscous flow reactor with quartz crystal microbalance for thin film growth by atomic layer deposition. Rev Sci Instrum. 2002;73(8):2981-7. doi: Doi 10.1063/1.1490410. PubMed PMID: WOS:000177055200026.
85. Whitney AV, Elam JW, Zou SL, Zinovev AV, Stair PC, Schatz GC, et al. Localized surface plasmon resonance nanosensor: A high-resolution distance-dependence study using atomic layer deposition. J Phys Chem B. 2005;109(43):20522-8. doi: Doi 10.1021/Jp0540656. PubMed PMID: WOS:000232959800067.

86. Haes AJ, Zou SL, Schatz GC, Van Duyne RP. Nanoscale optical biosensor: Short range distance dependence of the localized surface plasmon resonance of noble metal nanoparticles. J Phys Chem B. 2004;108(22):6961-8. doi: Doi 10.1021/Jp036261n. PubMed PMID: WOS:000221700300014.
87. Angel SM, Katz LF, Archibald DD, Lin LT, Honigs DE. Near-Infrared Surface-Enhanced Raman-Spectroscopy .1. Copper and Gold Electrodes. Applied Spectroscopy. 1988;42(8):1327-31. doi: Doi 10.1366/0003702884429698. PubMed PMID: WOS:A1988R471700001.
88. Zhao LL, Jensen L, Schatz GC. Pyridine-Ag-20 cluster: A model system for studying surface-enhanced Raman scattering. J Am Chem Soc. 2006;128(9):2911-9. doi: Doi 10.1021/Ja056326. PubMed PMID: WOS:000235942000042.
89. Moskovits M. Surface-enhanced Raman spectroscopy: a brief retrospective. J Raman Spectrosc. 2005;36(6-7):485-96. PubMed PMID: ISI:000230829200004.
90. Fusco M. Fdtd Algorithm in Curvilinear Coordinates. IEEE Trans Antennas Propag. 1990;38(1):76-89. PubMed PMID: ISI:A1990CH86500010.
91. Wang DS, Kerker M. Enhanced Raman-Scattering by Molecules Adsorbed at the Surface of Colloidal Spheroids. Phys Rev B. 1981;24(4):1777-90. doi: DOI 10.1103/PhysRevB.24.1777. PubMed PMID: WOS:A1981ME35500020.
92. Murphy CJ, San TK, Gole AM, Orendorff CJ, Gao JX, Gou L, et al. Anisotropic metal nanoparticles: Synthesis, assembly, and optical applications. J Phys Chem B. 2005;109(29):13857-70. doi: Doi 10.1021/Jp0516846. PubMed PMID: WOS:000230698100005.
93. Fleischm.M, Hendra PJ, Mcquilla.Aj. Raman-Spectra of Pyridine Adsorbed at a Silver Electrode. Chem Phys Lett. 1974;26(2):163-6. PubMed PMID: ISI:A1974T347700004.
94. Xue G, Dong J, Zhang MS. Surface-Enhanced Raman-Scattering (Sers) and Surface-Enhanced Resonance Raman-Scattering (Serrs) on Hno3-Roughened Copper Foil. Appl Spectrosc. 1991;45(5):756-9. PubMed PMID: ISI:A1991FV08300009.
95. Royer P, Goudonnet JP, Warmack RJ, Ferrell TL. Substrate Effects on Surface-Plasmon Spectra in Metal-Island Films. Phys Rev B. 1987;35(8):3753-9. PubMed PMID: ISI:A1987G366800009.
96. Abu Hatab NA, Oran JM, Sepaniak MJ. Surface-enhanced Raman spectroscopy substrates created via electron beam lithography and nanotransfer printing. Acs Nano. 2008;2(2):377-85. doi: Doi 10.1021/Nn7003487. PubMed PMID: ISI:000253503300029.
97. Haynes CL, Van Duyne RP. Nanosphere lithography: A versatile nanofabrication tool for studies of size-dependent nanoparticle optics. J Phys Chem B. 2001;105(24):5599-611. doi: Doi 10.1021/Jp010657m. PubMed PMID: ISI:000169371500005.
98. Yao JL, Pan GP, Xue KH, Wu DY, Ren B, Sun DM, et al. A complementary study of surface-enhanced Raman scattering and metal nanorod arrays. Pure Appl Chem. 2000;72(1-2):221-8. PubMed PMID: ISI:000087833100024.
99. Walsh RJ, Chumanov G. Silver coated porous alumina as a new substrate for surface-enhanced Raman scattering. Appl Spectrosc. 2001;55(12):1695-700. PubMed PMID: ISI:000173172000026.

100. Cintra S, Abdelsalam ME, Bartlett PN, Baumberg JJ, Kelf TA, Sugawara Y, et al. Sculpted substrates for SERS. Faraday Discuss. 2006;132:191-9. doi: Doi 10.1039/B508847j. PubMed PMID: WOS:000236772600016.
101. Van Duyne RP, Hulteen JC, Treichel DA. Atomic Force Microscopy and Surface-Enhanced Raman Spectroscopy. I. Ag Island Films and Ag Film Over Polymer Nanosphere Surfaces Supported On Glass. J Chem Phys. 1993;99:2101-15.
102. Jensen TR, Malinsky MD, Haynes CL, Van Duyne RP. Nanosphere lithography: Tunable localized surface plasmon resonance spectra of silver nanoparticles. J Phys Chem B. 2000;104(45):10549-56. doi: Doi 10.1021/Jp002435e. PubMed PMID: WOS:000165355800016.
103. Litorja M, Haynes CL, Haes AJ, Jensen TR, Van Duyne RP. Surface-enhanced Raman scattering detected temperature programmed desorption: Optical properties, nanostructure, and stability of silver film over SiO2 nanosphere surfaces. J Phys Chem B. 2001;105(29):6907-15. doi: Doi 10.1021/Jp010333y. PubMed PMID: WOS:000170152800023.
104. Anker JN, Hall WP, Lyandres O, Shah NC, Zhao J, Van Duyne RP. Biosensing with plasmonic nanosensors. Nat Mater. 2008;7(6):442-53. doi: Doi 10.1038/Nmat2162. PubMed PMID: WOS:000256110200016.
105. Camden JP, Dieringer JA, Zhao J, Van Duyne RP. Controlled Plasmonic Nanostructures for Surface-Enhanced Spectroscopy and Sensing. Accounts Chem Res. 2008;41(12):1653-61. doi: Doi 10.1021/Ar800041s. PubMed PMID: WOS:000261767600010.
106. Haynes CL, Van Duyne RP. From the fundamentals of nanoparticle optics to the development of practical chemical and biological sensors based on surface-enhanced Raman scattering. Abstr Pap Am Chem S. 2005;229:U143-U. PubMed PMID: WOS:000228177700666.
107. Haynes CL, Yonzon CR, Zhang XY, Van Duyne RP. Surface-enhanced Raman sensors: early history and the development of sensors for quantitative biowarfare agent and glucose detection. J Raman Spectrosc. 2005;36(6-7):471-84. doi: Doi 10.1002/Jrs.1376. PubMed PMID: WOS:000230829200003.
108. Yonzon CR, Jeoungf E, Zou SL, Schatz GC, Mrksich M, Van Duyne RP. A comparative analysis of localized and propagating surface plasmon resonance sensors: The binding of concanavalin a to a monosaccharide functionalized self-assembled monolayer. J Am Chem Soc. 2004;126(39):12669-76. doi: Doi 10.1021/Ja047118q. PubMed PMID: WOS:000224219900088.
109. Zhao J, Zhang XY, Yonzon CR, Haes AJ, Van Duyne RP. Localized surface plasmon resonance biosensors. Nanomedicine-Uk. 2006;1(2):219-28. doi: Doi 10.2217/17435889.1.1.219. PubMed PMID: WOS:000243835000012.
110. Kuncicky DM, Christesen SD, Velev OD. Role of the micro- and nanostructure in the performance of surface-enhanced Raman scattering substrates assembled from gold nanoparticles. Applied Spectroscopy. 2005;59(4):401-9. PubMed PMID: WOS:000228234900002.
111. Velev OD, Bhatt K, Prevo BG, Lumsdon SO. On-chip dielectrophoretic manipulation and assembly of nanoparticles, microparticles and droplets. Abstr Pap Am Chem S. 2003;226:U479-U. PubMed PMID: WOS:000187062502473.
112. Averitt RD, Sarkar D, Halas NJ. Plasmon resonance shifts of Au-coated Au2S nanoshells: Insight into multicomponent nanoparticle growth. Phys Rev Lett. 1997;78(22):4217-20. doi: DOI 10.1103/PhysRevLett.78.4217. PubMed PMID: WOS:A1997XB77900020.

113. Oldenburg SJ, Averitt RD, Westcott SL, Halas NJ. Nanoengineering of optical resonances. Chem Phys Lett. 1998;288(2-4):243-7. doi: Doi 10.1016/S0009-2614(98)00277-2. PubMed PMID: WOS:000074007900012.
114. Oldenburg SJ, Westcott SL, Averitt RD, Halas NJ. Surface enhanced Raman scattering in the near infrared using metal nanoshell substrates. J Chem Phys. 1999;111(10):4729-35. doi: Doi 10.1063/1.479235. PubMed PMID: WOS:000082222500041.
115. Westcott SL, Oldenburg SJ, Lee TR, Halas NJ. Formation and adsorption of clusters of gold nanoparticles onto functionalized silica nanoparticle surfaces. Langmuir. 1998;14(19):5396-401. doi: Doi 10.1021/La980380q. PubMed PMID: WOS:000076026900011.
116. Pham T, Jackson JB, Halas NJ, Lee TR. Preparation and characterization of gold nanoshells coated with self-assembled monolayers. Langmuir. 2002;18(12):4915-20. doi: Doi 10.1021/La015561y. PubMed PMID: WOS:000176091900055.
117. Bardhan R, Chen WX, Perez-Torres C, Bartels M, Huschka RM, Zhao LL, et al. Nanoshells with Targeted Simultaneous Enhancement of Magnetic and Optical Imaging and Photothermal Therapeutic Response. Adv Funct Mater. 2009;19(24):3901-9. doi: DOI 10.1002/adfm.200901235. PubMed PMID: WOS:000273359600008.
118. Choi MR, Bardhan R, Badve S, Nakshatri H, Halas NJ, Clare SE. Delivery of Therapeutic Nanoshells to Hypoxic Areas of Tumors Using a Cellular Trojan Horse. Cancer Res. 2009;69(24):860s-1s. PubMed PMID: WOS:000272920702236.
119. Freeman RG, Grabar KC, Allison KJ, Bright RM, Davis JA, Guthrie AP, et al. Self-Assembled Metal Colloid Monolayers - an Approach to Sers Substrates. Science. 1995;267(5204):1629-32. PubMed PMID: ISI:A1995QM39700031.
120. Aroca RF, Alvarez-Puebla RA, Pieczonka N, Sanchez-Cortez S, Garcia-Ramos JV. Surface-enhanced Raman scattering on colloidal nanostructures. Adv Colloid Interfac. 2005;116(1-3):45-61. doi: DOI 10.1016/j.cis.2005.04.007. PubMed PMID: WOS:000234078400004.
121. Haes AJ, Van Duyne RP. A nanoscale optical biosensor: Sensitivity and selectivity of an approach based on the localized surface plasmon resonance spectroscopy of triangular silver nanoparticles. J Am Chem Soc. 2002;124(35):10596-604. doi: Doi 10.1021/Ja020393x. PubMed PMID: WOS:000177881300057.
122. Haynes CL, McFarland AD, Van Duyne RP. Surface-enhanced Raman spectroscopy. Anal Chem. 2005;77(17):338a-46a. doi: Doi 10.1021/Ac053456d. PubMed PMID: WOS:000231652300010.
123. Natan MJ. Concluding remarks - Surface enhanced Raman scattering. Faraday Discuss. 2006;132:321-8. doi: Doi 10.1039/B601494c. PubMed PMID: WOS:000236772600027.
124. De Jesus MA, Giesfeldt KS, Sepaniak MJ. Use of a sample translation technique to minimize adverse effects of laser irradiation in surface-enhanced Raman spectrometry. Applied Spectroscopy. 2003;57(4):428-38. doi: Doi 10.1366/00037020360625970. PubMed PMID: WOS:000184358300010.
125. Cermakova K, Sestak O, Matejka P, Baumruk V, Vlckova B. Surface-Enhanced Raman-Scattering (Sers) Spectroscopy with Borohydride-Reduced Silver Colloids - Controlling Adsorption of the Scattering Species by Surface-Potential of Silver Colloid. Collect Czech Chem

C. 1993;58(11):2682-94. doi: Doi 10.1135/Cccc19932682. PubMed PMID: WOS:A1993MQ41400017.
126. Munro CH, Smith WE, Garner M, Clarkson J, White PC. Characterization of the Surface of a Citrate-Reduced Colloid Optimized for Use as a Substrate for Surface-Enhanced Resonance Raman-Scattering. Langmuir. 1995;11(10):3712-20. doi: Doi 10.1021/La00010a021. PubMed PMID: WOS:A1995TC04000021.
127. Turkevich J, Stevenson PC, Hillier J. A Study of the Nucleation and Growth Processes in the Synthesis of Colloidal Gold. Discuss Faraday Soc. 1951(11):55-&. PubMed PMID: WOS:A1951UL20200007.
128. Brust M, Walker M, Bethell D, Schiffrin DJ, Whyman R. Synthesis of Thiol-Derivatized Gold Nanoparticles in a 2-Phase Liquid-Liquid System. J Chem Soc Chem Comm. 1994(7):801-2. doi: Doi 10.1039/C39940000801. PubMed PMID: WOS:A1994NF89800007.
129. Perrault SD, Chan WCW. Synthesis and Surface Modification of Highly Monodispersed, Spherical Gold Nanoparticles of 50-200 nm. J Am Chem Soc. 2009;131(47):17042-+. doi: Doi 10.1021/Ja907069u. PubMed PMID: WOS:000272207300005.
130. Kelly KL, Coronado E, Zhao LL, Schatz GC. The optical properties of metal nanoparticles: The influence of size, shape, and dielectric environment. J Phys Chem B. 2003;107(3):668-77. doi: Doi 10.1021/Jp026731y. PubMed PMID: WOS:000180545300005.
131. GarciaVidal FJ, Pendry JB. Collective theory for surface enhanced Raman scattering. Phys Rev Lett. 1996;77(6):1163-6. doi: DOI 10.1103/PhysRevLett.77.1163. PubMed PMID: WOS:A1996VA47600046.
132. Zou SL, Schatz GC. Silver nanoparticle array structures that produce giant enhancements in electromagnetic fields. Chem Phys Lett. 2005;403(1-3):62-7. doi: DOI 10.1016/j.cplett.2004.12.107. PubMed PMID: WOS:000226934300010.
133. Braun G, Lee SJ, Dante M, Nguyen TQ, Moskovits M, Reich N. Surface-enhanced Raman spectroscopy for DNA detection by nanoparticle assembly onto smooth metal films. J Am Chem Soc. 2007;129(20):6378-9. Epub 2007/05/02. doi: 10.1021/ja070514z. PubMed PMID: 17469825.
134. Braun GB, Lee SJ, Laurence T, Fera N, Fabris L, Bazan GC, et al. Generalized Approach to SERS-Active Nanomaterials via Controlled Nanoparticle Linking, Polymer Encapsulation, and Small-Molecule Infusion. J Phys Chem C. 2009;113(31):13622-9. doi: Doi 10.1021/Jp903399p. PubMed PMID: WOS:000268478700027.
135. Perney NMB, Baumberg JJ, Zoorob ME, Charlton MDB, Mahnkopf S, Netti CM. Tuning localized plasmons in nanostructured substrates for surface- enhanced Raman scattering. Opt Express. 2006;14(2):847-57. PubMed PMID: ISI:000235012000045.
136. Perney NMB, de Abajo FJG, Baumberg JJ, Tang A, Netti MC, Charlton MDB, et al. Tuning localized plasmon cavities for optimized surface-enhanced Raman scattering. Phys Rev B. 2007;76(3). doi: Artn 035426
Doi 10.1103/Physrevb.76.035426. PubMed PMID: ISI:000248500800146.
137. Guicheteau J, Christesen S, Emge D, Wilcox P, Fountain AW. Assessing Metal Nanofabricated Substrates for Surface-Enhanced Raman Scattering (SERS) Activity and Reproducibility. Applied Spectroscopy. 2011;65(2):144-51. doi: Doi 10.1366/10-06080. PubMed PMID: WOS:000286549500003.

138. Hering K, Cialla D, Ackermann K, Dorfer T, Moller R, Schneidewind H, et al. SERS: a versatile tool in chemical and biochemical diagnostics. Anal Bioanal Chem. 2008;390(1):113-24. doi: DOI 10.1007/s00216-007-1667-3. PubMed PMID: ISI:000251841700015.
139. Mulvaney SP, Musick MD, Keating CD, Natan MJ. Glass-coated, analyte-tagged nanoparticles: A new tagging system based on detection with surface-enhanced Raman scattering. Langmuir. 2003;19(11):4784-90. doi: Doi 10.1021/La026706j. PubMed PMID: ISI:000183136900040.
140. Kalasinsky KS, Hadfield T, Shea AA, Kalasinsky VF, Nelson MP, Neiss J, et al. Raman chemical imaging spectroscopy reagentless detection and identification of pathogens: Signature development and evaluation. Anal Chem. 2007;79(7):2658-73. doi: Doi 10.1021/Ac0700575. PubMed PMID: ISI:000245304300004.
141. Monaghan PB, McCarney KM, Ricketts A, Littleford RE, Docherty F, Smith WE, et al. Bead-based DNA diagnostic assay for chlamydia using nanoparticle-mediated surface-enhanced resonance Raman scattering detection within a lab-on-a-chip format. Anal Chem. 2007;79(7):2844-9. doi: Doi 10.1021/Ac061769i. PubMed PMID: ISI:000245304300027.
142. Vo-Dinh T, Allain LR, Stokes DL. Cancer gene detection using surface-enhanced Raman scattering (SERS). J Raman Spectrosc. 2002;33(7):511-6. doi: Doi 10.1002/Jrs.883. PubMed PMID: ISI:000177232800004.
143. Zhang XY, Young MA, Lyandres O, Van Duyne RP. Rapid detection of an anthrax biomarker by surface-enhanced Raman spectroscopy. J Am Chem Soc. 2005;127(12):4484-9. doi: Doi 10.1021/Ja0436623b0b. PubMed PMID: ISI:000227895500069.
144. Farquharson S, Shende C, Inscore FE, Maksymiuk P, Gift A. Analysis of 5-fluorouracil in saliva using surface-enhanced Raman spectroscopy. J Raman Spectrosc. 2005;36(3):208-12. doi: Doi 10.1002/Jrs.1277. PubMed PMID: ISI:000227746900004.
145. Pinzaru SC, Pavel I, Leopold N, Kiefer W. Identification and characterization of pharmaceuticals using Raman and surface-enhanced Raman scattering. J Raman Spectrosc. 2004;35(5):338-46. PubMed PMID: ISI:000221490000003.
146. Ruperez A, Montes R, Laserna JJ. Identification of Stimulant-Drugs by Surface-Enhanced Raman-Spectrometry on Colloidal Silver. Vib Spectrosc. 1991;2(2-3):145-54. PubMed PMID: ISI:A1991GQ63700008.
147. Sutherland WS, Laserna JJ, Angebranndt MJ, Winefordner JD. Surface-Enhanced Raman Analysis of Sulfa Drugs on Colloidal Silver Dispersion. Anal Chem. 1990;62(7):689-93. PubMed PMID: ISI:A1990CW37800012.
148. Gish DA, Nsiah F, McDermott MT, Brett MJ. Localized surface plasmon resonance biosensor using silver nanostructures fabricated by glancing angle deposition. Anal Chem. 2007;79(11):4228-32. doi: Doi 10.1021/Ac0622274. PubMed PMID: WOS:000246842100033.
149. Nithipatikom K, McCoy MJ, Hawi SR, Nakamoto K, Adar F, Campbell WB. Characterization and application of Raman labels for confocal Raman microspectroscopic detection of cellular proteins in single cells. Anal Biochem. 2003;322(2):198-207. doi: Doi 10.1016/J.Ab.2003.07.020. PubMed PMID: WOS:000186610400009.
150. Qian XM, Zhou X, Nie SM. Surface-Enhanced Raman Nanoparticle Beacons Based on Bioconjugated Gold Nanocrystals and Long Range Plasmonic Coupling. J Am Chem Soc. 2008;130(45):14934-+. doi: Doi 10.1021/Ja8062502. PubMed PMID: WOS:000260682300016.

151. Thanh NTK, Rosenzweig Z. Development of an aggregation-based immunoassay for anti-protein A using gold nanoparticles. Anal Chem. 2002;74(7):1624-8. doi: Doi 10.1021/Ac011127p. PubMed PMID: WOS:000174841600033.
152. Wei F, Zhang DM, Halas NJ, Hartgerink JD. Aromatic amino acids providing characteristic motifs in the Raman and SERS spectroscopy of peptides. J Phys Chem B. 2008;112(30):9158-64. doi: Doi 10.1021/Jp8025732. PubMed PMID: WOS:000257926800042.
153. Krafft C, Knetschke T, Siegner A, Funk RHW, Salzer R. Mapping of single cells by near infrared Raman microspectroscopy. Vib Spectrosc. 2003;32(1):75-83. doi: Doi 10.1016/S0924-2031(03)00049-3. PubMed PMID: WOS:000184513800008.
154. Scaffidi JP, Gregas MK, Seewaldt V, Vo-Dinh T. SERS-based plasmonic nanobiosensing in single living cells. Anal Bioanal Chem. 2009;393(4):1135-41. doi: DOI 10.1007/s00216-008-2521-y. PubMed PMID: WOS:000263127500005.
155. Sujith A, Itoh T, Abe H, Yoshida KI, Kiran MS, Biju V, et al. Imaging the cell wall of living single yeast cells using surface-enhanced Raman spectroscopy. Anal Bioanal Chem. 2009;394(7):1803-9. doi: DOI 10.1007/s00216-009-2883-9. PubMed PMID: WOS:000268000600009.
156. Huang WE, Griffiths RI, Thompson IP, Bailey MJ, Whiteley AS. Raman microscopic analysis of single microbial cells. Anal Chem. 2004;76(15):4452-8. doi: Doi 10.1021/Ac049753k. PubMed PMID: WOS:000223010100043.
157. Barhoumi A, Zhang DM, Halas NJ. Correlation of molecular orientation and packing density in a dsDNA self-assembled monolayer observable with surface-enhanced-Raman spectroscopy. J Am Chem Soc. 2008;130(43):14040-1. doi: Doi 10.1021/Ja804367c. PubMed PMID: ISI:000260301700010.
158. Faulds K, Smith WE, Graham D. DNA detection by surface enhanced resonance Raman scattering (SERRS). Analyst. 2005;130(8):1125-31. doi: Doi 10.1039/B500248f. PubMed PMID: WOS:000230495900002.
159. Green M, Liu FM, Cohen L, Kollensperger P, Cass T. SERS platforms for high density DNA arrays. Faraday Discuss. 2006;132:269-80. doi: Doi 10.1039/B506636k. PubMed PMID: ISI:000236772600022.
160. Liu JW, Lu Y. Design of asymmetric DNAzymes for dynamic control of nanoparticle aggregation states in response to chemical stimuli. Org Biomol Chem. 2006;4(18):3435-41. doi: Doi 10.1039/B605799c. PubMed PMID: WOS:000240166800011.
161. Mirkin CA, Letsinger RL, Mucic RC, Storhoff JJ. A DNA-based method for rationally assembling nanoparticles into macroscopic materials. Nature. 1996;382(6592):607-9. doi: Doi 10.1038/382607a0. PubMed PMID: WOS:A1996VC30300046.
162. Park T, Lee S, Seong GH, Choo J, Lee EK, Kim YS, et al. Highly sensitive signal detection of duplex dye-labelled DNA oligonucleotides in a PDMS microfluidic chip: confocal surface-enhanced Raman spectroscopic study. Lab Chip. 2005;5(4):437-42. doi: Doi 10.1039/B414457k. PubMed PMID: ISI:000227893100010.
163. Vo-Dinh T. Nanobiosensing using plasmonic nanoprobes. IEEE Journal of Selected Topics in Quantum Electronics. 2008;14(1):198-205. doi: 10.1109/jstqe.2007.914738. PubMed PMID: ISI:000253558100026.

164. Porter MD, Lipert RJ, Siperko LM, Wang G, Narayanana R. SERS as a bioassay platform: fundamentals, design, and applications. Chem Soc Rev. 2008;37(5):1001-11. doi: Doi 10.1039/B708461g. PubMed PMID: WOS:000255444700013.
165. Rosi NL, Mirkin CA. Nanostructures in biodiagnostics. Chem Rev. 2005;105(4):1547-62. doi: Doi 10.1021/Cr030067f. PubMed PMID: WOS:000228412800011.
166. Fullam S, Rao SN, Fitzmaurice D. Noncovalent self-assembly of silver nanocrystal aggregates in solution. J Phys Chem B. 2000;104(26):6164-73. doi: Doi 10.1021/Jp0006173. PubMed PMID: WOS:000088057100013.
167. Sastry M, Lala N, Patil V, Chavan SP, Chittiboyina AG. Optical absorption study of the biotin-avidin interaction on colloidal silver and gold particles. Langmuir. 1998;14(15):4138-42. doi: Doi 10.1021/La9800755. PubMed PMID: WOS:000075159000025.
168. Liu JW, Lu Y. Adenosine-dependent assembly of aptazyme-functionalized gold nanoparticles and its application as a colorimetric biosensor. Anal Chem. 2004;76(6):1627-32. doi: Doi 10.1021/Ac0351769. PubMed PMID: WOS:000220225200011.
169. Aslan K, Zhang J, Lakowicz JR, Geddes CD. Saccharide sensing using gold and silver nanoparticles - A review. J Fluoresc. 2004;14(4):391-400. doi: Doi 10.1023/B:Jofl.0000031820.17358.28. PubMed PMID: WOS:000222057400007.
170. Kim YJ, Johnson RC, Hupp JT. Gold nanoparticle-based sensing of "spectroscopically silent" heavy metal ions. Nano Lett. 2001;1(4):165-7. doi: Doi 10.1021/Nl0100116. PubMed PMID: WOS:000173708300001.
171. Ellington AD, Szostak JW. In vitro selection of RNA molecules that bind specific ligands. Nature. 1990;346(6287):818-22. Epub 1990/08/30. doi: 10.1038/346818a0. PubMed PMID: 1697402.
172. Gold L, Polisky B, Uhlenbeck O, Yarus M. Diversity of Oligonucleotide Functions. Annu Rev Biochem. 1995;64:763-97. PubMed PMID: ISI:A1995RH35300026.
173. Gopinath SCB, Sakamaki Y, Kawasaki K, Kumar PKR. An efficient RNA aptamer against human influenza B virus hemagglutinin. J Biochem. 2006;139(5):837-46. doi: Doi 10.1093/Jb/Mvj095. PubMed PMID: ISI:000238357000004.
174. Tang JJ, Yu T, Guo L, Xie JW, Shao NS, He ZK. In vitro selection of DNA aptamer against abrin toxin and aptamer-based abrin direct detection. Biosens Bioelectron. 2007;22(11):2456-63. doi: DOI 10.1016/j.bios.2006.09.015. PubMed PMID: ISI:000246382500010.
175. James W. Aptamers in the virologists' toolkit. J Gen Virol. 2007;88:351-64. doi: DOI 10.1099/vir.0.82442-0. PubMed PMID: ISI:000243987100001.
176. Lee JH, Yigit MV, Mazumdar D, Lu Y. Molecular diagnostic and drug delivery agents based on aptamer-nanomaterial conjugates. Adv Drug Deliver Rev 2010;62(6):592-605. doi: DOI 10.1016/j.addr.2010.03.003. PubMed PMID: ISI:000279906200002.
177. Famulok M, Mayer G. Aptamers as tools in molecular biology and immunology. Curr Top Microbiol. 1999;243:123-36. PubMed PMID: ISI:000082903000007.
178. Goodacre R, Timmins EM, Burton R, Kaderbhai N, Woodward AM, Kell DB, et al. Rapid identification of urinary tract infection bacteria using hyperspectral whole-organism fingerprinting and artificial neural networks. Microbiol-Uk. 1998;144:1157-70. PubMed PMID: ISI:000073681800004.

179. Zeiri L, Bronk BV, Shabtai Y, Czege J, Efrima S. Silver metal induced surface enhanced Raman of bacteria. Colloid Surface A. 2002;208(1-3):357-62. doi: Pii S0927-7757(02)00162-0 Doi 10.1016/S0927-7757(02)00162-0. PubMed PMID: WOS:000177581200035.
180. Zeiri L, Bronk BV, Shabtai Y, Eichler J, Efrima S. Surface-enhanced Raman spectroscopy as a tool for probing specific biochemical components in bacteria. Applied Spectroscopy. 2004;58(1):33-40. doi: Doi 10.1366/000370204322729441. PubMed PMID: WOS:000187950400008.
181. Zeiri L, Efrima S. Surface-enhanced Raman spectroscopy of bacteria: the effect of excitation wavelength and chemical modification of the colloidal milieu. J Raman Spectrosc. 2005;36(6-7):667-75. doi: Doi 10.1002/Jrs.1349. PubMed PMID: WOS:000230829200025.
182. Patel IS, Premasiri WR, Moir DT, Ziegler LD. Barcoding bacterial cells: a SERS-based methodology for pathogen identification. J Raman Spectrosc. 2008;39(11):1660-72. doi: Doi 10.1002/Jrs.2064. PubMed PMID: WOS:000261206200022.
183. Efrima S, Bronk BV. Silver colloids impregnating or coating bacteria. J Phys Chem B. 1998;102(31):5947-50. doi: Doi 10.1021/Jp9813903. PubMed PMID: WOS:000075277400002.
184. Efrima S, Zeiri L. Understanding SERS of bacteria. J Raman Spectrosc. 2009;40(3):277-88. doi: Doi 10.1002/Jrs.2121. PubMed PMID: WOS:000264645600010.
185. Jarvis RM, Brooker A, Goodacre R. Surface-enhanced Raman scattering for the rapid discrimination of bacteria. Faraday Discuss. 2006;132:281-92. doi: Doi 10.1039/B506413a. PubMed PMID: WOS:000236772600023.
186. Jarvis RM, Law N, Shadi LT, O'Brien P, Lloyd JR, Goodacre R. Surface-enhanced Raman scattering from intracellular and extracellular bacterial locations. Anal Chem. 2008;80(17):6741-6. doi: Doi 10.1021/Ac800838v. PubMed PMID: WOS:000258865300040.
187. Kahraman M, Yazici MM, Sahin F, Bayrak OF, Culha M. Reproducible surface-enhanced Raman scattering spectra of bacteria on aggregated silver nanoparticles. Applied Spectroscopy. 2007;61(5):479-85. doi: Doi 10.1366/000370207780807731. PubMed PMID: WOS:000246433600004.
188. Kahraman M, Yazici MM, Sahin F, Culha M. Experimental parameters influencing surface-enhanced Raman scattering of bacteria. J Biomed Opt. 2007;12(5). doi: Artn 054015 Doi 10.1117/1.2798640. PubMed PMID: WOS:000251549600046.
189. Kahraman M, Yazici MM, Sahin F, Culha M. Convective assembly of bacteria for surface-enhanced Raman scattering. Langmuir. 2008;24(3):894-901. doi: Doi 10.1021/La702240q. PubMed PMID: WOS:000252777700048.
190. Laucks ML, Sengupta A, Junge K, Davis EJ, Swanson BD. Comparison of psychro-active arctic marine bacteria and common mesophillic bacteria using surface-enhanced Raman spectroscopy. Applied Spectroscopy. 2005;59(10):1222-8. doi: Doi 10.1366/000370205774430891. PubMed PMID: WOS:000232625800006.
191. Sengupta A, Laucks ML, Davis EJ. Surface-enhanced Raman spectroscopy of bacteria and pollen. Applied Spectroscopy. 2005;59(8):1016-23. doi: Doi 10.1366/0003702054615124. PubMed PMID: WOS:000231134300008.
192. Sengupta A, Mujacic M, Davis EJ. Detection of bacteria by surface-enhanced Raman spectroscopy. Anal Bioanal Chem. 2006;386(5):1379-86. doi: DOI 10.1007/s00216-006-0711-z. PubMed PMID: WOS:000241604700023.

193. Culha M, Adiguzel A, Yazici MM, Kahraman M, Sahin F, Gulluce M. Characterization of Thermophilic Bacteria Using Surface-Enhanced Raman Scattering. Applied Spectroscopy. 2008;62(11):1226-32. PubMed PMID: WOS:000261198300010.
194. Naja G, Bouvrette P, Hrapovic S, Luong JHT. Raman-based detection of bacteria using silver nanoparticles conjugated with antibodies. Analyst. 2007;132(7):679-86. doi: Doi 10.1039/B701160a. PubMed PMID: WOS:000247526600022.
195. Ivleva NP, Wagner M, Horn H, Niessner R, Haisch C. In Situ Surface-Enhanced Raman Scattering Analysis of Biofilm. Anal Chem. 2008;80(22):8538-44. doi: Doi 10.1021/Ac801426m. PubMed PMID: WOS:000260910900024.
196. Alexander TA, Pellegrino PM, Gillespie JB. Near-infrared surface-enhanced-Raman-scattering-mediated detection of single optically trapped bacterial spores. Applied Spectroscopy. 2003;57(11):1340-5. doi: Doi 10.1366/000370203322554482. PubMed PMID: WOS:000187943100005.
197. Xie C, Mace J, Dinno MA, Li YQ, Tang W, Newton RJ, et al. Identification of single bacterial cells in aqueous solution using confocal laser tweezers Raman spectroscopy. Anal Chem. 2005;77(14):4390-7. doi: Doi 10.1021/Ac0504971. PubMed PMID: WOS:000230530300014.
198. Schuster KC, Reese I, Urlaub E, Gapes JR, Lendl B. Multidimensional information on the chemical composition of single bacterial cells by confocal Raman microspectroscopy. Anal Chem. 2000;72(22):5529-34. doi: Doi 10.1021/Ac000718x. PubMed PMID: WOS:000165346800002.
199. Schuster KC, Urlaub E, Gapes JR. Single-cell analysis of bacteria by Raman microscopy: spectral information on the chemical composition of cells and on the heterogeneity in a culture. J Microbiol Meth. 2000;42(1):29-38. doi: Doi 10.1016/S0167-7012(00)00169-X. PubMed PMID: WOS:000089702800005.
200. Alexander TA. Development of methodology based on commercialized SERS-active substrates for rapid discrimination of Poxviridae virions. Anal Chem. 2008;80(8):2817-25. doi: Doi 10.1021/Ac702464w. PubMed PMID: WOS:000254969100023.
201. Shanmukh S, Jones L, Driskell J, Zhao YP, Dluhy R, Tripp RA. Rapid and sensitive detection of respiratory virus molecular signatures using a silver nanorod array SERS substrate. Nano Lett. 2006;6(11):2630-6. doi: Doi 10.1021/Nl061666f. PubMed PMID: ISI:000241856700043.
202. Shanmukh S, Jones L, Zhao YP, Driskell JD, Tripp RA, Dluhy RA. Identification and classification of respiratory syncytial virus (RSV) strains by surface-enhanced Raman spectroscopy and multivariate statistical techniques. Anal Bioanal Chem. 2008;390(6):1551-5. doi: DOI 10.1007/s00216-008-1851-0. PubMed PMID: ISI:000254233800015.
203. Bao PD, Huang TQ, Liu XM, Wu TQ. Surface-enhanced Raman spectroscopy of insect nuclear polyhedrosis virus. J Raman Spectrosc. 2001;32(4):227-30. doi: Doi 10.1002/Jrs.665.Abs. PubMed PMID: WOS:000168423800001.
204. Driskell JD, Kwarta KM, Lipert RJ, Porter MD, Neill JD, Ridpath JF. Low-level detection of viral pathogens by a surface-enhanced Raman scattering based immunoassay. Anal Chem. 2005;77(19):6147-54. doi: Doi 10.1021/Ac0504159. PubMed PMID: WOS:000232443700018.

205. Harpster MH, Zhang H, Sankara-Warrier AK, Ray BH, Ward TR, Kollmar JP, et al. SERS detection of indirect viral DNA capture using colloidal gold and methylene blue as a Raman label. Biosens Bioelectron. 2009;25(4):674-81. doi: DOI 10.1016/j.bios.2009.05.020. PubMed PMID: WOS:000272439800003.
206. Liang Y, Gong JL, Huang Y, Zheng Y, Jiang JH, Shen GL, et al. Biocompatible core-shell nanoparticle-based surface-enhanced Raman scattering probes for detection of DNA related to HIV gene using silica-coated magnetic nanoparticles as separation tools. Talanta. 2007;72(2):443-9. doi: DOI 10.1016/j.talanta.2006.11.002. PubMed PMID: WOS:000246321200017.
207. Suh JS, Moskovits M. Surface-Enhanced Raman-Spectroscopy of Amino-Acids and Nucleotide Bases Adsorbed on Silver. J Am Chem Soc. 1986;108(16):4711-8. PubMed PMID: ISI:A1986D522600005.
208. Storhoff JJ, Elghanian R, Mucic RC, Mirkin CA, Letsinger RL. One-pot colorimetric differentiation of polynucleotides with single base imperfections using gold nanoparticle probes. J Am Chem Soc. 1998;120(9):1959-64. doi: Doi 10.1021/Ja972332i. PubMed PMID: WOS:000072499100002.
209. Halas NJ. Playing with plasmons. Tuning the optical resonant properties of metallic nanoshells. Mrs Bull. 2005;30(5):362-7. doi: Doi 10.1557/Mrs2005.99. PubMed PMID: WOS:000229129000017.
210. Heck KN, Janesko BG, Scuseria GE, Halas NJ, Wong MS. Observing Metal-Catalyzed Chemical Reactions in Situ Using Surface-Enhanced Raman Spectroscopy on Pd-Au Nanoshells. J Am Chem Soc. 2008;130(49):16592-600. doi: Doi 10.1021/Ja803556k. PubMed PMID: WOS:000263320200048.
211. Lal S, Grady NK, Kundu J, Levin CS, Lassiter JB, Halas NJ. Tailoring plasmonic substrates for surface enhanced spectroscopies. Chem Soc Rev. 2008;37(5):898-911. doi: Doi 10.1039/B705969h. PubMed PMID: WOS:000255444700003.
212. Lassiter JB, Knight MW, Mirin NA, Halas NJ. Reshaping the Plasmonic Properties of an Individual Nanoparticle. Nano Lett. 2009;9(12):4326-32. doi: Doi 10.1021/Nl9025665. PubMed PMID: WOS:000272395400063.
213. Barhoumi A, Zhang D, Tam F, Halas NJ. Surface-enhanced Raman spectroscopy of DNA. J Am Chem Soc. 2008;130(16):5523-9. doi: Doi 10.1021/Ja800023j. PubMed PMID: ISI:000255041400042.
214. Graham D, Faulds K. Quantitative SERRS for DNA sequence analysis. Chem Soc Rev. 2008;37(5):1042-51. doi: Doi 10.1039/B707941a. PubMed PMID: WOS:000255444700016.
215. Graham D, Faulds K, Smith WE. Biosensing using silver nanoparticles and surface enhanced resonance Raman scattering. Chem Commun. 2006(42):4363-71. doi: Doi 10.1039/B607904k. PubMed PMID: WOS:000241470900001.
216. Graham D, Faulds K, Thompson D, McKenzie F, Stokes R, Dalton C, et al. Functionalized nanoparticles for bioanalysis by SERRS. Biochem Soc T. 2009;37:697-701. doi: Doi 10.1042/Bst0370697. PubMed PMID: WOS:000268902800012.
217. Graham D, Goodacre R. Chemical and bioanalytical applications of surface enhanced Raman scattering spectroscopy. Chem Soc Rev. 2008;37(5):883-4. doi: Doi 10.1039/B804297g. PubMed PMID: WOS:000255444700001.

218. Graham D, Thompson DG, Smith WE, Faulds K. Control of enhanced Raman scattering using a DNA-based assembly process of dye-coded nanoparticles. Nat Nanotechnol. 2008;3(9):548-51. doi: DOI 10.1038/nnano.2008.189. PubMed PMID: WOS:000259013100012.
219. Herne TM, Tarlov MJ. Characterization of DNA probes immobilized on gold surfaces. J Am Chem Soc. 1997;119(38):8916-20. doi: Doi 10.1021/Ja9719586. PubMed PMID: WOS:A1997XX82000019.
220. Herne TM, Tarlov MJ. Structural characterization and hybridization reactions of surface bound, single-stranded DNA. Abstr Pap Am Chem S. 1997;214:62-Mtls. PubMed PMID: WOS:A1997XQ85901793.
221. Olsen KG, Steel AB, Tarlov MJ. Immobilized DNA electrodes: The effect of target length on DNA hybridization. Abstr Pap Am Chem S. 2000;220:U273-U. PubMed PMID: WOS:000166091201444.
222. Petrovykh DY, Kimura-Suda H, Whitman LJ, Tarlov MJ. Quantitative analysis and characterization of DNA immobilized on gold. J Am Chem Soc. 2003;125(17):5219-26. doi: Doi 10.1021/Ja029450c. PubMed PMID: WOS:000182491700047.
223. Steel AB, Herne TM, Tarlov MJ. Electrochemical quantitation of DNA immobilized on gold. Anal Chem. 1998;70(22):4670-7. doi: Doi 10.1021/Ac980037q. PubMed PMID: WOS:000077003600004.
224. Tarlov M, Mckenney K, Poirier G, Gillen G, Hogan M, Powdrill T. DNA-Probe Modified Alkanethiol Monolayers. Abstr Pap Am Chem S. 1995;209:160-COLL. PubMed PMID: WOS:A1995QP23201671.
225. Villanueva M, Olsen KG, Steel AB, Tarlov MJ. DNA hybridization on electrode surfaces. Abstr Pap Am Chem S. 2000;220:U144-U. PubMed PMID: WOS:000166091200726.
226. Bunshah RF. Handbook of Deposition Technologies for Films and Coatings. Second ed. ed. Westwood, NJ: Noyes Publications; 1974.
227. Mahan JE. Physical Vapor Deposition of Thin Films. New York, NY: Wiley & Sons; 2000.
228. Ohring M. Material Science of Thin films. San Diego: Academic Press; 2002.
229. Thornton JA. Semiconductor Materials and Process Technology Handbook for Very Large Scale Integration (VLSI) and Ultra Large Scale Integration (ULSI) McGuire GF, editor. Park Ridge, NJ: Noyes Publications; 1988.
230. Maissel L, Glang R. Handbook of Thin Film Technology. New Yor, NY: McGraw-Hill; 1970.
231. Mucha JA, Hess DW, Aydil ES. Plasma Etching. Thompson W, Bowden E, editors: American Chemical Society; 1994.
232. Thornton JA. High Rate Thick Film Growth1977.
233. Powell A, Minson P, Trapaga G, Pal U. Mathematical modeling of vapor-plume focusing in electron-beam evaporation. Metall Mater Trans A. 2001;32(8):1959-66. doi: DOI 10.1007/s11661-001-0008-y. PubMed PMID: WOS:000170682200008.
234. Hawkeye MM, Brett MJ. Glancing angle deposition: Fabrication, properties, and applications of micro- and nanostructured thin films. J Vac Sci Technol A. 2007;25(5):1317-35. doi: Doi 10.1116/1.2764082. PubMed PMID: WOS:000249664400001.

235. Holland L. The Effect of Vapor Incidence on the Structure of Evaporated Aluminum Films. J Opt Soc Am. 1953;43(5):376-80. doi: Doi 10.1364/Josa.43.000376. PubMed PMID: WOS:A1953UG48900010.
236. Holland L. Vapor Deposition of Thin Films. New York, NY: Wiley & Sons; 1956.
237. Knorr TG, Hoffman RW. Dependence of Geometric Magnetic Anisotropy in Thin Iron Films. Physical Review. 1959;113(4):1039-46. doi: DOI 10.1103/PhysRev.113.1039. PubMed PMID: WOS:A1959WB76500016.
238. Kundt A. On the double refraction of light in metal layers which have been prepared by cathode sputtering. Ann Phys. 1986;27(59).
239. Smith DO, Cohen MS, Weiss GP. Oblique-Incidence Anisotropy in Evaporated Permalloy Films. J Appl Phys. 1960;31(10):1755-62. doi: Doi 10.1063/1.1735441. PubMed PMID: WOS:A1960WK25000014.
240. Smith DO, Huber EE, Cohen MS, Weiss GP. Anisotropy and Inversion in Permalloy Films. J Appl Phys. 1960;31(5):S295-S7. doi: Doi 10.1063/1.1984707. PubMed PMID: WOS:A1960WK24500121.
241. Nieuwenh.Jm, Haanstra HB. Microfractography of Thin Films. Philips Tech Rev. 1966;27(3-4):87-&. PubMed PMID: WOS:A19668288400003.
242. Konig H, Helwig G. *Uber Die Struktur Schrag Aufgedampfter Schichten Und Ihr Einfluss Auf Die Entwicklung Submikroskopischer Oberflachenrauhigkeiten. Optik. 1950;6(2):111-24. PubMed PMID: WOS:A1950YF64900004.
243. Brett MJ, Hawkeye MM. Materials science - New materials at a glance. Science. 2008;319(5867):1192-3. doi: DOI 10.1126/science.1153910. PubMed PMID: WOS:000253530600021.
244. Broughton JN, Brett MJ. Electrochemical capacitance in manganese thin films with chevron microstructure. Electrochem Solid St. 2002;5(12):A279-A82. doi: Doi 10.1149/1.1516412. PubMed PMID: WOS:000178821100004.
245. Colgan MJ, Brett MJ. Field emission from carbon and silicon films with pillar microstructure. Thin Solid Films. 2001;389(1-2):1-4. doi: Doi 10.1016/S0040-6090(01)00892-6. PubMed PMID: WOS:000169378200001.
246. Kiema GK, Colgan MJ, Brett MJ. Dye sensitized solar cells incorporating obliquely deposited titanium oxide layers. Sol Energ Mat Sol C. 2005;85(3):321-31. doi: DOI 10.1016/j.solmat.2004.05.001. PubMed PMID: WOS:000226212200003.
247. Bauer E, Vandermerwe JH. Structure and Growth of Crystalline Superlattices - from Monolayer to Superlattice. Phys Rev B. 1986;33(6):3657-71. doi: DOI 10.1103/PhysRevB.33.3657. PubMed PMID: WOS:A1986A463700004.
248. Koch R. The Intrinsic Stress of Polycrystalline and Epitaxial Thin Metal-Films. J Phys-Condens Mat. 1994;6(45):9519-50. doi: Doi 10.1088/0953-8984/6/45/005. PubMed PMID: WOS:A1994PQ90900005.
249. Reichelt K. Nucleation and Growth of Thin-Films. Vacuum. 1988;38(12):1083-99. doi: Doi 10.1016/0042-207x(88)90004-8. PubMed PMID: WOS:A1988R675900004.
250. Vook RW. Theories of Nucleation and Growth of Thin-Films. P Soc Photo-Opt Inst. 1982;346:2-8. PubMed PMID: WOS:A1982PK02100002.

251. Tait RN, Smy T, Brett MJ. Modeling and Characterization of Columnar Growth in Evaporated-Films. Thin Solid Films. 1993;226(2):196-201. doi: Doi 10.1016/0040-6090(93)90378-3. PubMed PMID: WOS:A1993KZ82200002.
252. Barabasi AL, Stanley HE. Fractal Concepts in Surface Growth. Cambridge: Cambridge University Press; 1995.
253. Kaminska K, Amassian A, Martinu L, Robbie K. Growth of vacuum evaporated ultraporous silicon studied with spectroscopic ellipsometry and scanning electron microscopy. J Appl Phys. 2005;97(1). doi: Artn 013511
Doi 10.1063/1.1823029. PubMed PMID: WOS:000226700300019.
254. Karabacak T, Wang GC, Lu TM. Quasi-periodic nanostructures grown by oblique angle deposition. J Appl Phys. 2003;94(12):7723-8. doi: Doi 10.1063/1.1621717. PubMed PMID: WOS:000186969900053.
255. Jensen MO, Brett MJ. Periodically structured glancing angle deposition thin films. Ieee T Nanotechnol. 2005;4(2):269-77. doi: Doi 10.1109/Tnano.2004.842061. PubMed PMID: WOS:000227594900015.
256. Elias AL, Harris KD, Brett MJ. Fabrication of helically perforated gold, nickel, and polystyrene thin films. J Microelectromech S. 2004;13(5):808-13. doi: Doi 10.1109/Jmems.2004.835760. PubMed PMID: WOS:000224413100011.
257. Harris KD, Huizinga A, Brett MJ. High-speed porous thin film humidity sensors. Electrochem Solid St. 2002;5(11):H27-H9. doi: Doi 10.1149/1.1512141. PubMed PMID: WOS:000178145200017.
258. Harris KD, McBride JR, Nietering KE, Brett MJ. Fabrication of porous platinum thin films for hydrocarbon sensor applications. Sensor Mater. 2001;13(4):225-34. PubMed PMID: WOS:000171035300003.
259. Harris KD, Vick D, Gonzalez EJ, Smy T, Robbie K, Brett MJ. Porous thin films for thermal barrier coatings. Surf Coat Tech. 2001;138(2-3):185-91. doi: Doi 10.1016/S0257-8972(00)01155-5. PubMed PMID: WOS:000167450200009.
260. Harris KD, Westra KL, Brett MJ. Fabrication of perforated thin films with helical and chevron pore shapes. Electrochem Solid St. 2001;4(6):C39-C42. doi: Doi 10.1149/1.1371255. PubMed PMID: WOS:000168107000008.
261. Robbie K, Sit JC, Brett MJ. Advanced techniques for glancing angle deposition. J Vac Sci Technol B. 1998;16(3):1115-22. doi: Doi 10.1116/1.590019. PubMed PMID: WOS:000074298300029.
262. Robbie K, Brett MJ. Sculptured thin films and glancing angle deposition: Growth mechanics and applications. Journal of Vacuum Science & Technology a-Vacuum Surfaces and Films. 1997;15(3):1460-5. doi: Doi 10.1116/1.580562. PubMed PMID: WOS:A1997XE73200063.
263. Hodgkinson I. Vacuum Deposition of Biaxial Films with Surface-Aligned Principle Axes and Large Birefringence. Washington DC: Optical Society of America; 1998.
264. Macleod HA. Thin-Film Optical Filters. New York, NY: McGraw-Hill; 1986.
265. Steele JJ, Brett MJ. Nanostructure engineering in porous columnar thin films: recent advances. J Mater Sci-Mater El. 2007;18(4):367-79. doi: DOI 10.1007/s10854-006-9049-8. PubMed PMID: WOS:000243397500001.

266. Hrudey PCP, Westra KL, Brett MJ. Highly ordered organic Alq3 chiral luminescent thin films fabricated by glancing-angle deposition. Adv Mater. 2006;18(2):224-+. doi: DOI 10.1002/adma.200501714. PubMed PMID: WOS:000234993700017.
267. Kaminska K, Brown T, Beydaghyan G, Robbie K. Vacuum evaporated porous silicon photonic interference filters. Appl Optics. 2003;42(20):4212-9. doi: Doi 10.1364/Ao.42.004212. PubMed PMID: WOS:000184029000010.
268. Kaminska K, Robbie K. Birefringent omnidirectional reflector. Appl Optics. 2004;43(7):1570-6. doi: Doi 10.1364/Ao.43.001570. PubMed PMID: WOS:000189378600013.
269. Kennedy SR, Brett MJ. Porous broadband antireflection coating by glancing angle deposition. Appl Optics. 2003;42(22):4573-9. doi: Doi 10.1364/Ao.42.004573. PubMed PMID: WOS:000184382000021.
270. Motohiro T, Taga Y. Thin-Film Retardation Plate by Oblique Deposition. Appl Optics. 1989;28(13):2466-82. PubMed PMID: WOS:A1989AE82600013.
271. Robbie K, Brett MJ, Lakhtakia A. Chiral sculptured thin films. Nature. 1996;384(6610):616-. doi: Doi 10.1038/384616a0. PubMed PMID: WOS:A1996VZ29600023.
272. Steele JJ, van Popta AC, Hawkeye MM, Sit JC, Brett MJ. Nanostructured gradient index optical filter for high-speed humidity sensing. Sensor Actuat B-Chem. 2006;120(1):213-9. doi: DOI 10.1016/j.snb.2006.02.003. PubMed PMID: WOS:000241489300031.
273. van Popta AC, Steele JJ, Tsoi S, Veinot JGC, Brett MJ, Sit JC. Porous nanostructured optical filters rendered insensitive to humidity by vapor-phase functionalization. Adv Funct Mater. 2006;16(10):1331-6. doi: DOI 10.1002/adfm.200500899. PubMed PMID: WOS:000239099100008.
274. Suzuki M, Taga Y. Numerical study of the effective surface area of obliquely deposited thin films. J Appl Phys. 2001;90(11):5599-605. doi: Doi 10.1063/1.1415534. PubMed PMID: WOS:000172129200022.
275. Oregan B, Gratzel M. A Low-Cost, High-Efficiency Solar-Cell Based on Dye-Sensitized Colloidal Tio2 Films. Nature. 1991;353(6346):737-40. doi: Doi 10.1038/353737a0. PubMed PMID: WOS:A1991GL69600062.
276. Saraf L, Matson DW, Shutthanandan V, Wang CM, Marina O, Thevuthasan S. Ceria incorporation into YSZ columnar nanostructures. Electrochem Solid St. 2005;8(10):A525-A7. doi: Doi 10.1149/1.2033607. PubMed PMID: WOS:000231390900010.
277. Steele JJ, Gospodyn JP, Sit JC, Brett MJ. Impact of morphology on high-speed humidity sensor performance. Ieee Sens J. 2006;6(1):24-7. doi: Doi 10.1109/Jsen.2005.859359. PubMed PMID: WOS:000234723300004.
278. Suzuki M, Ito T, Taga Y. Photocatalysis of sculptured thin films of TiO2. Appl Phys Lett. 2001;78(25):3968-70. doi: Doi 10.1063/1.1380730. PubMed PMID: WOS:000169339800015.
279. Tsoi S, Fok E, Sit JC, Veinot JGC. Superhydrophobic, high surface area, 3-D SiO(2) nanostructures through siloxane-based surface functionalization. Langmuir. 2004;20(24):10771-4. doi: Doi 10.1021/La0482507. PubMed PMID: WOS:000225207400058.
280. Tsoi SF, Fok E, Sit JC, Veinot JGC. Surface functionalization of porous nanostructured metal oxide thin films fabricated by glancing angle deposition. Chem Mater. 2006;18(22):5260-6. doi: Doi 10.1021/Cm061709t. PubMed PMID: WOS:000241492900020.

281. Pawar AB, Kretzschmar I. Patchy particles by glancing angle deposition. Langmuir. 2008;24(2):355-8. doi: Doi 10.1021/La703005z. PubMed PMID: WOS:000252208200003.
282. Pawar AB, Kretzschmar I. Multifunctional Patchy Particles by Glancing Angle Deposition. Langmuir. 2009;25(16):9057-63. doi: Doi 10.1021/La900809b. PubMed PMID: WOS:000268719900038.
283. McDermott JJ, Velegol D. Simple fabrication of metallic colloidal doublets having electrical connectivity. Langmuir. 2008;24(8):4335-9. doi: Doi 10.1021/La703894v. PubMed PMID: WOS:000254647400093.
284. Abell JL, Garren JM, Driskell JD, Tripp RA, Zhao Y. Label-Free Detection of Micro-RNA Hybridization Using Surface-Enhanced Raman Spectroscopy and Least-Squares Analysis. J Am Chem Soc. 2012. Epub 2012/07/14. doi: 10.1021/ja3043432. PubMed PMID: 22788749.
285. Beavers KR, Marotta NE, Bottomley LA. Thermal Stability of Silver Nanorod Arrays. Chem Mater. 2010;22(7):2184-9. doi: Doi 10.1021/Cm901791u. PubMed PMID: ISI:000276394800004.
286. Beavers KR, Marotta NE, Bottomley LA. Thermal Stability of Silver Nanorod Arrays. Chem Mater. 2010;22:2184-9.
287. Chaney SB, Shanmukh S, Dluhy RA, Zhao YP. Aligned Silver Nanorod Arrays Produce High Sensitivity Surface-Enhanced Raman Spectroscopy Substrates. Appl Phys Lett. 2005;87.
288. Chaney SB, Shanmukh S, Zhao Y-P, Dluhy RA. Randomly aligned silver nanorod arrays produce high sensitivity SERS substrates. Appl Phys Lett. 2005;87:31908-10.
289. Chu HY, Huang YW, Zhao YP. Silver nanorod arrays as a surface-enhanced Raman scattering substrate for foodborne pathogenic bacteria detection. Appl Spectrosc. 2008;62(8):922-31. PubMed PMID: ISI:000258418600014.
290. Driskell JD, Primera-Pedrozo OM, Dluhy RA, Zhao YP, Tripp RA. Quantitative Surface-Enhanced Raman Spectroscopy Based Analysis of MicroRNA Mixtures. Appl Spectrosc. 2009;63(10):1107-14. PubMed PMID: ISI:000274012000004.
291. Driskell JD, Shanmukh S, Liu Y, Chaney SB, Tang X-J, Zhao Y-P, et al. The Use of Aligned Silver Nanorod Arrays Prepared by Oblique Angle Deposition as Surface Enhanced Raman Scattering Substrates. J Phys Chem C. 2008;112:895-901.
292. Driskell JD, Shanmukh S, Liu Y-J, Hennigan S, Jones L, Zhao Y-P, et al. Infectious Agent Detection With SERS-Active Silver Nanorod Arrays Prepared by Oblique Angle Deposition. IEES Sens J. 2008;8(6):863-70.
293. Driskell JD, Tripp RA. Label-free SERS detection of microRNA based on affinity for an unmodified silver nanorod array substrate. Chem Commun. 2010;46(19):3298-300. doi: Doi 10.1039/C002059a. PubMed PMID: ISI:000277318000018.
294. Driskell JD, Zhu Y, Kirkwood CD, Zhao YP, Dluhy RA, Tripp RA. Rapid and Sensitive Detection of Rotavirus Molecular Signatures Using Surface Enhanced Raman Spectroscopy. Plos One. 2010;5(4). doi: ARTN e10222
DOI 10.1371/journal.pone.0010222. PubMed PMID: ISI:000276853800013.
295. Hennigan SL, Driskell JD, Dluhy RA, Zhao YP, Tripp RA, Waites KB, et al. Detection of Mycoplasma pneumoniae in Simulated and True Clinical Throat Swab Specimens by Nanorod Array-Surface-Enhanced Raman Spectroscopy. Plos One. 2010;5(10). doi: ARTN e13633
DOI 10.1371/journal.pone.0013633. PubMed PMID: ISI:000283487400023.

296. Hennigan SL, Driskell JD, Ferguson-Noel N, Dluhy RA, Zhao YP, Tripp RA, et al. Detection and Differentiation of Avian Mycoplasmas by Surface-Enhanced Raman Spectroscopy Based on a Silver Nanorod Array. Appl Environ Microbiol. 2012;78(6):1930-5. doi: Doi 10.1128/Aem.07419-11. PubMed PMID: ISI:000300629800034.
297. Hoang V, Tripp RA, Rota P, Dluhy RA. Identification of individual genotypes of measles virus using surface enhanced Raman spectroscopy. Analyst. 2010;135(12):3103-9. doi: Doi 10.1039/C0an00453g. PubMed PMID: ISI:000284265700013.
298. Liu Y-J, Zhang Z-Y, Dluhy RA, Zhao Y-P. The SERS response of semiordered Ag nanorod arrays fabricated by template oblique angle deposition. J Raman Spectrosc. 2010;In Press. doi: 10.1002/jrs.2567.
299. Marotta NE, Barber JR, Dluhy PR, Bottomley LA. Patterned Silver Nanorod Array Substrates for Surface-Enhanced Raman Scattering. Appl Spectrosc. 2009;63(10):1101-6. PubMed PMID: ISI:000274012000003.
300. Marotta NE, Bottomley LA. Surface-Enhanced Raman Scattering of Bacterial Cell Culture Growth Media. Appl Spectrosc. 2010;64(6):601-6. PubMed PMID: ISI:000278686100006.
301. Negri P, Marotta NE, Bottomley LA, Dluhy RA. Removal of Surface Contamination and Self-Assembled Monolayers (SAMs) from Silver (Ag) Nanorod Substrates by Plasma Cleaning with Argon. Appl Spectrosc. 2011;65(1):66-74. Epub 2011/01/08. doi: 10.1366/10-06037. PubMed PMID: 21211156.
302. Negri P, Chen G, Kage A, Nitsche A, Naumann D, Xu B, et al. Direct optical detection of viral nucleoprotein binding to an anti-influenza aptamer. Anal Chem. 2012;84(13):5501-8. Epub 2012/06/13. doi: 10.1021/ac202427e. PubMed PMID: 22687054.
303. Negri P, Kage A, Nitsche A, Naumann D, Dluhy RA. Detection of viral nucleoprotein binding to anti-influenza aptamers via SERS. Chem Commun. 2011;47(30):8635-7. doi: Doi 10.1039/C0cc05433j. PubMed PMID: ISI:000292986800047.
304. Gersten JI. The Effect of Surface-Roughness on Surface Enhanced Raman-Scattering. J Chem Phys. 1980;72(10):5779-80. PubMed PMID: ISI:A1980JU69700065.
305. Gersten JI. Rayleigh, Mie, and Raman-Scattering by Molecules Adsorbed on Rough Surfaces. J Chem Phys. 1980;72(10):5780-1. PubMed PMID: ISI:A1980JU69700066.
306. Schatz GC. Theoretical-Studies of Surface Enhanced Raman-Scattering. Acc Chem Res. 1984;17(10):370-6. PubMed PMID: ISI:A1984TT29300007.
307. Zhao YP, Chaney SB, Shanmukh S, Dluhy RA. Polarized surface enhanced raman and absorbance spectra of aligned silver nanorod arrays. J Phys Chem B. 2006;110(7):3153-7. doi: Doi 10.1021/Jp057406o. PubMed PMID: ISI:000235560900030.
308. Leverette CL, Jacobs SA, Shanmukh S, Chaney SB, Dluhy RA, Zhao YP. Aligned silver nanorod arrays as substrates for surface-enhanced infrared absorption spectroscopy. Appl Spectrosc. 2006;60(8):906-13. PubMed PMID: ISI:000239912900011.
309. Félidj N, Aubard J, Lévi G, Krenn JR, Salerno M, Schider G, et al. Controlling The Optical Response of Regular Arrays of Gold Particles for Surface-Enhanced Raman Scattering. Phys Rev B. 2002;65:075419-1 - -9.

310. Freeman RG, Grabar KC, Allison KJ, Bright RM, Davis JA, Guthrie AP, et al. Self-Assembled Metal Colloid Monolayers: An Approach to SERS Substrates. Science. 1995;267(5204):1629-32. doi: 10.1126/science.267.5204.1629.
311. Gupta R, Weimer WA. High enhancement factor gold films for surface enhanced Raman spectroscopy. Chem Physics Lett. 2003;374:302-6.
312. Hulteen JC, Van Duyne RP. Nanosphere Lithography: A Materials General Fabrication Process for Periodic Particle Array Surfaces. J Vac Sci Technol. 1995;13:1553-8.
313. Kerker MO, Siiman O, Wang D-S. Effect of aggregates on extinction and surface-enhanced Raman scattering spectra of colloidal silver. J Phys Chem. 1984;88:3168-70.
314. Li MD, Cui Y, Gao MX, Luo J, Ren B, Tian ZQ. Clean substrates prepared by chemical adsorption of iodide followed by electrochemical oxidation for surface-enhanced Raman spectroscopic study of cell membrane. Anal Chem. 2008;80(13):5118-25. doi: Doi 10.1021/Ac8003083. PubMed PMID: WOS:000257270600047.
315. Taylor CE, Garvey SD, Pemberton JE. Carbon contamination at silver surfaces: Surface preparation procedures evaluated by Raman spectroscopy and X-ray photoelectron spectroscopy. Anal Chem. 1996;68(14):2401-8. doi: Doi 10.1021/Ac950753h. PubMed PMID: WOS:A1996UY08700018.
316. Taylor CE, Schoenfisch MH, Pemberton JE. Sequestration of carbonaceous species within alkanethiol self-assembled monolayers on Ag by Raman spectroscopy. Langmuir. 2000;16(6):2902-6. PubMed PMID: ISI:000085984500070.
317. Cooney RP, Mahoney MR, Howard MW. Intense Raman-Spectra of Surface Carbon and Hydrocarbons on Silver Electrodes. Chem Phys Lett. 1980;76(3):448-52. PubMed PMID: ISI:A1980KY61300011.
318. Schoenfisch MH, Ross AM, Pemberton JE. Electrochemical cleaning of surface-confined carbon contamination in self-assembled monolayers on polycrystalline Ag and Au. Langmuir. 2000;16(6):2907-14. PubMed PMID: ISI:000085984500071.
319. Erol M, Han Y, Stanley SK, Stafford CM, Du H, Sukhishvili S. SERS Not To Be Taken for Granted in the Presence of Oxygen. J Am Chem Soc. 2009;131(22):7480-+. doi: Doi 10.1021/Ja807458x. PubMed PMID: WOS:000267177900001.
320. Zou SZ, Chen YX, Mao BW, Ren B, Tian ZQ. SERS studies on electrode/electrolyte interfacial water .1. Ion effects in the negative potential region. J Electroanal Chem. 1997;424(1-2):19-24. doi: Doi 10.1016/S0022-0728(96)04925-X. PubMed PMID: WOS:A1997XB38100004.
321. Cooper E, Leggett GJ. Influence of Tail-Group Hydrogen Bonding on the Stabilities of SAMs of Alkylthiols on Gold. Langmuir. 1994;15:1024-32.
322. English RD, Van Stipdonk MJ, Sabapathy RC, Crooks RM, Schweikert EA. Characterization of photooxidized self-assembled monolayers and bilayers by spontaneous desorption mass spectrometry. Anal Chem. 2000;72(24):5973-80. doi: Doi 10.1021/Ac0008892. PubMed PMID: WOS:000165879900016.
323. Hutt DA, Leggett GJ. Influence of adsorbate ordering on rates of UV photooxidation of self-assembled monolayers. J Phys Chem-Us. 1996;100(16):6657-62. doi: Doi 10.1021/Jp952734h. PubMed PMID: WOS:A1996UF87900045.

324. Munakata H, Oyamatsu D, Kuwabata S. Effects of omega-functional groups on pH-dependent reductive desorption of alkanethiol self-assembled monolayers. Langmuir. 2004;20(23):10123-8. doi: Doi 10.1021/La048878h. PubMed PMID: WOS:000224981600038.
325. Shepherd JL, Kell A, Chung E, Sinclar CW, Workentin MS, Bizzotto D. Selective reductive desorption of a SAM-coated gold electrode revealed using fluorescence microscopy. J Am Chem Soc. 2004;126(26):8329-35. doi: Doi 10.1021/Ja0494095. PubMed PMID: WOS:000222405400059.
326. Schneider TW, Buttry DA. Electrochemical Quartz Crystal Microbalance Studies of Adsorption and Desorption of Self-Assembled Monolayers of Alkyl Thiols on Gold. J Am Chem Soc. 1993;115:12391-7.
327. Norrod KL, Rowlen KL. Removal of Carbonaceous Contamination from SERS-Active Silver by Self-Assembly of Decanethiol
Anal Chem. 1998;70:4218-21.
328. Laibinis PE, Whitesides GM, Allara DL, Tao YT, Parikh AN, Nuzzo RG. Comparison of the Structures and Wetting Properties of Self-Assembled Monolayers of Normal-Alkanethiols on the Coinage Metal-Surfaces, Cu, Ag, Au. J Am Chem Soc. 1991;113(19):7152-67. PubMed PMID: ISI:A1991GF10400011.
329. Bryant MA, Pemberton JE. Surface Raman Scattering of Self-Assembled Monolayers Formed from 1-Alkanethiols: Behavior of Films at Au and Comparison to Films at Ag. J Am Chem Soc. 1991;113:8284-93.
330. Yuan M, Zhan S, Zhou X, Liu Y, Feng L, Lin Y, et al. A Method for Removing Self-Assembled Monolayers On Gold. Langmuir. 2008;24:8707-10.
331. Deschaines TO, Carron KT. Stability and Surface Uniformity of Selected Thiol-Coated SERS Surfaces. Appl Spectrosc. 1997;51:1355-9.
332. Abell JL, Driskell JD, Dluhy RA, Tripp RA, Zhao Y-P. Fabrication and Characterization of a Multiwell Array SERS Chip With Biological Applications. Biosens Bioelec. 2009.
333. Leverette CL, Jacobs SA, Shanmukh S, Chaney SB, Dluhy RA, Zhao Y-P. Aligned Silver Nanorod Arrays as Substrates for Surface-Enhanced Infrared Absorption Spectrocopy. Appl Spectrosc. 2006;60(8):906-13.
334. Alsmeyer YW, McCreery RL. Surface-Enhanced Raman Spectroscopy of Carbon Electrode Surfaces Following Silver Electrodeposition. Anal Chem. 1991;63:1289-95.
335. Yang W-H, Hulteen JC, Schatz GC, Van Duyne RP. A Surface-Enhanced Hyper-Raman and Surface-Enhanced Raman Scattering Study of trans-1,2-bis(4-pyridyl)ethylene Adsorbed Onto Silver Film Over Nanosphere Electrodes. Vibrational Assignments: Experiment and Theory. J Chem Phys. 1996;104.
336. Joo TH, Kim K, Kim MS. Surface-Enhanced Raman Scattering (SERS) of 1 - Propanethlol in Silver Sol. J Phys Chem. 1986;90:5816-9.
337. Erol M, Han Y, Stanley SK, Stafford CM, Du H, Sukhishvili S. SERS Not To Be Taken for Granted in the Presence of Oxygen. J Am Chem Soc. 2009;131:7480-1.
338. Haynes CL, McFarland AD, Zhao L, Duyne RPV, Schatz GC. Nanoparticle Optics: The Importance of Radiative Dipole Coupling in Two-Dimensional Nanoparticle Arrays. J Phys Chem. 2003;107.

339. Kahl M, Voges E. Analysis of Plasmon Resonance and Surface-Enhanced Raman Scattering On Periodic Silver Sutructures. Phys Rev B. 2000;61(20):14 078-14 88.
340. Liu YJ, Zhang ZY, Zhao Q, Dluhy RA, Zhao YP. The role of the nanospine in the nanocomb arrays for surface enhanced Raman scattering. Appl Phys Lett. 2009;94(3). doi: 033103
10.1063/1.3075958. PubMed PMID: ISI:000262724000032.
341. Smith T. The Hydrophilic Nature of a Clean Gold Surface. J Coll Inter Sci. 1980;75(1):51-5.
342. Bico J, Marzolin C, Quéré D. Pearl Drops. Europhys Lett. 1999;47:220-6.
343. Johnson RE, Dettre RH. Contact Angle, Wettability and Adhesion. Adv Chem Ser. 1964;43.
344. Cheng Y-T, Rodak DE, Angelopoulos A, Gacek T. Microscopic Observation of Condensation of Water On Lotus Leaves. Appl Phys Lett. 2005;87(19).
345. Chou IH, Benford M, Beier HT, Cote GL, Wang M, Jing N, et al. Nanofluidic biosensing for beta-amyloid detection using surface enhanced Raman spectroscopy. Nano Lett. 2008;8(6):1729-35. doi: Doi 10.1021/Nl0808132. PubMed PMID: ISI:000256742000031.
346. Kneipp K, Kneipp H, Itzkan I, Dasari RR, Feld MS. Surface-enhanced Raman scattering: A new tool for biomedical spectroscopy. Curr Sci. 1999;77(7):915-24. PubMed PMID: ISI:000083179400021.
347. Vo-Dinh T, Yan F, Wabuyele MB. Surface-enhanced Raman scattering for medical diagnostics and biological imaging. J Raman Spectrosc. 2005;36(6-7):640-7. doi: Doi 10.1002/Jrs.1348. PubMed PMID: ISI:000230829200022.
348. Kneipp K, Kneipp H, Itzkan I, Dasari RR, Feld MS. Surface-enhanced Raman scattering and biophysics. J Phys-Condens Mat. 2002;14(18):R597-R624. PubMed PMID: ISI:000175816300003.
349. Carey PR. Biochemical applications of Raman and resonance Raman spectroscopies. New York: Academic Press; 1982. xi, 262 p. p.
350. Guerrero AR, Aroca RF. Surface-Enhanced Fluorescence with Shell-Isolated Nanoparticles (SHINEF). Angew Chem Int Edit. 2011;50(3):665-8. doi: DOI 10.1002/anie.201004806. PubMed PMID: ISI:000286573700015.
351. Bantz KC, Meyer AF, Wittenberg NJ, Im H, Kurtulus O, Lee SH, et al. Recent progress in SERS biosensing. Phys Chem Chem Phys. 2011;13(24):11551-67. doi: Doi 10.1039/C0cp01841d. PubMed PMID: ISI:000291395200011.
352. Jarvis RM, Goodacre R. Characterisation and identification of bacteria using SERS. Chem Soc Rev. 2008;37(5):931-6. doi: Doi 10.1039/B705973f. PubMed PMID: ISI:000255444700006.
353. Chao RK, Fishaut M, Schwartzman JD, Mcintosh K. Detection of Respiratory Syncytial Virus in Nasal Secretions from Infants by Enzyme-Linked Immunosorbent Assay. J Infect Dis. 1979;139(4):483-6. PubMed PMID: ISI:A1979GT23700016.
354. Pedneault L, Robillard L, Turgeon JP. Validation of Respiratory Syncytial Virus Enzyme-Immunoassay and Shell Vial Assay Results. J Clin Microbiol Infect Dis. 1994;32(11):2861-4. PubMed PMID: ISI:A1994PM49500044.

355. Petitjean-Lecherbonnier J, Vabret A, Gouarin S, Dina J, Legrand L, Freymuth F. Mycoplasma pneumoniae infections: retrospective study in Basse-Normandie, 1997-2005. Epidemiology - Diagnostic utility of serology and PCR for a rapid diagnostic. Pathol Biol. 2006;54(10):603-11. doi: DOI 10.1016/j.patbio.2006.07.038. PubMed PMID: ISI:000242843700013.
356. Freymuth F, Eugene G, Vabret A, Petitjean J, Gennetay E, Brouard J, et al. Detection of Respiratory Syncytial Virus by Reverse Transcription Pcr and Hybridization with a DNA Enzyme-Immunoassay. J Clin Microbiol. 1995;33(12):3352-5. PubMed PMID: ISI:A1995TF01500062.
357. Henkel JH, Aberle SW, Kundi M, PopowKraupp T. Improved detection of respiratory syncytial virus in nasal aspirates by seminested RT-PCR. J Med Virol. 1997;53(4):366-71. PubMed PMID: ISI:A1997YJ68500009.
358. Pitcher D, Chalker VJ, Sheppard C, George RC, Harrison TG. Real-time detection of Mycoplasma pneumoniae in respiratory samples with an internal processing control. J Med Microbiol. 2006;55(2):149-55. doi: DOI 10.1099/jmm.0.46281-0. PubMed PMID: ISI:000235494600004.
359. Connor EM, Loeb MR. A Hemadsorption Method for Detection of Colonies of Hemophilus-Influenzae Type-B Expressing Fimbriae. J Infect Dis. 1983;148(5):855-60. PubMed PMID: ISI:A1983RR57200010.
360. Uhlendorff J, Matrosovich T, Klenk HD, Matrosovich M. Functional significance of the hemadsorption activity of influenza virus neuraminidase and its alteration in pandemic viruses. Arch Virol. 2009;154(6):945-57. doi: 10.1007/s00705-009-0393-x. PubMed PMID: ISI:000267028500005.
361. Premasiri WR, Moir DT, Klempner MS, Krieger N, Jones G, Ziegler LD. Characterization of the Surface Enhanced Raman Scattering (SERS) of bacteria. J Phys Chem B. 2005;109(1):312-20. doi: Doi 10.1021/Jp040442n. PubMed PMID: ISI:000226213200047.
362. Jarvis RM, Brooker A, Goodacre R. Surface-enhanced Raman spectroscopy for bacterial discrimination utilizing a scanning electron microscope with a Raman spectroscopy interface. Anal Chem. 2004;76(17):5198-202. doi: Doi 10.1021/Ac049663f. PubMed PMID: ISI:000223733400057.
363. Jarvis RM, Goodacre R. Discrimination of bacteria using surface-enhanced Raman spectroscopy. Anal Chem. 2004;76(1):40-7. doi: Doi 10.1021/Ac034689c. PubMed PMID: ISI:000187806100010.
364. Mandell GLD, R. G., Jr; Bennett, J. E. Principles and practice of infectious diseases. New York
John Wiley & Sons.; 1979.
365. Mazenko RS, Rieders F, Brewster JD. Filtration capture immunoassay for bacteria: optimization and potential for urinalysis. J Microbiol Methods. 1999;36(3):157-65. PubMed PMID: ISI:000080649600002.
366. Graham CRNaA. PCR. Oxford: Bios Scientific; 1997.
367. Levisohn S, Kleven SH. Avian mycoplasmosis (Mycoplasma gallisepticum). Rev Sci Tech OIE. 2000;19(2):425-42. PubMed PMID: ISI:000088194900007.

368. Avakian AP, Kleven SH, Glisson JR. Evaluation of the Specificity and Sensitivity of 2 Commercial Enzyme-Linked Immunosorbent-Assay Kits, the Serum Plate Agglutination-Test, and the Hemagglutination-Inhibition Test for Antibodies Formed in Response to Mycoplasma-Gallisepticum. Avian Dis. 1988;32(2):262-72. PubMed PMID: ISI:A1988P001500011.
369. Henle W. Interference Phenomena between Animal Viruses - a Review. J Immunol. 1950;64(3):203-36. PubMed PMID: ISI:A1950UE64200010.
370. Barenfanger J, Drake C, Leon N, Mueller T, Troutt T. Clinical and financial benefits of rapid detection of respiratory viruses: an outcomes study. J Clin Microbiol. 2000;38(8):2824-8. PubMed PMID: ISI:000088561700004.
371. Bartel B. MicroRNAs directing siRNA biogenesis. Nat Struct Mol Biol. 2005;12(7):569-71. doi: Doi 10.1038/Nsmb0705-569. PubMed PMID: ISI:000230248400007.
372. Bartel DP. MicroRNAs: Genomics, biogenesis, mechanism, and function. Cell. 2004;116(2):281-97. PubMed PMID: ISI:000188541700017.
373. Driskell JD, Seto AG, Jones LP, Jokela S, Dluhy RA, Zhao Y-P, et al. Rapid MicroRNA (miRNA) Detection and Classification Via Surface-Enhanced Raman Spectroscopy (SERS). Biosens Bioelec. 2008;24:917-22.
374. Basler CF, Aguilar PV. Progress in identifying virulence determinants of the 1918 H1N1 and the Southeast Asian H5N1 influenza A viruses. Antivir Res. 2008;79(3):166-78. doi: 10.1016/j.antiviral.2008.04.006. PubMed PMID: ISI:000258438600002.
375. Smith GJD, Vijaykrishna D, Bahl J, Lycett SJ, Worobey M, Pybus OG, et al. Origins and evolutionary genomics of the 2009 swine-origin H1N1 influenza A epidemic. Nature. 2009;459(7250):1122-5. doi: Doi 10.1038/Nature08182. PubMed PMID: ISI:000267636700042.
376. Garten RJ, Davis CT, Russell CA, Shu B, Lindstrom S, Balish A, et al. Antigenic and Genetic Characteristics of Swine-Origin 2009 A(H1N1) Influenza Viruses Circulating in Humans. Science. 2009;325(5937):197-201. doi: DOI 10.1126/science.1176225. PubMed PMID: ISI:000267802000046.
377. Nguyen-Van-Tam JS, Hampson AW. The epidemiology and clinical impact of pandemic influenza. Vaccine. 2003;21(16):1762-8. doi: 10.1016/s0264-410x(03)00069-0. PubMed PMID: ISI:000182575500006.
378. Amano Y, Cheng Q. Detection of influenza virus: traditional approaches and development of biosensors. Anal Bioanal Chem. 2005;381(1):156-64. doi: DOI 10.1007/s00216-004-2927-0. PubMed PMID: ISI:000226888300037.
379. Watcharatanyatip K, Boonmoh S, Chaichoun K, Songserm T, Woratanti M, Dharakul T. Multispecies detection of antibodies to influenza A viruses by a double-antigen sandwich ELISA. J Virol Methods. 2010;163(2):238-43. Epub 2009/10/13. doi: S0166-0934(09)00439-X [pii]
10.1016/j.jviromet.2009.09.027. PubMed PMID: 19819261.
380. Prabakaran M, Ho HT, Prabhu N, Velumani S, Szyporta M, He F, et al. Development of epitope-blocking ELISA for universal detection of antibodies to human H5N1 influenza viruses. Plos One. 2009;4(2):e4566. Epub 2009/02/25. doi: 10.1371/journal.pone.0004566. PubMed PMID: 19238211; PubMed Central PMCID: PMC2642733.
381. Song DS, Lee YJ, Jeong OM, Kim YJ, Park CH, Yoo JE, et al. Evaluation of a competitive ELISA for antibody detection against avian influenza virus. J Vet Sci.

2009;10(4):323-9. Epub 2009/11/26. doi: 200912323 [pii]. PubMed PMID: 19934598; PubMed Central PMCID: PMC2807269.
382. Ellington AD, Szostak JW. Selection in-vitro of single-stranded DNA molecules that fold into specific ligand-binding structures Nature. 1992;355(6363):850-2. PubMed PMID: ISI:A1992HF63600064.
383. Tuerk C, Gold L. Systematic evolution of ligands by exponential enrichment: RNA ligands to bacteriophage T4 DNA polymerase. Science. 1990;249(4968):505-10. Epub 1990/08/03. PubMed PMID: 2200121.
384. Hermann T, Patel DJ. Biochemistry - Adaptive recognition by nucleic acid aptamers. Science. 2000;287(5454):820-5. PubMed PMID: ISI:000085136400036.
385. Jayasena SD. Aptamers: An emerging class of molecules that rival antibodies in diagnostics. Clin Chem. 1999;45(9):1628-50. PubMed PMID: ISI:000082382100044.
386. Tombelli S, Minunni A, Mascini A. Analytical applications of aptamers. Biosens Bioelectron. 2005;20(12):2424-34. doi: DOI 10.1016/j.bios.2004.11.006. PubMed PMID: ISI:000229165000005.
387. Wang GQ, Wang YQ, Chen LX, Choo J. Nanomaterial-assisted aptamers for optical sensing. Biosens Bioelectron. 2010;25(8):1859-68. doi: DOI 10.1016/j.bios.2009.11.012. PubMed PMID: ISI:000276424200001.
388. Klussmann S, Nolte A, Bald R, Erdmann VA, Furste JP. Mirror-image RNA that binds D-adenosine. Nat Biotechnol. 1996;14(9):1112-5. PubMed PMID: ISI:A1996VF84300032.
389. Bruno JG, Kiel JL. In vitro selection of DNA aptamers to anthrax spores with electrochemiluminescence detection. Biosens Bioelectron. 1999;14(5):457-64. PubMed PMID: ISI:000081650000002.
390. Tang JJ, Xie JW, Shao NS, Yan Y. The DNA aptamers that specifically recognize ricin toxin are selected by two in vitro selection methods. Electrophoresis. 2006;27(7):1303-11. doi: DOI 10.1002/elps.200500489. PubMed PMID: ISI:000236845800004.
391. Brody EN, Gold L. Aptamers as therapeutic and diagnostic agents. J Biotechnol. 2000;74(1):5-13. Epub 2000/08/16. doi: S1389-0352(99)00004-5 [pii]. PubMed PMID: 10943568.
392. Tombelli S, Minunni M, Mascini M. Aptamers-based assays for diagnostics, environmental and food analysis. Biomol Eng 2007;24(2):191-200. doi: DOI 10.1016/j.bioeng.2007.03.003. PubMed PMID: ISI:000247422300004.
393. Guthrie JW, Hamula CLA, Zhang HQ, Le XC. Assays for cytokines using aptamers. Methods. 2006;38(4):324-30. doi: DOI 10.1016/j.ymeth.2006.01.001. PubMed PMID: ISI:000236599100011.
394. Bock LC, Griffin LC, Latham JA, Vermaas EH, Toole JJ. Selection of Single-Stranded-DNA Molecules That Bind and Inhibit Human Thrombin. Nature. 1992;355(6360):564-6. PubMed PMID: ISI:A1992HC52600065.
395. Purschke WG, Eulberg D, Buchner K, Vonhoff S, Klussmann S. An L-RNA-based aquaretic agent that inhibits vasopressin in vivo. Proc Natl Acad Sci USA. 2006;103(13):5173-8. doi: 10.1073/pnas.0509663103. PubMed PMID: ISI:000236472500068.

396. Wiegand TW, Williams PB, Dreskin SC, Jouvin MH, Kinet JP, Tasset D. High-affinity oligonucleotide ligands to human IgE inhibit binding to Fc epsilon receptor I. J Immunol. 1996;157(1):221-30. PubMed PMID: ISI:A1996UT10900028.
397. Jensen KB, Atkinson BL, Willis MC, Koch TH, Gold L. Using in vitro selection to direct the covalent attachment of human immunodeficiency virus type 1 Rev protein to high-affinity RNA ligands. Proc Natl Acad Sci U S A. 1995;92(26):12220-4. Epub 1995/12/19. PubMed PMID: 8618873; PubMed Central PMCID: PMC40328.
398. Gopinath SCB, Misono TS, Kawasaki K, Mizuno T, Imai M, Odagiri T, et al. An RNA aptamer that distinguishes between closely related human influenza viruses and inhibits haemagglutinin-mediated membrane fusion. J Gen Virol. 2006;87:479-87. doi: DOI 10.1099/vir.0.81508-0. PubMed PMID: ISI:000235744000001.
399. Jeon SH, Kayhan B, Ben-Yedidia T, Arnon R. A DNA aptamer prevents influenza infection by blocking the receptor binding region of the viral hemagglutinin. J Biol Chem. 2004;279(46):48410-9. doi: DOI 10.1074/jbc.M409059200. PubMed PMID: ISI:000224957000117.
400. Koch TH, Smith D, Tabacman E, Zichi DA. Kinetic analysis of site-specific photoaptamer-protein cross-linking. J Mol Bio. 2004;336(5):1159-73. doi: DOI 10.1016/j.jmb.2004.01.001. PubMed PMID: ISI:000189289300014.
401. Balamurugan S, Obubuafo A, Soper SA, Spivak DA. Surface immobilization methods for aptamer diagnostic applications. Anal Bioanal Chem. 2008;390(4):1009-21. doi: DOI 10.1007/s00216-007-1587-2. PubMed PMID: ISI:000252918100003.
402. Tombelli S, Minunni A, Luzi E, Mascini M. Aptamer-based biosensors for the detection of HIV-1 Tat protein. Bioelectrochemistry. 2005;67(2):135-41. doi: DOI 10.1016/j.bioelechem.2004.04.011. PubMed PMID: ISI:000232360800002.
403. Strehlitz B, Nikolaus N, Stoltenburg R. Protein detection with aptamer biosensors. Sensors. 2008;8(7):4296-307. doi: Doi 10.3390/S8074296. PubMed PMID: ISI:000258180500016.
404. Baldrich E, Restrepo A, O'Sullivan CK. Aptasensor development: Elucidation of critical parameters for optimal aptamer performance. Anal Chem. 2004;76(23):7053-63. doi: Doi 10.1021/Ac049258o. PubMed PMID: ISI:000225535300035.
405. Bonham AJ, Braun G, Pavel I, Moskovits M, Reich NO. Detection of sequence-specific protein-DNA interactions via surface enhanced resonance Raman scattering. J Am Chem Soc. 2007;129(47):14572-+. doi: Doi 10.1021/Ja0767837. PubMed PMID: ISI:000251142200022.
406. Sun L, Irudayaraj J. Quantitative Surface-Enhanced Raman for Gene Expression Estimation. Biophysical Journal. 2009;96(11):4709-16. doi: DOI 10.1016/j.bpj.2009.03.021. PubMed PMID: ISI:000266650400035.
407. Barhoumi A, Halas NJ. Label-Free Detection of DNA Hybridization Using Surface Enhanced Raman Spectroscopy. J Am Chem Soc. 2010;132(37):12792-3. doi: Doi 10.1021/Ja105678z. PubMed PMID: WOS:000282013700012.
408. Levin CS, Kundu J, Barhoumi A, Halas NJ. Nanoshell-based substrates for surface enhanced spectroscopic detection of biomolecules. Analyst. 2009;134(9):1745-50.
409. Moody B, McCarty G. Statistically Significant Raman Detection of Midsequence Single Nucleotide Polymorphisms. Anal Chem. 2009;81(5):2013-6. doi: 10.1021/ac802247y.

410. Neumann O, Zhang DM, Tam F, Lal S, Wittung-Stafshede P, Halas NJ. Direct Optical Detection of Aptamer Conformational Changes Induced by Target Molecules. Anal Chem. 2009;81(24):10002-6. doi: Doi 10.1021/Ac901849k. PubMed PMID: ISI:000272562200020.
411. Chen JW, Liu XP, Feng KJ, Liang Y, Jiang JH, Shen GL, et al. Detection of adenosine using surface-enhanced Raman scattering based on structure-switching signaling aptamer. Biosens Bioelectron. 2008;24(1):66-71. doi: DOI 10.1016/j.bios.2008.03.013. PubMed PMID: ISI:000259425300010.
412. Chen JW, Jiang JH, Gao X, Liu GK, Shen GL, Yu RQ. A New Aptameric Biosensor for Cocaine Based on Surface-Enhanced Raman Scattering Spectroscopy. Chem-Eur J. 2008;14(27):8374-82. doi: DOI 10.1002/chem.200701307. PubMed PMID: ISI:000259913900034.
413. Wang Y, Wei H, Li B, Ren W, Guo S, Dong S, et al. SERS opens a new way in aptasensor for protein recognition with high sensitivity and selectivity. Chem Commun. 2007(48):5220-2. doi: Doi 10.1039/B709492b. PubMed PMID: ISI:000251417600029.
414. Pagba CV, Lane SM, Cho H, Wachsmann-Hogiu S. Direct detection of aptamer-thrombin binding via surface-enhanced Raman spectroscopy. J Biomed Opt. 2010;15(4):047006. Epub 2010/08/31. doi: 10.1117/1.3465594. PubMed PMID: 20799837.
415. Pagba CV, Lane SM, Wachsmann-Hogiu S. Raman and surface-enhanced Raman spectroscopic studies of the 15-mer DNA thrombin-binding aptamer. J Raman Spectrosc. 2010;41(3):241-7. doi: Doi 10.1002/Jrs.2428. PubMed PMID: ISI:000276649900001.
416. Ochsenkuhn MA, Campbell CJ. Probing biomolecular interactions using surface enhanced Raman spectroscopy: label-free protein detection using a G-quadruplex DNA aptamer. Chem Commun. 2010;46(16):2799-801. doi: Doi 10.1039/B920941g. PubMed PMID: ISI:000276376000025.
417. Nitsche A, Kurth A, Dunkhorst A, Panke O, Sielaff H, Junge W, et al. One-step selection of Vaccinia virus-binding DNA aptamers by MonoLEX. BMC Biotechnol. 2007;7:-. doi: Artn 48
Doi 10.1186/1472-6750-7-48. PubMed PMID: ISI:000249733900001.
418. Tripp RA, Moore D, Jones L, Sullender W, Winter J, Anderson LJ. Respiratory syncytial virus G and/or SH protein alters Th1 cytokines, natural killer cells, and neutrophils responding to pulmonary infection in BALB/c mice. J Virol. 1999;73(9):7099-107. PubMed PMID: WOS:000081964700001.
419. Adams MJ. Chemometrics in Analytical Spectroscopy. 2nd Edition ed. Cambridge: Royal Society of Chemistry; 2004.
420. K. R. Beebe RJPaMBS. Chemometrics: A Practical Guide. New York: Wiley & Sons 1998.
421. Barker M, Rayens W. Partial least squares for discrimination. J Chemometr. 2003;17(3):166-73. doi: Doi 10.1002/Cem.785. PubMed PMID: ISI:000182005800002.
422. Basu S, Jana S, Pande S, Pal T. Interaction of DNA bases with silver nanoparticles: Assembly quantified through SPRS and SERS. J Colloid Interf Sci. 2008;321(2):288-93. doi: DOI 10.1016/j.jcis.2008.02.015. PubMed PMID: ISI:000255134300006.
423. Kneipp K, Flemming J. Surface-Enhanced Raman Scattering (SERS) of Nucleic Acids Adsorbed On Colloidal Silver Particles. J Mol Struc. 1986;145:173-9.

424. Kundu J, Neumann O, Janesko BG, Zhang D, Lal S, Barhoumi A, et al. Adenine- and Adenosine Monophosphate (AMP)-Gold Binding Interactions Studied by Surface-Enhanced Raman and Infrared Spectroscopies. J Phys Chem C. 2009;113(32):14390-7. doi: Doi 10.1021/Jp903126f. PubMed PMID: ISI:000268661300050.
425. Rycenga M, McLellan JM, Xia YN. A SERS study of the molecular structure of alkanethiol monolayers on Ag nanocubes in the presence of aqueous glucose. Chem Phys Lett. 2008;463(1-3):166-71. doi: DOI 10.1016/j.cplett.2008.08.062. PubMed PMID: ISI:000259150400033.
426. Basu S, Jana S, Pande S, Pal T. Interaction of DNA bases with silver nanoparticles: Assembly quantified through SPRS and SERS. J Coll Inter Sci. 2008;321(2):288-93. doi: DOI 10.1016/j.jcis.2008.02.015. PubMed PMID: ISI:000255134300006.
427. Naumann D. FT-infrared and FT-Raman spectroscopy in biomedical research. Appl Spectrosc Rev. 2001;36(2-3):239-98. PubMed PMID: ISI:000171286200004.
428. Podstawka E, Ozaki Y, Proniewicz LM. Adsorption of S-S containing proteins on a colloidal silver surface studied by surface-enhanced Raman spectroscopy. Applied Spectroscopy. 2004;58(10):1147-56. doi: Doi 10.1366/0003702042336073. PubMed PMID: WOS:000224815500002.
429. Podstawka E, Ozaki Y, Proniewicz LM. Part II: Surface-enhanced Raman spectroscopy investigation of methionine containing fleterodipeptides adsorbed on colloidal silver. Applied Spectroscopy. 2004;58(5):581-90. doi: Doi 10.1366/000370204774103417. PubMed PMID: WOS:000221415000014.
430. Podstawka E, Ozaki Y, Proniewicz LM. Part I: Surface-enhanced Raman spectroscopy investigation of amino acids and their homodipeptides adsorbed on colloidal silver. Applied Spectroscopy. 2004;58(5):570-80. doi: Doi 10.1366/000370204774103408. PubMed PMID: WOS:000221415000013.
431. Stewart S, Fredericks PM. Surface-enhanced Raman spectroscopy of peptides and proteins adsorbed on an electrochemically prepared silver surface. Spectrochim Acta A. 1999;55(7-8):1615-40. PubMed PMID: ISI:000081025900029.
432. Yarasi S, Billinghurst BE, Loppnow GR. Vibrational properties of thymine, uracil and their isotopomers. J Raman Spectrosc. 2007;38(9):1117-26. doi: Doi 10.1002/Jrs.1722. PubMed PMID: ISI:000249470600008.
433. Simoes EAF. Respiratory syncytial virus infection. Lancet. 1999;354(9181):847-52. doi: Doi 10.1016/S0140-6736(98)10263-5. PubMed PMID: WOS:000082400700040.
434. Culha M, Stokes D, Allain LR, Vo-Dinh T. Surface-enhanced Raman scattering substrate based on a self-assembled monolayer for use in gene diagnostics. Anal Chem. 2003;75(22):6196-201. doi: Doi 10.1021/Ac0346003. PubMed PMID: ISI:000186601500024.
435. Klumpp K, Ruigrok RWH, Baudin F. Roles of the influenza virus polymerase and nucleoprotein in forming a functional RNP structure. EMBO J. 1997;16(6):1248-57. PubMed PMID: ISI:A1997WQ71800012.
436. Ruigrok RWH, Baudin F. Structure of Influenza-Virus Ribonucleoprotein-Particles .2. Purified Rna-Free Influenza-Virus Ribonucleoprotein Forms Structures That Are Indistinguishable from the Intact Influenza-Virus Ribonucleoprotein-Particles. J Gen Virol. 1995;76:1009-14. PubMed PMID: ISI:A1995QR22600033.

437. Easterday BC, and V. S. Hinshaw. Influenza. 9th ed. In B. W. Calnek HJB, C. W. Beard, W. M. Reid, and H. W. Yoder, Jr. (ed.), editor. Iowa State University Press, Ames.1991.
438. Thompson WW, Shay DK, Weintraub E, Brammer L, Cox N, Anderson LJ, et al. Mortality associated with influenza and respiratory syncytial virus in the United States. Jama-J Am Med Assoc. 2003;289(2):179-86. PubMed PMID: ISI:000180226400028.
439. WHO. Inlfuenza (Seasonal) 2010 [updated 2010 2-15-2010; cited]. Available from: http://www.who.int/mediacentre/factsheets/fs211/en/index.html.
440. Beveridge WIB. The Chronicle of Influenza Epidemics. Hist Phil Life Sci. 1991;13(2):223-35. PubMed PMID: ISI:A1991HE62600002.
441. Dybing JK, Schultz-Cherry S, Swayne DE, Suarez DL, Perdue ML. Distinct pathogenesis of hong kong-origin H5N1 viruses in mice compared to that of other highly pathogenic H5 avian influenza viruses. J Virol. 2000;74(3):1443-50. PubMed PMID: ISI:000084738100041.
442. Yuen KY, Chan PKS, Peiris M, Tsang DNC, Que TL, Shortridge KF, et al. Clinical features and rapid viral diagnosis of human disease associated with avian influenza A H5N1 virus. Lancet. 1998;351(9101):467-71. PubMed PMID: ISI:000072097700009.
443. de Jong MD, Simmons CP, Thanh TT, Hien VM, Smith GJD, Chau TNB, et al. Fatal outcome of human influenza A (H5N1) is associated with high viral load and hypercytokinemia. Nat Med. 2006;12(10):1203-7. doi: Doi 10.1038/Nm1477. PubMed PMID: ISI:000241102200039.
444. Li ZJ, Jiang YP, Jiao PR, Wang AQ, Zhao FJ, Tian GB, et al. The NSI gene contributes to the virulence of H5N1 avian influenza viruses. J Virol. 2006;80(22):11115-23. doi: Doi 10.1128/Jvi.00993-06. PubMed PMID: ISI:000241821300021.
445. Mase M, Tanimura N, Imada T, Okamatsu M, Tsukamoto K, Yamaguchi S. Recent H5N1 avian Influenza A virus increases rapidly in virulence to mice after a single passage in mice. J Gen Virol. 2006;87:3655-9. doi: DOI 10.1099/vir.0.81843-0. PubMed PMID: ISI:000242468600022.
446. Muramoto Y, Le TQM, Phuong LS, Nguyen T, Nguyen TH, Sakai-Tagawa Y, et al. Pathogenicity of H5N1 influenza A viruses isolated in Vietnam between late 2003 and 2005. J Vet Med Sci. 2006;68(7):735-7. PubMed PMID: ISI:000239608000015.
447. Muramoto Y, Le TQM, Phuong LS, Nguyen T, Nguyen TH, Sakai-Tagawa Y, et al. Molecular characterization of the hemagglutinin and neuraminidase genes of H5N1 influenza A viruses isolated from poultry in Vietnam from 2004 to 2005. J Vet Med Sci. 2006;68(5):527-31. PubMed PMID: ISI:000238488800021.
448. Stevens J, Blixt O, Tumpey TM, Taubenberger JK, Paulson JC, Wilson IA. Structure and receptor specificity of the hemagglutinin from an H5N1 influenza virus. Science. 2006;312(5772):404-10. doi: DOI 10.1126/science.1124513. PubMed PMID: ISI:000236941800041.
449. Conenello GM, Zamarin D, Perrone LA, Tumpey T, Palese P. A single mutation in the PB1-F2 of H5N1 (HK/97) and 1918 influenza A viruses contributes to increased virulence. PLoS pathogens. 2007;3(10):1414-21. doi: ARTN e141
DOI 10.1371/journal.ppat.0030141. PubMed PMID: ISI:000251114100007.

450. Zamarin D, Garcia-Sastre A, Xiao XY, Wang R, Palese P. Influenza virus PB1-F2 protein induces cell death through mitochondrial ANT3 and VDAC1. PLoS pathogens. 2005;1(1):40-54. doi: ARTN e4
DOI 10.1371/journal.ppat.0010004. PubMed PMID: ISI:000202893700007.
451. Zamarin D, Ortigoza MB, Palese P. Influenza A virus PB1-F2 protein contributes to viral pathogenesis in mice. J Virol. 2006;80(16):7976-83. doi: Doi 10.1128/Jvi.00415-06. PubMed PMID: ISI:000239557700019.
452. Munier S, Larcher T, Cormier-Aline F, Soubieux D, Su B, Guigand L, et al. A Genetically Engineered Waterfowl Influenza Virus with a Deletion in the Stalk of the Neuraminidase Has Increased Virulence for Chickens. J Virol. 2010;84(2):940-52. doi: Doi 10.1128/Jvi.01581-09. PubMed PMID: ISI:000272994300025.
453. Zhou HB, Yu ZJ, Hu Y, Tu JG, Zou W, Peng YP, et al. The Special Neuraminidase Stalk-Motif Responsible for Increased Virulence and Pathogenesis of H5N1 Influenza A Virus. Plos One. 2009;4(7). doi: Artn E6277
Doi 10.1371/Journal.Pone.0006277. PubMed PMID: ISI:000268119500012.
454. Chen WS, Calvo PA, Malide D, Gibbs J, Schubert U, Bacik I, et al. A novel influenza A virus mitochondrial protein that induces cell death. Nat Med. 2001;7(12):1306-12. PubMed PMID: ISI:000172610300035.
455. Kash JC, Tumpey TM, Proll SC, Carter V, Perwitasari O, Thomas MJ, et al. Genomic analysis of increased host immune and cell death responses induced by 1918 influenza virus. Nature. 2006;443(7111):578-81. doi: Doi 10.1038/Nature05181. PubMed PMID: ISI:000240988200044.
456. Salomon R, Franks J, Govorkova EA, Ilyushina NA, Yen HL, Hulse-Post DJ, et al. The polymerase complex genes contribute to the high virulence of the human H5N1 influenza virus isolate A/Vietnam/1203/04. J Exp Med. 2006;203(3):689-97. doi: Doi 10.1084/Jem.20051938. PubMed PMID: ISI:000236520800022.
457. Boulo S, Akarsu H, Ruigrok RWH, Baudin F. Nuclear traffic of influenza virus proteins and ribonucleoprotein complexes. Virus Res. 2007;124(1-2):12-21. doi: DOI 10.1016/j.virusres.2006.09.013. PubMed PMID: ISI:000244924900002.
458. Berdat D, Rodriguez ACM, Herrera F, Gijs MAM. Label-free detection of DNA with interdigitated micro-electrodes in a fluidic cell. Lab Chip. 2008;8(2):302-8. doi: Doi 10.1039/B712609c. PubMed PMID: ISI:000252758100014.
459. Grajcar L, El Amri C, Ghomi M, Fermandjian S, Huteau V, Mandel R, et al. Assessment of adenyl residue reactivity within model nucleic acids by surface enhanced Raman spectroscopy. Biopolymers. 2006;82(1):6-28. doi: Doi 10.1002/Bip.20455. PubMed PMID: ISI:000236786200002.
460. Huh YS, Chung AJ, Erickson D. Surface enhanced Raman spectroscopy and its application to molecular and cellular analysis. Microfluid Nanofluid. 2009;6(3):285-97. doi: DOI 10.1007/s10404-008-0392-3. PubMed PMID: ISI:000264103500001.
461. Kustner B, Gellner M, Schutz M, Schoppler F, Marx A, Strobel P, et al. SERS Labels for Red Laser Excitation: Silica-Encapsulated SAMs on Tunable Gold/Silver Nanoshells. Angew Chem Int Edit. 2009;48(11):1950-3. doi: DOI 10.1002/anie.200804518. PubMed PMID: ISI:000264301500011.

462. Monaghan PB, McCarney KM, Ricketts A, Littleford RE, Docherty F, Smith WE, et al. Bead-based DNA diagnostic assay for chlamydia using nanoparticle-mediated surface-enhanced resonance Raman scattering detection within a lab-on-a-chip format. Anal Chem. 2007;79(7):2844-9. doi: Doi 10.1021/Ac061769i. PubMed PMID: ISI:000245304300027.
463. Yea K, Lee S, Kyong JB, Choo J, Lee EK, Joo SW, et al. Ultra-sensitive trace analysis of cyanide water pollutant in a PDMS microfluidic channel using surface-enhanced Raman spectroscopy. Analyst. 2005;130(7):1009-11. doi: Doi 10.1039/B501980j. PubMed PMID: ISI:000229861800006.
464. Papadopoulou E, Bell SEJ. Label-Free Detection of Nanomolar Unmodified Single- and Double-Stranded DNA by Using Surface-Enhanced Raman Spectroscopy on Ag and Au Colloids. Chem-Eur J. 2012;18(17):5394-400. doi: DOI 10.1002/chem.201103520. PubMed PMID: ISI:000302868100035.
465. Prado E, Daugey N, Plumet S, Servant L, Lecomte S. Quantitative label-free RNA detection using surface-enhanced Raman spectroscopy. Chem Commun. 2011;47(26):7425-7. doi: Doi 10.1039/C1cc11925g. PubMed PMID: ISI:000291823400039.
466. Driskell JD, Tripp RA. Label-free SERS detection of microRNA based on affinity for an unmodified silver nanorod array substrate. Chem Commun. 2010;46(19):3298-300. doi: Doi 10.1039/C002059a. PubMed PMID: ISI:000277318000018.
467. Musumarra G, Barresi V, Condorelli DF, Fortuna CG, Scire S. Potentialities of multivariate approaches in genome-based cancer research: identification of candidate genes for new diagnostics by PLS discriminant analysis. J Chemometr. 2004;18(3-4):125-32. doi: Doi 10.1002/Cem.846. PubMed PMID: ISI:000223467300002.
468. Brereton RG. Chemometrics for Pattern Recognition. Chichester: J. Wiley & Sons, Ltd.; 2009.